

2m11. 2823.10

Université de Montréal

**The Distribution and Origin of Radon, CO₂, and SO₂ Gases and Multifractal
Behaviour of SO₂ at Masaya Volcano, Nicaragua**

par

Katie St-Amand
Département de géologie
Faculté des Arts et des Sciences

Mémoire présenté à la Faculté des études supérieures
en vue de l'obtention du grade de
Maître ès sciences (M. Sc.)

Octobre 1999
Université de Montréal

© Katie St-Amand, 1999



Doc 272310

Université de Montréal

The Distribution and Origin of Radon, CO₂, and SO₂ Gases and Metalliferous
Hydrothermal SO₂ at Masaya Volcano, Nicaragua

QE

3

U54

1999

n. 006

Mention présentée à la Faculté des études supérieures
et au de l'obtention du grade de
Maître en sciences (M.Sc.)

Octobre 1999

Faculté de génie

2, rue St-Amand, 1001



Université de Montréal
Faculté des études supérieures

Ce mémoire intitulé

**The Distribution and Origin of Radon, CO₂, and SO₂ Gases and Multifractal
Behaviour of SO₂ at Masaya Volcano, Nicaragua**

Présenté par:

Katie St-Amand

a été évalué par un jury composé des personnes suivantes:

Président-rapporteur: Jacques G. Martignole

Membre du jury: John Stix

Membre du jury: Hélène Gaonac'h

Membre du jury: Walter E. Trzcienski

À Jeanne-Aimée Bisson (1922-1996), mon inspiration jusqu'au dernier jour et pour
l'éternité...

Abstract

Active volcanoes represent a challenge to human since a large portion of the world's population lives on rich and cultivable volcanic lands. Thus, it is important to find and develop safe ways to understand and forecast volcanic activity. Although difficult to sample directly, volcanic gases are considered good indicators of volcanic activities and may be remotely monitored in many cases. Soil gases such as CO₂ and radon are easy to sample around a volcano and are thought to respond to fluctuations of the activity of a volcano. SO₂ emissions are also relatively easy to monitor from a distance and may also reflect the state of the volcano.

This thesis investigates the ongoing degassing at Masaya volcano, Nicaragua. It is a basaltic-andesitic caldera, known to have been active since the Spanish arrival in the 16th century and continuing through the 20th century (lava lakes, strombolian explosions, and degassing). It is degassing a volcanic plume composed essentially of water, carbon dioxide, and sulfur dioxide since its reactivation in 1993. CO₂, carbon isotopes and radon profiles were measured perpendicularly to a suspected fracture in order to define spatial and temporal patterns of soil gases and the possible location of fractures. The results indicate CO₂ and radon concentrations maxima in the more active parts of the fumarolic fields, which may indicate a fracture on the northern flank of San Fernando crater. The origin and transport of such gases are discussed in a degassing model and results are correlated with other similar volcanoes. SO₂ measurements were made also to monitor degassing variations, on a daily and monthly basis, and compared to earlier measurements made at Masaya. The SO₂ values obtained in 1997 indicate level of degassing similar to the 1979-1980 degassing period. Values obtained in 1998 shows an increased in the

degassing compared to 1997. An estimate of the quantity of SO_2 is made and a study of the transport and removal of SO_2 in the volcanic plume is presented. The SO_2 measurements acquired were also used in a statistical approach in order to study the scaling and the degree of multifractality of the SO_2 degassing at the Masaya volcano. Parameters of universality obtained for SO_2 series suggest signatures characteristic of atmospheric turbulence.

Résumé

Le volcan Masaya est une caldeira basaltique localisée à 11.984° N de latitude et 86.161° W de longitude sur la partie ouest du graben nicaraguaïen. Cette caldeira fait partie de la chaîne volcanique quaternaire de l'Amérique centrale et est entourée à l'ouest par la Formation Las Sierras, à l'est par le lac Nicaragua et au nord par le lac Managua. Sa formation serait attribuable à des effondrements successifs de l'édifice volcanique Las Sierras. Des cônes de forme semi-circulaire, se sont formés à la suite de la formation de la caldeira. Deux cônes principaux se situent à l'intérieur de la caldeira et forment le complexe volcanique de Masaya, composé d'est en ouest des cratères d'effondrement de San Juan, San Fernando (Masaya), Santiago, Nindirí et San Pedro. Une particularité de Masaya est d'avoir été le site d'activités explosives basaltiques inusitées (20,000-6,500 ans). L'activité volcanique rencontrée au volcan Masaya au cours des derniers siècles comprend des coulées de lave (1670 et 1772), des lacs de lave épisodiques (le dernier en date fut présent de juin à août 1993). Des cycles de fort dégazage ont été enregistrés de façon cyclique. Le cratère Santiago est actuellement le site de dégazage intensif depuis la réactivation de 1993.

Les objectifs de ce mémoire sont premièrement d'évaluer la distribution spatiale et temporelle du CO₂, des isotopes de carbone et du radon. Une discussion de l'origine et du transport de ces gaz par un modèle de dégazage est présentée. Deuxièmement, estimer la quantité de SO₂ émis par le Masaya par des analyses pétrologiques et par télédétection (correlation spectrometry). Le transport et la diffusion du SO₂ de la colonne volcanique dans l'atmosphère sont discutés. Troisièmement, analyser statistiquement des séries de SO₂ suivant leur aspect scaling.

Afin d'atteindre ces objectifs, deux séjours au volcan Masaya ont été effectués en compagnie d'une équipe de recherches multidisciplinaires internationales de février à avril 1997 et 1998. Des mesures de gaz de sol et la surveillance de la colonne volcanique ont été entrepris dans le but d'établir l'état actuel de l'activité volcanique et de comparer les résultats de cette étude avec des études similaires effectuées précédemment au Masaya et à d'autres volcans. Le CO₂, le radon et le SO₂ sont relativement faciles à mesurer et considérés comme de bons indicateurs répondant aux fluctuations de l'activité volcanique d'un volcan.

Le cratère non actif San Fernando est traversé sur le flanc nord par une fracture dont on observe en partie l'expression à la surface. Cette fracture présente à plusieurs endroits des zones de fumerolles de basses températures. Des profils de mesures effectuées perpendiculairement à ces zones indiquent des maxima de concentration en CO₂ et radon et de flux de CO₂ dans les régions les plus actives des zones fumeroliques où la fracture est la plus susceptible de se localiser. Les variations rencontrées le long de ces profils suggèrent un dégazage plus efficace dans les régions où la fracture est la plus expressive. Cependant, l'hétérogénéité de la perméabilité du sol explique les concentrations de CO₂ relativement élevées dans le sol où aucun flux de CO₂ significatif n'a été mesuré. Les signatures isotopiques $\delta^{13}\text{C}$ obtenues indiquent un mélange de deux sources possibles telles que le CO₂ magmatique, le CO₂ de roches carbonatées, ou la fractionation du gaz pendant son transport.

Le cratère actif de Santiago émettait entre 240 et 1100 tonnes par jour de SO₂ en février et mars 1997. Les valeurs obtenues pour la période de février à avril

1998 varient de 200 et 7400 tonnes par jour. Des analyses pétrologiques effectuées sur des bombes éjectées le 12 novembre 1997 indiquent de faibles concentrations de soufre et de chlore. Ces analyses suggèrent que le magma à faible profondeur est partiellement à fortement dégazé. Afin de mieux comprendre la dispersion de la colonne de gaz, des mesures de flux SO_2 ont été effectuées simultanément à 5 et 15 km du cratère actif de Santiago. Une comparaison des profils correspondant à la même section de colonne à deux moments (et distances) différentes indiquent qu'il y a perte de gaz pendant le transport atmosphérique ou possiblement une accumulation de gaz proche de la source. Cependant, des mesures simultanées similaires faites le lendemain à 15 et 30 km du cratère indiquent un excès de SO_2 . Ces données suggèrent une influence important des brises marines sur le transport et la dispersion de la plume volcanique.

La variabilité temporelle d'un phénomène donné est un problème fréquemment rencontré. Les recherches sont souvent de courte durée et l'échantillonnage irrégulier dans le temps, deux semaines chaque année par exemple, ce qui a pour effet de sous échantillonner et de compliquer l'interprétation et la modélisation du phénomène étudié. L'observation de fortes variations du flux de SO_2 pendant la journée sont problématiques lors de l'interprétation et d'établissement de modèles de dégazage. De nouvelles techniques d'analyse statistique sont actuellement développées afin de mieux comprendre et modéliser les phénomènes atmosphériques tel que des champs de température, de vents et de données climatiques. Une approche statistique similaire fut utilisée afin de caractériser le scaling ou invariance d'échelle et d'évaluer le degré de fractalité des signaux obtenues par COSPEC. Les résultats obtenus démontrent une invariance d'échelle de

2 à 600 secondes avec un exposant $\beta=2.8 \pm 0.1$. Des paramètres d'universalité, $\alpha=1.88$, $C_1=0.02$ et $H=0.38$ sont caractéristiques de la turbulence atmosphérique dans laquelle le SO_2 est entraîné. Ces analyses ont permis de mieux cerner l'influence de l'atmosphère sur les mesures du SO_2 obtenues.

Élément important de compréhension et de prédiction de l'activité volcanique, les gaz volcaniques sont relativement faciles à échantillonner et analyser. Utilisés en combinaison avec d'autres techniques géophysiques, géochimiques et de télédétection, les gaz volcaniques peuvent faciliter l'étude et la compréhension globale d'un système volcanique.

Acknowledgements

First and foremost, I would like to thank my two supervisors, H  l  ne Gaonac'h and John Stix who have supported me throughout the duration of this thesis. I acknowledge Shaun Lovejoy of McGill University for his insight on the theory of atmospheric turbulence. I also would like to thank the people who have helped me in the field, particularly Alexandre Beaulieu, Glyn Williams-Jones and Pierre Delmelle. A big thanks to the personnel of INETER, Wilfried Strauch and Martha Navarro for their collaboration and also Oscar Perez and Alejandro Acosta who have been a great help with their knowledge of Masaya volcano and their support in the field. It is important to acknowledge Mrs. Gutierrez who granted us unlimited access to the Parque Nacional del Volc  n Masaya and the personnel of the park, rangers and guides who were indispensable. I acknowledge also Neil Arner from the University of Toronto and Glenn Poirier from McGill University without whom isotopic and petrologic analyses would have been much more difficult. A gigantic *Muchas Gracias* to the family G  mes de Castillo who welcomed us not only at their Hotel Regis but also into their hearts. A particular thanks to Sophie Leblanc, Kazuko Saruwatari and Roberto Cannav   for their encouragements and to the personnel of the Universit   de Montr  al, Lucie Charbonneau and Ginette for their support. Finally, I sincerely thank my family for their unconditional love and support and my late grand mother Jeanne Aim  e who, from her place among the stars, will inspire me to go beyond my dreams.

Table of Contents

Abstract	i
Résumé	iii
Acknowledgements	vii
List of Figures	x
List of Tables	xiv
General Introduction	1
Introduction	2
Objectives	3
Location	4
Geological Setting	9
Regional Geology	9
Local Geology	11
Volcanic Activity	16
References	19
Chapter I	23
Abstract	24
Introduction	25
Methodology	28
Station Locations	28
Soil Gas Measurements	30
Carbon Dioxide	30
Carbon Dioxide Fluxes	30
Carbon Isotopes in CO ₂ Soil Gas	31
Radon	31
Temperature	34
Results	34
Visual Observations	34
Carbon Dioxide	35
Carbon Dioxide Fluxes	38
Carbon Isotopes in CO ₂ Soil Gas	38
Radon	41
Temperature	43
Discussion	45
Origin of Carbon Dioxide	45
Origin of Radon	51
A Degassing Model	53
Conclusions	56
References	58

Chapter II	61
Abstract	62
Introduction	63
Methodology	64
SO ₂ Flux	64
SO ₂ Flux Errors	68
Petrology	70
Results	73
SO ₂ Fluxes, 1997-1998	73
Petrological Data	84
SO ₂ Budget at Masaya	88
17-18 March 1998 Gas Dispersion Studies	89
17 March 1998	90
18 March 1998	103
Discussion	109
Degassing at Masaya	109
Degassing Model	110
Plume Transport (17-18 March)	112
Petrology	114
Conclusions	115
References	117
Chapter III	120
Abstract	121
Introduction	122
Data acquisition	125
Scaling properties of the SO₂ degassing	127
Multiscaling	132
Conclusions	143
References	145
General Conclusions	149
Conclusions	150
Recommendations for Future Work	151
APPENDIX A	153
APPENDIX B	158
APPENDIX C	163
APPENDIX D	174
APPENDIX E	180
APPENDIX F	184
APPENDIX G	188
APPENDIX H	214
APPENDIX I	224
APPENDIX J	258

List of Figures

Figure I-1	Map of Nicaragua showing the location of Masaya Caldera (from Walker et al., 1993)._____	5
Figure I-2	Map of Masaya Caldera and its surroundings (from Maciejewski, 1995, after van Wyk de Vries, 1994)._____	6
Figure I-3	Map of the structural features of Masaya caldera enclosing Arenal, Cerro Montoso, Nindirí and Masaya cones (from Maciejewski, 1995, after Walker et al., 1993 and Bice, 1980)._____	7
Figure I-4	Map of Masaya caldera with its structural features such as fissures and the pit craters, Masaya (San Fernando), the active vent Santiago, Nindirí and San Pedro (from Rymer et al., 1998)._____	8
Figure I-5	Map of the volcanic centers (dots) of the Central American volcanic front (from Carr, 1984)._____	10
Figure I-6	Geological map of Masaya caldera (from Walker et al., 1993 after Williams, 1983)._____	12
Figure I-7	Map of the 1670 and 1772 lava flows at Masaya caldera (after Kieffer and Creusot-Eon, 1992)._____	14
Figure I-8	View of the active vent at the bottom of the Santiago crater in 1997. _____	15
Figure 1.1	Topographic map of Masaya showing the locations of CO ₂ , δ ¹³ C, radon and temperature measurements for the profiles B, C, A and MUSEO from the summit to the base of San Fernando Crater. Contour lines are every 20 meters._____	29
Figure 1.2	Topographic map of Masaya showing the location of CO ₂ , δ ¹³ C, radon and temperature of a) profile N at the Nindirí crater, b) profile ARENAL at the Arenal parasitic cone in the northwest part of the caldera._____	32
Figure 1.3	CO ₂ concentrations for (a) and (b) line A at the base of San Fernando, (c) line B near the summit of San Fernando crater, (d) Line C at approximately 200 meters south of line A, (e) Comalito (line C extension), (f) line Museo, (g) line Arenal, and (h) and (i) line N. Profiles (a) to (g) are oriented southeast-northwest, (h) and (i) are southwest-northeast oriented._____	36

- Figure 1.4 $\delta^{13}\text{C}$ signatures for (a) and (b) line A at the base of San Fernando, (c) line B near the summit of San Fernando crater, (d) line C at approximately 200 meters south of line A, (e) Comalito (line C extension) (f) line Museo, and (g) and (h) line N. Profiles (a) to (f) are oriented southeast-northwest, (g) and (h) are southwest-northeast oriented. _____ 40
- Figure 1.5 Radon measurements for (a) and (b) line A at the base of San Fernando, (c) line B near the summit of San Fernando crater, (d) line C at approximately 200 meters south of line A, and (e) line N. Profiles (a) to (d) are oriented southeast-northwest, (e) is southwest-northeast oriented. _____ 42
- Figure 1.6 Temperature profiles for (a) and (b) line A at the base of San Fernando, (c) line B near the summit of San Fernando crater, (d) line C at approximately 200 meters south of line A, and (e) line N. Profiles (a) to (d) are oriented southeast-northwest, (e) is southwest-northeast oriented. _____ 44
- Figure 1.7 (a) to (d) CO_2 -temperature, CO_2 - $\delta^{13}\text{C}$, temperature- $\delta^{13}\text{C}$, and CO_2 -radon correlations for line A, B and C for 1997, and line A for 1998. _____ 46
- Figure 1.8 CO_2 concentrations versus CO_2 fluxes for line A, B, and C on the north flank of San Fernando. _____ 47
- Figure 1.9 A schematic model of the degassing paths at Masaya Caldera, Nicaragua. _____ 55
- Figure 2.1 Road map of COSPEC segments (from Johnson et al., 1986). _____ 65
- Figure 2.2 Daily averaged SO_2 emission rate at Masaya volcano measured by COSPEC between February and March 1997. _____ 76
- Figure 2.3 Daily averaged SO_2 emission rate at Masaya volcano measured by COSPEC between February and April 1998. _____ 83
- Figure 2.4 Petrological analyses. (a) Chlorine concentrations versus sulfur concentrations. (b) Chlorine concentrations versus S/Cl ratio. (c) Sulfur concentrations versus S/Cl ratio. (d) Potassium concentrations versus FeO/MgO ratio. (e) Magnesium concentrations versus potassium concentrations. Note that the chlorine concentration is almost twice the sulfur concentrations. Note also that the glass inclusions are generally higher than Pél e's hair and the matrix which may indicate some weathering of the later. _____ 86

- Figure 2.5 Correlations between Ticuantepe measurements and El Crucero. a) T₃ and E₁, b) T₇-T₈ and E₂, c) T₈-T₉ and E₃ d) T₁₁ and E₄, e) T₁₂-T₁₃ and E₅, f) T₁₄ and E₆, g) T₁₅-T₁₆ and E₇, and h) T₁₇-T₁₈ and E₈._____92
- Figure 2.6 The removal factor and the SO₂ fluxes measured at Ticuantepe (5 km from the vent) (See Table 2.10). Note that a positive relation is observed._____99
- Figure 2.7 Schematic representations of (a) a valley breeze, and b) a mountain breeze (modified from Arya, 1999)._____101
- Figure 2.8 AVHRR image of Masaya on 1 March, 1998. Note the bifurcation (or doubling) of the volcanic plume (white clouds on the image). The lines are the surrounding roads. This may explain some unusually high SO₂ flux measurements made during this day (Courtesy of G. Williams-Jones)._____102
- Figure 2.9 Correlations between El Crucero and Masachapa. a) E₁ and M₁, b) E₂ and M₂, c) E₃-E₄ and M₃ d) E₅-E₆ and M₄, e) E₆-E₇ and M₅, f) E₇-E₈ and M₆._____116
- Figure 2.10 Effect of a sea breeze on a degassing source a) daytime, and b) night time. Note that in our case, it is suggested that a mountain/valley breeze may amplify a reverse sea breeze effect during the night.____119
- Figure 2.11 Earth and lunar tide correlations with SO₂ fluxes measurements at Masaya volcano, for nine days during February and March 1998.____98
- Figure 3.1 Map of Masaya volcano and its surrounding indicating the location of data acquisition. The three distances at which measurements were made are Ticuantepe at 5 km from the active crater, El Crucero at 15 km on the Llano Pacaya ridge, and Masachapa at 30 km (From Delmelle et al., submitted)._____126
- Figure 3.2 Examples of COSPEC SO₂ signals used for analysis. (a) temporal series e10a taken during one hour at El Crucero (15 km). (b) Spatial series 27t taken at Ticuantepe (5.5 km). (c) Representation of the temporal and spatial series relative to the volcanic plume._____128
- Figure 3.3 Power spectrum densities of SO₂ signal temporal series. A common $\beta=2.8 \pm 0.1$ fits all series. Note that one of the series exhibits a flat trend at high frequencies and that a break at ~100 seconds is visible but not precisely defined._____130

- Figure 3.4 Power spectrum densities of SO₂ signal spatial series, Ticuantepe 27t and 28t at 5 km from the crater, El Crucero 27e and 17e2 at 15 km, and also Masachapa 18m1 and 18m2 at 30 km. A common $\beta=2.8 \pm 0.1$ value fits all series. Note also the flat trend at high frequencies. There is no visible break at low frequencies in the spatial series. _____ 131
- Figure 3.5 Structure functions of SO₂ signal spatial series. Ticuantepe (a) 27t and (b) 28t at 5 km from the crater, El Crucero (c)27e and (d) 17e2 at 15 km, and also Masachapa (e) 18m1 and (f) 18m2 at 30 km from the source. _____ 133
- Figure 3.6 Structure functions of SO₂ signal temporal series. (a) Ticuantepe 97/03/28, (b) El Crucero 98/03/03, (c) El Crucero 98/03/10a, (d) El Crucero 98/03/10b, (e) El Crucero 98/03/15a. Note the presence of the transitional zone, a break at ~ 75 seconds and a second trend at low frequencies. _____ 135
- Figure 3.7 Example of multiscaling properties, El Crucero at 15 km west from the vent (98/03/17). (a) Scaling exponent structure function empirical curve (dots) and the monofractal curve qH (full line). Note the departure of the empirical curve from the monofractal curve which indicates multiscaling. Note also the linear trend for $q \geq 3.0$. (b) Universal parameters α and C_1 estimation. _____ 139
- Figure 3.8 Multiscaling properties of the temporal series t97 (97/03/28). First regime, (a) scaling exponent structure function. In this case, the empirical curve (dots) does not strongly deviate from the monofractal curve (full line). (b) Universal parameters α and C_1 estimation. Second regime, (c) scaling exponent structure function. Note the departure of the empirical curve from the monofractal curve which indicates multiscaling. Note also the linear trend for $q \geq 3.0$. (d) Universal parameters α and C_1 estimation. _____ 140
- Figure 3.9 Multiscaling properties of the temporal series sp9810a, (98/03/10). First regime, (a) scaling exponent structure function. In this case, the empirical curve (dots) deviate from the monofractal curve (full line). (b) Universal parameters α and C_1 estimation. Second regime, (c) scaling exponent structure function. Note that the empirical curve (dots) is convex and above the monofractal cure (full line) which indicates that this series is not of good quality. _____ 141

List of Tables

Table 1.1	CO ₂ fluxes measured at lines A, C, and B in 1997._____	39
Table 2.1	Segment parameters for COSPEC measurements._____	67
Table 2.2	COSPEC V/VI ratios._____	69
Table 2.3	Error calculations for SO ₂ measurements._____	71
Table 2.4	Normalized standard glass analyses._____	72
Table 2.5	Normalized standard analyses for plagioclase and olivine._____	72
Table 2.6	February-March 1997 SO ₂ flux measurements._____	74
Table 2.7	February-April 1998 SO ₂ flux measurements._____	78
Table 2.8	Average Pélé's hair, glass shards and glassy materials analyses._____	85
Table 2.9	17 March 1998, 5 km-15 km measurement correlations._____	91
Table 2.10	SO ₂ removal factor for 17 March 1998 at Masaya between Ticuantepe (5 km from the crater) and El Crucero (15 km from the crater)._____	98
Table 2.12	18 March 1998, 15 km-30 km measurement correlations._____	104
Table 3.1	α , C ₁ and H universal multifractal parameters._____	137

GENERAL INTRODUCTION

Introduction

Many techniques have been developed in order to study active volcanic sites such as the measurement and distribution of gas, geochemistry of gas, and volcanic materials. Volcanic gases are known to be indicators of volcanic activity but are sometimes dangerous to measure directly due to high level of activity of a volcano or are inaccessible areas of a volcano. However, soil gases such as CO₂ and radon are known to respond to volcanic variations and are relatively safe to sample around a volcanic centre (Allard et al., 1991; Baubron et al., 1991; Brantley and Koepenick, 1995; Heiligmann et al., 1997; Farrar et al., 1998). Remote sensing of sulphur dioxide of volcanic plumes has been found to relate to the subsurface activity such as geochemical variations, magma movement and seismicity of passively and actively degassing volcanoes (Stoiber et al., 1986; Andres et al., 1991; Kazahaya et al., 1994). In addition, remote sensing techniques also are used for atmospheric and environmental studies, which are useful for agricultural management and health risks to human populations living around volcanoes (Wilcox, 1952; Eatough et al., 1994; Bluth et al., 1997; Delmelle et al., 1998). However, high variability in natural phenomenon brings difficulties in the sampling and interpretation of data and the establishment of accurate models. It is important to consider the variability of a phenomenon on a large variety of scales. New statistical methods of analysis of remote sensing data have been recently developed and applied for the study of highly variable phenomenon such as temperature and wind fields, topography, and lava radiance fields (Schmitt et al., 1992; Lavallée et al., 1993; Schertzer et al., 1996; Laferrière et al., 1999). A similar approach may also be applied to study the

variability of SO₂ signals (St-Amand et al., 1998; Gaonac'h et al., 1999). The study of the variability may prove to be important to understand more accurately past and present behaviour and forecast future volcanic activity.

Masaya is a basaltic shield volcano within Masaya caldera located in the Quaternary volcanic chain along the western margin of Central America. A major volcanic edifice composed of several craters lies in the southwestern part of the caldera. Most of the caldera was declared a national park in 1975, and easy access by roads has been provided. Historic volcanic activity includes two major lava flows (1672 and 1770), periodic lava lakes and recurring episodes of intense degassing. Five degassing events have been recorded since 1852; a sixth episode began in 1993 and is still in progress at this moment. Crenshaw et al, (1982) have investigated the caldera structure by radon and mercury measurements. Stoiber et al. (1986) have studied gas compositions and plume concentrations variations at Masaya for the 1972-1978 period. Delmelle et al. (1998) have surveyed the degassing and the dispersion of the volcanic plume emitted by the volcano. Rymer et al. (1998), and Beaulieu (1999) have used combined microgravity techniques, GPS surveys and COSPEC measurements at Masaya. The volcano is presently monitored by a seismic station maintained by INETER (Instituto Nicaragüense de Estudios Territoriales), and the site is regularly visited by international research teams.

Objectives

The main objectives of this thesis are (1) to investigate the spatial and temporal distribution of CO₂, carbon isotope, and radon in soil gas various areas of

the caldera and discuss the origin of these gases, (2) to monitor the SO₂ degassing into the atmosphere by estimating the quantity of gas emitted using the COSPEC and petrological analyses, (3) to discuss the plume transport and dispersion, and (4) to examine the high variability of SO₂ degassing by a statistical approach which investigates scaling properties and the degree of fractality in terms of atmospheric and volcanic sources to the SO₂ variability observed. In order to achieve these goals, two field trips were made in February-April 1997 and 1998 where gas measurements were made and the monitoring of the plume by COSPEC was carried out. Six gas profiles were performed for CO₂, CO₂ fluxes, carbon isotopes, and radon in selected areas of the caldera. The plume gas measurements resulted in a total of 248 SO₂ flux measurements which include 53 measurements (5 days) in 1997 and 194 measurements (24 days) in 1998.

Location

Masaya Caldera and Masaya volcano itself, which lies within the caldera, are situated at 11.984°N 86.161°W in the southwestern part of Nicaragua, 20 km southeast from the capital, Managua (Figure I-1). Masaya is surrounded by the Apoyeque caldera and Nejapa cinder cones to the northwest and Apoyo caldera to the southeast, which are all part of the Quaternary volcanic chain (Figure I-2). The caldera has an elongated shape of about 6 km wide and 11.5 km long, oriented northwest-southeast. Within the caldera lie several volcanic edifices, semi-circularly disposed: Comalito, Masaya, Nindirí, Cerro Montoso and Arenal. These are the manifestations of post-caldera activity (Figure I-3). With an altitude of 624 meters

Figure I-1

Map of Nicaragua showing the location of Masaya Caldera (from Walker et al., 1993).

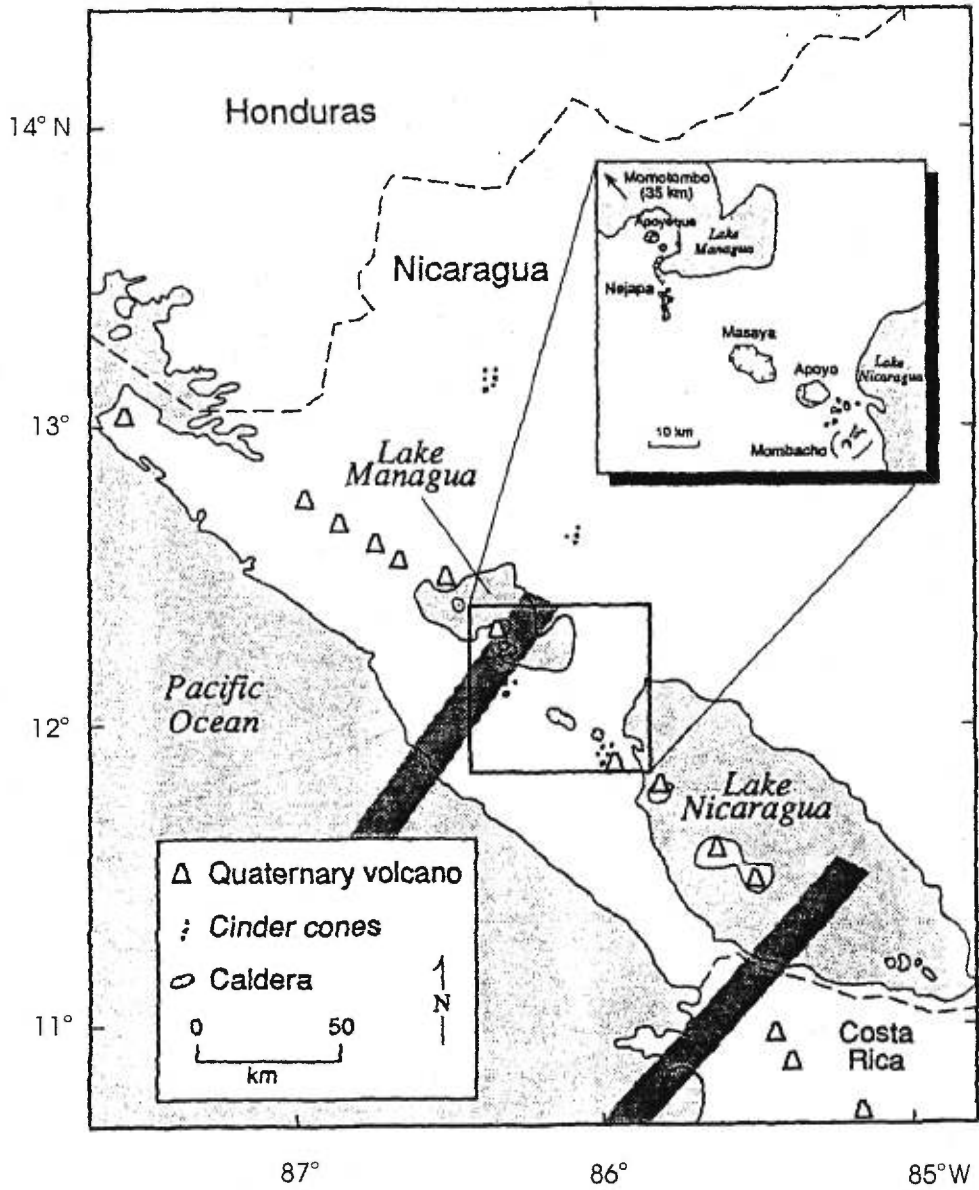


Figure I-2

Map of Masaya Caldera and its surrounding (from Maciejewski, 1995, after van Wyk de Vries, 1994).

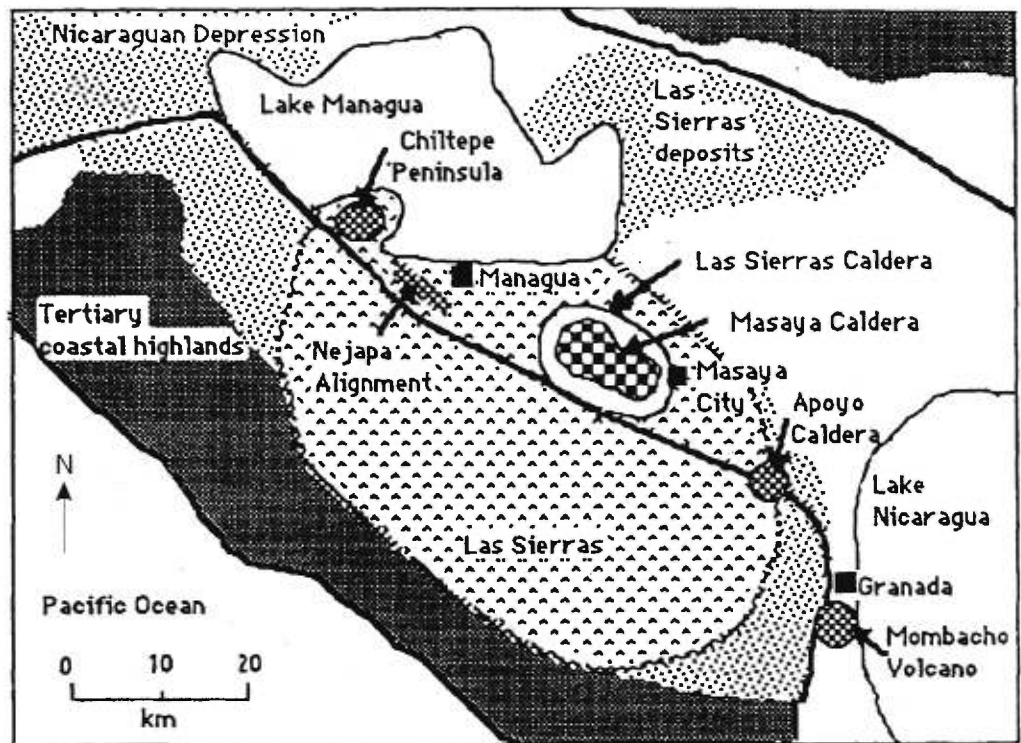


Figure I-3

Map of the structural features of Masaya caldera enclosing Arenal, Cerro Montoso, Nindirí and Masaya cones (from Maciejewski, 1995, after Walker et al., 1993, and Bice, 1980).

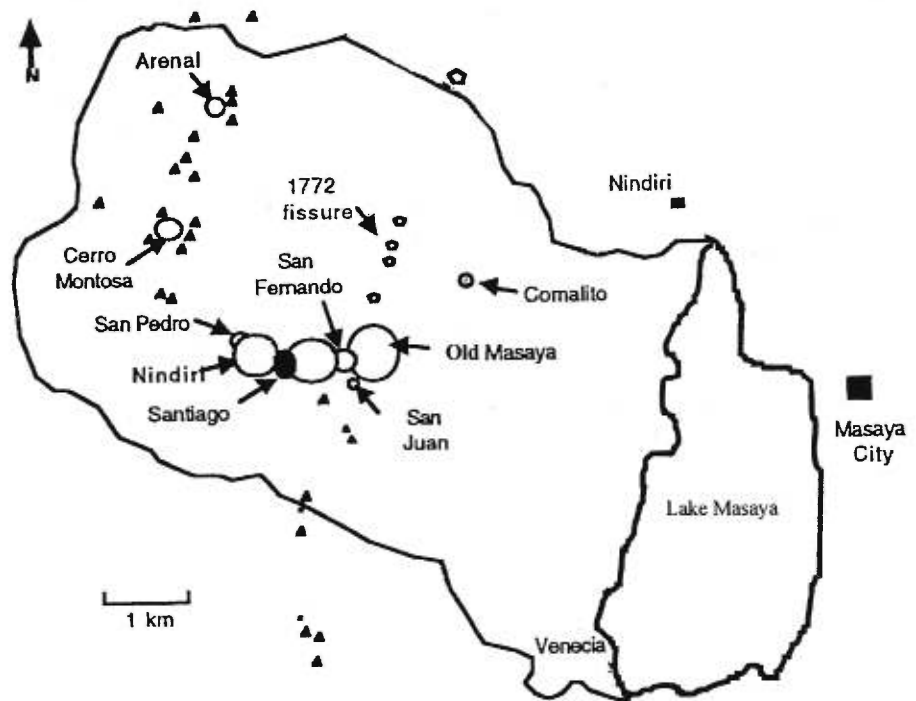
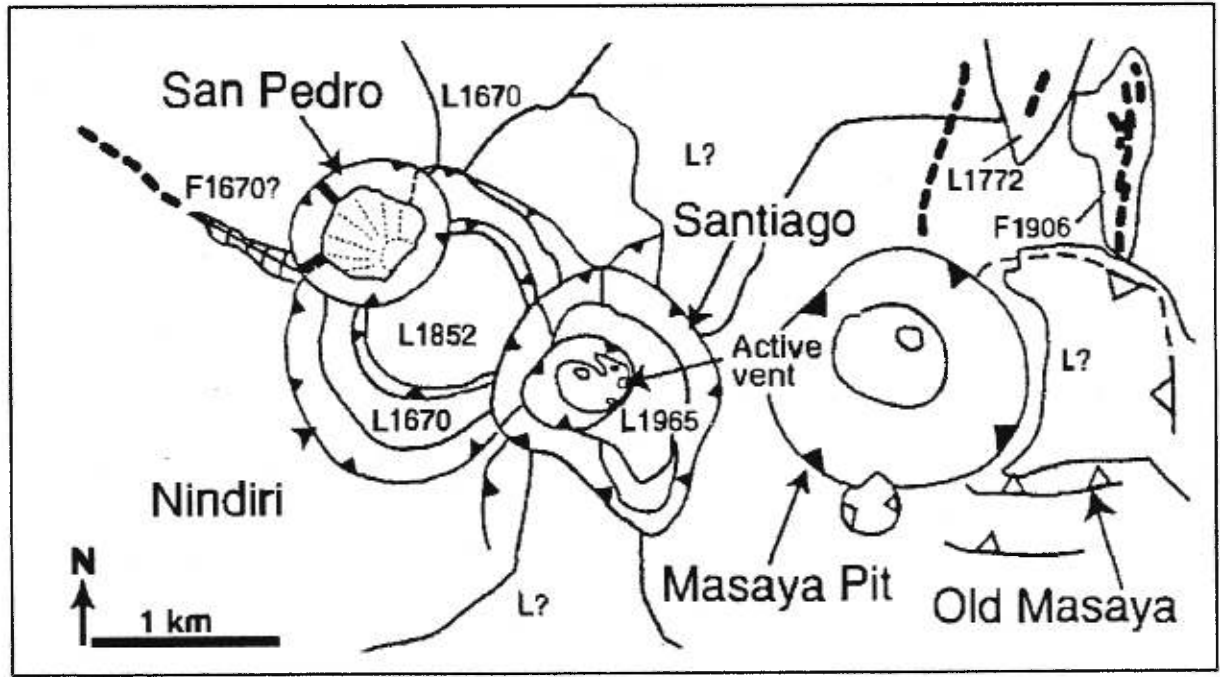


Figure I-4

Map of Masaya caldera with its structural features such as fissures and the pit craters, Masaya (San Fernando), the active vent Santiago, Nindirí and San Pedro (from Rymer et al., 1998).



above sea level, Masaya dominates the caldera's low topography, which average at 265 meters above sea level. The Masaya and Nindirí edifices contain four major pit craters, which are San Fernando, Santiago, Nindirí and San Pedro (Figure I-4).

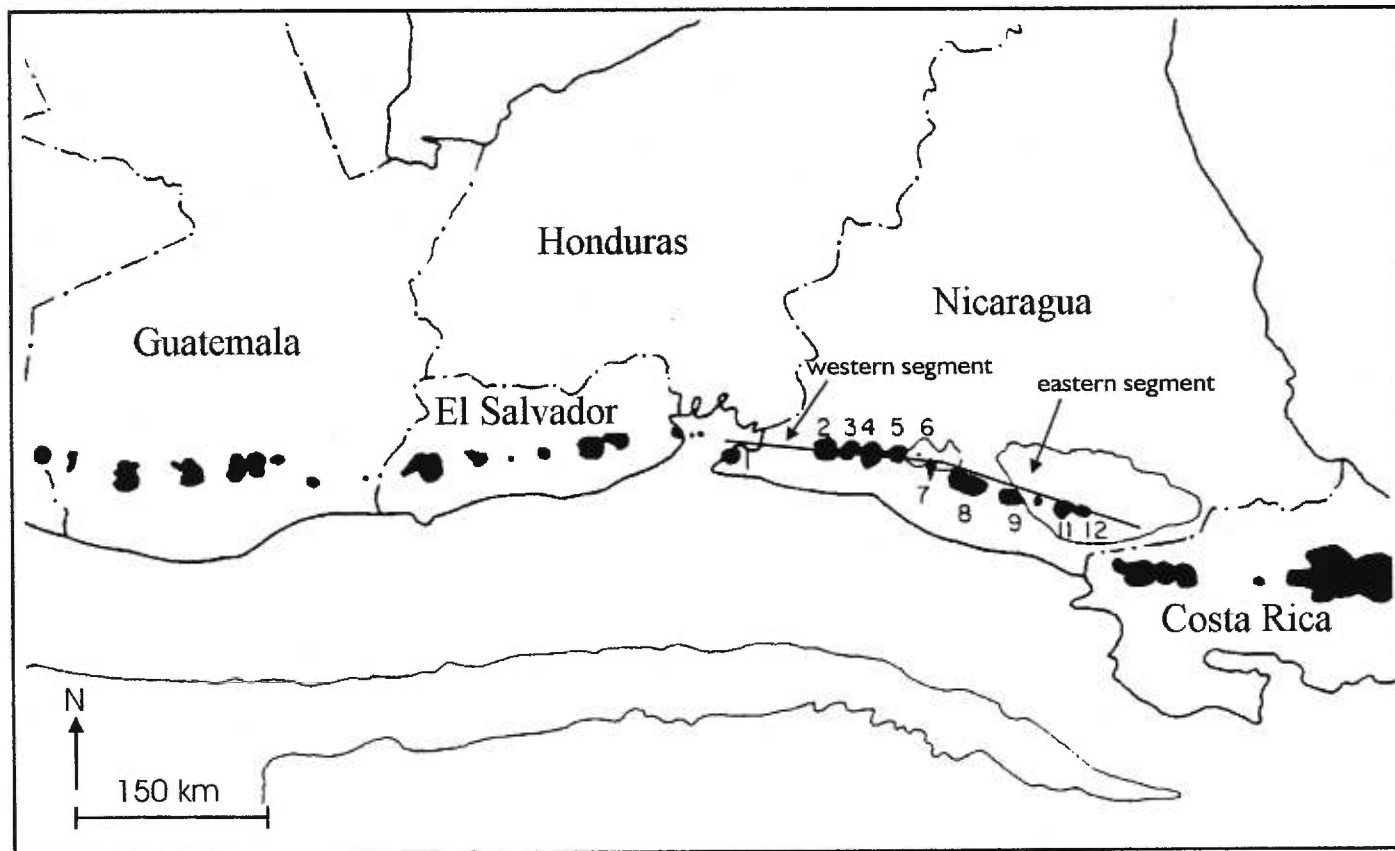
Geological setting

Regional Geology

The basement rocks of Central America may be divided into the northern and the southern terrain. The northern part is thought to be composed of continental sediments of Paleozoic age. In contrast, the southern part where Masaya volcano is located is thought to be of Tertiary age, and composed mainly of oceanic crust and marine sediments. The contact between these two structurally and chemically different terrains may underlie the Managua Graben in the area where the Nejapa cinder cones are aligned (Bice, 1980; Williams, 1983). A volcanic front composed of seven tectonically and volcanically different segments is caused by the convergence of the Cocos and the Caribbean plates and go through all Central America from northwest to southeast (Stoiber et Carr, 1973; Carr, 1984; Johnston et al., 1997). Masaya volcano is located in the eastern part of the Nicaraguan Quaternary volcanic chain, which is part of the Central American volcanic front. In Nicaragua, two segments divide the volcanic chain, the western and the eastern Nicaraguan segment where Masaya is located. On these two segments, 17 volcanoes lay on a line within or on the Nicaraguan Depression (Figure I-5). The Depression is a broad shallow graben filled in part by pyroclastic materials from the Las Sierras Group and by other volcanic debris from nearby volcanic complexes (Bice, 1980; Maciejewski, 1995).

Figure I-5

Map of the volcanic centres (dots) of the Central American volcanic front. There is at least 17 volcanic centres in Nicaragua which are: 1) Cosiguina, 2) San Cristobal, Casita and others, 3) Telica, 4) Cerro Negro, Las Pilas and El Hoyo, 5) Momotombo, 6) Momotombito, 7) Apoyeque and the Nejapa alignment, 8) Masaya and Apoyo calderas, 9) Mombacho, 10) Zapatera, 11) Concepción, 12) Madera (modified from Carr, 1984).



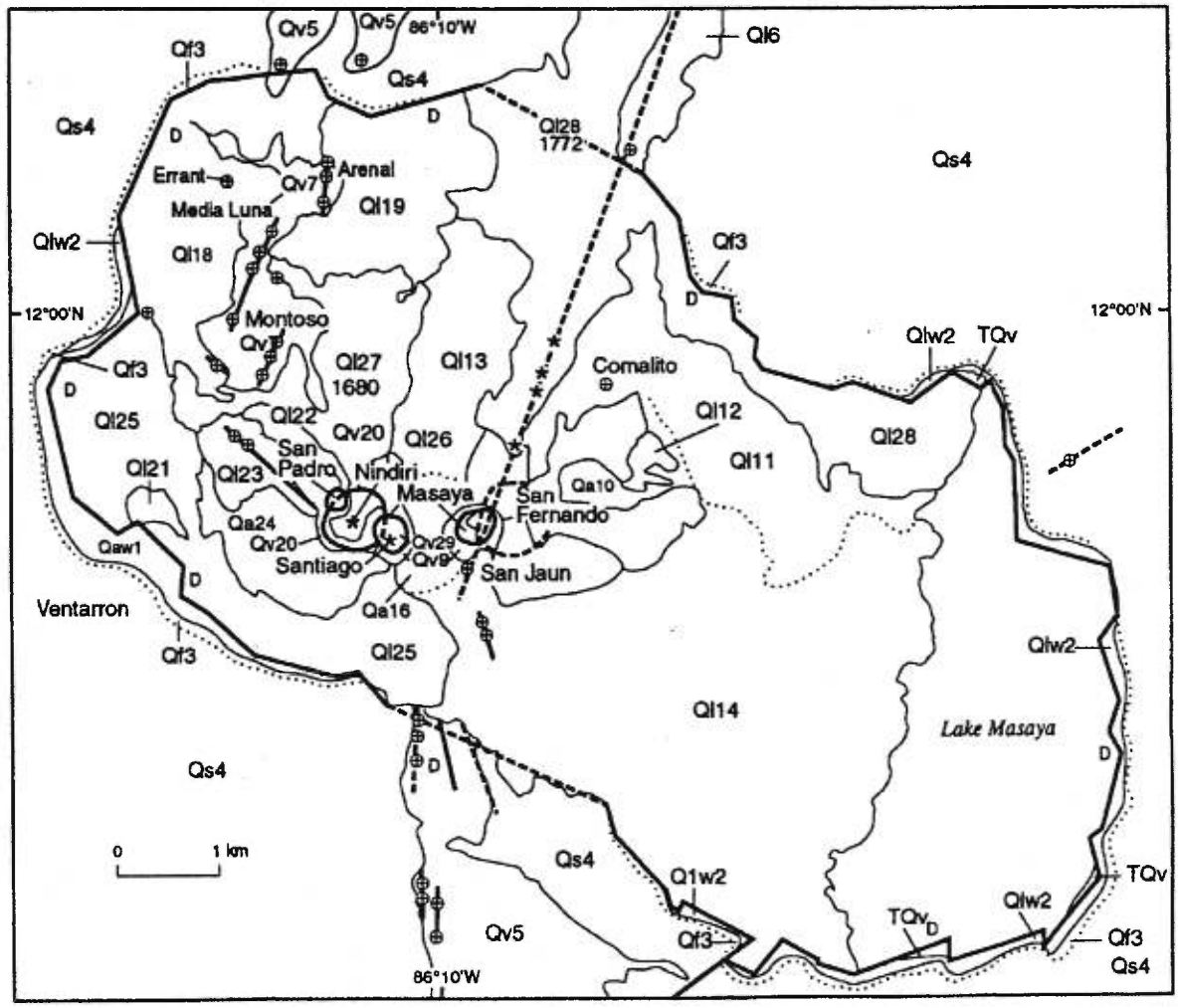
Nicaragua may be divided into physiographic units, which are from west to east: the Pacific Coastal Plain, the Nicaraguan Depression mentioned earlier, the Interior Highlands and the Atlantic Coastal Plain (McBirney and Williams, 1965). Thick sequences of Tertiary and Quaternary volcanic rocks and associated sediments constitute most of the overlying deposits in the western part of Nicaragua (Weyl, 1980).

Local Geology

Masaya is located within an older and larger caldera, the Las Sierras caldera estimated to be 25 000 to 35 000 years old. The formation of this large structure is thought to have produced the Masaya Lapilli Bed (van Wyk de Vries, 1993). The basement of Masaya Caldera is comprised mostly of the Las Sierras Formation estimated to be 680 meters thick (Kuang, 1971 in Williams, 1983). This formation includes the Fontana Lapilli, which is a 75 meters thick plinian deposit used as a major regional stratigraphic marker by Williams (1983). The Las Sierras Formation is overlain by pre-caldera lavas and other volcanic products such as ignimbrites, ash layers, lava flows and pyroclastic materials found mainly in the caldera walls (Williams, 1983). Surge deposits are widely found around the Masaya complex and are thought to be related to the collapse of the caldera. Masaya caldera is estimated to have formed during the eruption that produced the Masaya Tuff between 6000 and 2000 years ago (Williams, 1983). A more detailed geologic interpretation of the Masaya caldera complex was made by Williams (1983) (Figure I-6).

Figure I-6

Geological map of Masaya caldera (from Walker et al., 1993 after Williams, 1983)



Masaya Caldera Complex, Nicaragua

age	unit	description	event
	Ql 29	lava lake of 1965	
	Ql 28	aa lava flow and associated fissure-erupted ash and scoria of 1772	Santiago Crater collapse 1953
	Ql 27	aa lava flow and lava lake of 1670	
	Ql 26	pahoehoe lava flow of Oviedo	Nindirí Crater Collapse pre-1524
	Ql 25	pahoehoe lava flow with abundant lava tubes	
	Qa 24	scoria and ash (probably from site of Nindirí crater)	
	Ql 23	blocky lava and spatter erupted from fissure on NW flank of San Pedro crater	
	Ql 22	lava probably erupted from San Pedro crater	
	Ql 21	lava flow exposed below Ventarrón	
	Qv 20	Nindirí complex-cinder cones, lava flows and lava lakes	
	Ql 19	aa lava flow with possible compound nature	
	Ql 18	aa lava flow probably from fissure N of Montoso	
	Ql 17	blocky lava flow and lava lake	Masaya Crater collapse
	Qa 16	scoria and ash, locally agglutinated	
	Ql 14	aa lava flow with abundant vesicles, overlain at head by scoria and ash, locally agglutinated	
	Ql 13	pahoehoe lava flow	
	Ql 12	Casa Vieja lava flow	
	Ql 11	Comalito aa lava flow and associated fissure-erupted scoria and ash (widely agglutinated)	
	Qa 10	ash and scoria	
	Qv 9	Masaya Crater Complex-cinder cones, lava flows, and lava lakes; Santiago Crater Complex-cinder cones and lava flows	
	Qv 7	Lava and scoria and ash deposits (oldest of caldera flow, correlation and exact stratigraphic position uncertain)	San Fernando Crater collapse
	Ql 6	Railroad flow-massive lava erupted from N caldera margin	
	Qv 5	lavas and scoria and ash deposits erupted after caldera collapse from caldera-bounding faults or on flanks	
	Qs 4	pyroclastic surge deposits	Caldera collapse 2,250-6,500 y.b.p.
	Ql 3	pyroclastic flow deposits	
	Qlw 2	lavas of caldera wall (includes minor ashfall and pyroclastic flow deposits)	Masaya Tuff (Bice, 1985)
	Qaw 1	scoria and ashfall deposits of caldera wall (includes Masaya Triple Layer and Masaya Lapilli plinian deposits (Williams, 1983 and Bice, 1985))	
PLIO- PLEISTOCENE	TQv	Las Sierras Formation-pyroclastic flow or mudflow deposits exposed in area of Lake Masaya	
	*	historically active volcanic vent	
	⊕	vent	
	---	fault or eruptive fissure; concealed	
	contact; location approximate	

QUATERNARY

Masaya caldera is the object of much controversy over its formation. Many scientists have proposed different formation scenarios, which are most often contradictory. McBirney (1956) has suggested that a series of subsidence episodes caused by magma withdrawal from the chamber produced the present-day caldera. Williams (1983) and Bice (1985) have proposed major magmatic eruptions of basaltic composition, which caused a series of collapses. Kieffer and Creusot-Eon (1992) believed that a phreatomagmatic eruption of immense proportions formed a "maar" type depression, which constitutes the caldera of Masaya. The formation of the caldera is thus still in the centre of a debate among scientists today.

Masaya volcano is a unique structure among composite volcanoes which are most common in Central America and Nicaragua. The pre-caldera low shield configuration, the unusual explosive basaltic activity such as plinian and ignimbrite eruptions do not have any equivalents elsewhere in Nicaragua. The floor of the caldera has a low topography mostly covered by poorly vegetated lava flows. Two episodes of lava flows in 1670 and 1772 have been recorded since the Spanish arrival. The lava flow of 1670 was the result of a lava lake overflowing from the Nindirí pit crater. The 1772 eruption occurred from a fissure on the northern flank of the older Masaya crater (San Fernando crater) (Figure I-7). The other recent lavas are in the Nindirí crater pit where there are the remnants of the 1852 lava lake and at the bottom of the Santiago crater where there are the remains of the 1965 lava lake.

Currently, the main site of activity is Santiago crater, which was formed in 1858-1859. The original dimensions were 600 meters wide and 150 meters deep and the lava, which covered the floor (1948 and 1965) is now broken by concentric faults

Figure I-7

Map of the 1670 and 1772 lava flows at Masaya caldera (after Kieffer and Creusot-Eon, 1992).

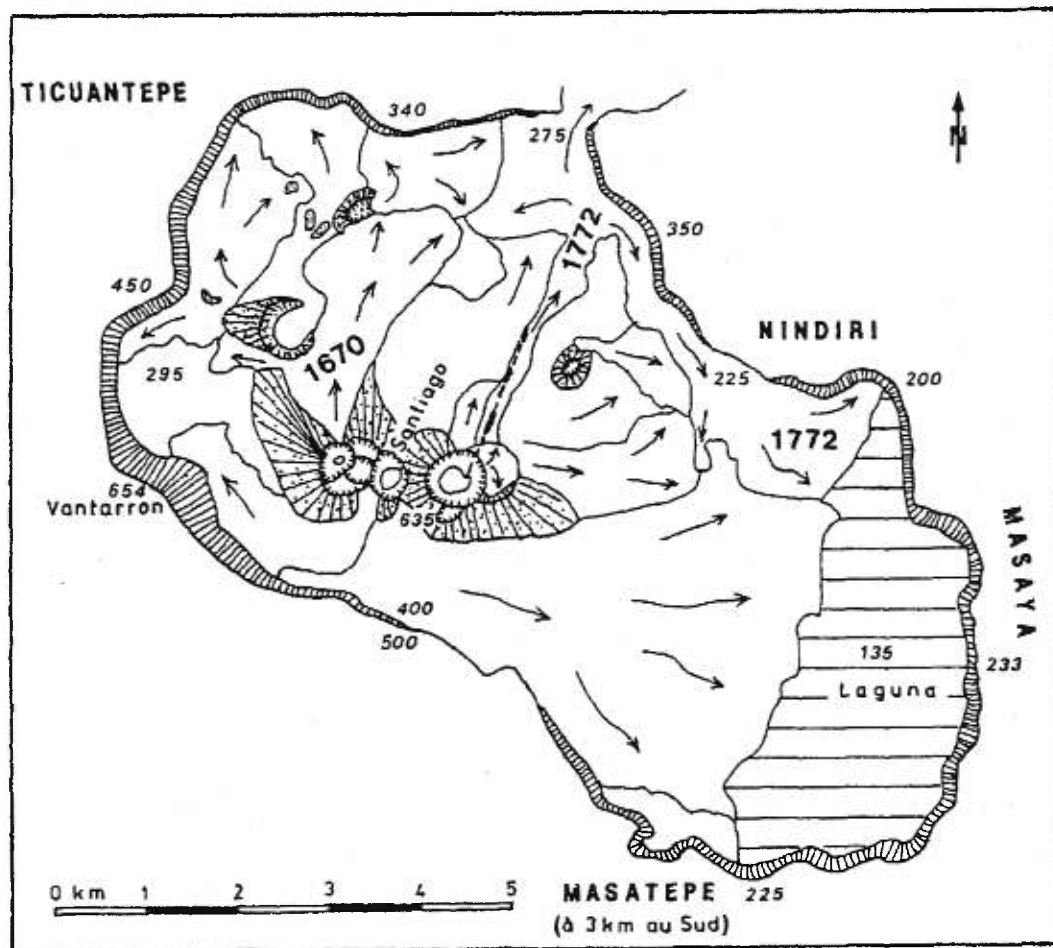


Figure I-8

View of the active vent at the bottom of Santiago crater in 1997.



(McBirney, 1956). The activity has been located in a small vent, which remained stable for the period 1948-1986 (Rymer, 1998). After 1986, collapses in the Santiago crater created an inner crater, which was followed by a deepening of the degassing vent. At the present time, a vent of approximately 30 meters wide is degassing at the bottom of Santiago (BGVN, 1999) (Figure I-8). The composition of the volcanic material is basalt or basaltic andesites which is more mafic than other Central American volcanoes. Masaya volcanic products show low Al_2O_3 and high FeO concentrations, a tholeiitic differentiation trend. Also a high large-ion-lithophile elements (LILE) concentrations is found at Masaya. It is suggested that these particular compositional variations are the results of magmatic differentiation in an open-system in the magma chamber (Walker et al., 1993).

Volcanic Activity

Evidence of explosive eruptions and effusion of lava in the history of the Las Sierras and Masaya calderas have been widely found in and around Masaya caldera. Earlier evidence of basaltic explosive activity has been dated at around 25,000 to 35,000 years BP which corresponds to the Las Sierras caldera. The present caldera is thought to have formed between 2,500 to 6,000 years ago by a basaltic ignimbrite eruption that produced the Masaya Tuff, estimated to have a volume of 8 km^3 (Williams, 1983). A volume of approximately $33 \times 10^6 \text{ m}^3$ of basaltic lavas has been erupted since the Conquistador arrival (Stoiber et al., 1986).

Since the sixteenth century, most of the volcanic activity has been continuous in the form of lava flows (1670 and 1772), periodic lava lakes and cyclic strong

degassing. Santiago crater, the currently active vent appeared in 1858-1859 during mild strombolian eruption at the Nindirí pit crater which probably also formed the San Pedro crater (McBirney, 1956; Williams, 1983). Since then, several periods of intense degassing have been recorded at Masaya (Stoiber et al., 1986). One particularity of the degassing at Masaya is that it is not associated with a major eruption. The first degassing crisis occurred in 1850-1859. Another crisis began in June 1902 and was intermittent until 1906. The 1919-1927 degassing crisis caused serious damage to the surrounding vegetation (Wilcox, 1952, Stoiber et al., 1986). Strong degassing resumed in 1947 and continued until it abruptly stopped in 1959. A lava lake covered the floor of the Santiago crater in 1948 and in 1965. The 1979-1989 degassing period was marked by several collapses of the crater floor creating and closing vents and revealing a lava lake in February 1989. Stoiber et al. (1986) recorded SO_2 fluxes of 380 to $1200 \text{ t}\cdot\text{d}^{-1}$. Strombolian activity was reported in 1989 until late November when a large wall collapse filled the bottom of the crater (Rymer et al., 1998). For the 1990-1993 period, no major activity was recorded and the SO_2 emission of Santiago crater was less than $25 \text{ t}\cdot\text{d}^{-1}$ (BGVN, 1992). The present degassing crisis began in mid-1993 when a degassing vent reappeared filled with a lava lake. Since then, several strombolian explosions have been reported in December 1996, in November 1997 and in September 1998 (BGVN, 1997; 1999).

There is also a low temperature fumarolic field located on the northern flank of Masaya (San Fernando) crater. This area is believed to be the site of the 1772 eruption fissure. Fumarole temperature increased from 70 to 84°C and showed increased CO_2 concentrations of 23-31% between March 1997 and March 1998 (BGVN, 1998).

Microgravity surveys made by Rymer et al. (1998) and Beaulieu (1999) show small decreases in gravity beneath Santiago. The crater of Santiago also has constant tremor which may indicate magma and/or gas movement in the plumbing system beneath Santiago crater.

References

- Allard, P., Carbonelle, J., Dajlevic, D., Le Bronec, J., Morel, P., Robe, M. C., Maurenas, J. M., Faivre-Pierret, R., Martin, D., Sabroux, J.C., and Zettwoog, P., 1991.** Eruptive and diffuse emissions of CO₂ from Mount Etna. *Nature*, 351: 387-391.
- Andres, R. J., Rose, W. I., Kyle, P. R., deSilva, S., Francis, P., Gardeweg, M., and Moreno Roa, H., 1991.** Excessive sulfur dioxide emissions from Chilean volcanoes. *Journal of Volcanology and Geothermal Research*, 46: 323-329.
- Baubron, J.-C., Allard, P., Sabroux, J.-C., Tedesco, D., and Toutain, J.-P., 1991.** Soil gas emanations as precursory indicators of volcanic eruptions. *Journal of the Geological Society of London*, 148: 571-576.
- Beaulieu, A., 1999.** The nature and origin of spatial and temporal variations in the gravity fields of Telica and Masaya volcanoes, Nicaragua. Unpublished M.Sc. thesis, Département de géologie, Université de Montréal, Montréal, Canada, 138 pp.
- Bice, D. C., 1980.** Tephra stratigraphy and physical aspects of recent volcanism near Managua, Nicaragua. Unpublished Ph.D. Dissertation, University of California, Berkeley, U.S.A., 422 pp.
- Bluth, G. J. S., Rose, W. I., Sprod, I. E., and Krueger, A. J., 1997.** Stratospheric loading of sulfur from explosive volcanic eruptions. *Journal of Geology*, 105: 671-683.
- Brantley, S. L., and Koepenick, K. W., 1995.** Measured carbon dioxide emissions from Oldoinyo Lengai and the skewed distribution of passive volcanic fluxes. *Geology*, 23: 933-936.
- Bulletin of the Global Volcanism Network, 1992.** Masaya volcano. Smithsonian Institution 17 (4): 7.
- Bulletin of the Global Volcanism Network, 1997.** Masaya volcano. Smithsonian Institution 22 (3): 6-7.
- Bulletin of the Global Volcanism Network, 1998.** Masaya volcano. Smithsonian Institution 23 (9): 7.
- Bulletin of the Global Volcanism Network, 1999.** Masaya volcano. Smithsonian Institution 24 (4): 5.

- Carr, M. J., 1994.** Symmetrical and segmented variations of physical and geochemical characteristics of the Central American volcanic front. *Journal of Volcanology and Geothermal Research*, 20: 231-252.
- Crenshaw, W. B., 1982.** Ground radon and mercury concentration surveys for location of faults systems, Masaya Caldera, Nicaragua. M.S. Thesis, Dartmouth College, Hanover, New Hampshire, U.S.A., 82 pp.
- Crenshaw, W. B., Williams, S. N., and Stoiber, R. E., 1982.** Fault location by radon and mercury detection at an active volcano in Nicaragua. *Nature*, 300: 345-346.
- Delmelle, P., St-Amand, K., Stix, J., Baxter, P., Oppenheimer, C., Burton, M., and Francis, P., 1998.** COSPEC measurements at Masaya volcano Nicaragua: Part II- SO₂ plume dispersion and subsequent removal downwind. American Geophysical Union Fall Meeting, San Francisco, 977-978.
- Eatough, D. J., Caka, F. M., and Farber, R. J., 1994.** The conversion of SO₂ to sulfate in the atmosphere. *Israel Journal of Chemistry*, 34: 301-314.
- Farrar, C. D., Sorey, M. L., Evans, W. C., Howie, J. F., Kerr, B. D., Kennedy, B. M., King, C.-Y., and Suthon, J. R., 1995.** Forest-killing diffuse CO₂ emission at Mammoth Mountain as a sign of magmatic unrest. *Nature*, 376: 675-678.
- Gaonac'h, H., Lovejoy, S., Schertzer, D., St-Amand, K., and Stix, J., 1999.** Direct measurements of the elliptical dimension of atmospheric dynamics using remote sensing of volcanic SO₂ gas. European Geophysical Society General Assemblies, LaHaye.
- Heiligmann, M., Stix, J., Williams-Jones, G., Sherwood-Lollar, B., and Garzón V., G., 1997.** Distal degassing of radon and carbon dioxide on Galeras volcano, Colombia. *Journal of Volcanology and Geothermal Research*, 77: 267-284.
- Johnson, N. and Parnell, R. A., 1986.** Composition, distribution and neutralization of "acid rain" derived from Masaya volcano, Nicaragua. *Tellus*, 38B: 106-117
- Johnston, S. T. and Thorkelson, D. J., 1997.** Cocos-Nazca slab window beneath Central America. *Earth and Planetary Science Letters*, 146: 465-474.
- Kazahaya, K., Shinohara, H., and Saito, G., 1994.** Excessive degassing of Izu-Oshima volcano: magma convection in a conduit. *Bulletin of Volcanology*, 56: 207-216.
- Kieffer, G., and Creusot-Eon, A., 1992.** La caldeira de Masaya (Nicaragua): une dépression polyphasée de type «maar». *Comptes rendus de l'Académie des sciences, Paris, Série II*, 315: 1403-1409.

- Laferrière, A., and Gaonac'h, H., 1999.** Multifractal properties of visible reflectance fields from basaltic volcanoes. *Journal of Geophysical Research*, 104: 5115-5126.
- Lavallée, D. S., Lovejoy, S., Schertzer, D., and Ladoy, P., 1993.** Nonlinear variability and landscape topography: analysis and simulation. In: Eds. L. De Cola, N. L., *Fractals in Geography*, 158-192.
- Maciejewski, A. J. H., 1995.** Evolution and present-day activity of the Masaya Volcanic Complex, Nicaragua. Unpublished manuscript, The Open University, 37 pp.
- McBirney, A. R., 1956.** The Nicaraguan volcano Masaya and its caldera. *American Geophysical Union Transactions*, 37: 83-96.
- McBirney, A. R., and Williams, H., 1965.** Volcanic history of Nicaragua. University of California, Publication in Geological Sciences, 55: 1-73.
- Rymer, H., van Wyk de Vries, B., Stix, J., and Williams-Jones, G., 1998.** Pit crater structure and processes governing persistent activity at Masaya Volcano, Nicaragua. *Bulletin of Volcanology*, 59: 345-355.
- St-Amand, K., Beaulieu, A., Stix, J., Gaonac'h, H., and Lovejoy, S., 1998.** SO₂ flux, CO₂ and radon degassing at Masaya Caldera, Nicaragua. GAC/MAC Spring Meeting, Québec 1998, Abstract Volume 23:178.
- St-Amand, K., Stix, J., Delmelle, P., Gaonac'h, H., Lovejoy, S., and Williams-Jones, G., 1998.** COSPEC Measurements at Masaya Volcano Nicaragua: Part I- SO₂ fluxes, petrology, of melt inclusions, and multifractal analysis of COSPEC signals. AGU Fall Meeting, San Francisco, 977.
- Schertzer, D., and Lovejoy, S., 1996.** Resolution dependence and multifractals in remote sensing and geographical information systems. McGill University, Lectures Notes. Unpublished, 390 pp.
- Schmitt, F., Lavallée, D., Lovejoy, S., Schertzer, D., and Hooge, C., 1992.** Estimations directe des indices de multifractals universels dans le champ de vent et de température. *Comptes rendus de l'Academie des sciences, Paris, Série II*, 314: 749-754.
- Stoiber, R. E., and Carr, M. J., 1973.** Quaternary volcanic and tectonic segmentation of Central America. *Bulletin Volcanologique*, 37: 304-325.
- Stoiber, R. E., and Williams, S. N., and Huebert, B. J., 1986.** Sulphur and halogen gases at Masaya Caldera complex, Nicaragua: Total flux and variations with time. *Journal of Geophysical Research*, 91: 12 215-12 231.

- Van Wyk de Vries, B., 1993.** Tectonics and magma evolution of Nicaraguan volcanic systems. Unpublished Ph.D. Thesis, Department of Earth Sciences, Open University, Milton Keynes, UK, 328 pp.
- Walker, J. A., Williams, S. N., Kalamarides, R. I., and Feigenson, M. D., 1993.** Shallow open system evolution of basaltic magma beneath a subduction zone volcano: the Masaya Caldera complex, Nicaragua. *Journal of Volcanology and Geothermal Research*, 56: 379-400.
- Weyl, R., 1980.** *Geology of Central America*. Gebruder Borntraeger, Berlin, Germany, 371 pp.
- Williams-Jones, G., 1997.** The Distribution and Origin of Radon, CO₂, and SO₂ Gases at Arenal Volcano, Costa-Rica. Unpublished M.Sc. thesis, Département de géologie, Université de Montréal, Montréal, 135 pp.
- Williams, S. N., 1983.** Geology and eruptive mechanisms of Masaya Caldera Complex, Nicaragua. Unpublished Ph.D. thesis, Dartmouth College, Hanover, New Hampshire, U.S.A., 169 pp.

CHAPTER I

Diffuse Degassing of CO₂ and Radon at Masaya Volcano, Nicaragua

Katie St-Amand

Département de géologie
Université de Montréal
Montréal, Québec, H3C 3J7
Canada

ABSTRACT

Radon, CO₂, δ¹³C, and temperatures in soil have been measured at Masaya Volcano, Nicaragua in 1997 and 1998. Three areas were surveyed, a suspected fracture on the northern flank of San Fernando crater (three lines), another fracture on the northern rim of Nindirí crater and the west zone of the Arenal cinder cone in the northwest part of Masaya caldera. Rn and CO₂ concentrations ranged from 2.2 to 169 pCiL⁻¹ and 0 to 31.1 % volume, respectively. Soil gas values reached maxima along the San Fernando north oriented fracture in an area of fumarolic activity. The δ¹³C values varied from -4.4 to -1 ‰. The heaviest isotopic values were observed where the highest CO₂ concentrations and temperatures occurred in the fumarolic field. The δ¹³C values may represent mixing of different sources of CO₂, such as magmatic CO₂ and CO₂ from carbonate rocks in the sub-surface or fractionation.

Measurements of CO₂ flux range from 196 to 8544 g·d⁻¹·m⁻², indicating highly variable degassing over a restricted zone in the fumarolic field. The zones where the high concentrations and fluxes are measured probably represent the location of the fracture. Heterogeneous permeability of soil and ash layers and altered sections in the subsurface may explain the relatively high CO₂ concentrations and low to non-existent CO₂ fluxes in some areas around the fumarolic field.

The observed Rn, CO₂ and δ¹³C values indicate that the degassing 1) is influenced by the presence of structural features and the heterogeneity of the sub-surface; 2) has a mixed source composed of magmatic gas and CO₂ from carbonate rocks or a fractionated source; and 3) is the result of an open system.

Introduction

Since historic time, Masaya caldera is known to have had various types of volcanic activity such as lava lakes, strombolian explosions, fumarolic activity, and degassing of an active vent. Three volcanic events in the last three years were recorded by INETER. In early December 1996, a strombolian explosion of small scale was observed in the active vent of Santiago. A decrease in visible degassing was noticed before the explosion (GVN, 1997). On 12 November 1997, a similar explosion occurred (GVN, 1999). Juvenile bombs were projected in the Santiago, Nindirí and San Pedro areas. A decrease and cessation of degassing of the active vent also was observed before the second explosion. Another similar event occurred in September 1998 (GVN, 1999). Monthly temperature measurements of fumaroles at Comalito showed increases of approximately 6 °C from 75 °C to 81 °C for the hottest fumaroles (M. Navarro, INETER, pers. com., 1998).

Masaya caldera is known to have cyclic degassing activity. Studying soil gas distributions enables us to determine fracture systems and possibly where volcanic activity may occur in the future in the form of a major eruption or increased degassing activity. In this chapter, I present the results of a soil gas study at Masaya volcano. The objectives of this research are 1) to locate structural feature such as fractures and faults; 2) to discuss the origin and the transport of gas; and 3) to propose a model of degassing at Masaya volcano. To achieve these goals, I made a gas survey of CO₂ and radon for the following reasons: 1) these gases are comparatively simple to measure in the field; 2) similar research has been conducted at other volcanoes so that

comparisons may be made; and 3) these volatiles are known to respond to variations in the conditions governing volcanic activity.

The measurement and sampling of gases on an active volcano may be problematic for many reasons. Unpredictability of eruptions, difficult access and unstable ground constitute risks. However, monitoring of degassing processes on a volcano is an important element to understand its past history, present and future behaviour. By studying the variations in degassing behaviour, such as changes in the distribution of soil gases like CO₂ and radon, and past and present patterns of eruption, a model of the degassing process may be developed.

CO₂ is generally the second most abundant gas species emitted by an active volcano after H₂O. Its low solubility in silicate melts at moderate to low pressures allows it to be exsolved in the early stages of degassing, making CO₂ a good marker of the degassing of a sub-surface magma body (Baubron et al., 1991). However, the source of CO₂ may vary according to the geologic environment. Four major sources are: 1) the mantle; 2) carbonate rocks; 3) organic materials; and 4) a combination of the three previous sources (Irwin et al., 1980).

Two stable carbon isotopes exist, ¹²C and ¹³C, with a distribution of 98.89% and 1.11 %, respectively. The δ¹³C variation is expressed relative to the Pee Dee Belemnite (PDB) standard. The mantle or magmatic source has values between -4 to -8 ‰, carbonate rocks are usually near 0‰, and organic sources have values between -20 and -40 ‰ (Faure, 1986).

²²²Radon is a radioactive noble gas that occurs naturally in the disintegration chain of ²³⁸U. The half-life of ²²²Rn is 3.82 days, and it may be emitted by any

terrestrial material that contains uranium or its immediate parent isotope, radium (Tilsley, 1992). ^{219}Rn and ^{220}Rn are two other radon isotopes with short half-lives that also occur naturally (Ozima et al., 1983).

Many processes may affect the concentrations and the distributions of soil gas. First, climatic variations such as temperature, wind, rain and atmospheric pressure may affect the concentrations (Schery et al., 1983). Second, deformation of the ground may play a role in gas transport by opening or closing pathways. Third, volcanic and seismic activity may affect the degassing. Connor et al. (1996) were able to measure an increase in concentration of radon during the 1995 eruption of Cerro Negro, Nicaragua, suggesting a relation between the volcanic unrest and the variation in gas concentration. Thomas et al. (1986) showed in five years of radon monitoring that variations of Rn concentrations may be related to volcanic activity observed at Kilauea, Hawaii. Baubron et al. (1991) presented a study of several volcanoes in Italy, the Lesser Antilles and Indonesia that suggests a strong relation between soil gas emanations on the flanks of volcanoes and volcanic eruptions. Lastly, tectonic activity is important. Irwin and Barnes (1980) did a comparative review of seismic zones and CO_2 discharges, showing that regional tectonic and earthquakes may affect the CO_2 that is discharged along these zones. Heiligmann et al. (1997) made a study at Galeras volcano, Colombia, which also suggests that deep degassing of soil gas is related, in part, to tectonic events. Soil development has a marked effect, along with alteration of the sub-surface, by decreasing the permeability of the soil. Local heterogeneity in soil and ash layers may cause accumulation of gas

pockets. Thus, measurements give relatively high CO₂ concentrations in the soil but no effective degassing occur.

The field area within Masaya caldera consists of three different zones. The first area is the Nindirí fracture zone in the northern part of Nindirí crater, which is located on the west side of the active crater of Santiago. This area is characterised by the presence of a visible east-west fracture with a fumarolic zone just west of Santiago. The second area is the north-south Masaya-Comalito fracture zone on the northern flank of San Fernando (Masaya) crater (Crenshaw, 1982). This area is characterised by several fumarolic fields distributed from the summit to the northern base of the Comalito parasite cone. These fumarolic fields are separated by vegetated zones and at some places by lava flows. The third area is the Arenal parasite cone, northwest of the active crater complex, in the caldera ring fracture (McBirney, 1956). This area once had a visible fumarolic field on Arenal, but it is presently densely vegetated without observable activity.

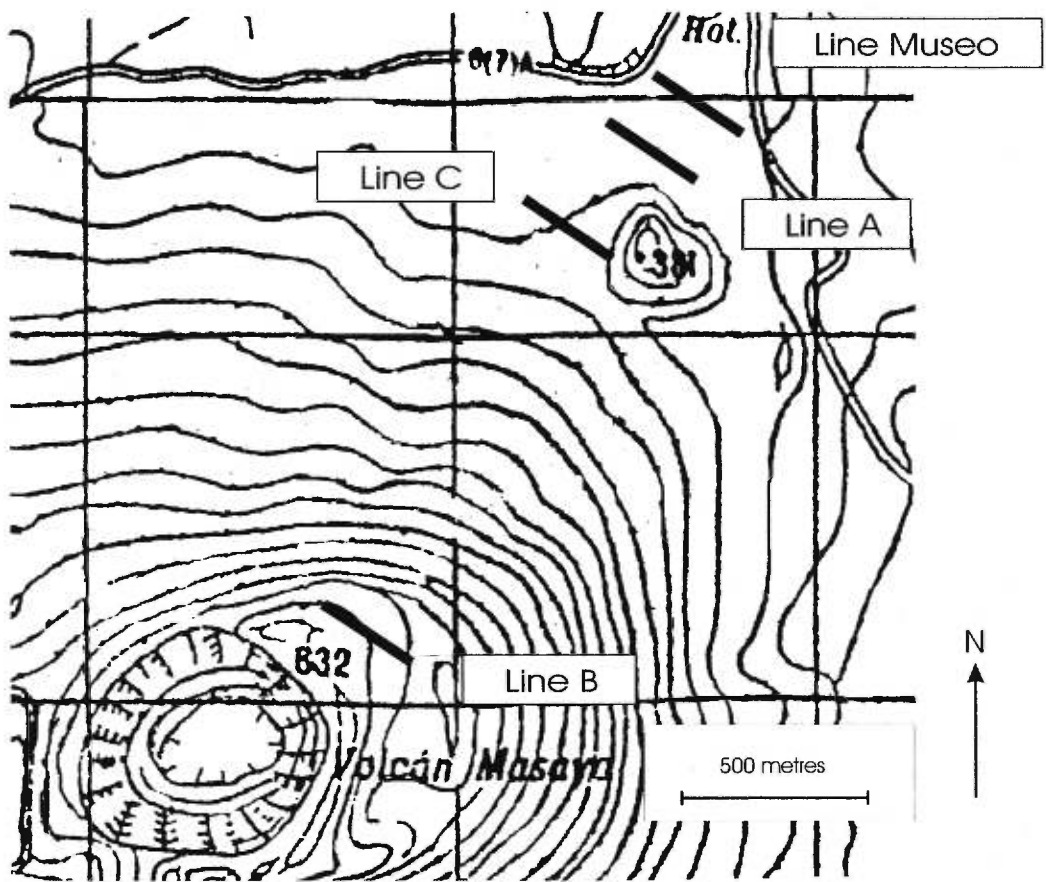
Methodology

Station Locations

The accessibility to the Masaya Volcanic complex is provided by several roads surrounding the complex. In 1997, three lines of stations were established on a suspected fracture on the northern side of San Fernando (B-C-A from summit of San Fernando to base, Figure 1.1). Line B is located near the summit, while lines C and A are located at the base of the San Fernando cone and the Comalito parasite cone. Another line (N) transects a fracture at the summit in the Nindirí crater adjacent to the

Figure 1.1

Topographic map of Masaya showing the locations of CO₂, δ¹³C, radon and temperature measurements for the profiles B, C, A and MUSEO from the summit to the base of San Fernando Crater. Contour lines are every 20 meters.



active vent of Santiago (Figure 1.2). In 1998, line A and two other lines (MUSEO and ARENAL) were surveyed for CO₂ and Rn, and line C was extended to the southeast onto the Comalito cinder cone (Figures 1.1 and 1.2).

Soil Gas Measurements

Carbon Dioxide

CO₂ concentration measurements were done using an infrared gas analyser (ADC LFG-20 Landfill Gas Analyser) in combination with a metal soil probe for real-time measurements. The CO₂ range of the instrument is 0-10 % and 10-100 %, with 0.5 % and 3.0 % precision, respectively.

Carbon Dioxide Fluxes

For CO₂ flux measurements, a custom-made flux chamber was installed on undisturbed ground in the vicinity of stations previously surveyed for CO₂ concentrations. Measurements were taken every 30 seconds until the CO₂ values reached a plateau. With a plot of CO₂ concentration versus time, a value of the slope of the first linear segment was made. A flux rate (g·m⁻²·d⁻¹) was calculated with the following formula:

$$Flux = \left(\frac{\Delta CO_2}{\Delta t} \right) \left(\frac{1}{M_{air}} \right) (M_{CO_2}) (V) (A^{-1}) (\delta_{air}) (1000 \text{ mg/g}) (10^{-6} \text{ ppm}) \quad (1.1)$$

where ΔCO₂ is the difference between initial and final CO₂ concentrations (ppm); Δt is the elapsed time (min); M_{air} is the molecular weight of air (28.964 g/mole); M_{CO₂} is the molecular weight of CO₂ (44 g/mole); V is the chamber volume (15.7 l); A is the

area of the chamber bottom (0.0490 m^2); and δ_{air} is the density of air (g/l) calculated using $[(P/T) \cdot (0.3483677)]$ where P is the pressure in mbar and T is the temperature in K.

Carbon Isotopes in CO₂ Soil Gas

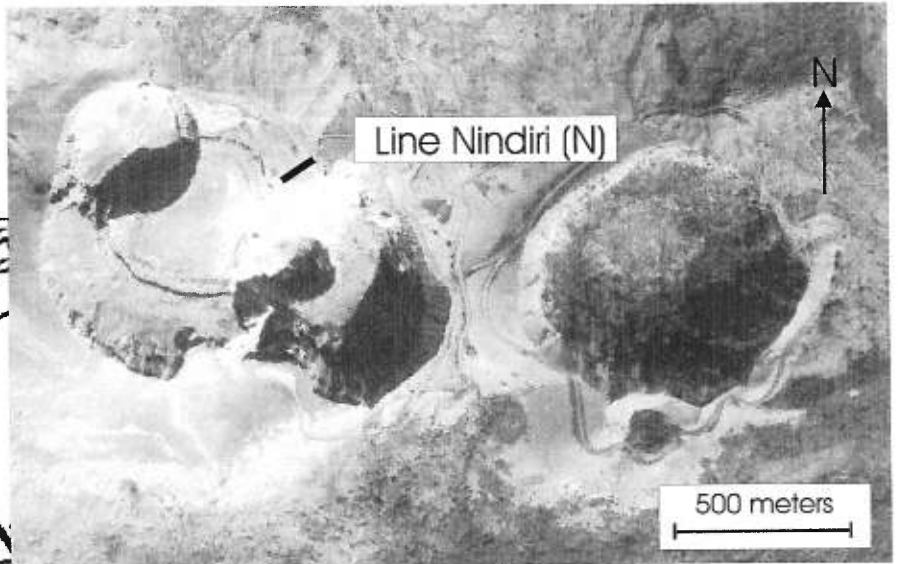
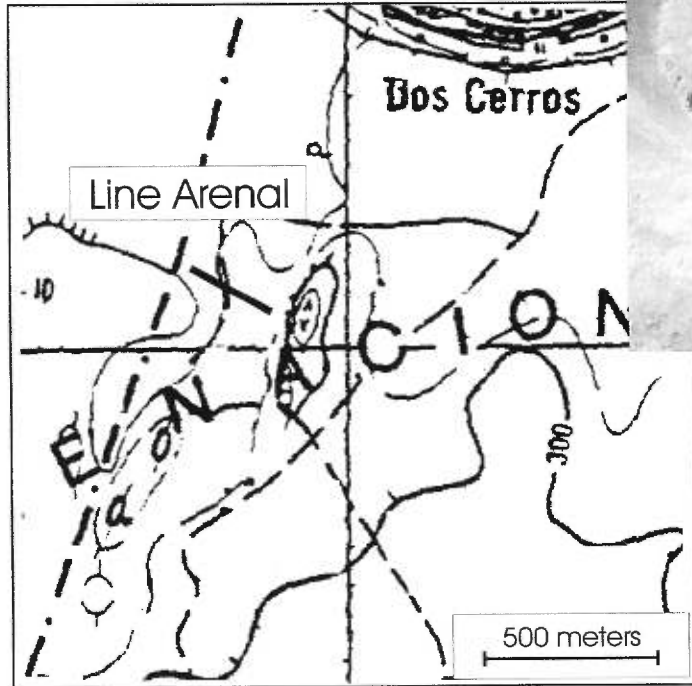
In 1997 and 1998, CO₂ gas samples were taken from stations with CO₂ concentrations exceeding 0.5%. A 40-50 ml gas sample from a depth of 75 cm was collected by a syringe and transferred into a stoppered, crimped 25 ml bottle. The vials were pre-evacuated and neutralized by a mercuric chloride solution to prevent biogenic CO₂ contamination. These samples were analysed for carbon isotopes. Isotopic analyses were performed by a Finnigan MAT 252 gas source mass spectrometer (MS) linked to a Varian 3400 gas chromatograph (GC) equipped with a capillary column (GC-C-IRMS) at the Stable Isotope Laboratory, University of Toronto. Carbon isotope ratios ($\delta^{13}\text{C}$) are expressed in ‰ deviation from a Pee Dee Belemnite (PDB) standard. Accuracy and reproducibility of the isotopic analyses are both 0.4 ‰ or less.

Radon

Each Rn station was determined by choosing representative points from the previous CO₂ survey made along a particular line. ²²²Rn was measured using the E-Perm technique developed by Rad Elec. (Rad Elec., 1993). Blue short-term electrets and L chambers were used. The electret consists of an electrostatically charged Teflon disk attached to an ion chamber of known volume. A hole was dug, electrets

Figure 1.2

Topographic map of Masaya showing the location of CO₂, δ¹³C, radon and temperature of a) profile N at the Nindirí crater, b) profile ARENAL at the Arenal parasitic cone in the northwest part of the caldera.



were covered with a plastic bowl of 600 ml volume and installed at a constant depth of 35 cm in the soil for approximately seven days. A decrease of electret voltage is the result of radioactive decay of radon in the chamber, ionising the air and producing negative ions. The concentration of radon is calculated by the following formula:

$$[Rn] = \left(\frac{V_i - V_f}{CF \cdot T} \right) - (0.120 \cdot M) \quad (1.2)$$

where Rn is the concentration of radon in pCiL⁻¹; V_i and V_f are the initial and final voltages of the electret; T is the time of exposure of the electret in days; 0.120 is a calibration factor in pCiL⁻¹ per μRad/hour; and M is the ambient gamma radiation in μR/hour. For the combination of electrets and chambers used, the calibration factor (CF) is calculated as follows:

$$CF = 0.2613 + 0.0001386 \cdot \left(\frac{V_i + V_f}{2} \right) \quad (1.3)$$

where 0.2613 and 0.0001386 are calibration constants in pCiL⁻¹ per μR/h (Rad Elec., 1993).

As in all measurements, there are associated instrumental errors. Three sources of errors are possible. First, instrumental imperfections may induce errors in the measurements. This first source of error is about 5 % (Kotrappa et al, 1990). The second source of error is linked to the residual background radon in the chamber and is 1.4 volts between the initial and final measurement. Thus:

$$E_2 \% = \left(\frac{100 \cdot 1.4}{V_i - V_f} \right) \quad (1.4)$$

The background gamma radiation is the third source of instrumental error and is estimated at 0.1-0.2 pCiL⁻¹. Thus:

$$E_3 \% = \left(\frac{100 \cdot 0.1}{[Rn]} \right) \quad (1.5)$$

The final estimated total error is:

$$E_{total} \% = \left(E_1^2 + E_2^2 + E_3^2 \right)^{1/2} \quad (1.6)$$

Thus, the total error on the measurements typically ranged from 5 to 38%.

Temperature

Temperatures were taken with an Omega chromel-alumel thermocouple. Real-time measurements at a depth of 75 cm were taken at each CO₂ station surveyed along all profiles. Approximately 20 seconds were allowed to stabilise the measurement. Temperature monitoring during CO₂ flux measurements was made with a copper-constantan thermocouple.

Results

Visual observations

Masaya is poorly vegetated due to the ongoing volcanic activity and the semi-arid climate. Variations in soil development and vegetation damaged by volcanic gases are visible. The northern part of San Fernando crater showed a large zone from the summit to base consisting of sparse vegetation such as grass and some bushes surrounded by lava flows from the 1772 eruption. Patches of trees are visible at the summit, at the middle slope and at the base but are scarce. The base of San Fernando

where the Comalito parasite cone and line C are located shows a poorly vegetated area of approximately 300 m². In February and March 1998, profile C showed similar but larger patches of devegetated zones (about ~100 m² more for a total of 400m²). The three profiles surveyed (A, C and B) have central zones of fumarolic activity 60 m, 30 m, and 50 m wide, respectively, of which a 15 to 20 m zone represents areas of highest activity. The borders of the affected areas are bounded by forest. The fumarolic areas consist of scarce patches of grass.

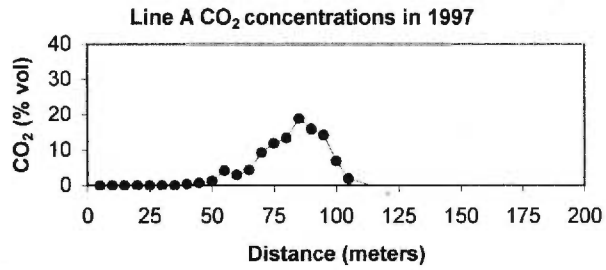
Carbon Dioxide

In 1997, a survey was conducted around the San Pedro, Nindirí, Santiago and San Fernando complexes to prospect for CO₂ and radon. On the northern flank of San Fernando, three transects (A, B, C) were made across the active fracture (Crenshaw, 1982). The values for these lines range from 0 % vol. to 18.8 % vol. in March 1997. There is a general trend toward increasing CO₂ approaching the central zone of fumaroles. Line A has the highest values of 18.8 %, while the two other lines have maxima of 2.76 % for line B and 2.53 % for line C, which is an order of magnitude less than line A (Figure 1.3 a, c, and d). A line also was surveyed on Nindirí crater (line N). At this location, the CO₂ values range from 0 % to 4.12 % (Figure 1.3 h). For all profiles, a positive relation of the high CO₂ values with the active, hottest, part of the fumarole field was observed.

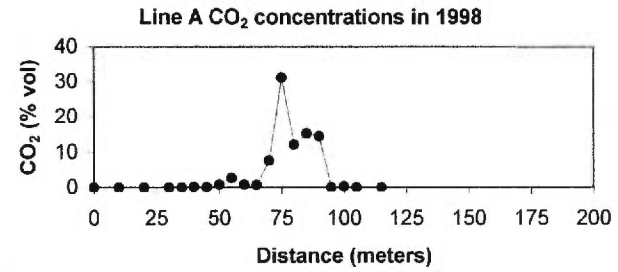
In March 1998, a higher value of 31.1 % on line A was observed at the same location (± 5 meters) compared to the 1997 18.8 % CO₂ value (Figure 1.3 b). The Comalito line (on the parasite cone) show CO₂ concentrations of 0.55 to 6.25 %

Figure 1.3

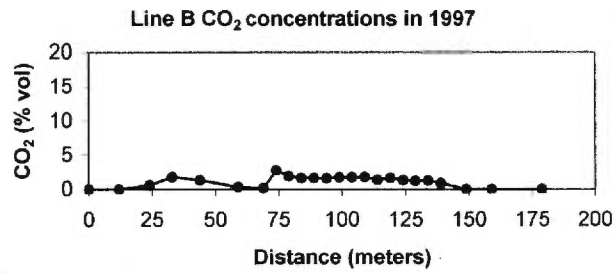
CO₂ concentrations for (a) and (b) line A at the base of San Fernando, (c) line B near the summit of San Fernando crater, (d) Line C at approximately 200 meters south of line A, (e) Comalito (line C extension), (f) line Museo, (g) line Arenal, and (h) and (i) line N. Profiles (a) to (g) are oriented southeast-northwest, (h) and (i) are southwest-northeast oriented.



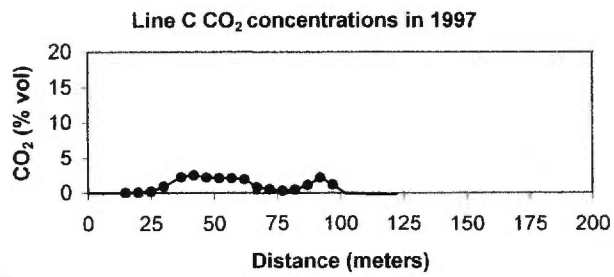
a)



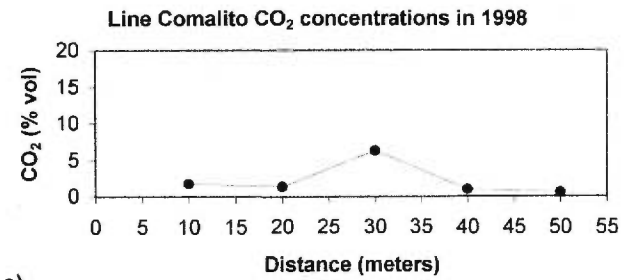
b)



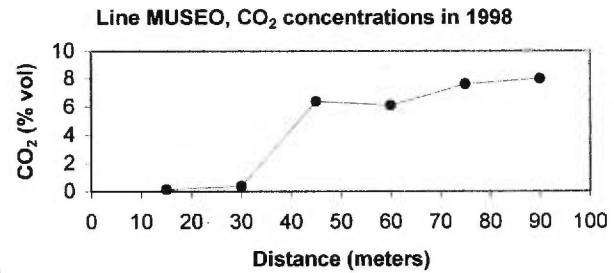
c)



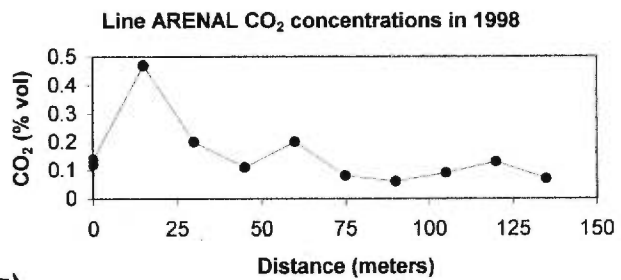
d)



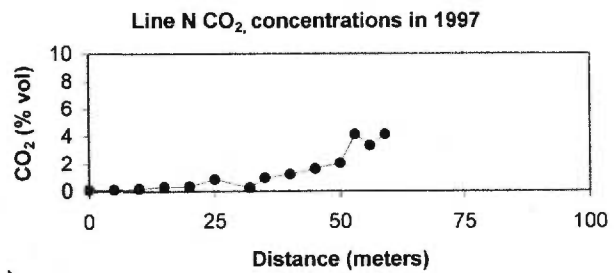
e)



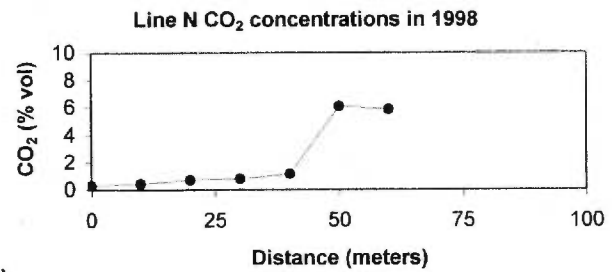
f)



g)



h)



i)

where, in 1997 no gas was detected. The Museo profile made in March 1998, located approximately 300 m north from line A, show a CO₂ values of 0.14 % to a peak of 7.98 % at the end of the profile on the side of a paved road (Figure 1.3 f). For line N, the final measurement made at the base of the ridge, 6.09 % in 1998, is the highest value obtained on this line (Figure 1.3 i). An increase of CO₂ is observable from south to north where the line ends on rubble. At the parasite cone of Arenal, a line (ARENAL) had comparatively low CO₂ values ranging from 0.06 % to 0.47 % in 1998 (Figure 1.3 g). This profile is located on the west side of the cinder cone in a vegetated area where no fumaroles are observed. The concentrations show a decreasing trend along the profile from east to west indicating a possible link with the position of the ring fracture and the Arenal parasite cone (McBirney, 1956; Crenshaw, 1982; Williams, 1983). Generally, the 1998 values do not differ substantially from the 1997 measurements made at the same period. However, CO₂ concentrations may vary significantly more during the year. Since no measurement were made between the two surveys, no changes were recorded. The CO₂ increase of line A maxima may represents superficial soil conditions. Measurements made at different depth in the soil at some station have shown that the CO₂ concentrations are variable. For example, at station A₂₁, the CO₂ values varied, at 32 cm the CO₂ concentration is 2.6 % while at 75 cm, it is 6.6 %. It is thus likely that there is a CO₂ stratification, with differences in permeability at different depths in the soil profile. Deposit layers of variable porosity may explain the presence of variable permeability, which give different CO₂ values as a function of depth. Alteration by heat, moisture and gas may have produced argilous minerals which may sealed partially the gas pathways and

contribute to the accumulation of gas. The presence of water may also decrease the permeability of the soil. Thus, it is the conditions of the superficial deposit layers that are relevant to the variable CO₂ concentrations obtained at line A. However, the observation of larger patches of devegetated zones at line C and CO₂ concentrations on the Comalito cone in 1998 may indicate reactivation of parts of the fracture.

Carbon Dioxide Fluxes

CO₂ flux measurements were conducted on lines A, B and C in 1997. The stations were chosen according to the CO₂ measurements done previously and in areas where the soil was undisturbed. The CO₂ flux ranges from 196 to 8544 g·m⁻²·d⁻¹ with an average of 3549 g·m⁻²·d⁻¹ for the entire area (Table 1.1). Line A shows the highest CO₂ fluxes of the survey with 8540 g·m⁻²·d⁻¹. Line B and C show high fluxes of 4240 g·m⁻²·d⁻¹ and 3400 g·m⁻²·d⁻¹ respectively, which are lower than line A. The observations show increased CO₂ flux in areas of fumarolic activity and high CO₂. However, lower fluxes were also measured around stations of high CO₂ in area of high fumarolic activity.

Carbon Isotopes in CO₂ Soil Gas

The δ¹³C values obtained range from -1 ‰ to -4.4 ‰ in 1997. Values ranging from -1.1 ‰ to -2.3 ‰ with an average of -1.7 ‰ are observed at line A in the Comalito parasite cone area (Figure 1.4 a). Line B has a δ¹³C average of -1.8 ‰ ± 0.1, values ranging from -2.7 ‰ to -1.7 ‰ (Figure 1.4 c). Line C has an average δ¹³C value of -2.5 ‰ with extremes ranging from -1.9 ‰ to -4.4 ‰ (Figure 1.4 d).

Table 1.1 CO₂ fluxes measured on line A, B, and C in 1997.

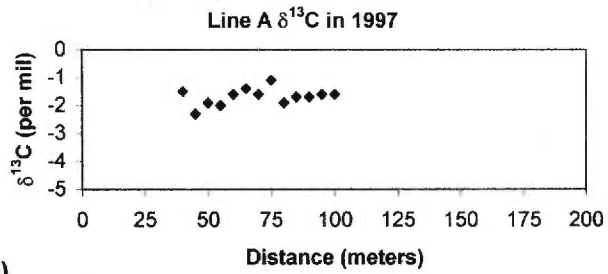
Chamber parameters: volume 15.7 L bottom,

bottom area 0.049 m².

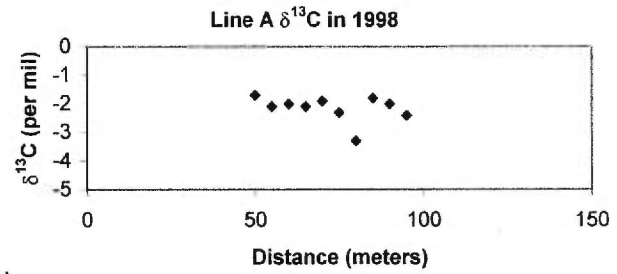
	g*d ⁻¹ *m ⁻²	Total fluxes ¹ t*d ⁻¹	CO ₂ %
<u>Stations line A</u>			
A ₁₄₋₁₅	4940	1.48	10.6
	5640	1.69	10.6
A ₁₅	8540	2.56	11.9
A _{15 (min)}	6310	1.89	11.9
A _{15 (max)}	7350	2.20	11.9
A ₁₅₋₁₆	200	0.06	12.7
A ₁₅₋₁₆	7020	2.11	12.7
A ₁₅₋₁₆	8540	2.56	12.7
A ₂₁	2000	0.60	1.9
<u>Stations line C</u>			
C ₈	2940	0.88	2.6
C ₈	3400	1.02	2.2
C ₈	1550	0.46	2.4
C ₈₋₉	1260	0.38	2.4
C ₁₃	510	0.15	2.2
<u>Stations line B</u>			
B ₈	4240	1.27	1.8
B ₈	3340	1.0	1.8
B ₈	1550	0.47	1.8
B ₁₃₋₁₄	1560	0.47	1.3
B ₁₃₋₁₄	3860	1.16	0.9

Figure 1.4

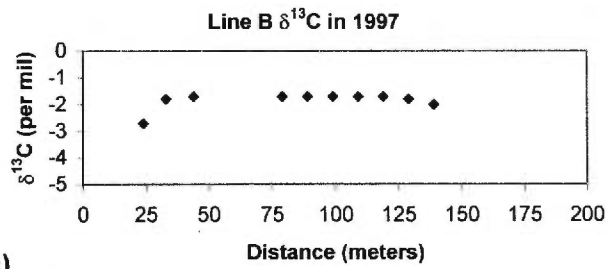
$\delta^{13}\text{C}$ signatures for (a) and (b) line A at the base of San Fernando, (c) line B near the summit of San Fernando crater, (d) line C at approximately 200 meters south of line A, (e) Comalito (line C extension) (f) line Museo, and (g) and (h) line N. Profiles (a) to (f) are oriented southeast-northwest, (g) and (h) are southwest-northeast oriented.



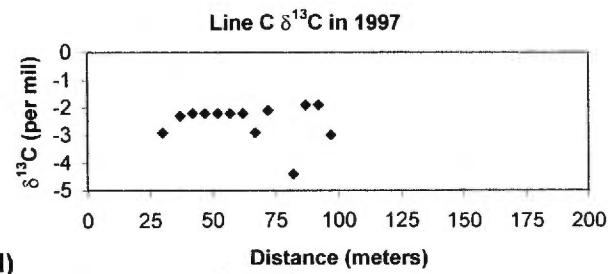
a)



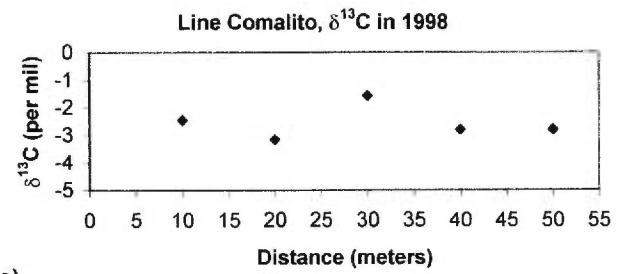
b)



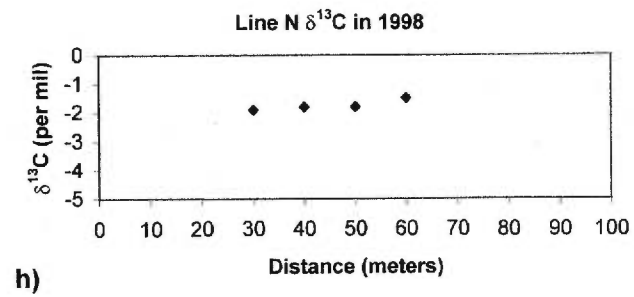
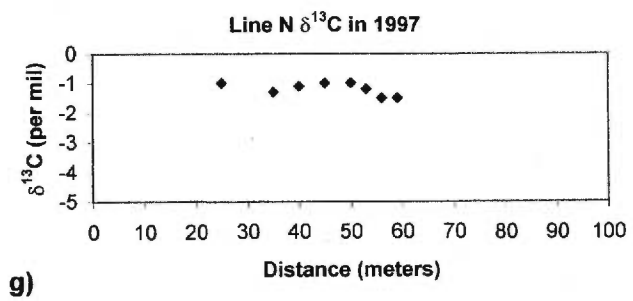
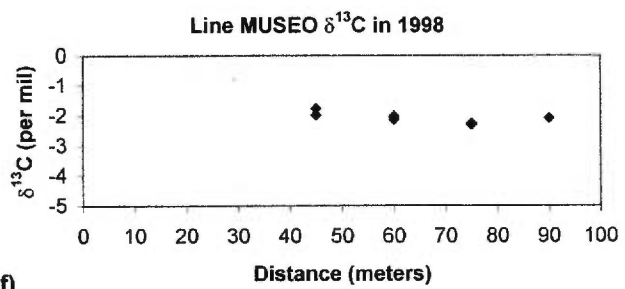
c)



d)



e)



For line N, the average is -1.2 ‰ with extreme values of -1.5 ‰ and -1.0 ‰ (Figure 1.4 g).

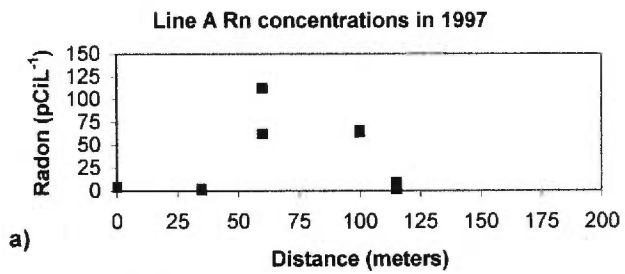
In March 1998, $\delta^{13}\text{C}$ values ranged from -6.6 ‰ to -1.5 ‰ in resampled and new locations. The resampled line A gave $\delta^{13}\text{C}$ values ranging from -2.1 ‰ to -1.7 ‰ with an average of -2.0 ‰ (Figure 1.4 b). Lines B and C were not resampled, but an extension of line C on the Comalito parasite cone was surveyed. An average value of -2.6 ‰ with a range of -3.2 ‰ and -1.6 ‰ were obtained (Figure 1.4 e). Line N showed $\delta^{13}\text{C}$ values ranging from -1.5 ‰ to -2.1 ‰ with an average of -1.8 ‰ (Figure 1.4 h). Line Museo located northern of line A had $\delta^{13}\text{C}$ values ranging from -2.3 ‰ to -1.8 ‰, with an average of -2.1 ‰ (Figure 1.4 f). Line Arenal was also sampled but only one sample had sufficiently high CO_2 concentrations required for analysis (0.47 ‰). A $\delta^{13}\text{C}$ value of -6.6 ‰ was obtained for this part of the caldera where there is abundant vegetation such as bushes and scattered trees.

Radon

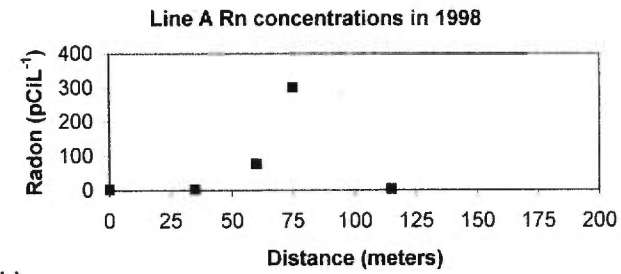
In March 1997, radon values range from 1.6 pCiL^{-1} to 300 pCiL^{-1} . However, there are variations for each line. The radon maxima are generally located directly at the active fumarolic zone. By contrast, Rn values are very low (0.8 to 28.8 pCiL^{-1}) in areas where there is vegetation such as grass, bushes and dry tropical forest. Line A shows high values with 112 pCiL^{-1} in the fumarole field (Figure 1.5 a). Line B near the summit of San Fernando gave the highest radon values from all surveyed lines from 7.7 to 136.4 pCiL^{-1} (Figure 1.5 c). Line C exhibits values ranging from 1.6 to

Figure 1.5

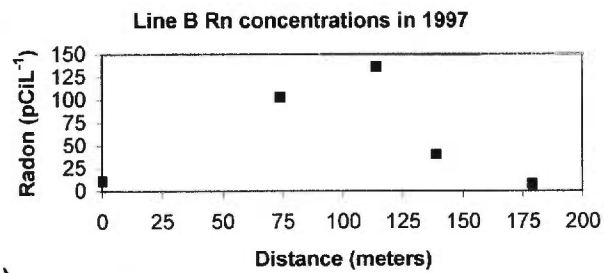
Radon measurements for (a) and (b) line A at the base of San Fernando, (c) line B near the summit of San Fernando crater, (d) line C at approximately 200 meters south of line A, and (e) line N. Profiles (a) to (d) are oriented southeast-northwest, (e) is southwest-northeast oriented.



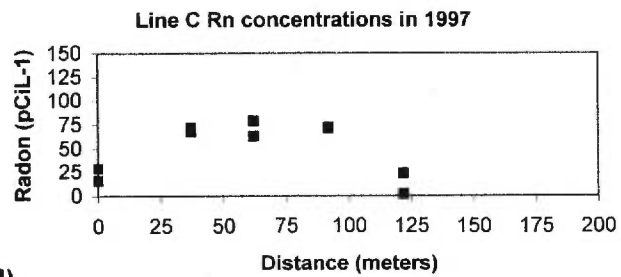
a)



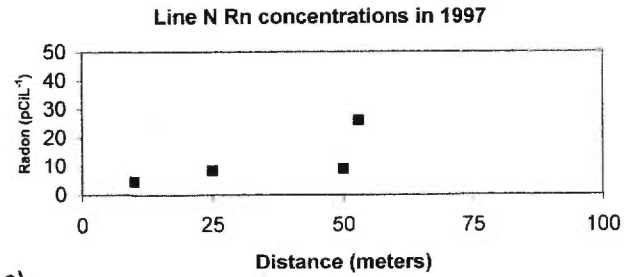
b)



c)



d)



e)

78.7 pCiL⁻¹ (Figure 1.5 d). Line N at Nindirí crater was also surveyed for radon. The values range from 4.6 pCiL⁻¹ to 25.9 pCiL⁻¹ (Figure 1.5 e).

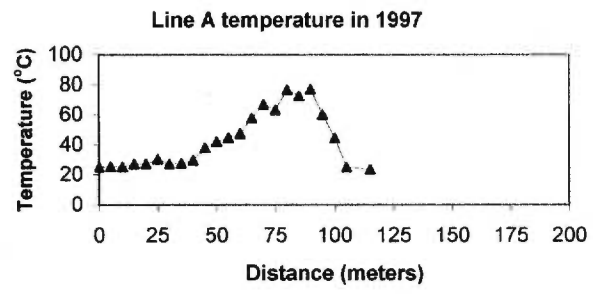
In March 1998, line A was resurveyed to see if any major changes had occurred since March 1997. Rn values ranged from 1.5 pCiL⁻¹ to 300 pCiL⁻¹ (Figure 1.5 b). The high radon value of 300 pCiL⁻¹ may indicate an increase in radon flux. However, radon measurements were done only once for 1998 and not exactly at the same location (± 15 meters).

Temperature

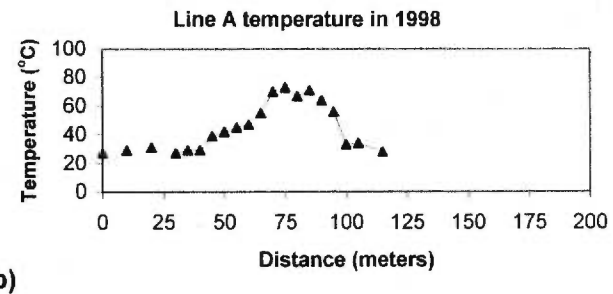
For the four lines surveyed on the northern flank of San Fernando, the temperature ranges from 25 °C to 77 °C. There is a direct relation between the increase of temperature, high CO₂ concentrations and fluxes, high radon flux and the presence of visible fumaroles for each profile. In March 1997 at line A, temperatures ranged from 24 °C to 77 °C in the fumarolic field (Figure 1.6 a). Line B near the summit of San Fernando had values ranging from 25 °C to 62 °C (Figure 1.6 c). Line C had temperature values ranging from 24 °C to 51 °C (Figure 1.6 d). Line N showed values ranging from 28 °C to 32 °C indicating less heat emanating from this area (Figure 1.6 e). However, the soil consists in dark ash which it is easily heated by the sun. In March 1998, line A had temperatures ranging from 27 to 73 °C (Figure 1.6 b). Some individual fumarole temperatures reached 81 °C near line A (M. Navarro, INETER, pers. com., 1998).

Figure 1.6

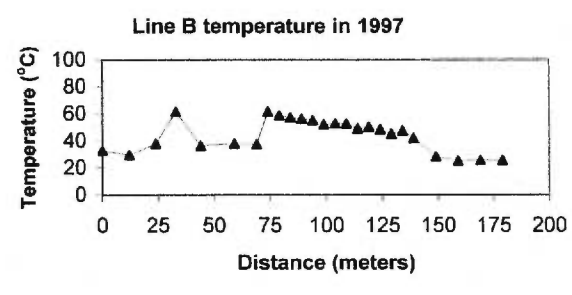
Temperature profiles for (a) and (b) line A at the base of San Fernando, (c) line B near the summit of San Fernando crater, (d) line C at approximately 200 meters south of line A, and (e) line N. Profiles (a) to (d) are oriented southeast-northwest, (e) is southwest-northeast oriented.



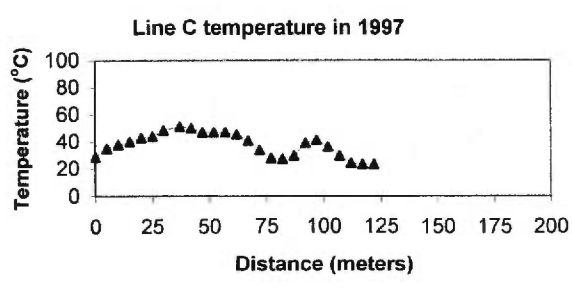
a)



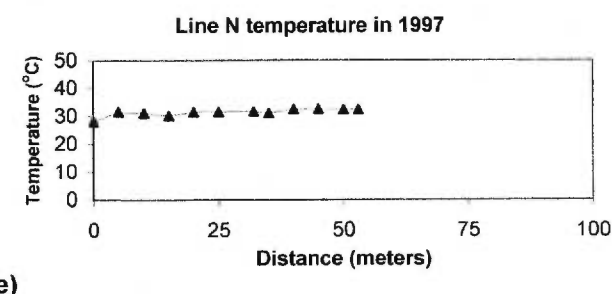
b)



c)



d)



e)

Discussion

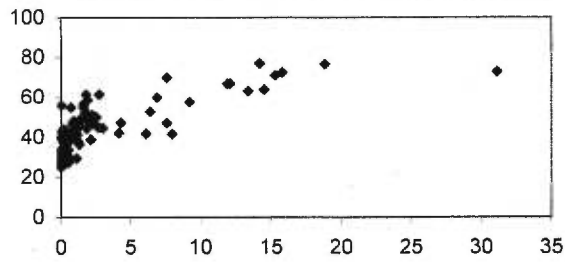
Origin of CO₂

CO₂ is one of the first volatiles to be exsolved in the early stages of degassing, due to its low solubility in silicate melts (Baubron et al., 1991). However, it is a gas that also may be produced by organic activity and by decarbonation of calcareous rocks. At Masaya, there is a positive relation between the high concentrations of CO₂, high radon, high temperatures and the presence of fumaroles (Figure 1.7). The CO₂ flux measurements support the idea that the degassing is concentrated along fractures or faults in the volcanic complex. Beyond the active fumarolic zones, there was no significant or low CO₂ flux, indicating a low permeability of the soil and/or inactive parts of the fracture system. The CO₂ fluxes are higher where CO₂ concentrations are higher which support also the degassing in the fumaroles field (Figure 1.8). At a distance from the fumaroles, it is often observed that there is some accumulation of CO₂ in the soil but no significant flux, showing that the soil in these areas has a low permeability. By contrast with lines C and B, line A may be located in an area where the fracture is more open or more permeable. Line A has the most elevated CO₂ concentrations and fluxes, with 31.1 % and 8540 g·m⁻²·d⁻¹ of CO₂. In contrast, lines C and B have maxima of 2.53 %, 3400 g·m⁻²·d⁻¹, and 2.76 %, 4240 g·m⁻²·d⁻¹, respectively. The transport distance may be greater at these two lines, dispersing the gas before reaching the surface. Also, the permeability may be greater at line A, which may explain the differences with line C and B. Nevertheless, CO₂ fluxes at lines C and B indicate that there is active degassing at these locations and that the fracture reaches to the top of San Fernando crater.

Figure 1.7

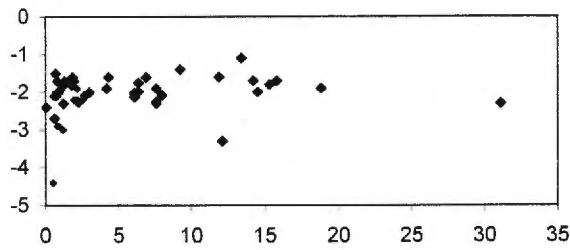
(a) to (d) CO₂-temperature, CO₂-δ¹³C, temperature-δ¹³C, and CO₂-radon correlations for line A, B and C for 1997, and line A for 1998.

CO₂ vs temp. for lines A(97-98), B, C, and Museo



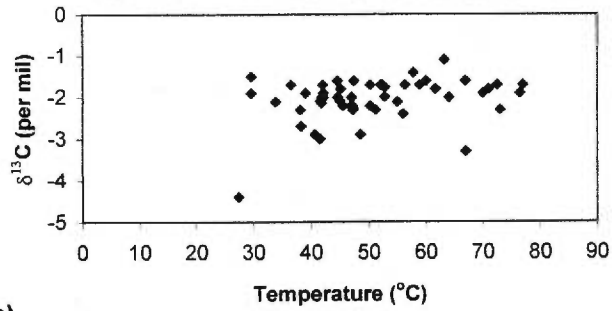
a)

CO₂ vs $\delta^{13}\text{C}$ for lines A (97-98), B, C, and Museo



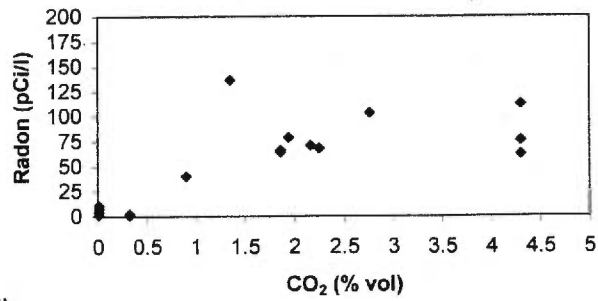
b)

Temp. vs $\delta^{13}\text{C}$ for lines A (97-98), B, C, and Museo



c)

CO₂ vs radon for lines A (97-98), B, and C

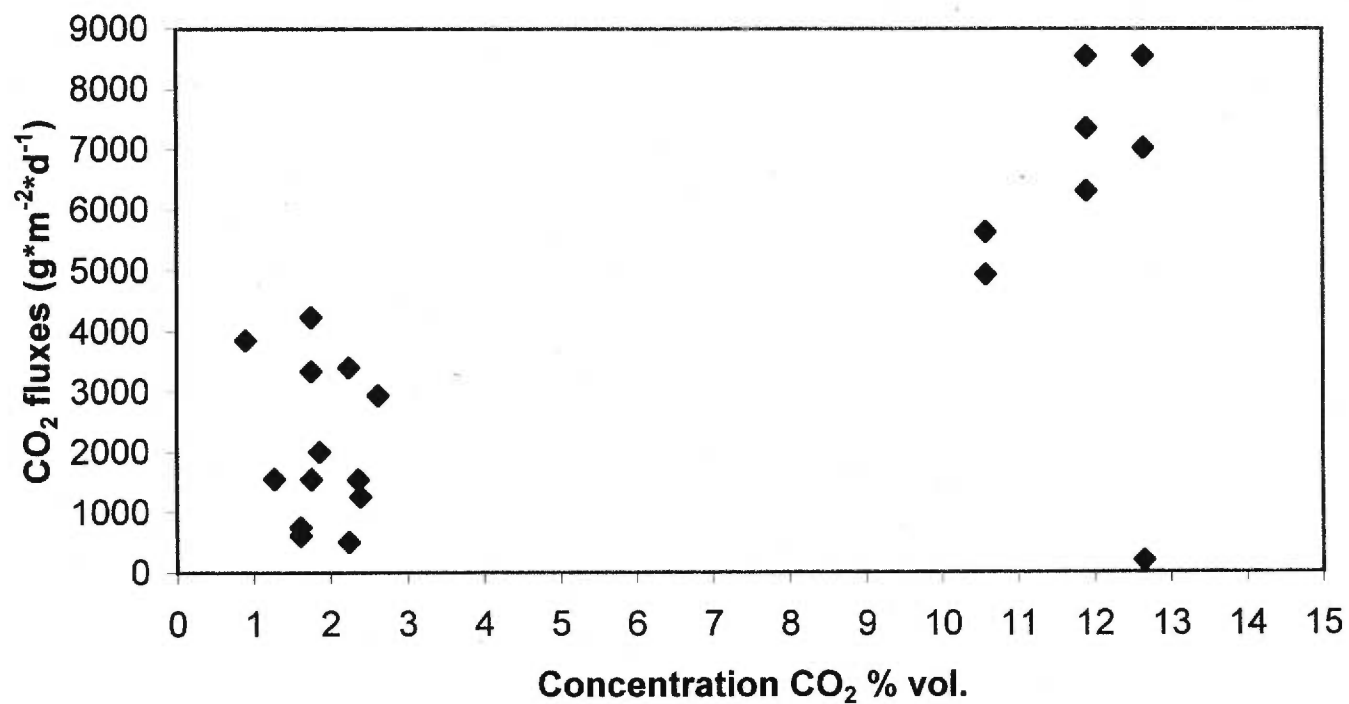


d)

Figure 1.8

CO₂ concentrations versus CO₂ fluxes for line A, B, and C on the north flank of San Fernando.

CO₂ concentration vs CO₂ fluxes



A parallel may be made with the tree-kill occurring since 1989 at Mammoth Mountain, Long Valley Caldera, California, U.S.A. Trees in an apparently healthy forest were killed by CO₂ degassing on the western side of the mountain following an earthquake swarm in 1989. CO₂ concentrations measured in two tree-kill zones from August to October 1994 ranged from 9.4 % to 78.5 % vol., even 90 % vol. in some areas (Farrar et al., 1995). In the same areas and other affected zones, measurements made the subsequent year shown similar CO₂ concentration values (Sorey et al., 1998). It is suggested that the higher CO₂ concentrations observed are the results of a snow cover during the winter or moisture in the soil after a period of rain. At Masaya, with maximum values of 18.8 % in March 1997 and 31.1 % in March 1998, no concentrations of the scale of Mammoth Mountain were encountered. However, CO₂ concentrations in the soil would probably be greater during or following period of rain than concentrations measured during the dry season. The accumulation of CO₂ at the bottom of natural depressions or confined spaces represents less of a hazard at Masaya than at Mammoth Mountain due to the lower concentrations and the open nature of the system in all seasons. There is also the fact that the degassing is more concentrated in a fumarolic field, which is absent in the case of Horseshoe Lake at Mammoth Mountain. CO₂ fluxes ranged from 300 t·d⁻¹ in 1995 and 1996 and dropped to 150 t·d⁻¹ in 1997 in the 145 000 m² Horseshoe Lake tree-kill area (Gerlach et al., 1998). At Masaya, considering an approximate diffuse degassing area of 300 m², we estimated CO₂ fluxes of 0.06 t·d⁻¹ to 2.6 t·d⁻¹, which are conservative since it applies only to the fumarolic field surveyed in 1997. These fluxes are much lower than those encountered at Mammoth Mountain. These differences may be explained

by a smaller and less important fracture system at Masaya. Local CO₂ fluxes ranging from 73 to 2950 g·m⁻²·d⁻¹ were measured in 1996 in the area of the tree-kill at Mammoth Mountain (Sorey et al 1998). By comparison, I measured CO₂ fluxes ranging from 196 g·m⁻²·d⁻¹ to 8544 g·m⁻²·d⁻¹ on the northern flank of San Fernando crater at Masaya. High fluxes were obtained directly in the line A fumarolic area. In the case of Mammoth Mountain, CO₂ monitoring during winter showed an increase in the concentrations in areas covered by snow. During March and April 1995, off scale concentrations (~65 %, sensor maximum) were even encountered at a continuous monitoring station at Horseshoe Lake tree-kill (McGee et al., 1998).

The source of CO₂ degassing at Mammoth Mountain is considered to be the result of a magmatic intrusion or degassing of a crystallised magma body with δ₁₃C values of -4.7 ‰ to -2 ‰ (Farrar et al., 1995; Rahn et al., 1996; Sorey et al., 1998). However, carbonate rocks with δ¹³C values similar to the Mammoth Mountain Fumaroles are present in the area and may contribute to the isotopic signature (Sorey et al., 1998). Momotombo Volcano, located ~100 km from Masaya, also showed similar δ¹³C values as Mammoth Mountain and Masaya. Values from -3.5 ‰ to -2.9 ‰ in 1978 (Allard et al., 1980) and from -0.5 to +2.2 ‰ in 1982 (Menyailov et al., 1986) were obtained at the five summit fumaroles. These values appear to be too heavy to be purely magmatic. It is proposed by Allard et al. (1980) that three sources of heavy carbon, magma, carbonate rocks from the sedimentary coastal series, and carbonate sediments subducted under the crust, are contributing to these signatures. The δ¹³C values obtained at Masaya are comparatively heavy as well, ranging from -4.4 ‰ ±0.1 to -1.0 ‰ ±0.1. In the vicinity of Masaya and Momotombo, it is likely

that carbonate rocks in the subsurface are a major contributor for the heavy signature, since they are found in core samples from the Momotombo geothermal plant (Moore et al., 1981). Thus, the similar pre-volcanic geological history of Momotombo and Masaya indicates that similar basement rocks may be present in both localities. This, along with the contribution of subducted sediment, may explain the heavy values obtained at the summit fumaroles of Momotombo.

At a smaller scale, the isotopic signature may differ according the different physical and chemical conditions of release and transport. At Masaya, average values of -2.0 ‰ , -1.8 ‰ and -2.5 ‰ , for lines A, B and C, respectively, may indicate underlying carbonate layers contamination similar to Momotombo. Line N, with values ranging from -1.0 ‰ to -1.5 ‰ and an average of -1.2 ‰ is even heavier. Located directly at the side of Santiago crater on the Nindirí crater/plateau, in close proximity to the magma source, the CO_2 may have a greater contribution of $\delta^{13}\text{C}$ due to carbonate country rocks, which are efficiently heated by the magma.

In addition to contamination, fractionation processes may contribute to heavy isotopic signatures. It was determined experimentally in MORB that in the case of closed and open system degassing, $\delta^{13}\text{C}$ values show fractionation of CO_2 during nucleation of bubbles, which gives heavier signatures for vapour than melt (Blank et al., 1993; Blank et al, 1994; Pineau and Javoy, 1994). In a closed magmatic system, even if gas vesicles are isotopically heavier than the melt, the bulk isotopic composition remains constant. In the case of an open system, the gas is removed from the magma and variations of the isotopic composition will follow a Rayleigh fractionation trend. In the context of natural environments such as Masaya, they are

more complex than these end members. However, heavier signatures than the original melt are expected for the exsolved gas, since Masaya is considered closer to the open-system model. Experimentally determined equilibrium fractionation factors of -4.5‰ and -2.2‰ for mid-oceanic ridge basalt were found by Blank et al., (1978) and Matthey et al., (1990).

Considering the combined effect of contamination and fractionation for lines A, B, C and N, the -6.6‰ lighter value at Arenal may be the result of less contamination and may reflect only fractionation in “cold” pathways (less chance of addition of a heavier CO₂ source). It thus may represent a more magmatic signature. However, there is also a possible light organic contribution, which may lower the signature. A partial sealing of the main conduit may have an important effect on the degassing along structural weaknesses. The transport of gas through the edifice at different temperature conditions and rock compositions may change the $\delta^{13}\text{C}$ signature of certain zones. Nevertheless, contamination by sedimentary carbonate from the underlying sedimentary coastal series carbonate rocks and/or subducted marine sediment is probably the best explanation for the heavy signature.

Origin of radon

Radon has a short half-life. It is therefore unlikely that all the gas comes directly from the magma chamber. Rather, radon needs structural paths along which to travel. It also may be transported by a vapour phase in a hydrothermal system. However, the high values observed demonstrate that radon is present mainly in places where there is some surface activity (e.g., fumaroles) and where there are structural

features such as fractures, zones of fumarolic alteration, and cinder cones. Recent lava covers much of the surface of the caldera, hiding and sealing certain structural features that would probably contribute to the diffuse degassing. Four profiles on the northern flank of San Fernando show high values near fumaroles and support the presence of a fracture or fault mapped by Williams (1983) in this part of the caldera. Crenshaw (1982) did a radon and mercury survey of several fissures in and around the caldera. His results ranged from 5.3 to 18.9 pCiL⁻¹ for radon and 22.1 to 11 885 ppm for Hg on the northern flank of San Fernando crater near lines A, B and C. His explanation for these low Rn values is that the soil is composed of ash and other materials that have weathered, permitting radon to escape more easily, a permeable soil being more likely to release volatiles from various depths. Crenshaw (1982) made his survey in January to April 1982 corresponding to a period of unrest (1979-1988). However, measurements made during the 1997-1998 surveys show substantially higher Rn values than Crenshaw (1982) measured. The high Rn values of 40 pCiL⁻¹ to 300 pCiL⁻¹ observed on the three transects indicate that a shallow source such as a crystallizing body may be present and contributing to the in situ production of radon. Another explanation is that degassing has increased in this zone since 1982. For example, the fracture system may have enlarged with time, opening pathways for Rn to travel. An increase in pressure due to the blocking of the active vent of Santiago may force more heat and volatiles into the surrounding fracture systems, thereby increasing the rate of transport of radon. Low Rn values of 0.8 pCiL⁻¹ to 28.8 pCiL⁻¹ at the edges of the transects show that there are low levels of Rn in vegetated zones where grass and trees grow in a better-developed soil.

Nevertheless, few measurements were made and it is possible that these values do not represent real variability in the degassing activity, in which case a situation of under-sampling may exist.

A Degassing Model

Degassing processes at Masaya occur in different areas and in different ways. With the exception of the emission of a volcanic plume at the Santiago active crater, passive degassing is occurring at very localised areas. The northern flank of San Fernando is one of the few areas where the degassing is observable in the form of fumaroles. Since it is known that a shallow source of magma may be at 0.5 to 5 kilometres depth in the crust, the principal source of the gas is likely to be there (Rymer et al., 1998). However, several processes may alter the composition and the spatial distribution of the gas. Beginning at the emission from the source, removal of volatiles species will occur during transport. At the fumarole field, no sulphur is detected. Absorption of SO₂ and other sulphurous compounds in the subsurface is taking place during transport. Decarbonation of calcareous rocks in contact with the magma chamber may add CO₂ and result in heavier $\delta^{13}\text{C}$ values. Fractionation of the CO₂ may also affect the $\delta^{13}\text{C}$ signature by lightening the CO₂ isotopic concentration. This may explain the differences observed between lines A, B, and C with average $\delta^{13}\text{C} = -2.0$ ‰, respectively, Museo with -2.1 ‰, line N with -1.2 ‰, and the unusually light value of Arenal of -6.6 ‰. While an organic contribution cannot be ruled out, the Arenal value also may represent a more magmatic signature. It is possible that the pathway by which the gas has travelled was more direct and that

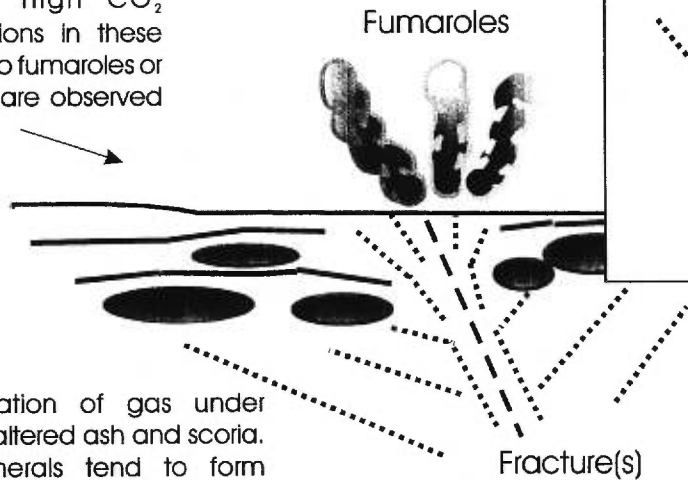
contamination was less pronounced due to the comparatively large distance between Arenal and the hot magma. Absence of fumaroles and the presence of suspected ring fracture (McBirney, 1956; Crenshaw, 1982; Williams, 1983) are consistent with the lack of contamination. By contrast, $\delta^{13}\text{C}$ values from line N (Nindirí crater) show the contribution of a source with a heavier carbon signature. A greater interaction of the high temperature magma with the country rocks surely contributes to the heavier signature encountered at the crater.

At a smaller scale, the CO_2 concentrations, CO_2 fluxes, radon concentrations and temperature variations observed on the northern flank of San Fernando are explained by the local structure and local alteration of the subsurface (Figure 1.9). Inside the caldera, there are various layers of lava and tephras, contributing to a variable permeability. It is logical that all gas travelled along structural weaknesses such as fractures and faults. After escaping from the magma chamber and passing through the various layers, the gas released at the surface depends on the permeability of the subsurface. At the surveyed locations, CO_2 concentrations and fluxes do not always concord. Some locations show relatively high CO_2 concentrations but low to non-existent fluxes. This may indicate gas accumulation under relatively impermeable layers (Figure 1.9). Moisture and relatively high temperature cause alteration of the soil and rocks. This is more visible at locations surrounding fumaroles. Alteration to clay minerals causes a decrease in permeability by sealing pathways. The variability encountered in the spatial degassing was expected due to the heterogeneous nature of the volcanic substrate. The heterogeneous distribution of

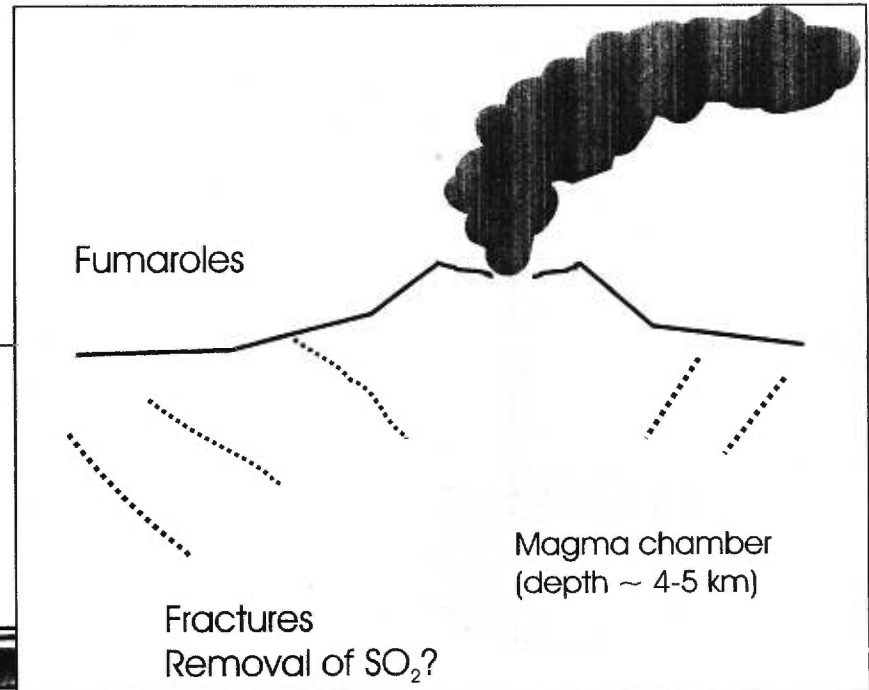
Figure 1.9

A schematic model of the degassing paths at Masaya Caldera, Nicaragua

It is possible to obtain relatively high CO_2 concentrations in these areas but no fumaroles or CO_2 fluxes are observed



Accumulation of gas under zones of altered ash and scoria. Clay minerals tend to form impermeable layers and favor accumulation of gas without any measurable flux.



the degassing is not unique and is encountered not only in volcanic phenomena but also in geology in general.

Conclusions

The study of soil gas on a volcano may be helpful to understanding its behaviour and may also help determine the nature of structural features. For the Masaya gas study, the main conclusions are the following:

- 1) CO₂ gas profiles demonstrate the structural control of degassing. This control is due to the low permeability of the recent volcanic material overlying the volcanic complex, allowing gas to travel principally through weaknesses in the sub-surface, such as fractures and faults.
- 2) The CO₂ flux demonstrates that the degassing occurs mainly in the fumarolic field where the highest CO₂ concentrations are found. However, accumulation of gas occurs in areas with layers of different permeability in the sub-surface, and no significant fluxes were observed despite moderate to high CO₂ concentrations.
- 3) The $\delta^{13}\text{C}$ values indicate a mixed source of CO₂. There are two possible sources: 1) mantle gases from the magma chamber, and 2) CO₂ derived from carbonate rocks.
- 4) Radon gas is probably structurally transported along fractures. The radon maxima are observed along the main fracture system where there is fumarolic activity. In this region, the system is more likely to be open.
- 4) Masaya is a volcano with an open conduit that permits the degassing of magmatic gas (H₂O, CO₂, SO₂, HCl, etc.) and a partially closed transport system

surrounding the volcanic edifice, formed by fractures, faults and volcanic deposits of variable permeability covering the caldera. Periodic closing of the main conduit as well as the evolution of the fracture and fault system, may lead to variations in the distributions of CO₂ and CO₂ fluxes at a distance from the conduit.

References

- Allard, P., 1980.** Composition isotopique du carbone dans les gaz d'un volcan d'arc: Le Momotombo (Nicaragua). *Comptes rendus de l'Academie des Sciences, Paris, Série D*, 290: 1525-1528.
- Baubron, J.-C., Allard, P., Sabroux, J.-C., Tedesco, D., and Toutain, J.-P., 1991.** Soil gas emanations as precursory indicators of volcanic eruptions. *Journal of the Geological Society of London*. 148: 571-576.
- Blank, J. G., and Brooker, R. A., 1994.** Carbon Dioxide in Silicate Melts. In: M. R. Carroll and J. R. Holloway (Editors), *Volatiles in Magma. Reviews in Mineralogy*, 30: 157-186.
- Blank, J. G., Delaney, J. R., and Des Marais, D. J., 1993.** The concentration and isotopic composition of carbon in basaltic glasses from the Juan de Fuca Ridge, Pacific Ocean. *Geochimica et Cosmochimica Acta*, 57: 875-887.
- Bulletin of the Global Volcanism Network, 1997.** Masaya volcano. *Smithsonian Institution* 22 (3): 6-7.
- Bulletin of the Global Volcanism Network, 1998.** Masaya volcano. *Smithsonian Institution* 23 (9): 7.
- Bulletin of the Global Volcanism Network, 1999.** Masaya volcano. *Smithsonian Institution* 24 (4): 5.
- Connor, C., Hill, B., LaFemina, P., Navarro, M., and Conway, M., 1996.** Soil ²²²Rn during the initial phase of the June-August 1995 eruption of Cerro Negro, Nicaragua. *Journal of Volcanology and Geothermal Research*, 73: 199-127.
- Crenshaw, W. B., 1982.** Ground radon and mercury concentration surveys for location of faults systems, Masaya Caldera, Nicaragua. Unpublished M.S. thesis, Dartmouth College, Hanover, New Hampshire, U.S.A., 82 pp.
- Crenshaw, W. B., Williams, S. N., and Stoiber, R. E., 1982.** Fault location by radon and mercury detection at an active volcano in Nicaragua. *Nature*, 300: 345-346.
- Farrar, C. D., Sorey, M. L., Evans, W. C., Howie, J. F., Kerr, B. D., Kennedy, B. M., King, C.-Y., and Suthon, J. R., 1995.** Forest-killing diffuse CO₂ emission at Mammoth Mountain as a sign of magmatic unrest. *Nature*, 376: 675-678.
- Faure, G., 1986.** *Principles of Isotope Geology*. 2nd Ed. John Wiley & Sons, Inc., New York, 589 pp.

- Gerlach, T. M., Doukas, M. P., McGee, K.A., and Kessler, R., 1998.** Three-year decline of magmatic CO₂ emission from soils of a Mammoth Mountain tree kill: Horseshoe Lake, CA, 1995-1997. *Geophysical Research Letters*, 25: 1947-1950.
- Heiligmann, M., Stix, J., Williams-Jones, G., Sherwood-Lollar, B., and Garzón V., G., 1997.** Distal degassing of radon and carbon dioxide on Galeras volcano, Colombia. *Journal of Volcanology and Geothermal Research*, 77: 267-284.
- Irwin, P. W. and Barnes, I., 1980.** Tectonic relations of carbon dioxide discharge and earthquakes. *Journal of Geophysical Research*. 85: 3115-3121.
- Javoy, M., Pineau, F., and Iiyama, I., 1978.** Experimental determination of the isotope fractionation between gaseous CO₂ and carbon dissolved in tholeiitic magma: preliminary results. *Contribution to Mineralogy and Petrology*, 67: 35-39.
- Kotrappa, P., Dempsey, J. C., Rasey, R. W., and Stieff, L.R., 1990.** A practical E-Perm (electret passive environmental monitor) system for indoor radon measurement. *Health Physics*, 58: 461-467.
- Maciejewski, A. J. H., 1995.** Evolution and present-day activity of the Masaya Volcanic Complex, Nicaragua. Unpublished manuscript, The Open University, 37 pp.
- Mattey, D. P., 1991.** Carbon dioxide solubility and carbon isotope fractionation in basaltic melt. *Geochimica et Cosmochimica Acta*, 55: 3467-3473.
- McBirney, A. R., 1956.** The Nicaraguan volcano Masaya and its caldera. *American Geophysical Union Transactions*, 37: 83-96.
- McGee, A. K., and Gerlach, T. M., 1998.** Annual cycle of magmatic CO₂ in a tree-kill at Mammoth Mountain, California: Implications for soil acidification. *Geology*, 26: 463-466.
- Menyailov, I. A., Nikitina, L. P., Shapar, V. N., and Pilipenko, V. P., 1986.** Temperature increase and chemical change of fumarolic gases at Momotombo volcano, Nicaragua, in 1982-1985: are these indicators of a possible eruption? *Journal of Geophysical Research*, 91: 12199-12214.
- Ozima, M., and Podosek, F. A., 1983.** *Noble Gas Geochemistry*. Cambridge University Press, Cambridge, England, 367 pp.
- Rad Elec. Inc., 1993.** E-Perm^R system manual. Rad Elec Inc., Virginia.

- Rahn, T. A., Fessenden, J. E., and Wahlen, M., 1996.** Flux chamber measurements of anomalous CO₂ emission from the flanks of Mammoth Mountain, California. *Geophysical Research Letters*, 23: 1861-1864.
- Schery, S. D., and Petschek, A. G., 1983.** Exhalation of radon and thoron: the question of the effect of thermal gradients in soil. *Earth and Planetary Science Letters*, 64: 56-60.
- Sorey, M. L., Kennedy, B. M., W. C. Evans, Farrar, C. D., and Suemnicht, G. A., 1993.** Helium isotope and gas discharge variations associated with crustal unrest in Long Valley Caldera, California, 1989-1992. *Journal of Geophysical Research*, 98: 15871-15889.
- Sorey, M. L., Evans, W. C., Kennedy, B. M., Farrar, C. D., Hainsworth, L. J., and Hausback, B., 1998.** Carbon dioxide and helium emissions from a reservoir of magmatic gas beneath Mammoth Mountain, California. *Journal of Geophysical Research*, 103: 15303-15323.
- Tilsley, J. E., 1992.** Radon: Sources, hazards and control. *Geoscience Canada*, 19: 163-167.
- Thomas, D. M., Cuff, K. E., and Cox, M. E., 1986.** The association between ground gas radon variations and geologic activity in Hawaii. *Journal of Geophysical Research*, 91: 12186-12198.
- Williams, S. N., 1983.** Geology and eruptive mechanisms of Masaya Caldera Complex, Nicaragua. Unpublished Ph.D. thesis, Dartmouth College, Hanover, New Hampshire, U.S.A., 169 pp.

CHAPTER II

Mechanism of SO₂ Degassing at Masaya Caldera, Nicaragua

Katie St-Amand

Département de géologie
Université de Montréal
Montréal, Québec, H3C 3J7
Canada

Abstract

Masaya volcano is one of many volcanoes that present continuous degassing. Previous activity has consisted of extrusion of basaltic lava in 1670 and 1772, active lava lakes in 1989 and 1993, and strombolian eruptions in June 1993, December 1996, November 1997, and September 1998. COSPEC measurements were conducted in 1996-1998. On 16 March 1996, COSPEC measurements at Masaya ranged from 240 to 1100 tonnes per day. In 1997 and 1998, values ranged from 200 to 7400 tonnes per day with a clear increase in 1998. Petrologic analyses were conducted on bombs from the 12 November 1997 strombolian explosion. Results show low concentration of sulfur and chlorine in glass inclusions, the glassy matrix, and Pél e's hair. This suggests that the magma at shallow levels may be degassed or partially degassed with the majority of SO₂ coming from another level in the conduit or the magma chamber. Injection of magma, convection in the magma chamber and/or in the conduit of the vent may explain the high fluxes. Intermittent degassing such as emission of gas puffs at the crater, convection of magma, and atmospheric dispersion (fragmentation of the plume during transport) may explain the variations in the SO₂ fluxes. In 1998, measurements with two COSPEC instruments were conducted for two days along roads at distances of 5.5 km and 15 km from the active crater for 17 March and 15 km and 30 km for 18 March. Measurements for 17 March indicate that from 5 km from the vent to 15 km from the vent there is no significant dry or wet deposition of SO₂ from the plume. For 18 March, values obtained at 30 km from the vent show SO₂ fluxes two to three times higher than the SO₂ fluxes at 15 km from the vent, showing significant wind and topographic effects.

Introduction

Masaya caldera is a basaltic shield volcano associated with the subduction of the Cocos plate beneath the Caribbean plate. Its size is approximately 11 km long by 6 km wide, with a central complex within the caldera, which reaches 635 m at its highest point at the rim of the crater of San Fernando. Masaya is located in the eastern part of Nicaragua approximately 25 km southeast of Managua (11.98°N 86.15°W). It is part of the Quaternary volcanic chain of Central America and is aligned with the Nicaragua graben. Past activity includes plinian explosive eruptions at approximately 20,000 and 6,500 years ago (Bice, 1980; Williams, 1983), basaltic lava flows, periodic lava lakes, passive degassing of Santiago crater and mild strombolian explosions. In 1972, average SO₂ fluxes of 180 t·d⁻¹ were measured, the gas being expelled from a hole through the frozen lava lake present at that time (Stoiber, 1973). From 1980 to 1982, Stoiber et al. (1986) measured SO₂ fluxes ranging from 380 t·d⁻¹ to 1200 t·d⁻¹. On 16 March 1996, an average value of 600 t·d⁻¹ was obtained (Rymer et al., 1998). Masaya is presently actively degassing (1993 to present). Three recent small strombolian explosions occurred on 5 December 1996, on 12 November 1997 and on 14 September 1998. The 1997 explosion extruded bombs around the active Santiago crater and onto the old lava lake of Nindirí.

Variations in the quantity and composition of gas before, during, and after eruptions make sampling and monitoring of gas an important method to monitor the activity of an active volcano. Health risk and public safety may depend on these observations. Correlation spectrometry measurements (COSPEC) and petrological analysis of glass inclusions in erupted material may reveal to understand the

degassing processes and eruptive state of an active volcano. With these points in mind, COSPEC measurements were made at Masaya in February-April 1997 and 1998. The surveys were conducted on five days in 1997 and 20 days in 1998. For three days in 1998, SO₂ fluxes measurements were made by two COSPEC instruments that were used simultaneously on three roads at 5.5, 15 and 30 km distance from the active vent in order to observe transport and dispersion processes of the volcanic plume. Petrologic analyses were conducted on glassy materials erupted by the 12 November 1998 strombolian explosion. Sulfur, chlorine and major element oxides were measured in glass inclusions of feldspar, in matrix glasses and in samples of Pélé's hair.

The objectives of this work are (1) to monitor the degassing of Masaya and present a model of degassing at the active vent, (2) explain the variations on an hourly, daily and annual basis, and (3) to analyse the amounts of SO₂ in the volcanic plume and present a preliminary model of SO₂ transport and removal downwind from the vent.

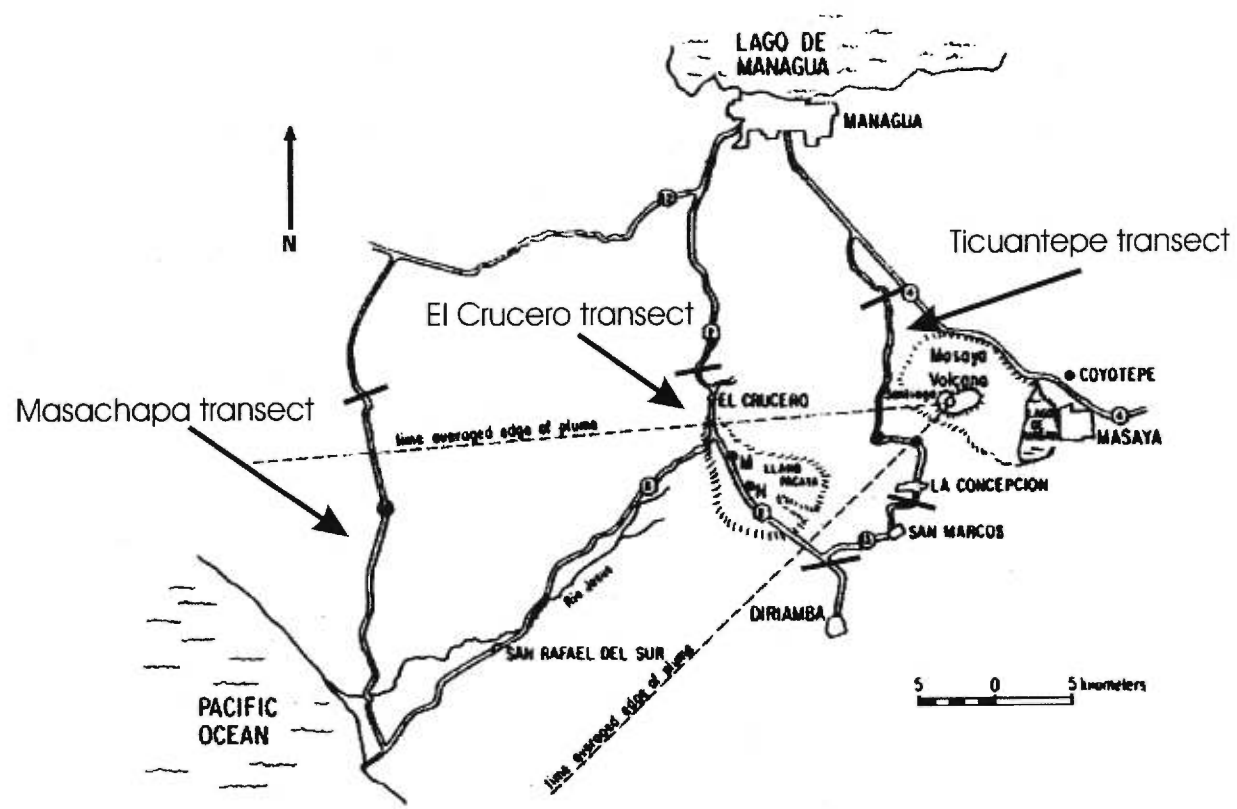
Methodology

SO₂ Fluxes

A typical day of measurements consisted of an average of 8-10 traverses of approximately 20 minutes each. The plume was blown mostly west of the active vent towards the Pacific coast. Three roads at 5.5, 15, and 30 km distance northwest of the active vent were used for SO₂ fluxes traverses (Figure 2.1). To maximize the amount of ultraviolet radiation available, measurements were conducted from 0900 to 1630

Figure 2.1

Road map of COSPEC segments (from Johnson et al., 1986)



hours local time. For several days in 1998, SO₂ fluxes were measured using two COSPEC correlation spectrometers. The spectrometer uses solar ultraviolet radiation to detect SO₂. The ultraviolet radiation passes through a set of lenses, is detected by the spectrometer and transformed into an electric signal, which recorded by a chart recorder and/or a computer. A typical measurement consists of driving beneath the volcanic plume, perpendicularly if possible. Gas cells of known concentration were placed in the field of view of the instrument at the beginning and at the end of each traverse to calibrate the SO₂ signals from the plume. For the COSPEC IV instrument, the low and high concentration gas cells were 64 and 339.2 ppm·m, respectively. The COSPEC V had low and high cells of 138 and 430 ppm·m, respectively, in 1997; and 103 and 326 ppm·m, respectively, in 1998. Individual traverses were divided into segments to permit corrections of deviation from perpendicularity of the traverse with respect to the column (Figure 2.1, Table 2.1). An SO₂ calculation for each segment was made and then summed to determine the total SO₂ flux for a given traverse. The SO₂ flux in metric tonnes per day was calculated using the following equation:

$$\text{SO}_2 \text{ flux} = (\cos(\theta))(d_{\text{col}})(n_{\text{wind}})(0.00023)([\text{SO}_2]_{\text{col}}) \quad (2.1)$$

where $q(\theta)$ is the deviation in degree from perpendicularity of the segment of the road with respect to the gas column; d_{col} is the width (m) of a given segment determined on a map; n_{wind} is the wind speed ($\text{m}\cdot\text{s}^{-1}$) at ground level, at the time of measurement when possible or at the time closest to the measurement; $0.00023 \text{ t}\cdot\text{s}\cdot\text{m}^{-3}\cdot\text{d}^{-1}\cdot\text{ppm}^{-1}$ is a factor to convert $\text{ppm}\cdot\text{m}^3\cdot\text{s}^{-1}$ into metric tonnes per day; and $[\text{SO}_2]_{\text{col}}$ is the path-length concentration of SO₂ (ppm·m) in the column. The concentration of SO₂ is calculated as:

$$[\text{SO}_2]_{\text{col}} = (P_{\text{avg}}/P_{\text{cal}})*(C_{\text{cal}}) \quad (2.2)$$

Table 2.1 Segment parameters for COSPEC measurements.

Section	Length of each segment (m)	Azimuth (°)	Section	Length of each segment (m)	Azimuth
Ticuantepe, 5 km from the vent			El Crucero, 15 km from the vent		
4 _a -5	6550	12	L ₂ -L ₁	3350	285
5-6	4100	293	L ₁ -L ₀	650	248
6-7	2600	13	L ₀ -L ₁	5000	350
			L ₁ -L ₂	7300	312
			L ₂ -L ₃	3400	337
			L ₃ -L ₄	1400	0
			L ₄ -L _{4.5}	3600	325
			L _{4.5} -L ₅	1700	28
			L ₅ -L ₆	2800	9
			L ₆ -L ₇	5500	343
			L ₇ -L ₈	3000	15
			L ₈ -L ₉	1800	14
Masachapa, 30 km from the vent					
MM _{.1} -MM ₀	3850	18			
MM ₀ -MM ₁	5250	0			
MM ₁ -MM ₂	6500	350			
MM ₂ -MM ₃	3250	14			
MM ₃ -MM ₄	3000	4			
MM ₄ -MM ₅	1250	23			
MM ₅ -MM ₆	3250	212			
MM ₆ -MM ₇	6750	42			
MM ₇ -Pochc	2150	113			

where P_{cal} is the peak height of the calibration gas cell in arbitrary units; P_{avg} is the average height for the segment; and C_{cal} is the concentration of the calibration gas cell in ppm·m.

On 14 March 1998, a COSPEC survey was conducted with the two COSPEC instruments simultaneously in the same vehicle. It enabled us to calculate a correction factor between the two instruments needed for accurate measurements. The two instruments were installed on the same side of the vehicle and were connected to the same chart recorder so that each profile of the plume was recorded at the same time by the two COSPECs. Fluxes for each traverse were calculated according to the methods described above. Differences between the COSPEC IV and V measurements were observed. The first measurement was not used due to the large variation of background for the COSPEC IV. A COSPEC V/IV ratio profile was obtained for each traverse (Table 2.2). This ratio ranges between 1.12 and 1.36. An average correction factor of 1.26 was obtained. All measurements made by the COSPEC IV were multiplied by this value.

SO₂ Flux Error

Many factors affect the measured SO₂ fluxes. Instrumental errors along with external factors such as variations of the cloud cover change in sun angle, wind speed and direction of the plume, and ash content add to the uncertainties of the values. For the instrumental uncertainty, instrument calibration is 2 %, chart reading ± 3 %, vehicle speed ± 5 %, wind speed measurement $\pm 6-26$ % in 1997 and $\pm 3-10$ % in 1998 (error on the anemometers used in 1997 and 1998). Another source of error of

Table 2.2 COSPEC VM ratio

Local time (hours)	Windspeed ms ⁻¹	Cospec IV						Cospec V					Ratio VM
		Glyn	John	Katie	Katie ¹	Avg. td ¹	Std dev.	Glyn	John	Katie	Avg. td ¹	Std dev.	
1126-1141	16.2	1080	992	1019	1033	1031	32	1450	1398	1349	1399	41	1.35693501
1143-1158	15.5	1010	845	847	915	904	67	1131	1045	1133	1103	41	1.21979541
1159-1214	15.5	1471	1388	1382	1447	1422	38	1730	1728	1707	1722	10	1.21097046
1215-1229	17.0	2047	1884	1911	2096	1985	89	2230	2223	2234	2229	5	1.12320484
1231-1246	15.6	1362	1379	1444	1407	1398	31	1952	1922	1849	1908	43	1.36480687

¹The SO₂ fluxes were evaluated a second time a different method

Avg. ratio 1.26 ± 0.09

7 % comes from the ratio used to adjust the COSPEC IV measurements. Thus, average flux errors range from 9 % to 28 % in 1997 with an average 15 %, and from 10 % to 14 % with an average of 11 % for 1998 (Table 2.3).

Wind speed measurements were made with a handheld anemometer at the summit of San Fernando crater, 635 m a.s.l., and at 15 km from the active vent on the Llano Pacaya ridge at 930 m a.s.l., west of the caldera. Measurements were made at the highest accessible point at San Fernando crater and the Llano Pacaya ridge each half hour, at the time of COSPEC measurements when possible. The variability of the wind may be related to the variability of the SO₂ fluxes. However

Petrology

Petrological analyses of glass were made with a JEOL 8900 electron microprobe at McGill University. Calibration using basaltic and silicic glass standards VG-2, KN-9 and KE-12 was done for glass inclusions, the glassy matrix and Pélé's hair samples (Table 2.4). Since the results for sulfur obtained on the standards were underestimated by half of those of the accepted values, all sulfur values obtained were multiplied by a factor of 1.97. Plagioclases and olivines also were analysed with appropriate standards (Table 2.5). The error on the sulfur contents is ± 60 -80 ppm, and ± 12 ppm for Cl, which are the detection limits of the microprobe. Major oxide results were normalized to 100 weight percent.

Table 2.3 Error calculation for SO₂ measurements

Calibration cell concentrations:		
	COSPEC IV:	2%
	COSPEC V:	2%
	Chart recorder reading error:	3%
	Variation in car speed:	5%
Windspeed measurements:		
	1997: 6-26%	14%
	1998: 3-10%	5%
	COSPEC IV/V ratio (in 1998 only):	7%
Total error (square root of the sum of the squares):		
1997:	Minimum:	9%
	Maximum:	27%
	Average:	15%
1998:	Minimum:	10%
	Maximum:	14%
	Average:	11%

Table 2.4 Normalised standard glass analyses.

	KE-12	KE-12 ¹	KN-9	KN-9	KN-9 ¹	VG-2	VG-2	VG-2	VG-2 ¹
SiO ₂	71.41	70.43	70.95	74.81	74.66	50.66	51.36	51.01	50.83
TiO ₂	0.28	0.33	0.27	0.18	0.18	1.83	1.90	1.86	1.85
Al ₂ O ₃	8.19	7.63	8.20	11.26	10.46	14.22	13.92	14.17	14.06
FeO*	8.91	8.61	9.30	3.69	3.63	12.02	11.77	11.70	12.06
MnO	0.28	0.26	0.26	0.048	0.06	0.21	0.18	0.19	0.23
MgO	0.02	0.02	0.03	0.003	0.00	6.78	6.66	6.65	6.72
CaO	0.38	0.35	0.40	0.10	0.14	11.24	11.02	11.24	11.12
Na ₂ O	5.54	7.29	5.75	4.67	5.48	2.63	2.61	2.60	2.62
K ₂ O	4.44	4.29	4.34	4.53	4.44	0.18	0.20	0.18	0.19
P ₂ O ₅	0.01	0.02	0.002	0.01	0.00	0.20	0.20	0.20	0.20
Total	100.00	100.00	100.00	100.00	100.00	100.00	100.00	100.00	100.00
F	4985	4400	4381	8118	6400	0	0	0	0
Cl	0	3300	0	0	3100	0	0	0	0
S	161	0	161	16	0	1313	1266	1318	1300

¹ Accepted values for KE-12, KN-9, and VG-2.**Table 2.5** Normalised standard analyses for plagioclase and olivine.

Plagioclase and olivine standards						
	orthoclase	albite ¹	diopside	andradite	swolstd ¹	
SiO ₂	64.76	68.21	55.33	36.71	39.25	
Al ₂ O ₃	17.00	20.13	0.56	0.10	0.00	
FeO	1.07	0.01	0.84	28.80	16.49	
MnO	-	-	-	-	0.35	
MgO	0.01	0.00	17.85	0.22	43.91	
CaO	0.00	0.61	25.02	34.14	0.01	
Na ₂ O	0.42	10.89	0.39	0.01	-	
K ₂ O	16.73	0.16	0.02	0.03	-	
Cr ₂ O ₃	-	-	-	-	0.02	
Total	100.00	100.00	100.00	100.00	100.00	

¹ Mean microprobe analysis

Results

SO₂ Fluxes, 1997-1998

In 1997, daily averaged measurements ranged from 160 to 520 tonnes per day. Extreme punctual values correspond to a minimum of 60 t·d⁻¹, and a maximum value of 1050 t·d⁻¹. Observations showed that the direction of the plume was stable, blowing to the west. Variations may be attributed to the variability of the wind and a visible puffing effect. Hourly variations were observed for each day surveyed, which Stoiber et al. (1986) also observed for 0.5-1.5 hour intervals. For example, on 25 March 1997, an initial value of 500 t·d⁻¹ was obtained at 1204 hours local time, while a decrease in the degassing gave a value of 330 t·d⁻¹ at 1342 hours. The final value made at 5.5 km distance from the crater shows an increase, with a value of 1050 t·d⁻¹ at 1536 hours (Table 2.6, Figure 2.2).

In 1998, the average daily SO₂ fluxes varied from 675 to 5575 t·d⁻¹. Large hourly and daily variations were observed during this survey. Extreme values ranged from a low of 280 t·d⁻¹ to a high of 7390 t·d⁻¹. Variations occur on a wide range of time interval from hours to day. For example, on 13 March a low SO₂ flux of 280 t·d⁻¹ at 1200 hours and a high flux of 1250 t·d⁻¹ at 1420 hours were obtained at 15 km from the vent (El Crucero). The average of this particular day is 700 t·d⁻¹. On 1 March, the highest SO₂ fluxes of the entire survey were obtained at 15 km distance from the volcano on the El Crucero road. Values ranged from 3040 to 7390 t·d⁻¹ with an average of 5580 t·d⁻¹. On this day, the plume visibly seemed to be very low in the sky, staying near the ground. Wind speeds of 4.2 to 5.3 m·s⁻¹ were recorded on this day.

Table 2.6 February-March 1997 SO₂ fluxe measurements.

Date	Start at	End at	Windspeed (ms ⁻¹)	5 km (td ⁻¹)	15 km (td ⁻¹)	Total av. (td ⁻¹)	1ms ⁻¹ fluxes (td ⁻¹)	Total av. 1ms ⁻¹ (td ⁻¹)	Comments
12-02-97			3.53	214		159			
			3.53	207					
			3.53	56					
			3.53	157					
13-02-97			2.76	399		363			
			2.76	352					
			2.76	463					
			2.76	635					
			1.36	169					
			1.36	157					
14-02-97			3.9	280		312			
			3.9	409					
			3.9	269					
			3.9	290					
07-03-97	1030	1100	8.74	368		370	42	39	
	1109	1130	8.74	484			55		
	1137	1157	8.74	372			43		
	1230	1300	8.74		436		50		
	1305	1346	10.45		232		22		
	1350	1422	10.45		380		36		
	1426	1450	10.45		288		28		
	1455	1310	10.45	403			39		
12-03-97	926	947	8.16	568		342	70	43	
	1015	1033	8.16		323		40		
	1037	1055	8.16		368		45		
	1104	1122	8.16		317		39		
	1130	1148	8.16		321		39		
	1151	1212	8.16		312		38		
	1215	1232	8.16		213		26		
	1235	1258	8.48		398		50		
	1332	1352	8.48		197		23		
	1355	1417	7.77		267		34		
	1426	1445	7.77		414		53		
	1448	1507	7.77		445		57		
	1510	1530	7.77		345		44		
	1546	1607	6.83	305			45		

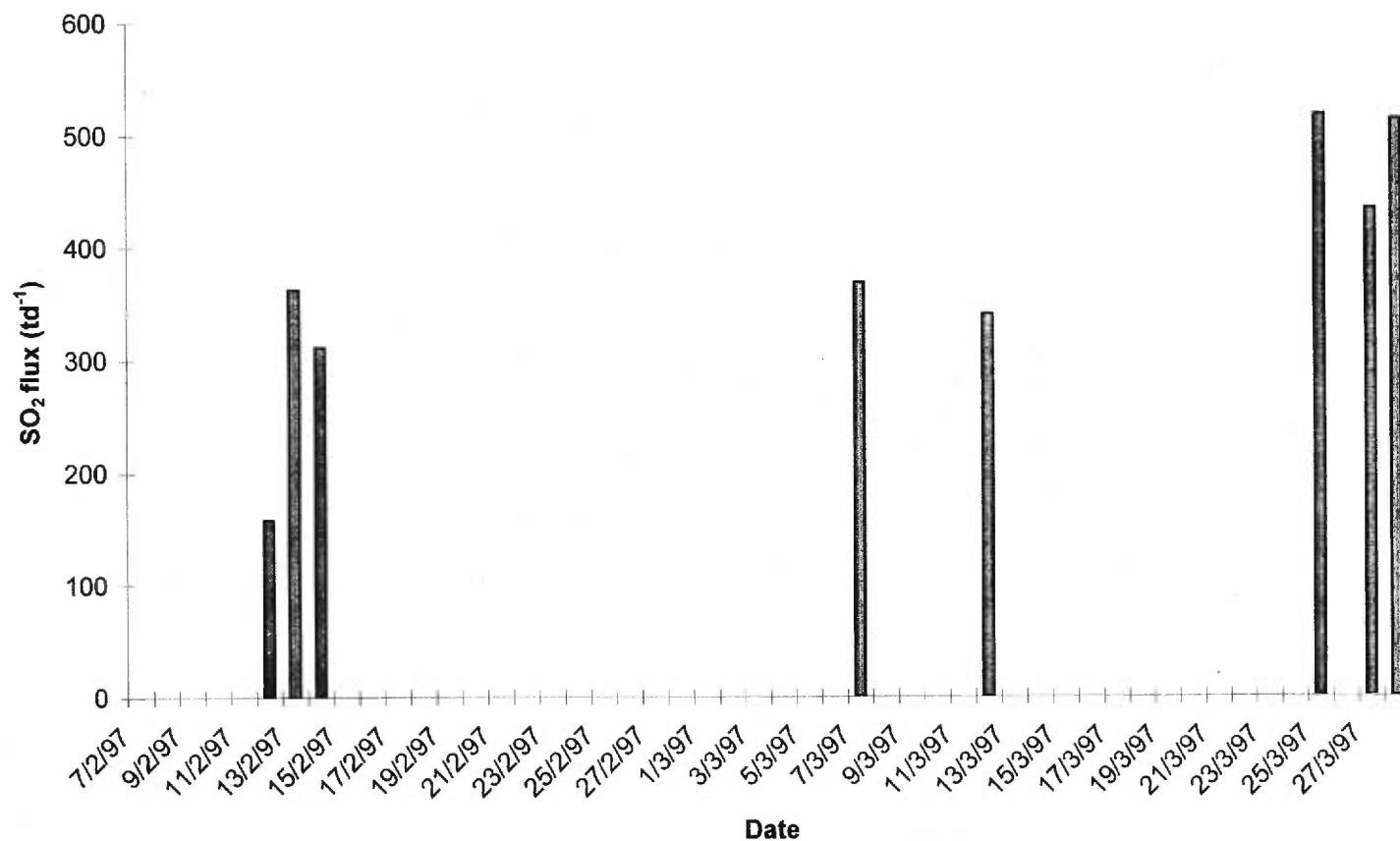
Table 2.6 Continued.

Date	Start at	End at	Windspeed (ms ⁻¹)	5 km (td ⁻¹)	15 km (td ⁻¹)	Total av. (td ⁻¹)	1ms ⁻¹ fluxes (td ⁻¹)	Total av. (1ms ⁻¹) (td ⁻¹)	Comments
25-03-97	1204	1229	5.27	501		520	95	85	
	1342	1410	5.27		331		63		
	1417	1436	6.61		384		58		
	1449	1528	6.61		333		50		
	1536	1603	6.61	1053			159		
27-03-97	1243	1306	5.6	993		436	177	87	
	1324	1335	5.06		424		84		
	1340	1405	5.06		277		55		
	1410	1434	5.44	285			52		
	1559	1618	4.13	323			78		
	1623	1638	4.13	315			76		
28-03-97	1019	1042	7.38	561		516	76	74	
	1059	1132	7.38		444		60		
	1137	1157	7.38		560		76		
	1223	1242	7.38		630		85		
	1245	1301	7.38	469			63		

Figure 2.2

Daily averaged SO₂ emission rate at Masaya volcano measured by COSPEC between February and March 1997.

Daily averaged SO₂ fluxes from Masaya volcano, 1997 survey



For the 1998 survey, measurements were usually between 1000 and 3000 t·d⁻¹, with an average of 1970 t·d⁻¹ (Table 2.7, Figure 2.3).

Prior to 1979, SO₂ fluxes averaged 380 t·d⁻¹ (Stoiber et al., 1986). A new degassing crisis began in 1979, when SO₂ increased to an average of 1200 t·d⁻¹ in February 1980. Activity decreased until 1989, when a weakly degassing lava lake appeared. SO₂ fluxes were less than 25 t·d⁻¹ in April 1992 (S. N. Williams, pers. com., quoted in Rymer et al., 1998). In 1993, reactivation occurred, and strong degassing resumed. In 1996, SO₂ fluxes ranged from 240 to 1100 t·d⁻¹ with an average of 600 t·d⁻¹ (Rymer et al., 1998). In 1997, the daily average SO₂ fluxes ranged from 160 to 520 t·d⁻¹, which fall in the range of the fluxes measured for the period prior to 1979. In November 1997 a period of decreased degassing caused by cooled magma or a collapse in the conduit was observed, followed by a strombolian explosion on 12 November, ejecting bombs in the crater area. After this event, the strong degassing resumed with an increasing trend. It was suggested by Rymer et al. (1998) that the 1993 degassing crisis was triggered by convective movement in the magma chamber, allowing volatile-rich magma to degas; it is possible that a similar event occurred in November 1997. In 1998, the increase in degassing was shown by SO₂ fluxes ranging from 700 to 5580 t·d⁻¹ with an average of 2040 t·d⁻¹. This increase in degassing is approximately two to five times higher than in 1997. In gravity surveys made in 1997 and 1998 by Beaulieu et al. (1998), no major changes in microgravity were observed, suggesting that no injection of new magma occurred. Also, Stoiber et al. (1986) have suggested that a large magma body under the vent is responsible for the degassing over the last hundred years, with no injection of gas rich magma.

Table 2.7 February-April 1998 SO₂ flux measurements.

Date	COSPEC V		Low cal = 103 ppm*m		High cal = 326 ppm*m		Ajust. (*1.26)	Total av. (td ⁻¹)	1ms ⁻¹ fluxes (td ⁻¹)	Total av. 1ms ⁻¹ (td ⁻¹)	Comments
	Start at	End at	Windspeed (ms ⁻¹)	5 km (td ⁻¹)	15 km (td ⁻¹)	30 km (td ⁻¹)					
21-02-98	1325	1350	10.4		989			1203	95	144	CO. V ¹
	1354	1419	10.9		1208				111		
	1421	1447	10.9		1370				126		
	1450	1504	6.9		686				100		
	1507	1526	6.7		1168				174		
	1531	1550	7		1798				257		
22-02-98			5.8		830			1874			CO. V ¹
			5.1		1070						
			6.9		2510						
			5.9		1620						
			6.1		2390						
			7.1		2030						
23-02-98			7.7		2930						CO. V ¹
			5.8		1610						
			9.1		3880			3624			
			9.1		3670						
24-02-98			9.1		3670						CO. V ¹
			9.1		3275						
	1109	1123	8.5		2062			1172	243	130	
	1126	1141	8.5		1214				143		
	1154	1210	8.5		775				91		
	1212	1226	8.5		963				113		
	1231	1247	8.5		884				104		
	1327	1342	9.7		940				97		
	1346	1402	9.7		1476				152		
	1403	1418	9.7		1250				129		
25-02-98	1427	1444	9.7		1250				129		CO. V ¹
	1450	1511	9.7		909				94		
			7.4		1170			1103			
			7.4		860						
			8.5		1020						
			8.5		789						
			8.5		1360						
			8.5		1050						
			8.5		1210						
			8.5		1000						
		6.5		1530							
		6.5		1040							

¹ Measurements were made with the COSPEC V.² Measurements were made with the COSPEC IV.

Table 2.7 Continued.

Date	Start at	End at	Windspeed (ms ⁻¹)	5 km (td ¹)	15 km (td ¹)	30 km (td ¹)	Ajust. (*1.26)	Total av. (td ¹)	1ms ⁻¹ fluxes (td ¹)	Total av. 1ms ⁻¹ (td ¹)	Comments
01-03-98			4.9		6130			5575			CO. V ¹
			4.2		5740						
			5.4		7390						
			5		3040						
02-03-98	1021	1054	8		2184			1963	273	218	CO. V ¹
	1057	1126	8		1151				144		
	1130	1158	8		2342				293		
	1200	1228	8		2176				160		
03-03-98	1227	1244	4.7		523			675	111	144	CO. V ¹
	1246	1302	4.7		696				148		
	1504	1513	4.7		807				172		
07-03-98	1022	1041	5.8		1004			953	173	164	CO. V ¹
	1045	1101	5.8		574				99		
	1105	1120	5.8		823				142		
	1201	1216	5.8		843				145		
	1217	1237	5.8		873				150		
	1238	1258	5.8		802				138		
	1306	1329	5.8		1289				222		
1331	1354	5.8		1419				245			
08-03-98	1014	1045	5.8		3204			2876	552	496	CO. V ¹
	1048	1122	5.8		2011				347		
	1129	1211	5.8		3414				589		
10-03-98	1057	1111	5.1		598			752	117	118	CO. V ¹
	1130	1124	6.5		790				121		
	1404	1420	6.9		1111				161		
	1616	1620	6.9		510				74		
13-03-98	1157	1208	10.6		277			699	26	67	CO. V ¹
	1221	1232	10.6		824				78		
	1243	1254	10.6		728				69		
	1258	1307	10.6		771				73		
	1332	1344	10.6		645				61		
	1347	1358	10.6		321				30		
	1401	1413	10.6		633				60		
	1416	1427	10.6		606				57		
	1431	1443	10.4		1248				120		
	1446	1457	10.4		618				59		
	1506	1511	10.4		771				74		
	1514	1525	10.4		950				91		

¹ Measurements were made using the COSPEC V.² Measurements were made using the COSPEC IV.

Table 2.7 Continued.

Date	Start at	End at	Windspeed (ms ⁻¹)	5 km (td ⁻¹)	15 km (td ⁻¹)	30 km (td ⁻¹)	Ajust. (*1.26)	Total av. (td ⁻¹)	1 ms ⁻¹ fluxes (td ⁻¹)	Ajust. (*1.26)	Total av. 1ms ⁻¹ (td ⁻¹)	Comments
14-03-98	1035	1051	16.2		1536			1635	95		102	CO. V ¹
	1126	1141	16.2		1349				83			
	1143	1158	15.5		1133				73			
	1159	1214	15.5		1707				110			
	1215	1229	17		2234				131			
	1231	1246	15.6		1849				119			
14-03-98	1035	1051	16.2		1670		2104	1737	103	127	106	CO. IV ²
	1126	1141	16.2		1049		1284		63	77		
	1143	1158	15.5		847		1067		55	68		
	1159	1214	15.5		1382		1741		89	109		
	1215	1229	17		1911		2408		112	138		
	1231	1246	15.6		1444		1819		93	114		
15-03-98	1025	1050	15			1936		2069	129		138	CO. V ¹
	1055	1116	15			2202			147			
17-03-98	1120	1131	10.6		3060			2527	289		240	CO. V ¹
	1159	1230	10.6		2259				213			
	1235	1256	10.9		2872				264			
	1258	1329	10.9		2136				196			
	1328	1349	12.5		2681				215			
	1352	1416	9.7		2244				231			
	1421	1446	8.6		1736				202			
	1504	1532	10.4		3228				310			
17-03-98	1030	1047	10.6	2014			2538	3018	190	234	273	CO. IV ²
	1058	1108	10.6	1484			1870		140	172		
	1110	1120	10.6	2342			2951		221	272		
	1125	1134	10.6	1602			2019		151	186		
	1136	1146	10.6	1800			2268		170	209		
	1151	1201	10.6	1843			2322		174	214		
	1203	1213	10.6	2170			2734		205	252		
	1218	1228	10.6	2520			3175		238	293		
	1229	1238	10.6	2325			2930		219	269		
	1242	1252	10.6	1850			2331		175	215		
	1254	1303	10.9	2477			3121		227	279		
	1306	1315	10.9	2007			2529		184	226		
	1322	1341	12.5	4363			5497		349	429		
	1344	1400	12.5	3312			4173		265	326		
	1402	1418	9.7	3754			4730		387	476		
	1422	1437	9.7	2023			2549		209	257		
	1439	1456	8.8	1805			2274		210	258		
	1510	1528	10.4	2925			3686		210	258		
	1530	1547	10.4	2321			2924		223	274		
	1549	1602	10.4	2967			3738		285	351		

¹ Measurements were made using the COSPEC V.² Measurements were made using the COSPEC IV.

Table 2.7 Continued.

Date	Start at	End at	Windspeed (ms ⁻¹)	5 km (td ¹)	15 km (td ¹)	30 km (td ¹)	Ajust. (*1.26)	Total av. (1ms ⁻¹)	1ms ⁻¹ fluxes (td ¹)	Ajust. (*1.26)	Total av. 1ms ⁻¹ (td ¹)	Comments
18-03-98	1145	1221	8.8			3420		4032	389		507	CO. V ¹
	1235	1255	8.4			4011			478			
	1258	1327	6.5			4541			699			
	1337	1401	8.1			4794			592			
	1416	1432	8.6			3972			462			
	1435	1456	8.2			3454			421			
18-03-98	1133	1153	8.7		1332		1678	1577	153	188	189	CO. IV ²
	1157	1217	8.4		1706		2150		203	250		
	1218	1237	8.4		1299		1637		155	191		
	1243	1300	8.3		1259		1586		155	191		
	1303	1321	6.5		635		800		98	121		
	1325	1342	8.1		1204		1517		149	183		
	1357	1418	8.6		1394		1756		159	196		
	1423	1441	8.2		1657		2088		202	248		
	1444	1512	8.2		1200		1512		146	180		
	1513	1535	7.3		830		1046		114	140		
21-03-98	1010	1043	5.2		3192			1536	614		322	CO. V ¹
	1050	1139	5.2		1076				207			
	1134	1201	5.2		1325				255			
	1204	1228	5.1		1255				246			
	1233	1257	5.1		1758				345			
	1304	1329	4.6		1693				368			
	1338	1404	5.2		2202				423			
	1411	1435	4.9		1365				278			
	1440	1505	4.4		1745				397			
	1511	1535	3.1		825				266			
1539	1607	3.1		455				147				
25-03-98	1146	1202	8.4		939			1092	112		125	CO. V ¹
	1206	1219	8.4		871				104			
	1233	1251	9.8		1684				172			
	1253	1311	10.2		1149				113			
	1313	1328	10.2		1070				105			
	1333	1340	8.4		1133				135			
	1342	1353	8.4		1020				121			
	1354	1405	8.4		681				81			
	1409	1417	7.7		709				92			
	1418	1428	7.7		1659				215			

¹ Measurements were using the COSPEC V.² Measurements were using the COSPEC IV.

Table 2.7 Continued.

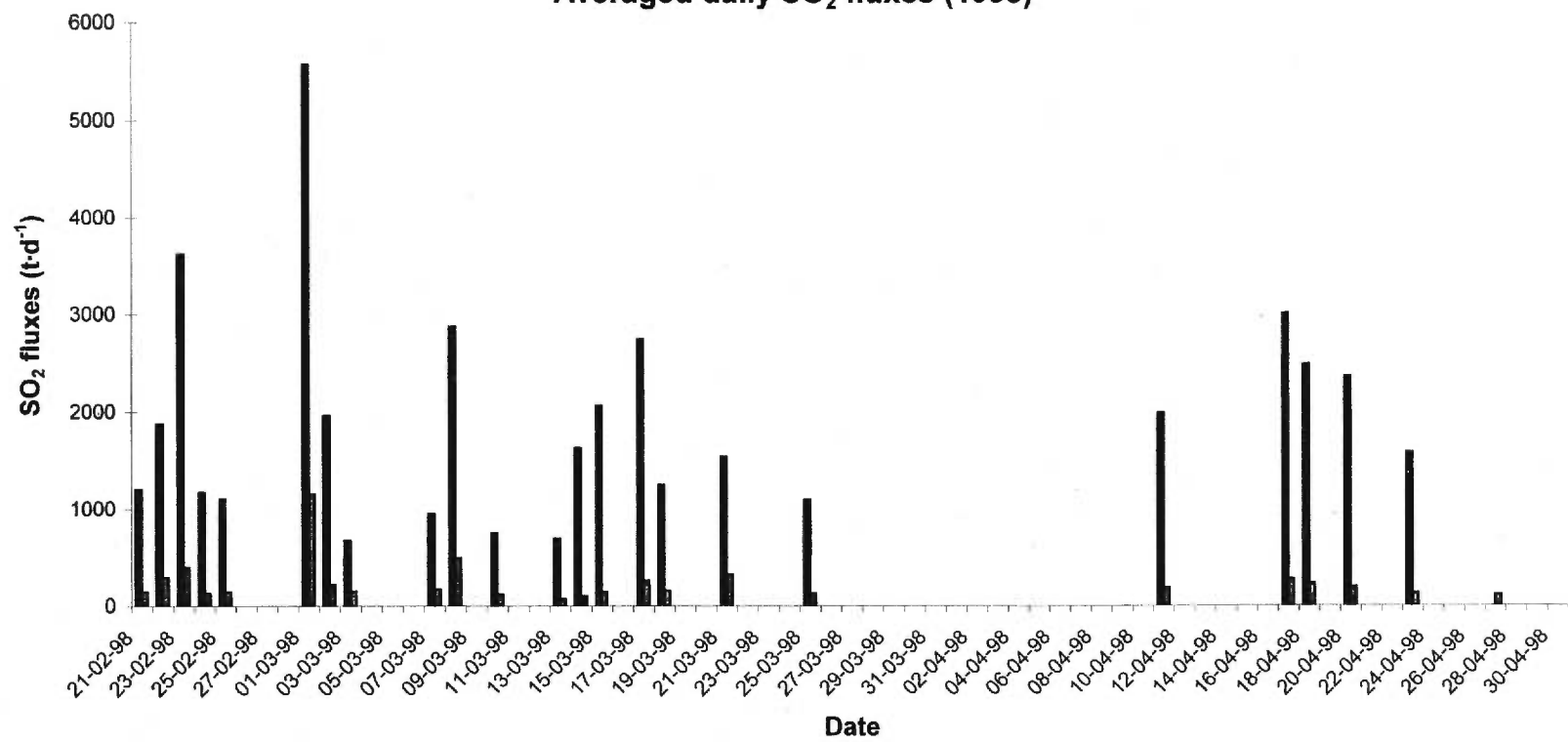
Date	Start at	End at	Windspeed (ms ⁻¹)	5 km (td ⁻¹)	15 km (td ⁻¹)	30 km (td ⁻¹)	Ajust. (*1.26)	Total av. (1ms ⁻¹)(td-1)	1ms ⁻¹ fluxes (td ⁻¹)	Ajust. (*1.26)	Total av. (1ms ⁻¹)	Comments
11-04-98	1140	1148	13.51		4404			1989	326		183	CO. V ¹
	1155	1205	13.56		2129				157			
	1211	1221	12.07		1364				113			
	1226	1237	12.94		1346				104			
	1242	1249	10.82		2196				203			
	1256	1307	9.54		2223				233			
	1312	1320	9.56		1396				146			
	1333	1344	9.7		1979				204			
	1348	1352	10.17		2380				234			
	1413	1422	8.8		1311				149			
1447	1457	8.24		1154				140				
17-04-98	1204	1228	11.78		3958			3016	336		270	CO. V ¹
	1238	1246	12.09		2031				168			
	1255	1307	11.19		2965				265			
	1312	1329	10.73		2865				267			
	1334	1349	10.92		3003				275			
	1355	1410	11.97		2765				231			
	1420	1431	11.6		3167				273			
	1438	1449	10.42		2751				264			
	1512	1525	10.48		3637				347			
18-04-98	1229	1246	12.31		2524			2489	205		227	CO. V ¹
	1257	1306	11.62		2336				201			
	1315	1323	10.85		2723				251			
	1330	1337	10.92		2184				200			
	1355	1359	10.56		2112				200			
	1407	1414	10.17		2685				264			
	1426	1439	10.55		2859				271			
20-04-98	1348	1403	12.38		3231			2369	261		193	CO. V ¹
	1408	1415	12.1		1997				165			
	1434	1441	12.11		2047				169			
	1450	1456	12.21		2418				198			
	1511	1515	11.95		2294				192			
	1526	1537	13.02		2226				171			
23-04-98	1318	1335	13.32		1199			1578	90		124	CO. V ¹
	1337	1350	12.85		1503				117			
	1356	1405	12.56		2248				179			
	1419	1423	12.71		1767				139			
	1439	1443	12.82		897				70			
	1507	1510	12.28		1854				151			

¹ Measurements were made using the COSPEC V.² Measurements were made using the COSPEC IV.

Figure 2.3

Daily averaged SO₂ emission rate at Masaya volcano measured by COSPEC between February and April 1998.

Averaged daily SO₂ fluxes (1998)



Petrological Data

Petrological analyses were performed on bombs from the 12 November 1997 strombolian explosion. Pélé's hair, glass inclusions and matrix glasses from three different bombs were analysed for a total of 65 analyses (Table 2.8). Data showing anomalous values in major elements were rejected. Data normalized to 100 % anhydrous are used in the following discussion.

The samples are basaltic tholeiite in composition. Pélé's hair shows an average SiO₂ content of 51.72 weight percent and Al₂O₃ of 14.18 wt. %, typical of a basaltic glass. For the glassy materials, an average SiO₂ content of 51.85 wt % and Al₂O₃ of 14.22 wt % have been obtained. Glass inclusions show an average SiO₂ content of 51.80 wt % and Al₂O₃ of 13.91 wt %, which also fall in the range of a basaltic glass. The glasses in the three groups are enriched in FeO, with an average of 14.02 wt %, which is one of the compositional characteristics of Masaya volcano (Walker et al., 1993). Another major element, MgO, presents an average value of 4.86 wt %, with little variation. The glass inclusions are higher in K₂O than the Pélé's hair and the matrix glass, which may indicate weathering alteration of the matrix glass and Pélé's hair (Figure 2.4d and e). Many glass shards were showing evidence of devitrification.

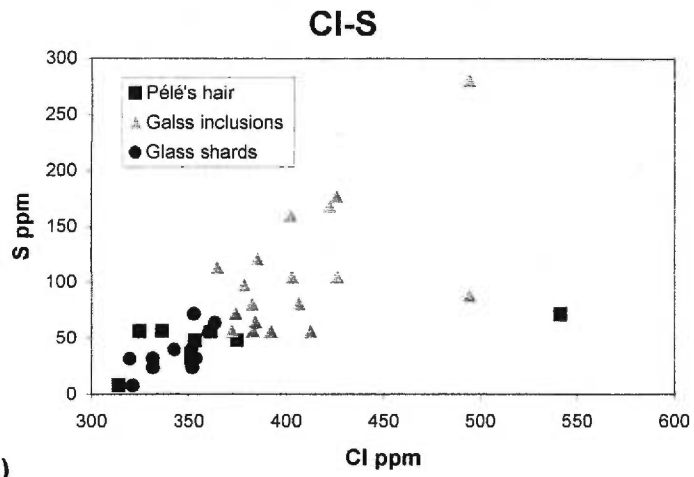
Three volatiles were analysed: sulfur, fluorine and chlorine. No fluorine was detected in all analyses with the exception of the standards KN-9 and KE-12. In the Pélé's hair, an average sulfur content of 50 ± 40 ppm and chlorine concentration of 370 ± 70 ppm were measured. In glass inclusions and matrix glasses, average contents of sulfur and chlorine of 110 ± 60 ppm and 410 ± 40 ppm, and 40 ± 20 ppm and 340 ± 20 ppm were measured, respectively. It is possible that the initial sulfur

Table 2.8 Average Pélé's hair, glass shards and glassy materials analyses.

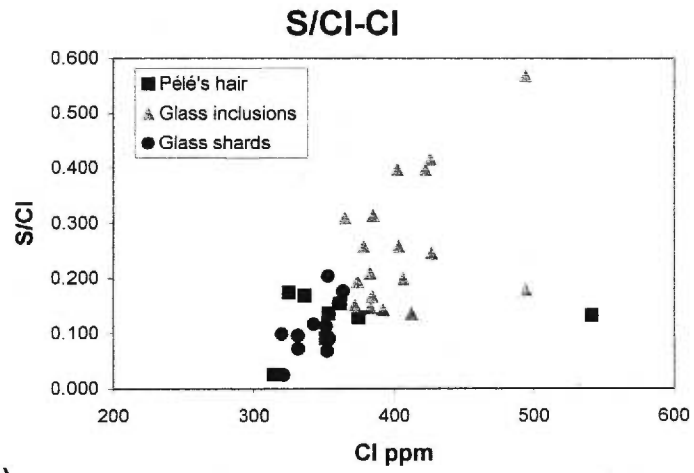
	Pélé's hair analyses		Glass inclusions		Glass shards		
	cp97	cp96	001i	003i	001e	003e	005e
SiO ₂	51.80	51.64	51.75	51.63	51.73	52.33	51.61
TiO ₂	1.35	1.39	1.43	1.43	1.34	1.42	1.33
Al ₂ O ₃	14.17	14.19	13.79	14.30	14.15	14.43	14.16
FeO	13.91	13.91	14.53	13.86	13.96	14.03	13.97
MnO	0.25	0.26	0.29	0.24	0.26	0.27	0.26
MgO	4.81	4.83	4.89	4.76	4.84	4.88	4.83
CaO	9.07	9.14	7.80	9.15	9.11	8.64	9.17
Na ₂ O	2.96	2.98	2.72	2.94	2.96	2.46	2.99
K ₂ O	1.46	1.45	2.53	1.45	1.44	1.33	1.47
P ₂ O ₅	0.20	0.21	0.20	0.20	0.21	0.21	0.20
Total	100.00	100.00	100.00	100.00	100.00	100.00	100.00
Cl	344	396	457	336	337	358	339
S	54	40	148	57	36	53	31

Figure 2.4

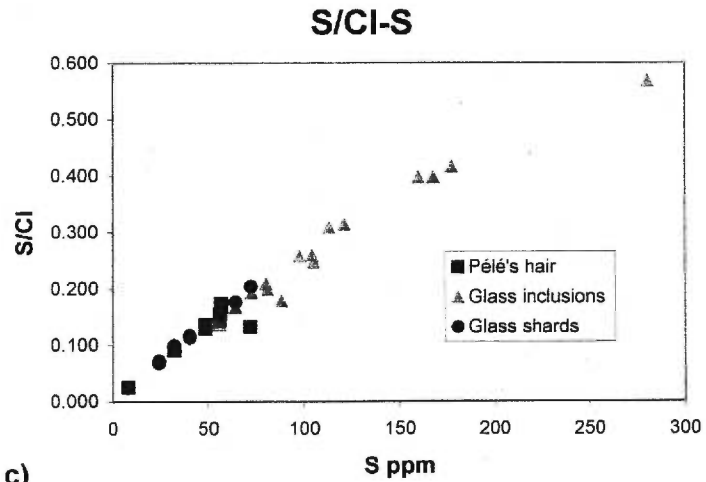
Petrological analyses. (a) Sulfur concentrations versus chlorine concentrations. (b) S/Cl ratio versus chlorine concentrations. (c) S/Cl versus sulfur concentrations. (d) Potassium concentrations versus FeO/MgO ratio. (e) Magnesium concentrations versus potassium concentration. Note that the glass inclusions are generally higher in potassium than Pélé's hair and the matrix, which may indicate some weathering of the later.



a)



b)



c)

content of the magma is not homogenous. The surface magma may be more depleted in volatiles considering the continuous degassing. Deeper in the conduit or magma chamber, the magma is more likely richer in gas. The sulfur and the chlorine present an interesting relation, where the chlorine is substantially higher than the sulfur. An average S/Cl mass ratio of 0.26 was obtained for glass inclusions. The S/Cl-sulfur plot shows a linear relation indicating enhanced degassing of sulfur over chlorine, which is logical since sulfur is more soluble than chlorine in basaltic magma (Carroll and Webster, 1994)(Figure 2.4c). However this linear relation may be due in part to the error on the sulfur analyses. Stoiber et al. (1986) measured S and Cl concentrations of 320 ppm and 300 ppm, respectively, which is a higher sulfur content than our results. It is possible that the analyses we made were underestimated, or more likely that the material we analysed was more depleted in volatiles than the Stoiber et al. (1986) samples. A high S/Cl mass ratio is expected in the case of magmatic volatile emissions. Stoiber et al. (1986) measured an average sulfur/chlorine mass ratio of 0.8 at the edge of the Santiago crater and 1.6 at the Llano Pacaya ridge (El Crucero) with gas filters. In March 1998, OP-FTIR (Open-Path Fourier Transform Infrared Radiometry) analyses were made at the Santiago crater by a team from the Open University, and a S/Cl mass ratio of 1.5 was obtained (Delmelle et al., in press). These higher S/Cl ratios indicate also higher solubility of SO₂ gas over HCl, which will stay longer in the magma before being degassed.

Plagioclases and olivines were analysed to determine their composition. A small proportion of plagioclases were zoned. The analyses showed calcic compositions, which fall in the bytownite range (An₈₅Ab₁₅). The analysed olivines give (Fo₇₄Fa₂₆). Small crystals of clinopyroxene, oxides such as hematite and

spinel, which are common in basaltic lava, were encountered.

SO₂ Budgets at Masaya

Estimates of the quantity of SO₂ emitted and the volume of magma that has been degassed since the mid-1993 reactivation may be calculated using glass inclusion data from juvenile materials erupted by the 12 November 1997 strombolian explosion. We assume that the melt inclusions represent the non-degassed sulfur content of the magma, and the glassy matrix represents the sulfur content after degassing. The difference between the two concentrations represents the sulfur released during degassing of the magma. A petrologic estimate of the SO₂ emission for Masaya may be made using the following equation (Gerlach and McGee, 1994):

$$E_{\text{SO}_2} = (2 \times 10^{-15}) * \Delta S_m * \rho_m * \phi_m * V \quad (2.3)$$

where E_{SO_2} is the quantity of SO₂ (Mt) degassed during a known period of time, the constant 2×10^{-15} is a conversion factor for S (ppm) into SO₂ (Mt); ΔS_m is the amount of sulfur lost by the melt during degassing (65 ppm) determined by the difference between the mean sulfur concentration of 18 melt inclusions (106 ppm) and 11 glassy materials (41 ppm) of the 12 November 1997 bombs; ρ_m is the basaltic melt density assumed to be $2800 \text{ k}\cdot\text{g}\cdot\text{m}^{-3}$; ϕ_m is the melt volume fraction of 0.85 (visual estimate) estimated from the bombs; and V is the volume of magma degassed. With average SO₂ fluxes of $400 \text{ t}\cdot\text{d}^{-1}$ for the 1993-1996 period (Rymer et al., 1998), $380 \text{ t}\cdot\text{d}^{-1}$ for 1997, $2030 \text{ t}\cdot\text{d}^{-1}$ for the first part of 1998 and $1840 \text{ t}\cdot\text{d}^{-1}$ for the last part of 1998 (Williams-Jones, unpublished data) obtained by COSPEC measurements, an estimation of 1.4 Mt of SO₂ has been degassed from the active vent since 1993. To

be able to degas this amount of gas, we need a volume of 4.5 km³ of magma if we use the 65 ppm difference in sulfur concentrations. However, this value of 65 ppm is more representative of the residual sulfur concentration of a degassed magma. Using a higher sulfur content of 240 ppm (Stoiber et al., 1986), 500 ppm, 1000 ppm, and 2000 ppm, 1.23 km³, 0.59 km³, 0.29 km³, 0.15 km³ of magma, respectively, are necessary to degas 1.4 Mt of SO₂. It has been suggested that a possible magma chamber of 10 km³ lies in the upper crust (Stoiber et al., 1986; Connor and Williams, 1990; Walker et al., 1993). It is more likely that a medium-sized magma body relatively rich in sulfur and /or a deeper sulfur-rich magma is the principal source of sulfur, the magma at the surface being almost completely degassed. Indeed, the petrological analyses indicate that the samples come from the shallow conduit and represent a magma, which is depleted in volatiles.

Using the 1.4 Mt of SO₂ estimated by COSPEC measurements and molar ratios of 3.86 for H₂O/SO₂ and 2.18 for CO₂/SO₂ (Williams et al., 1992; Symonds et al., 1994), we obtained 1.5 Mt of H₂O, 2.1 Mt of CO₂ for a total of 5 Mt of gas emitted by the volcano since 1993.

17-18 March 1998 Gas Dispersion Studies

For two days, simultaneous COSPEC measurements were conducted on roads at 5.5 and 15 km (17 March), and 15 and 30 km (18 March) distance from the active vent. A quantitative comparison of the two COSPEC datasets was made to detect any pattern, process or anomaly that occurs during transport and dispersion of the gas. For accurate comparison of the data, a back-calculation is necessary to estimate the period of time that the plume was transported between the two measurements sites.

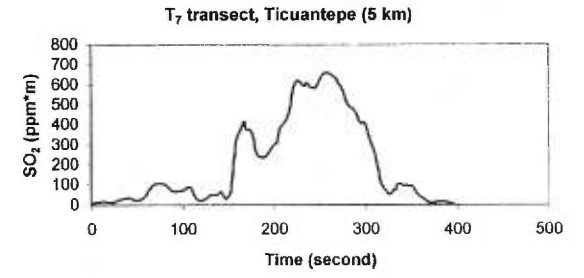
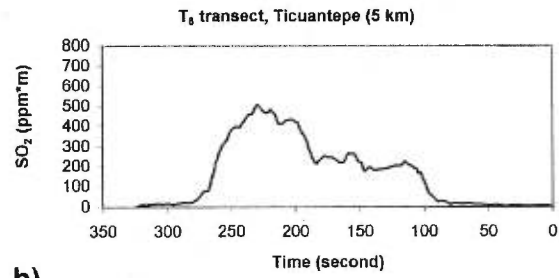
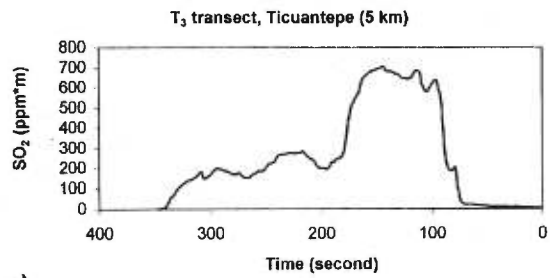
Because the degassing at the vent is visibly variable and there is production of puffs, by calculating the time of transport of the plume, it is possible to compare the same section of the plume at the different distances from the plume. Using the wind speed at the time of measurements, the distance that the plume travelled between the two measurement sites (9.5 km for 17 March and 15 km for 18 March), and the time at which the measurements were made, it is possible to correlate the SO₂ fluxes made at the two different sites. Since fewer measurements were made at the distal site due to a wider gas column, the back-calculation sometimes fell between two measurements at the proximal site. In this case, both proximal flux values falling on either side of the back-calculated time were considered. The SO₂ flux values were compared using the measured wind speed and a standard wind speed of 1 m·s⁻¹.

17 March 1998

On 17 March, 20 traverses (T₁ to T₂₀) were done on the Ticuantepe road (5.5 km from the crater), and 8 traverses (E₁ to E₈) on the El Crucero road (Llano Pacaya ridge, 15 km from the crater). All plume profiles from El Crucero were matched with one or two plume profiles from Ticuantepe based on the back-calculated time of measurements and the form of the profiles. A ratio was determined by dividing the Ticuantepe flux value by the El Crucero flux value (T/E ratio). SO₂ fluxes ranged from 1830 t·d⁻¹ to 5370 t·d⁻¹ for the 5.5 km road and from 1740 t·d⁻¹ to 3230 t·d⁻¹ for the 15 km road. To remove error due to the wind, a ratio with the SO₂ flux value calculated with a standard wind speed of 1 m·s⁻¹ also was used. T/E ratios range from 0.69 to 2.66 with the measured wind speed, and 0.83 to 2.35 with a standard wind of 1 m·s⁻¹ (Table 2.9, Figure 2.5).

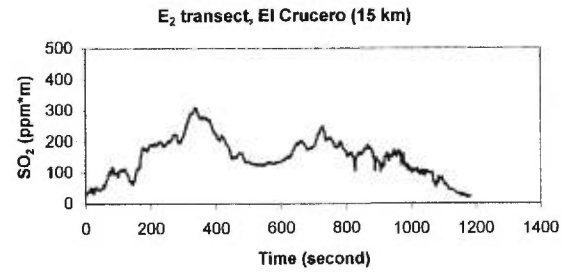
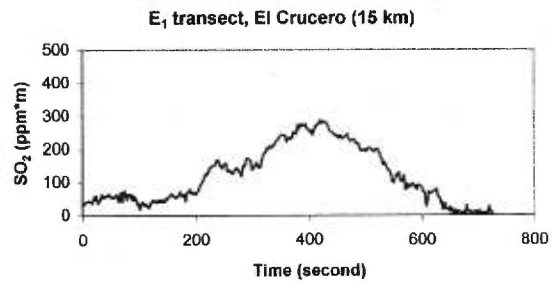
Figure 2.5

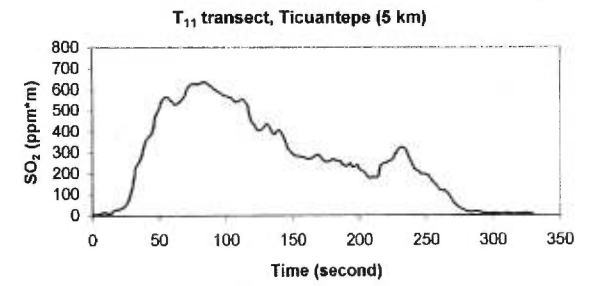
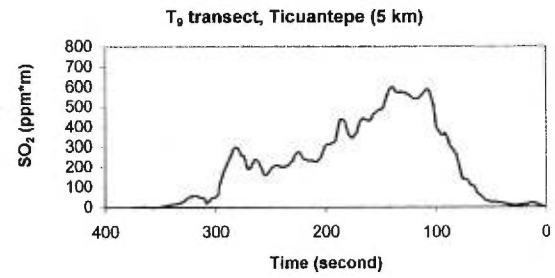
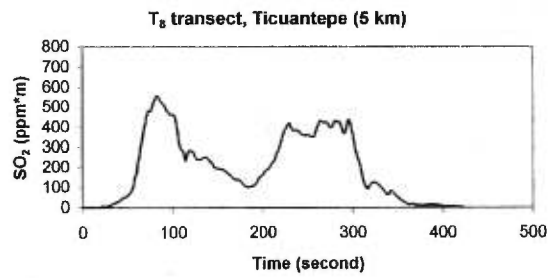
Correlations between Ticuantepe measurements and El Crucero. a) T₃ and E₁, b) T₇-T₈ and E₂, c) T₈-T₉ and E₃ d) T₁₁ and E₄, e) T₁₂-T₁₃ and E₅, f) T₁₄ and E₆, g) T₁₅-T₁₆ and E₇, and h) T₁₇-T₁₈ and E₈. (The last charts are unused transects. In order to have the same direction for transect comparison some (X) axes are reverse.)



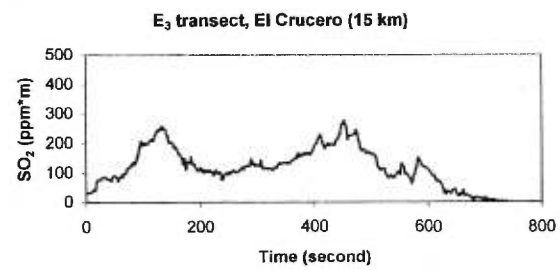
a)

b)

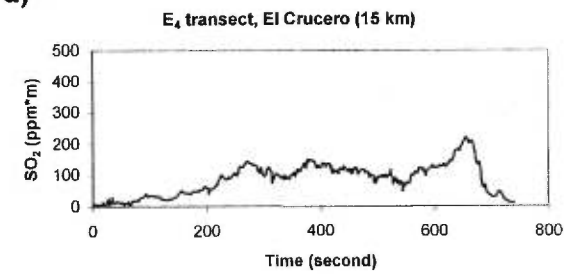


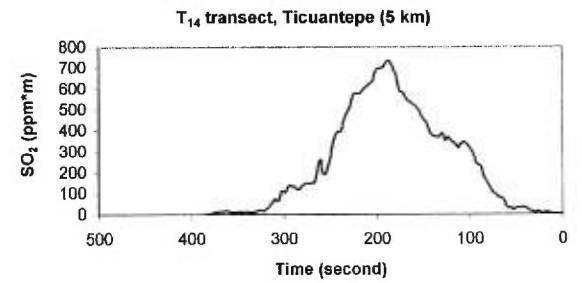
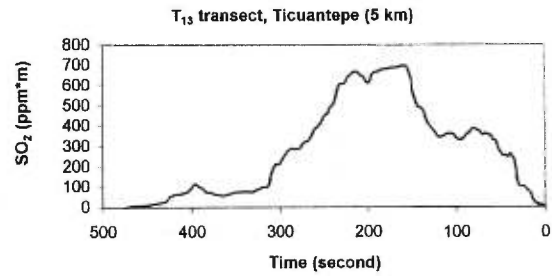
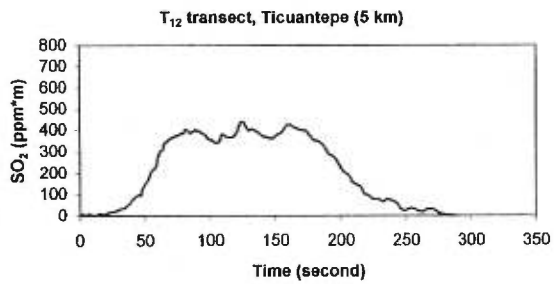


c)

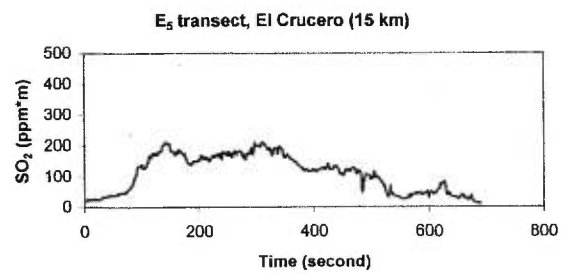


d)

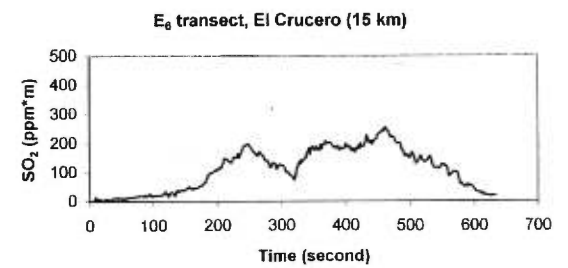


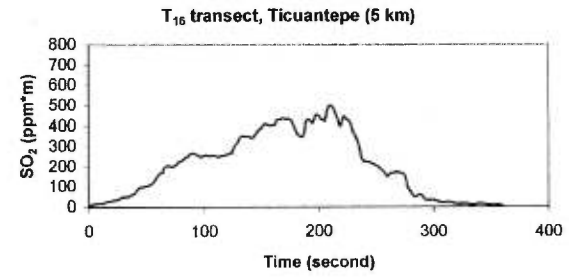
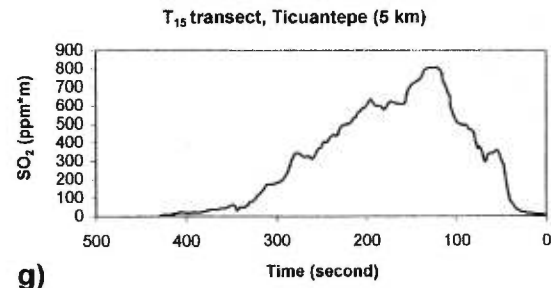


e)

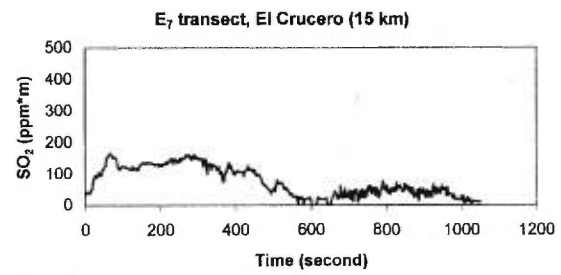


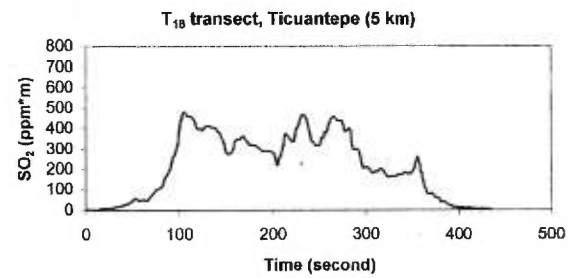
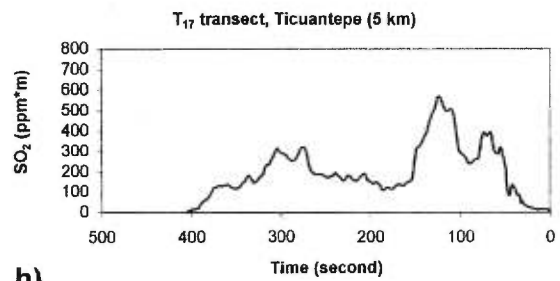
f)



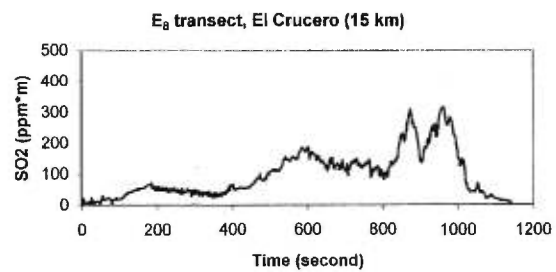


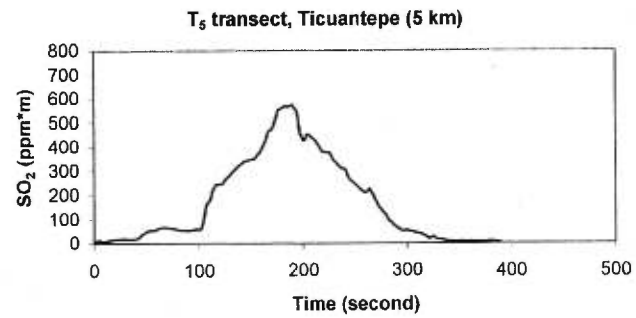
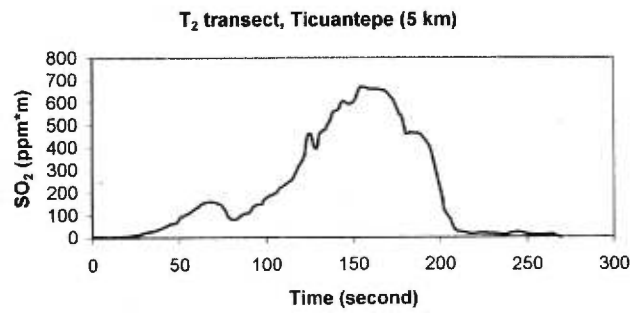
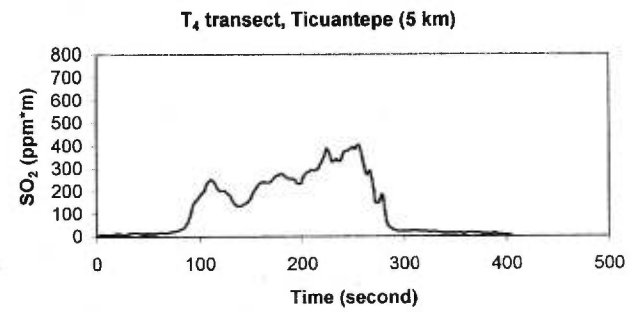
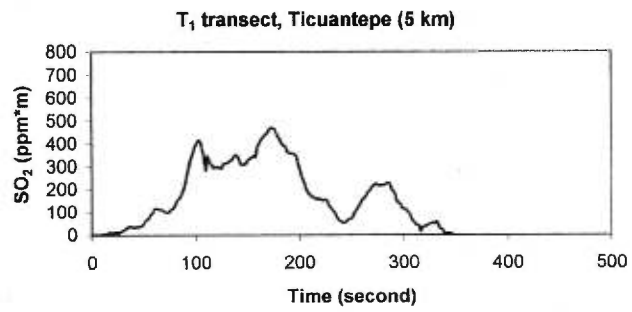
g)

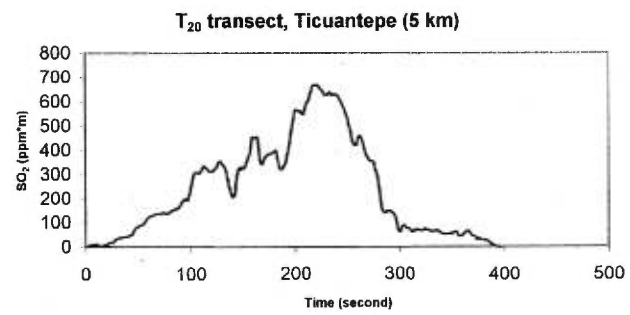
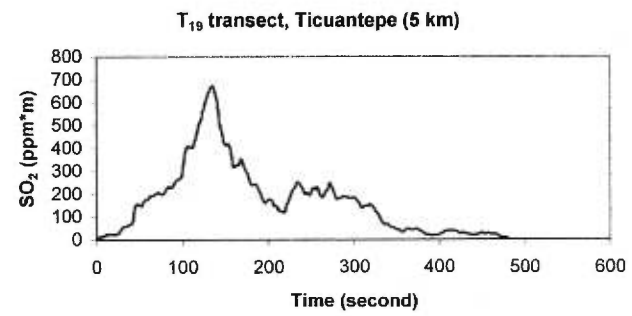
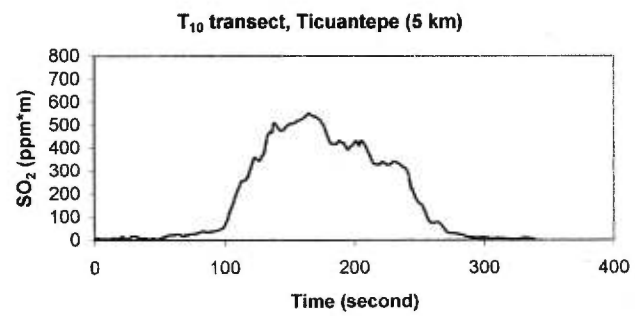




h)







$E_{1(1120h-1131h)}-T_{3(1110h-1120h)}$

An estimate of 15.7 minutes transport time from Ticuantepe (5.5 km) to El Crucero (15 km) permits associating the E₁ traverse with the T₃ traverse. The profile of Ticuantepe shows one principle peak that is also recognisable on the El Crucero profile. Other features of T₃ are smoothed or blended during transport and are not visible on the E₁ profile. The SO₂ flux of E₁ is 3060 t·d⁻¹ compared with 2880 t·d⁻¹ for T₃, giving a Ticuantepe/El Crucero ratio of 0.94 for measured wind. The ratio using standard wind (1 m·s⁻¹) gives the same ratio value of 0.94.

$E_{2(1159h-1230h)}-T_{6(1151h-1201h)-7(1203h-1213h)}$

E₂ and T₆₋₇ present three features that are roughly recognisable on the three profiles. Three depressions located south to north on the profiles are matched. However, two major peaks representing high concentrations on T₆ and T₇ are not found on E₂ whose entire profile is smoother than T₆ or T₇. Flux values are 2260 t·d⁻¹ for E₂, 2280 t·d⁻¹ for T₆ and 2650 t·d⁻¹ for T₇. Ratios are 1.00 for T₆/E₂, 1.18 for T₇/E₂, with an average of 1.09 using both the measured and standard wind.

$E_{3(1235h-1256h)}-T_{8(1218h-1228h)-9(1229h-1238h)}$

E₃, T₈ and T₉ have three similar features in all three profiles. From south to north, a high peak is followed by a depression, then another peak is visible. However, in E₃ and T₈, the two peaks seem to be the result of bifurcation. However, T₉ does not seem to be as bifurcated as the two others. Flux values are 2870 t·d⁻¹, 3100 t·d⁻¹, and 2860 t·d⁻¹ for E₃, T₈ and T₉ respectively. Ratios are 1.08 for T₈/E₃ and 1.00 for T₉/E₃, with an average of 1.04 with measured wind, and 1.01 to 1.11 with an

average of 1.06, using with a standard wind of 1 m·s⁻¹.

$E_{4(1158h-1319h)}-T_{11(1253-1303)}$

The comparison of E_4 and T_{11} shows three similar features. Two principal peaks at the southern extremity of each profile are separated by a depression or trough. These peaks have very sharply defined southern edges. The E_4 profile is wider showing a smoother pattern. SO₂ flux values are 2140 t·d⁻¹ and 3050 t·d⁻¹ for E_4 and T_{11} respectively. Ratios are 1.43 with measured wind and 1.42 with standard wind.

$E_{5(1328h-1349h)}-T_{12(1306h-1315h)-T_{13(1322h-1341)}}$

E_5 shows two features that are also present on the T_{12} - T_{13} profiles. E_5 is asymmetric and T_{12} and T_{13} are roughly symmetric. Only one steep slope located at the south and a minor peak in the middle of the profiles are visible on the three traverses. E_5 may be more compatible with T_{13} comparing the shape of the plume. Fluxes are 2680 t·d⁻¹, 2470 t·d⁻¹ and 5370 t·d⁻¹ for E_5 , T_{12} and T_{13} , respectively. Ratios are for T_{12}/E_5 0.92, for T_{13}/E_5 2.00, with an average of 1.46 using the measured wind. With the standard wind, the ratios are 1.05, 1.99 and an average of 1.52.

$E_{6(1352h-1416h)}-T_{14(1344h-1400h)}$

T_{14} presents a roughly symmetrical major peak. This feature is also recognisable on E_6 . A small shoulder located on the northern flank of T_{14} may be matched with a more pronounced peak on E_6 . E_6 and T_{14} have SO₂ fluxes of 2240 t·d⁻¹

¹ and 4070 t·d⁻¹ respectively. Ratios are 1.82 and 1.41 using measured wind and standard wind, respectively.

$E_{7(1421h-1437h)}-T_{15(1402h-1418h)-16(1422h-1437h)}$

Profiles T₁₅ and T₁₆ present similar profiles with a major southern peak and 2-3 minor peaks on the northern slope. Notably, all profiles are clearly asymmetric, with steep southern slopes and more gradual northern slopes. E₇ shows only the summit of the major peak, while the rest of the profile is comparatively smooth. There is only a vague similarity between the minor peaks of T₁₅₋₁₆ and the smooth profiles on the northern part of E₇ possibly representing a more diluted version of the minor peaks. SO₂ fluxes are 1740 t·d⁻¹, 4620 t·d⁻¹ and 2490 t·d⁻¹ for E₇, T₁₅ and T₁₆, respectively. Ratios are 2.66 for T₁₅/E₇, 1.43 for T₁₆/E₇, with an average of 2.05 using the measured wind. Ratios are 2.36 for T₁₅/E₇ and 1.27 for T₁₆/E₇ with an average of 1.81 using a standard wind.

$E_{8(1504h-1532h)}-T_{17(1439h-1456h)-18(1510h-1528h)}$

The E₈-T₁₇ profiles are the best example of a correlation of the general morphology of the plume. Three major peaks, two on the southern part and another at the north, are visible on both traverses. E₈-T₁₇ present features indicating a possible bifurcation. However, T₁₈ may also correlate as shown by the back-calculation time but presents a morphology more compact with no evident bifurcation. Peaks are visible on T₁₈ but visual correlation with E₈ is difficult. Fluxes are 3230 t·d⁻¹, 2220 t·d⁻¹ and 3600 t·d⁻¹ for E₈, T₁₇ and T₁₈, respectively. Ratios are 0.69 for E₈-T₁₇, 1.11 for E₈-T₁₈ with an average of 0.90 with measured wind. The

ratio is 0.83 for E₈-T₁₇, E₈-T₁₈ and the average with standard wind.

The E₁-T₃, E₂-T₆₋₇, E₃-T₈₋₉, E₈-T₁₇, and E₈-T₁₈ comparisons with ratios of 0.94, 1.09, 1.04, 0.69, and 1.11, respectively, indicate that the plume has not lost appreciable SO₂ during 10 km of transport during 10-20 minutes. However, the E₄-T₁₁, E₅-T₁₂₋₁₃, E₆-T₁₄ and E₇-T₁₅₋₁₆ profiles with ratios of 1.43, 1.46, 1.82, and 2.05, respectively, correspond to SO₂ fluxes 1.5-2 times higher at Ticuantepe than at El Crucero. These differences may be explained by several processes occurring at the source and during transport. Weather conditions play a role in the rapid or slow removal of SO₂. High temperature and high humidity may accelerate the transformation of SO₂ into aerosols. The winds and the conditions at the crater may also contribute to the difficulties of correlating different profiles at different distances. The fragmentation of gas during transport (atmospheric turbulence) is one important factor that affects the correlation. However, removal of SO₂ by dry deposition during transport does not occur on a large scale (Delmelle et al., 1998). The topography also likely affects the COSPEC measurements, and correlation is difficult due to the low altitude of the Santiago vent and the higher altitude where the measurements were made. Thus, it is possible that there is accumulation of gas in the Ticuantepe area produced by the circulation of a less dense air mass beneath the plume, which contribute to the descent of the denser plume.

During transport, it is obvious that there is some removal of SO₂ from the volcanic plume; the question is how much. Different processes such as conversion of SO₂ into aerosols (sulphate) and dry deposition do occur. Stoiber et al. (1986) estimated that 7 % of SO₂ is lost during transport from the vent to the Llano Pacaya

ridge at 15 km distance. Eatough et al. (1994) estimated the removal of SO₂ at 1-10% per hour depending on the temperature and the humidity conditions. One way to estimate the loss is to calculate a constant k_1 (Oppenheimer et al., 1998):

$$\Phi_{t1} = \Phi_{t2} e^{k_1(t_2-t_1)} \quad (2.4)$$

$$k_1 = \frac{\ln\left(\frac{\Phi_{t1}}{\Phi_{t2}}\right)}{t_2 - t_1} \quad (2.5)$$

where Φ represents an observed flux and plume cross-section at a given time, and k_1 represents all mechanisms (chemical and physical) of SO₂ removal. Negative values such as -6.4×10^{-5} for E₁-T₃, -4.5×10^{-6} for E₃-T₉, -1.06×10^{-4} for E₅-T₁₃, and -3.9×10^{-4} for E₈-T₁₇, show that there is more gas at El Crucero than at Ticuantepe indicating accumulation of some kind at the Llano Pacaya ridge, possibly by a bifurcation or doubling of the plume at these particular moments (Table 2.10). Positive values range from 8.58×10^{-4} to 3.75×10^{-6} with an average of 3.18×10^{-4} . However, values less than to 10^{-4} are too small to be significant. Only eight k_1 constants are above 10^{-4} , E₂-T₇, E₄-T₁₁, E₅-T₁₂₋₁₃, E₅-T₁₃, E₆-T₁₄, E₇-T₁₅₋₁₆, E₇-T₁₅, E₇-T₁₆ and E₈-T₁₈. A positive relation of k_1 factor and the SO₂ fluxes is observed (Figure 2.6). The high values correspond mainly at noon and later (1430 local time), indicating that an accumulation of gas may occur at Ticuantepe when the sea breeze and/or a valley breeze may have the most influence. However, the errors associated with the COSPEC measurements, the rapid transport, the puffing effect, the variable wind and the difficult correlation between profiles suggest that these numbers do not represent significant loss of SO₂ at El Crucero.

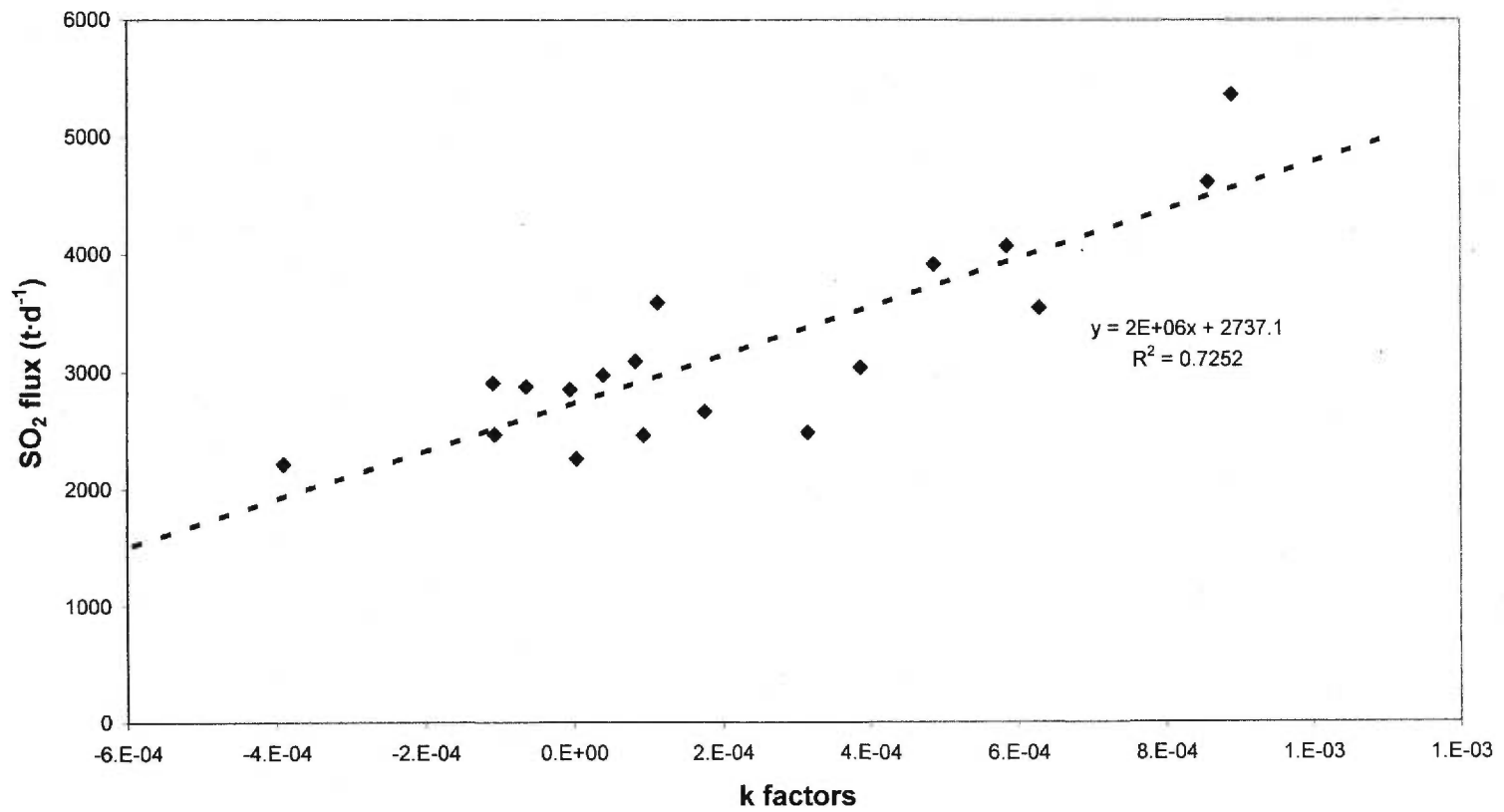
Table 2.10 SO₂ removal factor for 17 March at Masaya between Ticuantepe (5km from the crater) to El Crucero (15 km from the crater)

El C.\Ticu comparison	SO ₂ (t·d ⁻¹) Ticuantepe	SO ₂ (t·d ⁻¹) El Crucero	Transport time(min)	Windspeed (m·s ⁻¹)	k ₁ factor (s ⁻¹)
E ₁ -T ₃	2881	3060	15.7	10.6	-6.40E-05
E ₂ -T ₆₋₇	2468	2259	15.7	10.6	9.39E-05
E ₂ -T ₆₋₇	2267				3.75E-06
E ₂ -T ₇	2669				1.76E-04
E ₃ -T ₈₋₉	2980	2872	15.3	10.9	4.02E-05
E ₃ -T ₈	3100				8.32E-05
E ₃ -T ₉	2860				-4.50E-06
E ₄ -T ₁₁	3047	2136	15.3	10.9	3.87E-04
E ₅ -T ₁₂₋₁₃	3918	2681	13.0	12.5	4.86E-04
E ₅ -T ₁₂	2469				-1.06E-04
E ₅ -T ₁₃	5366				8.90E-04
E ₆ -T ₁₄	4074	2244	17.0	9.7	5.85E-04
E ₇ -T ₁₅₋₁₆	3553	1736	19.0	8.6	6.28E-04
E ₇ -T ₁₅	4617				8.58E-04
E ₇ -T ₁₆	2488				3.16E-04
E ₈ -T ₁₇₋₁₈	2909	3228	16.0	10.4	-1.08E-04
E ₈ -T ₁₇	2220				-3.90E-04
E ₈ -T ₁₈	3598				1.13E-04

Figure 2.6

The removal factor and SO₂ fluxes measured at Ticuantepe (5 km from the vent) (See Table 2.10). Note that a positive relation is observed.

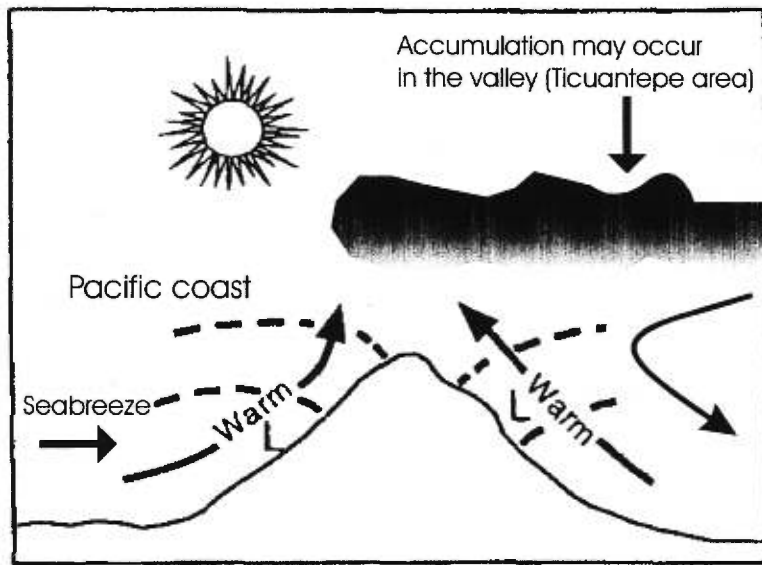
k factors vs SO₂ fluxes (5 km from the vent) at Masaya volcano



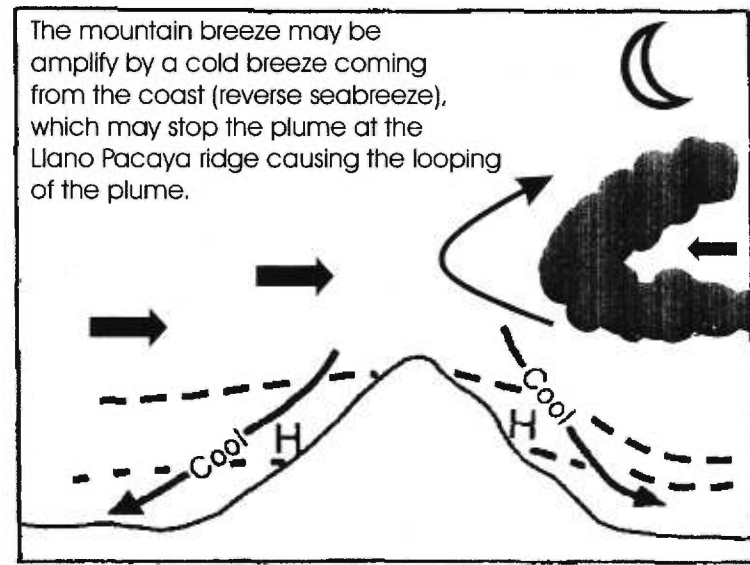
For 17 March 1998, correlations between the Ticuantepe road and the El Crucero road are feasible. The visual comparison of plume profiles shows that the shape of the plume changed between the two locations, letting only large features to be recognisable, which were nevertheless smoothed or accentuated by mixing with air and transport by the trade winds. The resulting correlations, with the exception of the T₃-E₁ and T₁₇₋₁₈-E₈, suggest that the fluxes can be 1.5 to 2 times higher at 5 km from the vent than at 15 km from the vent, suggesting a possible loss of SO₂ during transport by removal or atmospheric dispersion. However, as noted above, several of the correlations show no significant differences between 5 km and 15 km. Additionally, dry and wet deposition data do not support a high physical removal rate but indicate that mechanisms such as transformation of SO₂ to aerosols may be the important removal process for this particular day at Masaya volcano (Delmelle et al., 1998). SO₂ accumulation between the crater and the Llano Pacaya ridge (El Crucero road, 15 km from the crater) also may have occurred; this is possible by the effect of air density contrast combined with the high topography of the Llano Pacaya ridge obstructing to the passage of the plume. The gas accumulation may be explained by a valley breeze that produces ascending warm air circulation on the side of ridge or valley making a part of the plume rise near the ridge and the cooler part of the plume sink in the lower part of the valley (Figure 2.7). Early in the morning, the effect of the mountain breeze dissipates and thereafter a valley breeze arises. The influence of the valley breeze is at its maximum at noon (Arya, 1999). At night, the air circulation is reverse and a mountain breeze occurred sometimes making the plume to “loop” (Figure 2.8). Even if the k_1 loss rate indicates a small to medium removal of SO₂ for most correlations, it is hazardous to interpret these data as proof of a significant removal of SO₂, considering the various sources of uncertainties.

Figure 2.7

Schematic representation of (a) a valley breeze, and b) a mountain breeze (modified from Arya, 1999)



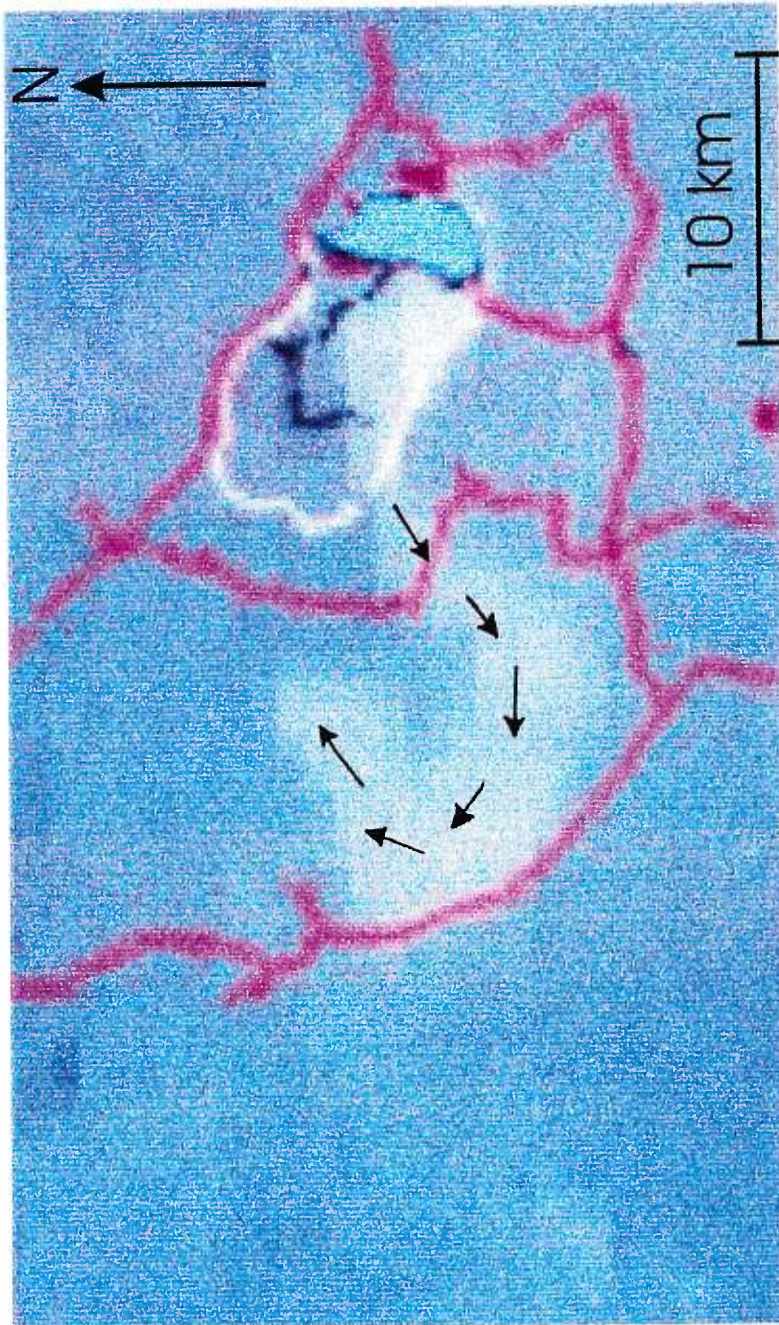
a) Valley breeze



b) Mountain breeze

Figure 2.8

AVHRR image of Masaya on 1 March 1998. Note the bifurcation (or doubling) of the volcanic plume (white clouds on the image). The lines are the surrounding roads. That may explained some unusually high SO₂ fluxes measurements made during that day. (Courtesy of Williams-Jones)



18 March 1998

The data of 18 March present a challenge to compare and interpret, since all profiles have very different shapes and SO₂ fluxes. Six traverses were made along the Pacific coast at 30 km from the crater (Masachapa, M₁-M₆) and 10 traverses along the El Crucero road at 15 km from the crater (El Crucero, EC₁-EC₁₀). SO₂ fluxes at El Crucero range from 780 td⁻¹ to 2100 td⁻¹ with an average of 1540 td⁻¹. Values at Masachapa range from 3420 td⁻¹ to 4790 td⁻¹ with an average of 4030 td⁻¹. EC/M ratio values range from 0.16 to 0.59 with an average of 0.40 ± 0.12 (Table 2.11, Figure 2.9).

M_{1(1145h-1221)}-E_{1(1133h-1153h)}

Two features on E₁ are also recognisable on M₁. A steep slope in the southern part of the plume is visible but accentuated in the middle of M₁. A plateau is also visible in the northern part of the two profiles but is on a larger scale on M₁. However, the plateau appears to be more pronounced for E₁. SO₂ fluxes are 1640 td⁻¹ and 3420 td⁻¹ for E₁ and M₁, respectively. There is an excess of 1780 td⁻¹ M₁ relative to E₁. E/M ratios are 0.48 for both measured and standard wind.

M_{2(1235h-1155h)}-E_{2(1157h-1217h)}

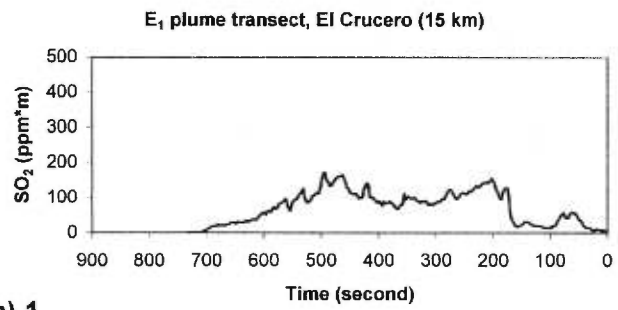
On E₂, the principal peak in the southern section of the plume is observed in the middle of the M₂ section. This peak is accentuated on M₂. SO₂ fluxes are 4010 td⁻¹ and 2100 td⁻¹ for M₂ and E₂, respectively, with a difference of 1910 td⁻¹ between the two locations. A ratio of 0.52 is calculated for both measured and standard wind.

Table 2.11 15 km-30km measurements correlations.

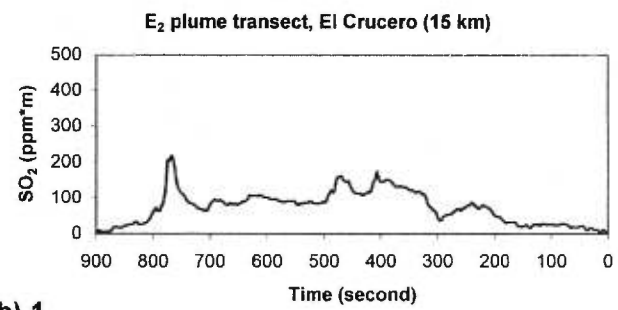
15 km El Cru.	Azimuth	Local time	SO ₂ (t·d ⁻¹), mea.winspeed	Av.	SO ₂ (t·d ⁻¹) std windsod (1m·s ⁻¹)	Av.	30 km Masachapa	Azimuth	Time	Recalc. Time	SO ₂ (t·d ⁻¹)	SO ₂ (t·d ⁻¹)	Ratio (E/M)	Diff.	Ratio (E/M)	Diff.
E1	273	1133-1153	1638		188		M1	257	1145-1221	1115-1146	3420	389	0.479	-1782	0.483	-201
E2	270	1157-1217	2098		250		M2	264	1235-1255	1205-1225	4011	478	0.523	-1913	0.523	-228
E3	267	1218-1237	1598		191		M3	257	1258-1327	1220-1249	4541	699	0.352	-2943	0.273	-508
E4	262	1243-1300	1549		191						4541	699	0.341	-2992	0.273	-508
				1574		191					4541	699	0.347	-2968	0.273	-508
E5	270	1303-1321	781		121		M4	257	1337-1401	1306-1330	4794	592	0.163	-4013	0.204	-471
E6	267	1325-1342	1481		183						4794	592	0.309	-3313	0.309	-409
				1131		152					4794	592	0.236	-3663	0.257	-440
E6	267	1325-1342	1481		183		M5	255	1416-1432	1347-1403	3972	462	0.373	-2491	0.396	-279
E7	262	1357-1418	1715		196						3972	462	0.432	-2257	0.424	-266
				1598		190					3972	462	0.402	-2374	0.410	-273
E7	262	1357-1418	1715		196		M6	255	1435-1456	1405-1426	3454	421	0.497	-1739	0.466	-225
E8	256	1423-1441	2038		248						3454	421	0.590	-1416	0.589	-173
				1877		222					3454	421	0.543	-1578	0.527	-199
E9	262	1444-1512	1476		180											
E10	249	1513-1535	1021		140											

Figure 2.9

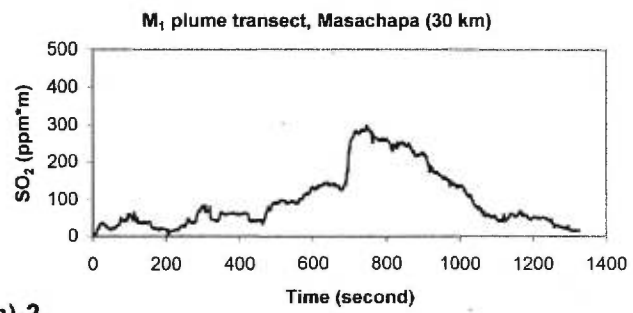
Correlation between El Crucero and Masachapa. a) E₁ and M₁, b) E₂ and M₂, c) E₃-E₄ and M₃ d) E₅-E₆ and M₄, e) E₆-E₇ and M₅, f) E₇-E₈ and M₆. (The last two charts are unused transects. Some (X) axes are reverse in order to have the same direction for comparison.)



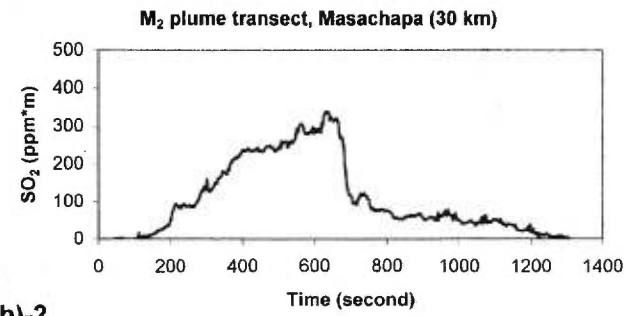
a)-1



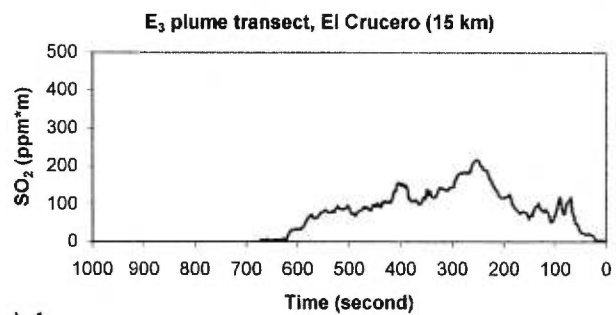
b)-1



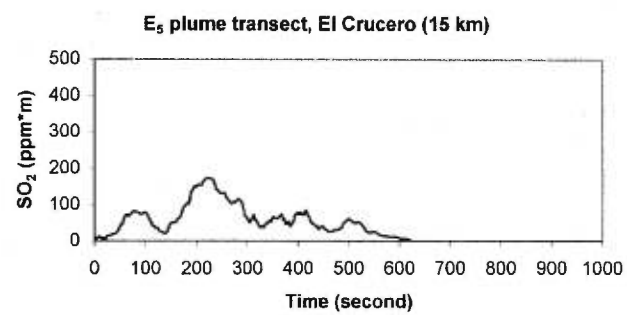
a)-2



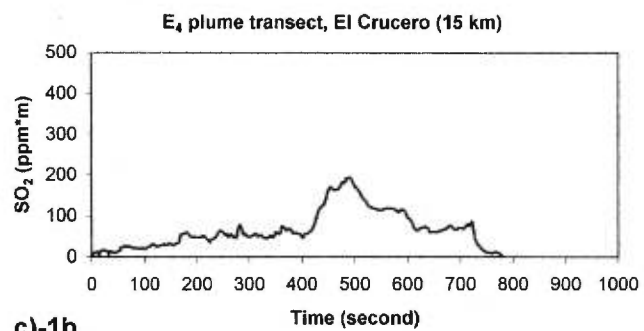
b)-2



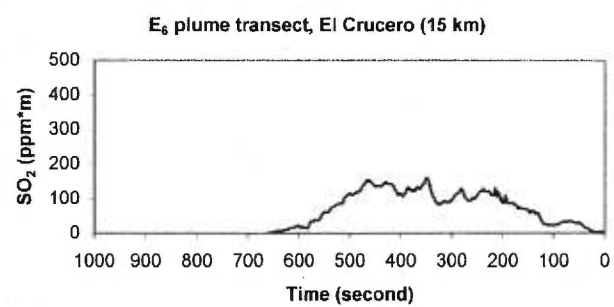
c)-1a



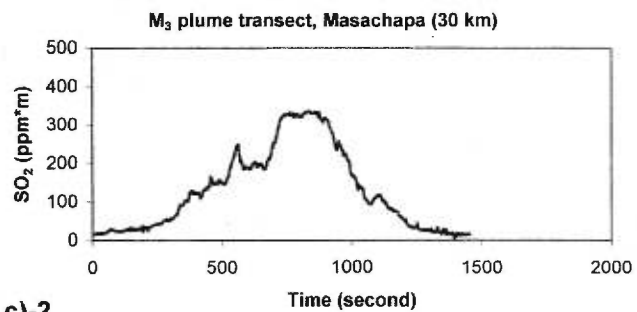
d)-1a



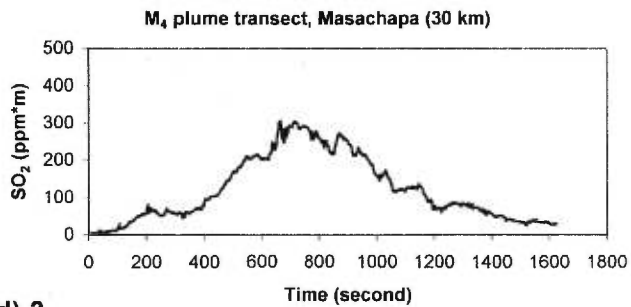
c)-1b



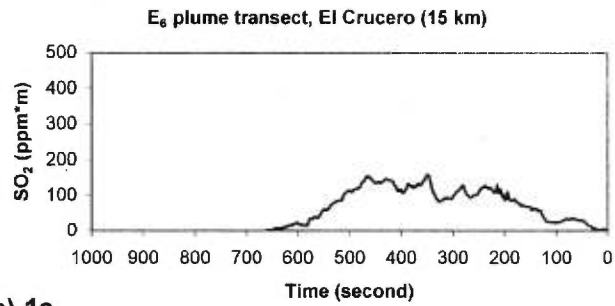
d)-1b



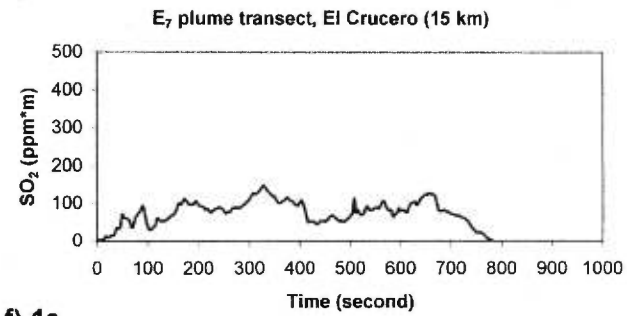
c)-2



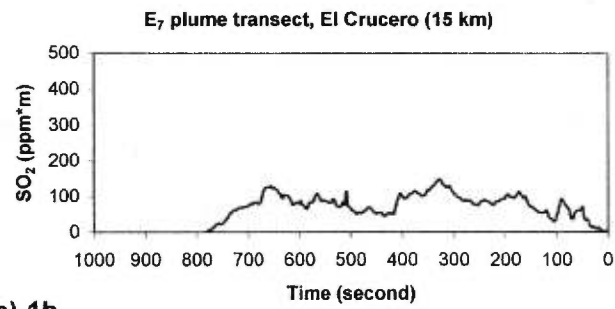
d)-2



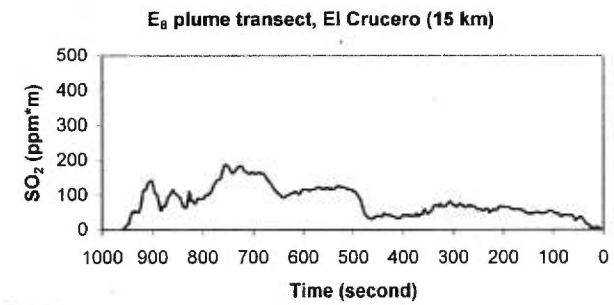
e)-1a



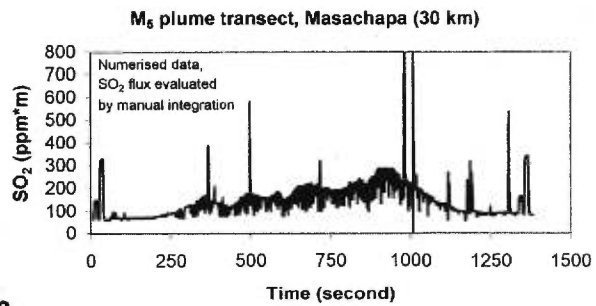
f)-1a



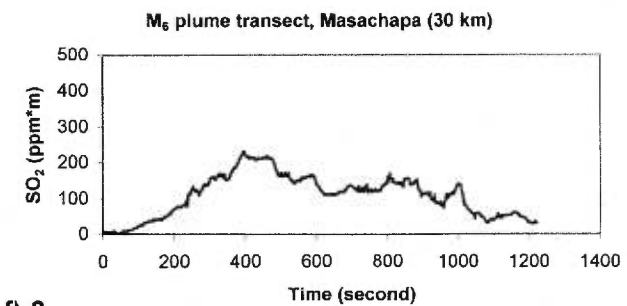
e)-1b



f)-1b

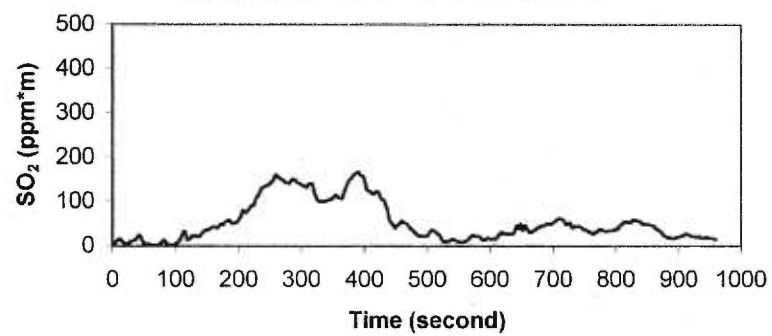


e)-2

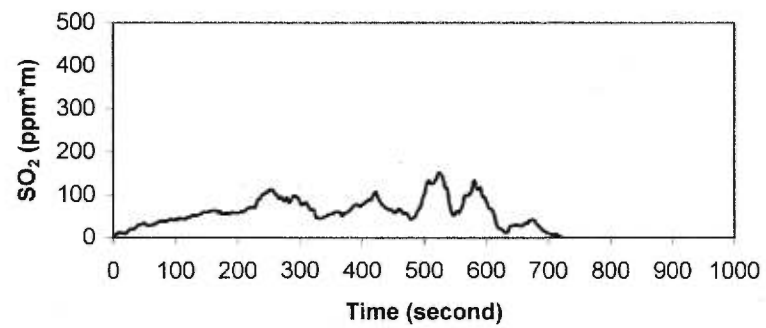


f)-2

E₉ plume transect, El Crucero (15 km)



E₁₀ plume transect, 98/03/18, El Crucero (15 km)



M₃(1258h-1327h)-E₃(1218h-1237h)-4(1243h-1300h)

The comparison of M₃, E₃ and E₄ shows that E₃ has three peaks also found on M₃, which are accentuated. However, only the main middle peak is present on all three profiles. SO₂ fluxes are 4540 td⁻¹ for M₃, 1600 td⁻¹ and 1550 td⁻¹ for E₃ and E₄, respectively, giving an average of 1570 td⁻¹ for E₃ and E₄ and a difference of 2970 td⁻¹ between M₃ and the two E profiles. Average ratios are 0.35 for M₃-E₃, 0.34 for M₃-E₄ with an average of 0.35 for M₃-E₃₋₄ using measured wind. With standard wind, the ratio is 0.27.

M₄(1337h-1401h)-E₅(1303h-1321h)-6(1325h-1342h)

From E₅ and E₆, four features are observed on M₄. However, M₄ and E₆ are both more or less symmetrical while E₅ exhibits more irregularity. Despite the back-calculated time falling between the two profiles, E₆ is easier to correlate with M₄. SO₂ fluxes are 4790 td⁻¹ for M₄ and 780 td⁻¹ and 1480 td⁻¹ for E₅ and E₆, respectively. Ratios differ with the profile used in the calculation. Using the measured wind, ratios are 0.16 for E₅/M₄ and 0.31 for E₇/M₄ with an average of 0.24. Using a standard wind, ratios are 0.20 for E₅/M₄ and 0.30 for E₇/M₄ with an average of 0.26.

M₅(1416h-1432h)-E₆(1325h-1342h)-7(1357h-1418h)

M₅, E₆ and E₇ present four parts that are similar in shape. On the northern section of the three profiles, two convex curves are recognisable but are attenuated on the M₅ profile. On the middle and the southern part section of M₅, two similar convex curves found on E₆ and E₇ are also visible. SO₂ fluxes are 3970 td⁻¹, 1480 td⁻¹ and 1720 td⁻¹ for M₅, E₆ and E₇, respectively. Ratios are 0.37 for E₆/M₅, 0.43 for E₇/M₅

with an average of 0.40 using measured wind. With standard wind, the ratios are 0.40 for E₆/M₅, 0.42 for E₇/M₅ for an average of 0.41.

M₆(1435h-1456h)-E₇(1357h-1418h)-8(1423h-1441h)

This correlation shows only one peak in the northern section of the plume that is common to the three profiles. However, E₇ and M₆ share a convex curve on the southern part of the plume. SO₂ fluxes are 3450 t·d⁻¹, 1720 t·d⁻¹ and 2040 t·d⁻¹ for M₆, E₇ and E₈, respectively. Ratios are 0.50 for E₇/M₆, 0.59 for E₈/M₆ for an average of 0.54 considering measured wind. For values with standard wind, the ratios are 0.47 for E₇/M₆, 0.59 for E₈/M₆ with an average of 0.53.

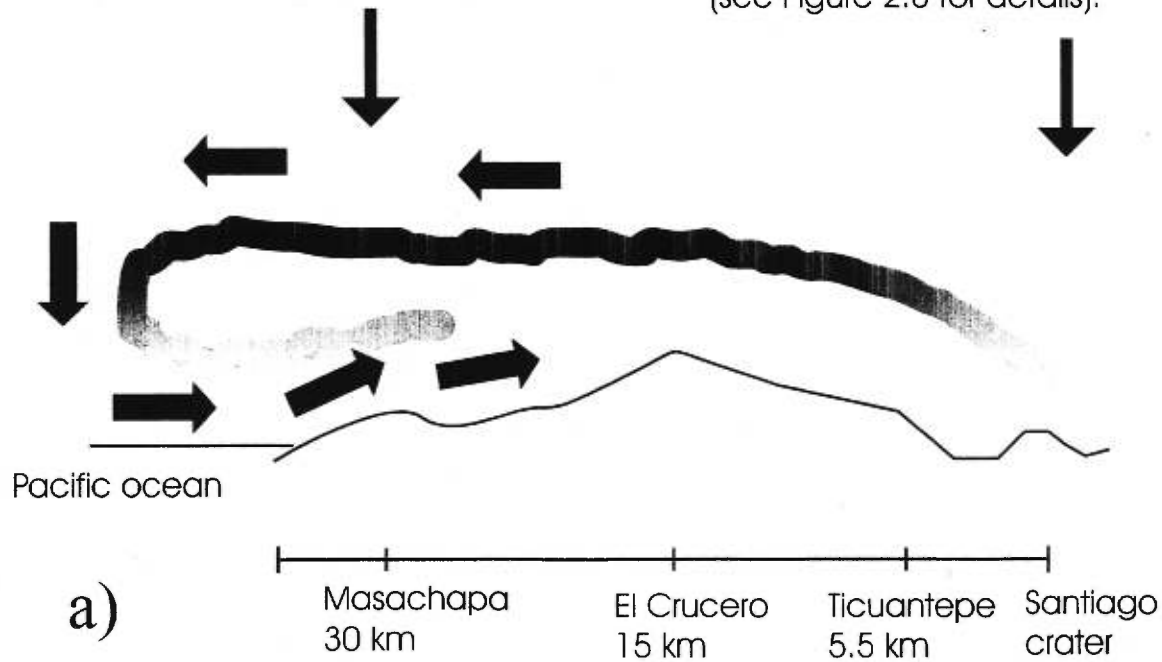
All E/M ratios indicate a large excess of SO₂ at Masachapa relative to El Crucero. Thus, there is evidence for an accumulation of SO₂ at the coastal region, with SO₂ fluxes two to four times higher than those measured in the El Crucero area. An apparent increase of SO₂ fluxes at 1237 hours is observed at the coastal road but no trend is apparent for the El Crucero traverses during the day except for some variations that can be explained by a puffing effect. Accumulation due to the topography, the altitude of the plume, and the wind system of the coastal area are factors that may explain these excess of SO₂ fluxes. There is a strong possibility that the plume was affected, particularly in the morning, by a sea breeze produced by a temperature contrast between the land and the sea. The sea breeze front (coming from the southwest on the Nicaraguan coast) is known to influence areas several kilometres inland (Arya, 1999). This may lead to a doubling of the plume at the coast and sometimes further inland during the day when the sea breeze has the most

Figure 2.10

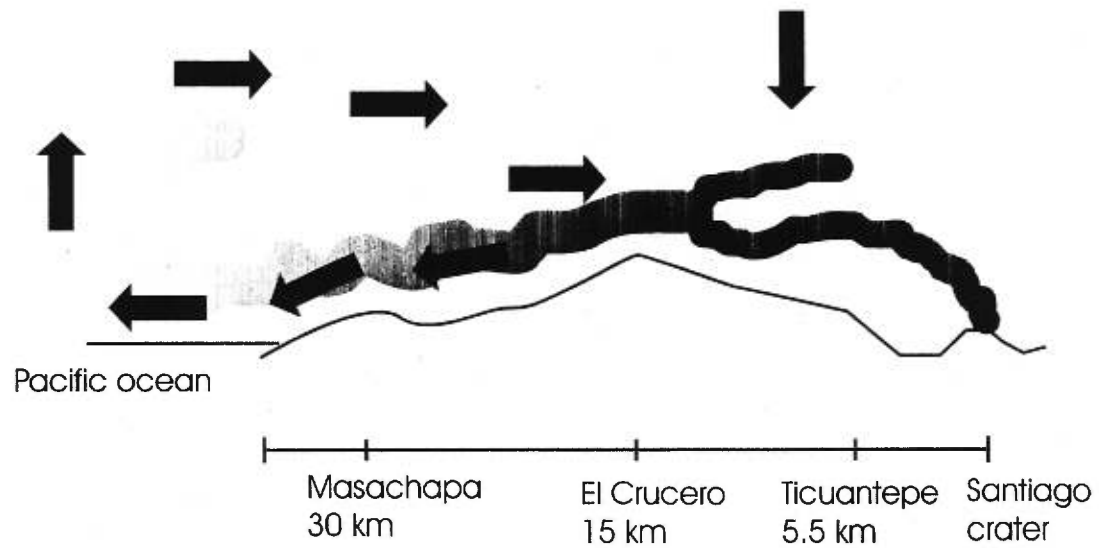
Effect of a sea breeze on a degassing source a) daytime, and b) night time. Note that in our case, it is suggested that a mountain-valley breeze may amplify a reverse sea breeze effect during the night.

Looping or doubling of the plume produced by the advance of the sea breeze (day time).

Some accumulation may occur at Ticuantepe by a valley breeze producing the denser part of the plume to sink at the bottom of the valley (see Figure 2.8 for details).



Dispersion of the plume gas may occur over the coast and the sea and the plume may occasionally be stopped at the Llano Pacaya ridge by the reverse circulation of the sea breeze from the coast (night-time).



b) Night reverse seabreeze

important effect (Figure 2.10). During this particular day, a sea breeze coming from the southwest direction was detected during a traverse at the coast. The morphology of COSPEC profiles shows rare roughly similar shapes in corresponding plume profiles, but generally no clear correlation are possible.

This set of comparisons demonstrates that wind systems and the topography affect the transport and dispersion of a volcanic plume. Between Masachapa at the coast to the crater 30 km northeast, there is the Llano Pacaya ridge (El Crucero, 15 km from the crater), which is higher than the crater itself. This ridge may stop the flow of the plume between the crater and the coast but may also be a wall where gas may accumulate on the side. This phenomenon may explain the higher values obtained at Masachapa (30 km from the vent).

Discussion

Degassing at Masaya

From the end of the last degassing crisis in 1990 to 1993, there was no important degassing due to a large collapse at the bottom of the active crater. The vent reappeared in June 1993 and a lava lake was formed. Several collapses in the active crater have occurred since then, and now a ~30 m wide vent exists and is in the process of widening by collapse. Degassing began in 1993 and is presently continuing. Since that time, seismic data show continuous tremor associated with the degassing, with no major change of behaviour. On several occasions, collapses in the crater occurred and mild strombolian explosions have been recorded in October 1996, the 12 November 1997 and in 1998. These events were preceded by a decrease and

interruption of the degassing. A temporary obstruction of the conduit thus may have occurred. A collapse in the conduit or more likely cooling of the magma surface in the conduit may have triggered the cessation of degassing. Increase in pressure then occurred, leading to an explosion, which could erupt solid materials around the active crater on one occasion. After the November 1997 episode, an apparent increase in the degassing in 1998 relative to prior episodes of activity was observed. It is interesting to note that these events happened at the end of the rainy season in which the contribution of water may have influenced, in part, the cooling or obstruction of the conduit and contributed to these explosions.

Degassing model

The observations made from 1996 to 1998 can help constrain a model of the degassing behaviour of Masaya. After the 12 November 1997 eruption, SO₂ emissions appear to have increased substantially. From an average of 380 td⁻¹ in March 1997, the degassing reached an average of 2030 td⁻¹ in March 1998. This is an indication of important changes in the magmatic system beneath the vent of Santiago. The collapse of the vent in November 1997 may have increased the pressure in the plumbing system or in the shallow magma chamber. A release of pressure by the small scale explosion on 12 November 1997 may have been preceded or followed by a convective overturn, but no gravity changes were observed (Rymer et al., 1998; Beaulieu, 1999). A possible explanation for the increased degassing is an accumulation of SO₂ in the magma under the cooled crust, leading to a period of intense degassing from the surface magma in the chamber or in the conduit after its re-opening. However, this style of degassing is likely to decrease rapidly with time.

A more plausible explanation is that a “major” movement in the magma chamber occurred in November 1997. The denser, degassed magma at the surface moved down in the magma chamber and less degassed magma ascended to the surface of the chamber or the conduit. Rymer et al. (1998) interpreted the 1993 degassing crisis at Masaya by a convective overturn in the magma chamber, which may have also happened in November 1997. The recent six years of microgravity monitoring at Masaya shows no sign of new magma intrusion. In the 1997-98 microgravity survey by Beaulieu (1999), no evidence of ground deformation and only small microgravity variations were observed. Convection at different time scales in the plumbing system or the upper part of the magma chamber beneath the Santiago vent may explain the puffing effect that we see during degassing from the crater. Kazahaya et al. (1994) suggest a similar convection model in conduits for Izu-Oshima volcano; to explain the excess of SO₂ degassing at this volcano, convection in the conduit brings the non-degassed or less degassed magma in the shallow part of the conduits.

Daily variations of degassing show SO₂ fluxes ranging from 680 t·d⁻¹ to 5580 t·d⁻¹ (excluding the problematic coastal measurements from Masachapa at 30 km from the crater). Hourly variations show differences as large as 3250 t·d⁻¹ on April 11. This particular day shows a minimum flux of 1154 t·d⁻¹ at 1452 hours and a maximum flux of 4400 t·d⁻¹ at 1144 hours. Daily and hourly variations of SO₂ fluxes may be explained by magma movement in the plumbing system, which may be affected by earth and lunar tides. Stoiber and al. (1986) have observed that peak degassing at Masaya corresponds to points of inflection on the tidal curve. However, for many days, a tendency for higher degassing occurs at midday or sometimes at the end of the day, suggesting that the evolution of atmospheric conditions through the

day (heating by the sun, maximum effect of the sea breeze) also may affect daily degassing. The earth and lunar tide do not affect the degassing in any clear way (Figure 2.11). Another process that may occur is the accumulation of gas in the conduit or in the surface magma. After reaching a saturation state, a burst of gas or a “puff” is released from the plumbing system. COSPEC measurements reflect these processes, and some low and high SO₂ fluxes values may be attribute to these phenomena.

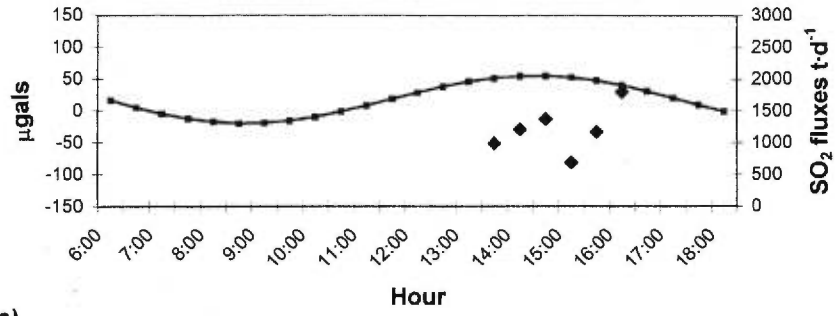
Plume transport (17-18 March)

The major components of the plume consist of H₂O, CO₂ and SO₂. At Masaya, SO₂ degassing is a serious health and agricultural risk. Due to the wind being blown mainly west of the crater, towns and coffee plantations downwind are severely affected by acid rain and dry deposition of SO₂ and other components like HCl and H₂SO₄. The high topography and the relatively low altitude of the plume put the Llano Pacaya ridge directly in the path of the plume. Two days of simultaneous COSPEC measurements allowed us to obtain data on the behaviour of the plume during its transport. On 17 March 1998, average T/E ratios of 0.8 to 2.1 show that there is a removal or accumulation of some kind from the plume. T/E ratios of ~1 suggest also that the plume may not have significant removal or accumulation of gas, suggesting that variations may be attributed to the poor correlation between measurements at the two distances or fragmentation of the plume by the wind during transport. Nevertheless, average k_1 factors of 3.2×10^{-4} are low, indicating that the processes of SO₂ removal are relatively slow and difficult to pinpoint. On 18 March 1998, E/M ratios from 0.16 to 0.59 demonstrate an accumulation effect, possibly due

Figure 2.11

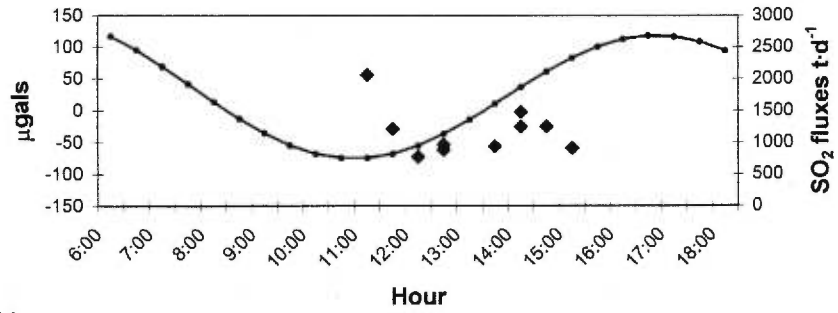
Earth and lunar tidal correlations with SO₂ fluxes measurements at Masaya volcano, for nine days during February and March 1998.

98/02/21, SO₂ fluxes and solid earth tide



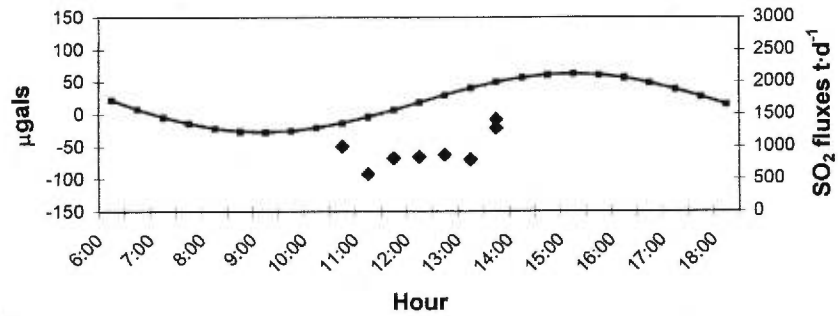
a)

98/02/24 SO₂ fluxes and solid earth tide



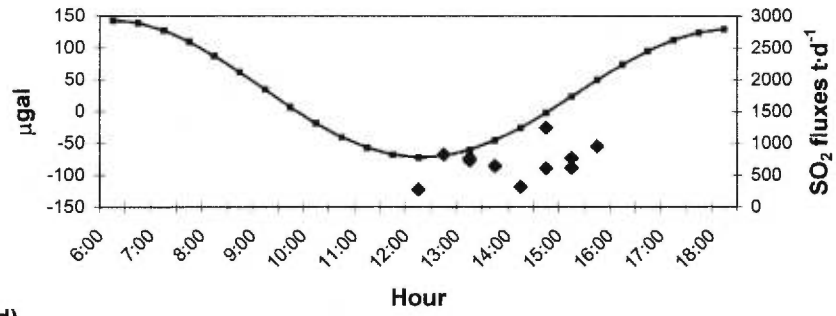
b)

98/03/07 SO₂ fluxes and solid earth tide



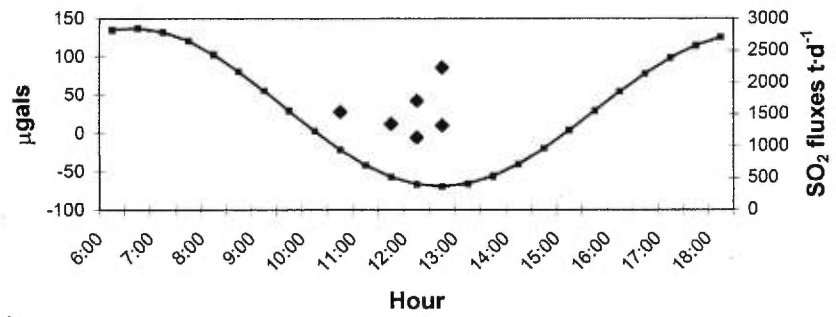
b)

98/03/13 SO₂ fluxes solid earth tide



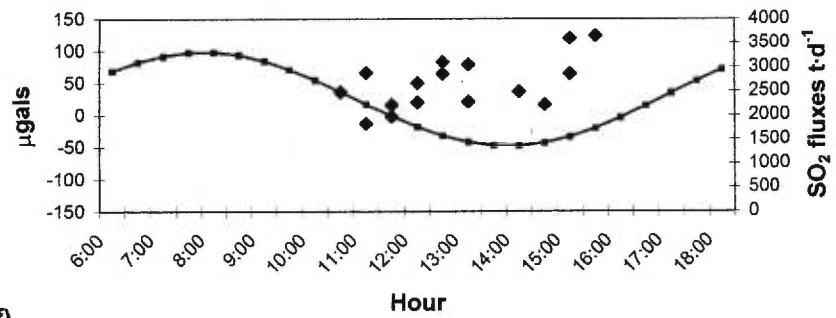
d)

98/03/14 SO₂ fluxes and solid earth tide



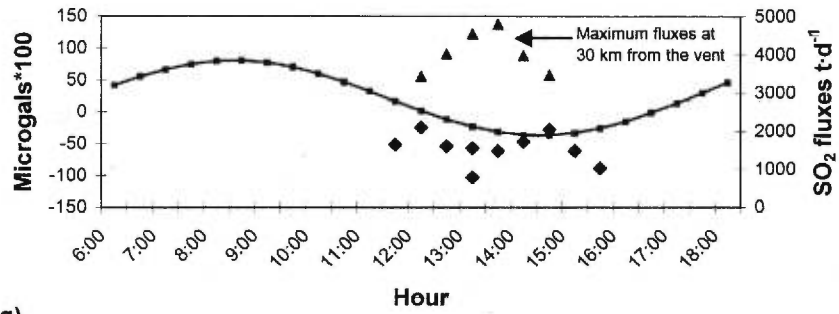
e)

98/03/17 SO₂ fluxes and solid earth tide



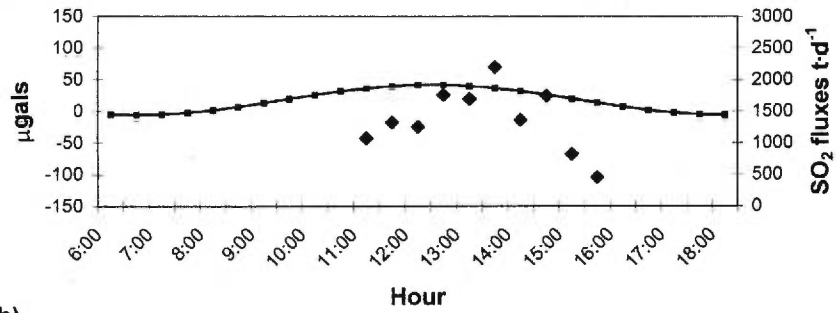
f)

98/03/18 SO₂ fluxes solid earth tide



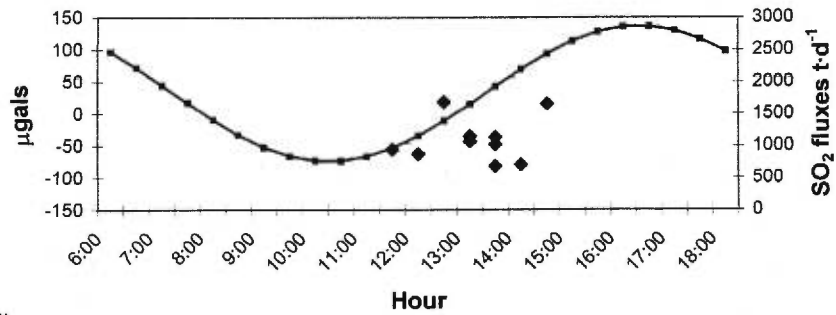
g)

98/03/21 SO₂ fluxes and solid earth tide



h)

98/03/25 SO₂ fluxes and solid earth tide



i)

to a sea breeze that stops and folds the plume at the coast so that the SO₂ values increased substantially near the coast relative to El Crucero, which is 30 km inland. An AHVRR image on 1 March 1998 clearly shows the plume looping at the Llano Pacaya ridge accumulation of gas at the Llano Pacaya ridge (Figure 2.8). This picture indicates a major problem if COSPEC measurements were made that day. The plume would be measured almost twice on the Ticuantepe road (5 km), and only a small part of the plume would be in the path of the COSPEC at the El Crucero road (15 km). The same phenomenon may occur on the west side of the Llano Pacaya ridge due to the sea breeze. When measuring at Masachapa along the coast at 30 km from the crater, it is possible that the measurements include twice the true width of the plume as well as several folds, which may explain the excess of SO₂ measured at Masachapa.

Petrology

At Masaya, the low sulfur concentrations in plagioclase melt inclusions suggest that the plagioclase crystallized from a partially to almost completely degassed melt. The sulfur concentrations in the glasses do not represent the amount of SO₂ degassed at the vent. A way to explain this anomaly is that the sulfur is not only dissolved in the magma but also exists as bubbles. The ultimate source of sulfur is probably a large magma reservoir with a higher sulfur concentration. Stoiber et al. (1986) have suggested that a “spherical” magma body with a radius of 665 m or a sill 180 m wide under the active vent may be the source of the degassed sulfur. Using an averaged SO₂ flux of 400 td⁻¹ and a release of 240 ppm (Stoiber et al., 1986) of sulfur, Rymer et al. (1998) have estimated that a total of 1.5 Mt of magma (5.5x10⁻⁴ km³)

had been degassed from 1993 to 1997.

Conclusions

With its unique nature, Masaya volcano has an important place in the field of volcanology. Masaya has easy access and thus facilitates COSPEC studies and monitoring of the plume evolution. In 1997 the degassing was similar to the preceding degassing crisis. However, the degassing significantly increased in 1998 following a minor explosion in November 1997. The SO₂ fluxes exhibit variability over days, weeks, and even months. Many factors affect the degassing including the pressure in the degassing conduit and the level of the magma in the sub-surface. The daily SO₂ variations suggest that magma convection occurs in the conduits beneath the vent.

The simultaneous measurements made at two distances from the crater demonstrate the problems associated with atmospheric SO₂ transport and measurement limitations. The 17 March data set made relatively near the crater (5 and 15 km) shows little removal of gas in the plume. The variability is mostly attributed to emissions by puffs. The 18 March correlations (15 and 30 km from the volcano) show the importance of atmospheric dynamics. Folding or bifurcation of the volcanic plume occurred at the coast, which may explain the two folds to four folds increase of SO₂ fluxes measured at the coast. No evident correlation of SO₂ peaks degassing with tides are observed. However, the open nature of Masaya makes it sensitive to minor stresses, which may be measurable with other monitoring techniques such as microgravity (Beaulieu et al., 1998). Variations in the plumbing system of the volcano may have an effect in the style of degassing that occurs,

leading to passive degassing when the system is open and more explosive behaviour when there is collapse around the vent. Ground water also may contribute to the explosions, since they occur at the end of the rainy season.

Petrologic data show a small amount of dissolved sulfur in the melt, suggesting superficial degassed magma and a deeper more volatile-rich magma, explaining the intense degassing of Masaya volcano.

REFERENCES

- Arya, S. P., 1999.** Air Pollution Meteorology and Dispersion. Oxford University Press, N.Y., 310 pp.
- Beaulieu, A., Williams-Jones, G., St-Amand, K., Stix, J., and Rymer, H., 1998.** Temporal gravity variations of variable timescale at Masaya volcano, Nicaragua. AGU fall Meeting, San Francisco, p. 960.
- Beaulieu, A., 1999.** The nature and origin of spatial and temporal variations in the gravity fields of Telica and Masaya Volcanoes, Nicaragua. Unpublished M.Sc. thesis, Département de géologie, Université de Montréal, Montréal, Canada, 138 pp.
- Bice, D. C., 1980.** Tephra stratigraphy and physical aspects of recent volcanism near Managua, Nicaragua. Unpublished Ph.D. Dissertation, University of California, Berkeley, U.S.A., 422 pp.
- Bulletin of the Global Volcanism Network, 1992.** Masaya volcano. Smithsonian Institution 17 (4): 7.
- Bulletin of the Global Volcanism Network, 1997.** Masaya volcano. Smithsonian Institution 22 (3): 6-7.
- Bulletin of the Global Volcanism Network, 1998.** Masaya volcano. Smithsonian Institution 23 (9): 7.
- Bulletin of the Global Volcanism Network, 1999.** Masaya volcano. Smithsonian Institution 24 (4): 5.
- Carroll, M. R., and Webster, J. D., 1994.** Solubilities of sulfur, noble gases, nitrogen, chlorine, and fluorine in magmas. In Carroll, M., Holloway, J. R., (Editors), Volatiles in Magmas: Mineralogical Society of America Reviews in Mineralogy, 30: 231-279.
- Connor, C. B., and Williams, S. N., 1990.** Interpretation of gravity anomalies, Masaya Caldera complex, Nicaragua. Transactions of the 12th Caribbean Geological Conference, 495-502.
- Delmelle, P., St-Amand, K., Stix, J., Baxter, P., Oppenheimer, C., Burton, M., and Francis, P., 1998.** COSPEC measurements at Masaya volcano Nicaragua: Part II- SO₂ plume dispersion and subsequent removal downwind. AGU Fall Meeting, San Francisco, p. 977-978.

- Delmelle, P., Baxter, P.J., Beaulieu, A., Burton, M., Francis, P.W., Garcia-Alvarez, J., Horrocks, L., Navarro, M., Oppenheimer, C., Rothery, D., Rymer, H., St. Amand, K., Stix, J., Strauch, W., and Williams-Jones, G., (in press).** Origin and effects of Masaya volcano's continued unrest probed in Nicaragua. *Eos, Transaction, American Geophysical Union.*
- Gerlach, T. M., and McGee, K. A., 1994.** Total sulfur dioxide emissions and pre-eruption vapour saturated magma at Mount St. Helens, 1980-1988. *Geophysical Research Letters*, 21: 2 833-2 836.
- Johnson, N., and Parnell, R. A., 1986.** Composition, distribution and neutralization of "acid rain" derived from Masaya volcano, Nicaragua. *Tellus*, 38B: 106-117.
- Kazahaya, K., Shinohara, H., and Saito, G., 1994.** Excessive degassing of Izu-Oshima volcano: magma convection in a conduit. *Bulletin of Volcanology*, 56: 207-216.
- Maciejewski, A. J. H., 1995.** Evolution and present-day activity of the Masaya Volcanic Complex, Nicaragua. Unpublished manuscript, The Open University, 37 pp.
- McBirney, A. R., 1956.** The Nicaraguan volcano Masaya and its caldera. *American Geophysical Union Transactions*, 37: 83-96.
- Oppenheimer, C., Francis, P., and Stix, J., 1998.** Depletion rates of sulfur dioxide in tropospheric volcanic plumes. *Geophysical Research Letters*, 25: 2 671-2 674.
- Rymer, H., van Wyk de Vries, B., Stix, J., and Williams-Jones, G., 1998.** Pit crater structure and processes governing persistent activity at Masaya Volcano, Nicaragua. *Bulletin of Volcanology*, 59: 345-355.
- St-Amand, K., Beaulieu, A., Stix, J., Gaonac'h, H., and Lovejoy, S., 1998.** SO₂ flux, CO₂ and radon degassing at Masaya caldera, Nicaragua. *GAC/MAC Spring Meeting, Québec 1998, Abstract Volume 23:178.*
- St-Amand, K., Stix, J., Delmelle, P., Gaonac'h, H., Lovejoy, S., and Williams-Jones, G., 1998.** COSPEC Measurements at Masaya volcano Nicaragua: Part I- SO₂ fluxes, petrology of melt inclusions, and multifractal analysis of COSPEC signals. *AGU Fall Meeting, San Francisco, 977.*
- Stoiber, R. E., and Rose, W. I., 1973.** Cl, F, and SO₂ in Central American volcanic gases. *Bulletin of Volcanology*, 37:454-461.

- Stoiber, R. E., Williams, S. N., and Huebert, B. J., 1986.** Sulphur and halogen gases at Masaya Caldera Complex, Nicaragua: Total flux and variations with time. *Journal of Geophysical Research*, 91: 12 215-12 231.
- Symonds, R. B., Rose, W.I., Bluth G.J.S., Gerlach, T. M., 1994.** Volcanic gas studies: Methods, results, and applications. In Carroll, M., Holloway, J. R., eds., *Volatiles in Magmas: Mineralogical Society of America Reviews in Mineralogy*, 30: 1-66.
- Walker, J. A., Williams, S. N., Kalamarides, R. I., and Feigenson, M. D., 1993.** Shallow open system evolution of basaltic magma beneath a subduction zone volcano: the Masaya Caldera Complex, Nicaragua. *Journal of Volcanology and Geothermal Research*, 56: 379-400.
- Williams, S. N., 1983.** Geology and eruptive mechanisms of Masaya Caldera Complex, Nicaragua. Unpublished Ph. D. thesis, Dartmouth College, Hanover, New Hampshire, U.S.A., 169 pp.

CHAPTER III

Scale invariance of volcanic SO₂ plumes: a case study at
Masaya Volcano, Nicaragua.

Katie St-Amand

Département de géologie
Université de Montréal
Montréal, Qc, H3C 3J7
Canada

Abstract

A new statistical approach has been used in order to study the scaling and the behaviour of SO₂ degassing. Temporal series and spatial transversal series of the SO₂ plume have been analysed. The energy spectrum of all series shows a scaling behaviour from 0.5 to 600 seconds with $\beta = 2.8 \pm 0.1$. Another regime is observed at lower frequencies in temporal series. The multifractality was then investigated through structure functions. While spatial series show only a scaling trend from the highest available scale to the length of the series, temporal series are composed of two distinct scaling regimes, which are separated by a transition zone beginning at approximately 100 seconds. The first regime associated with high frequencies gives universal multifractal parameters of $\alpha=1.74$, $C_1=0.039$ with an H value around 0.88. We propose this regime to be characteristic of the turbulent behaviour of the SO₂ puffs. Despite a limited number of points, the second regime may exhibit universal multifractality with $\alpha=1.71$, $C_1=0.049$ and $H=0.40$. We expect the second regime to be associated with the long-term characteristics of the degassing of the volcano.

Introduction

Seismic monitoring, gravity surveys, soil gas analyses, and plume composition analyses are some of the ways used to study and understand the dynamic behaviour of active volcanoes. Gases such as H₂O, CO₂ and SO₂ are thought provide important information regarding the state of the volcano (Menyailov, 1975), and variations in the amount and composition may indicate changes in the equilibrium and stability of the volcano. Correlation spectrometry (COSPEC), originally developed for monitoring industrial emission of SO₂ pollution from industrial sources, is now commonly used for monitoring passively degassing and erupting volcanoes (Stoiber et al., 1983). COSPEC measurements, in conjunction with our knowledge of sulfur solubility, petrology of melt inclusions and volcanic glass, may help to evaluate the minimum volume of magma degassed and extrapolate the size of a magma chamber. This approach was applied at several volcanoes such as Masaya (Stoiber et al., 1982), Mount St.Helens (Gerlach et al., 1994), and Lascar and Lonquimay, Chile (Andres et al., 1991). COSPEC technology was successfully used (sometimes with TOMS and TIMS satellites imaging) for monitoring the evolution of volcanic activity during repose and explosive episodes at Mount St.Helens, (Casadevall et al., 1983), Redoubt volcano, Alaska, (Casadevall et al., 1994), Galunggung volcano Java, Indonesia (Bluth et al., 1994) Kilauea volcano, Hawaii (Realmuto et al., 1997), and Arenal volcano, Costa Rica (Williams-Jones, 1997). The annual contribution of volcanic SO₂ to the atmosphere may be evaluated with COSPEC measurements (Stoiber et al., 1973; Stoiber et al., 1987). Atmospheric SO₂ loading, plume transport and dispersion also can be monitored by correlation

spectrometry (Cadle et al., 1979; Eatough et al., 1994; Bluth et al., 1997; Oppenheimer et al., 1998).

However, the conventional way to use COSPEC presents many difficulties and many sources of errors. The duration of these measurements is often relatively short, and the sampling scattered or irregular in time (e.g. from 10 days to once a year or even longer). The effect is to undersample the large geodynamic variability of volcanic processes, producing difficulties of interpretation and oversmoothing modelling. As an example, Rymer et al. (1998) have argued that little variation occurred in the gravity field of Masaya volcano for the 1994-1997 period. However, new measurements also made at Masaya by Beaulieu (1999) demonstrate gravity variations on hourly, daily and monthly scales which shed new light on the measurements and interpretations of Rymer et al. (1998). Because of the highly variable SO₂ degassing, COSPEC measurements show the same problem. During a single day, SO₂ fluxes may vary extensively, sometimes up to nearly an order of magnitude (e.g., 280 t·d⁻¹ to 1250 t·d⁻¹ on 13 March 1998). Variable factors such as wind speed, dominant wind directions, confining pressure conditions at the crater, the dynamic nature of the volcano, and topography may influence the final SO₂ fluxes which are measured. These indicate the difficulties associated with scattered measurements and interpretation of data that may not truly represent significant variations in the time interval surveyed.

In 1997 and 1998, COSPEC surveys were conducted at Masaya volcano, Nicaragua, for a monitoring study of the SO₂ degassing. We often observed high variability of the degassing on an hourly and daily basis. Visual observations of the volcanic plume showed irregular emissions of gas puffs (mainly H₂O, CO₂, SO₂).

Some of the information acquired during these surveys was analysed in order to investigate and characterize the variability of the degassing of Masaya volcano observed on a wide range of scales. Our objectives in this paper are: first, to demonstrate the scaling properties of volcanic SO₂ plume. Second, investigate the universality of the behaviour properties of the SO₂ plume by determination of multifractal parameters (α , C_1 and H), defining the multifractality of the particular field.

Scaling properties and multifractal nature of geophysical and geographical fields are part of a new approach developed by geophysicists to find ways to understand and explain chaotic behaviour and variability. Landscape topography, a system characterized by high spatial and temporal variability, has been approached from a scale invariance and multifractal point of view (Lavallée et al., 1993). Laferrière et al. (1999) have studied the multifractal properties of visible reflectance fields of basaltic volcanoes such as Etna and Mauna Loa. Lovejoy et al. (1991) have characterized the turbulent behaviour of atmospheric dynamics as a multifractal laboratory. Schmitt et al. (1995) have applied scaling analyses and multifractal properties to ice core climatic data. Scaling and multifractality of temperature and wind fields were also investigated by Schmitt et al. (1992). Tropospheric diffusion of particles also was found to show a scaling behaviour power law (Arya, 1999). It was found early on that the atmosphere comprised turbulent cells at different scales (Richardson, 1922). This led to the basis of cascade models which includes scale invariance, the conservation of energy (Kolmogorov, 1941) and a dynamic mechanism by which the structures of similar sizes will interact more than structures of various sizes (Schertzer and Lovejoy, 1996). The SO₂ transported by the

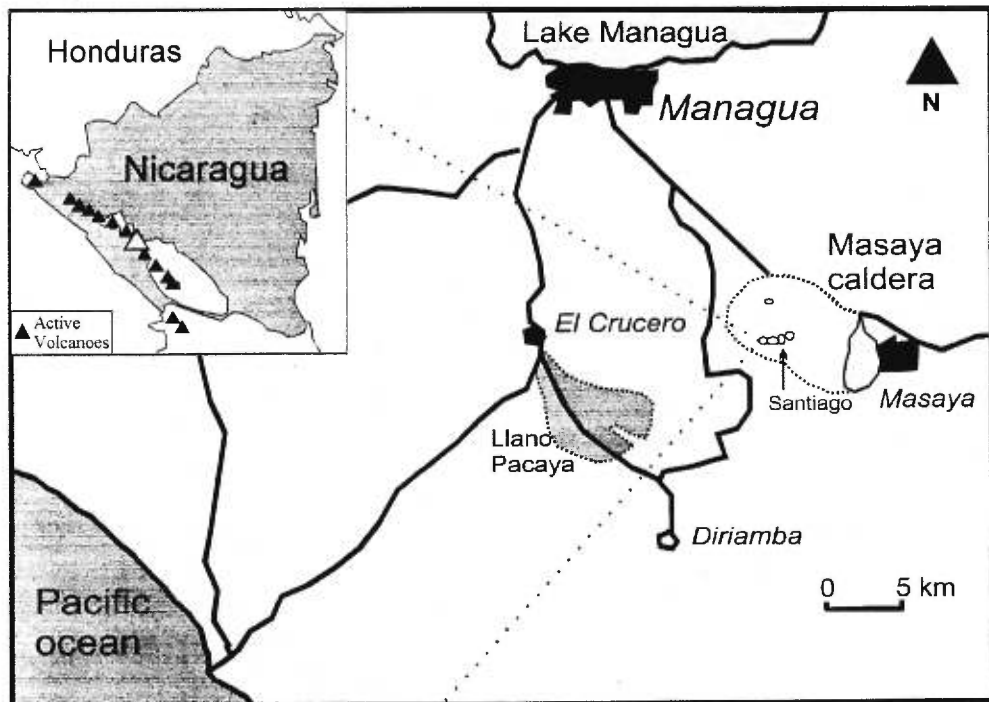
atmosphere exhibits fluctuations of gas concentrations in the volcanic plume. At a certain level, the atmospheric turbulence may control the variability of SO₂. It is suggested that the presence of atmospheric swirls at different scales may be related to the small and large fluctuations of SO₂ concentrations in the volcanic plume.

Data Acquisition

Sulfur dioxide after H₂O and CO₂ is quantitatively one of the most important volatiles degassed by active volcanoes. COSPEC, correlation spectrometry uses ultraviolet rays to detect SO₂ in the atmosphere. The amount of ultraviolet radiation that passes through the set of COPSEC lenses is transformed into an electric signal and stored in a computer file or on a chart recorder (paper) which corresponds to the vertical integration of the SO₂ concentrations at a point under the plume. Cells of known SO₂ concentration (ppm·meter) are used to calibrate the SO₂ signal concentration in the atmosphere. By horizontal integration of a complete transversal plume profile on paper, an SO₂ flux is obtained (Chapter II, SO₂ degassing). Measurements were conducted at three distances from the active crater: Ticuantepe at 5 km from the crater, El Crucero (Llano Pacaya ridge) at 15 km, and Masachapa (coastal region) at 30 km (Figure 3.1). Time series of SO₂ concentrations were acquired at fixed locations (5 km and 15 km) under the volcanic plume. These measurements represent the evolution of the SO₂ emission in time. However, the majority of the data were obtained by driving on a road at a constant speed, transversely to the volcanic plume, which is considered an approximately

Figure 3.1

Map of Masaya volcano and its surrounding indicating the location of data acquisition. The three distances at which measurements were made are Ticuantepe at 5 km from the active crater, El Crucero at 15 km on the Llano Pacaya ridge, and Masachapa at 30 km. Note that during the dry season the zone affected by the volcanic plume is located mainly west of the volcano (from Delmelle et al., submitted).



perpendicular “slice” of the plume, considering the relatively high speed of the vehicle when taking measurements (Figure 3.2).

Masaya volcano, Nicaragua, is a basaltic caldera located 20 km west from Managua. The caldera has a dimensions of 6 km by 11 km and is known to have been active during historical time. For the last century, activity has consisted of degassing of a volcanic plume, mild strombolian explosions and periodic lava lakes. Masaya is presently experiencing strong degassing from Santiago crater.

Scaling Properties of SO₂ Degassing

In geology, many processes and phenomena are difficult to scale without knowing the spatial or temporal resolution. This particularity reflects what is called scale invariance, e.g., a similar structure exists over a large range of scales. For example, a particular topographic features such as a stone may be considered a mountain in miniature, or just a grain on a pile of sand. Folded rocks and fracture systems may be of various sizes. A largely known concept is the Gutenberg-Richter power scale for determination of earthquake frequency-magnitude relations. Many dynamic processes exhibit scaling over a wide range of scales. In the present study, Fourier energy spectra were performed on the spatial/temporal SO₂ series. For non-linear scaling processes, we expect the Fourier energy spectrum of the series to follow a power law such as:

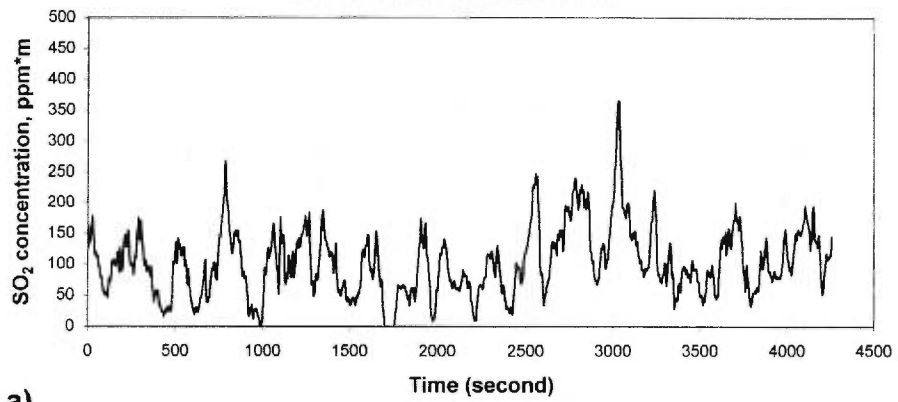
$$E(f) \propto f^{\beta} \quad (3.1)$$

where $E(f)$ is the Fourier energy spectrum energy (modulus square of the amplitude of a given frequency), f is the frequency in second⁻¹ and β is the scaling exponent of

Figure 3.2

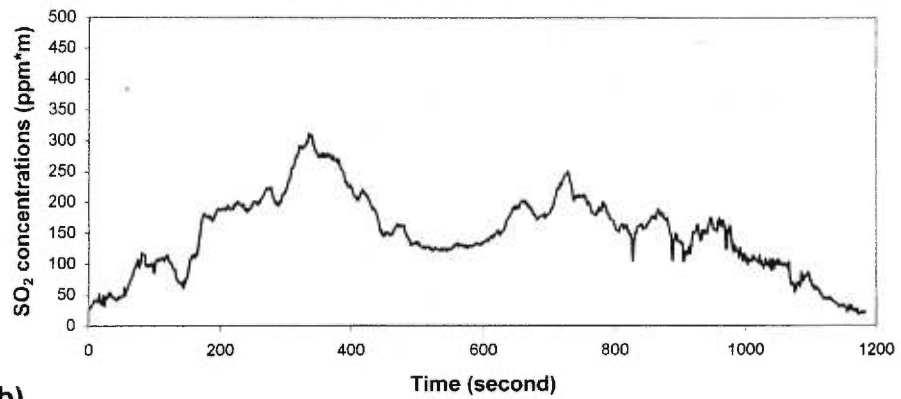
Examples of COSPEC SO₂ signals used for analysis. (a) Temporal series e10a taken during one hour at El Crucero (15 km). (b) Spatial series 27t taken at Ticuantepe (5.5 km). (c) Representation of the spatial and temporal series relative to the volcanic plume.

**SO₂ concentration of temporal series
98/03/10, El Crucero 15 km**

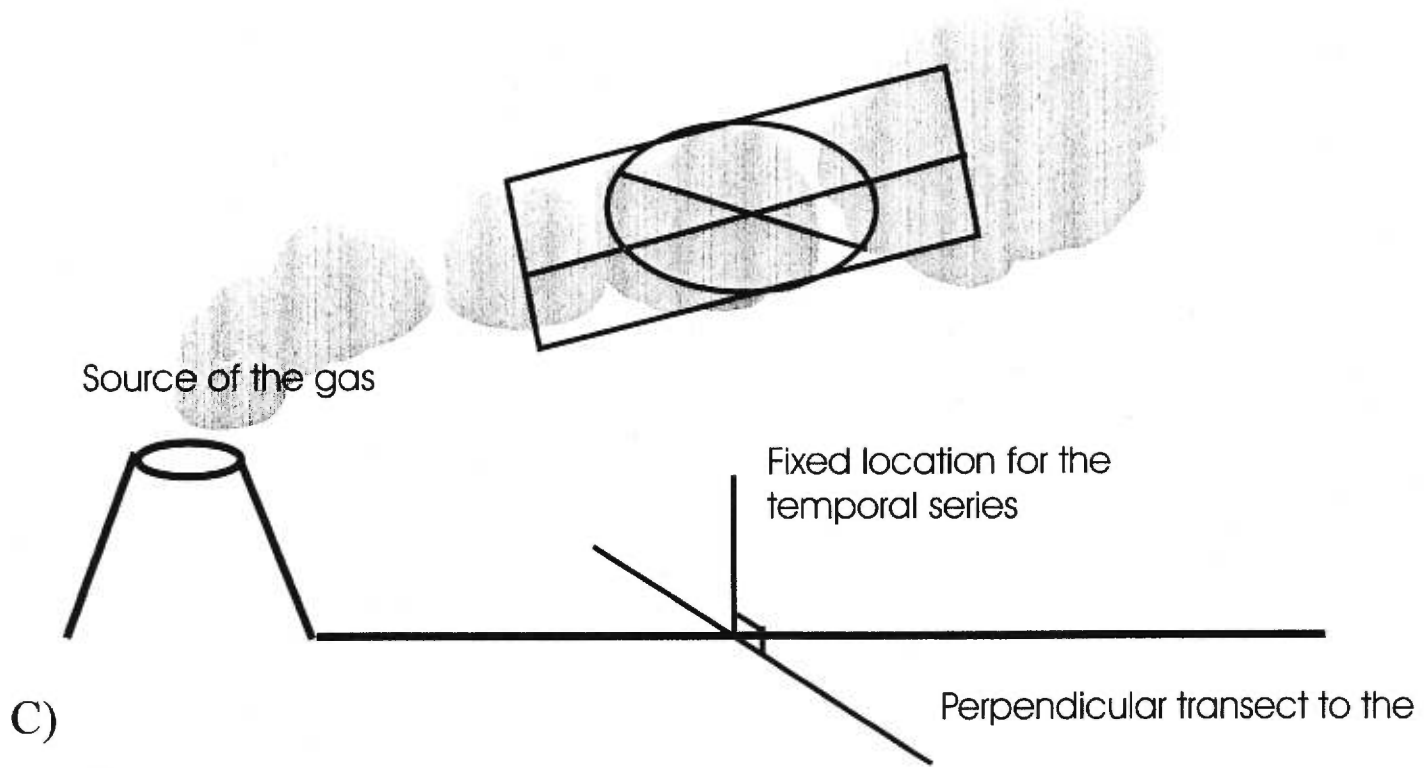


a)

**SO₂ concentration of spatial series,
98/03/17, El Crucero 15 km**



b)



the energy spectrum. Energy spectra of spatial and temporal series show scaling and do not differ greatly from one to another. Despite some variation in the individual β values, a common β value may fit all temporal and spatial series. We found that a $\beta=2.8 \pm 0.1$ nicely fits the statistical trends from 0.5 to 600 seconds (Figure 3.3 and 3.4). Most of the temporal series show a second trend for $f < \sim 75 \text{ seconds}^{-1}$ ($\beta \approx 0.2$) which is not the case for spatial series. However, this trend is not clearly defined, due in part to the limited number of points of on the low frequency range. This β value fits for spectral densities from series taken on different days. The same β value applies also to spectral densities from series taken at different distances (5 km, 15 km, and 30 km). Variations in SO_2 fluxes do not appear to affect the scaling exponent β . One temporal series acquired at 15 km from the crater out of the direct path of the volcanic plume which also shows scaling behaviour with a distinct $\beta=1.2$. We suggest that this particular signal is characteristic of the atmosphere where some very diluted SO_2 is still present.

The $\beta=2.8$ exponent which fits the statistical trend of the SO_2 spectral density analyses may be explained by the results obtained from other work (Schmitt et al, 1996; Chigirinskaya et al., 1994; Lovejoy et al., 1999): Empirical results of the atmosphere reveal scaling behaviour of the passive atmospheric scalars such as temperature or gas components with an average β exponent of 1.66 ± 0.5 (Gaonac'h et al., 1999). The vertical integration of the SO_2 signal in a stratified atmosphere leads to a β value of ≈ 2.8 . Hence the SO_2 measurements represent a vertical fractional integration of passive scalars, which exhibits statistical characteristics similar to other atmospheric passive scalar such as T, H_2O , and SF_6 (Schmitt et al.,

Figure 3.3

Power spectrum densities of SO₂ signals temporal series. A common $\beta=2.8 \pm 0.1$ fits all series. Note that a break at ~100 seconds is visible but not precisely defined.

Power spectrum densities,
temporal series

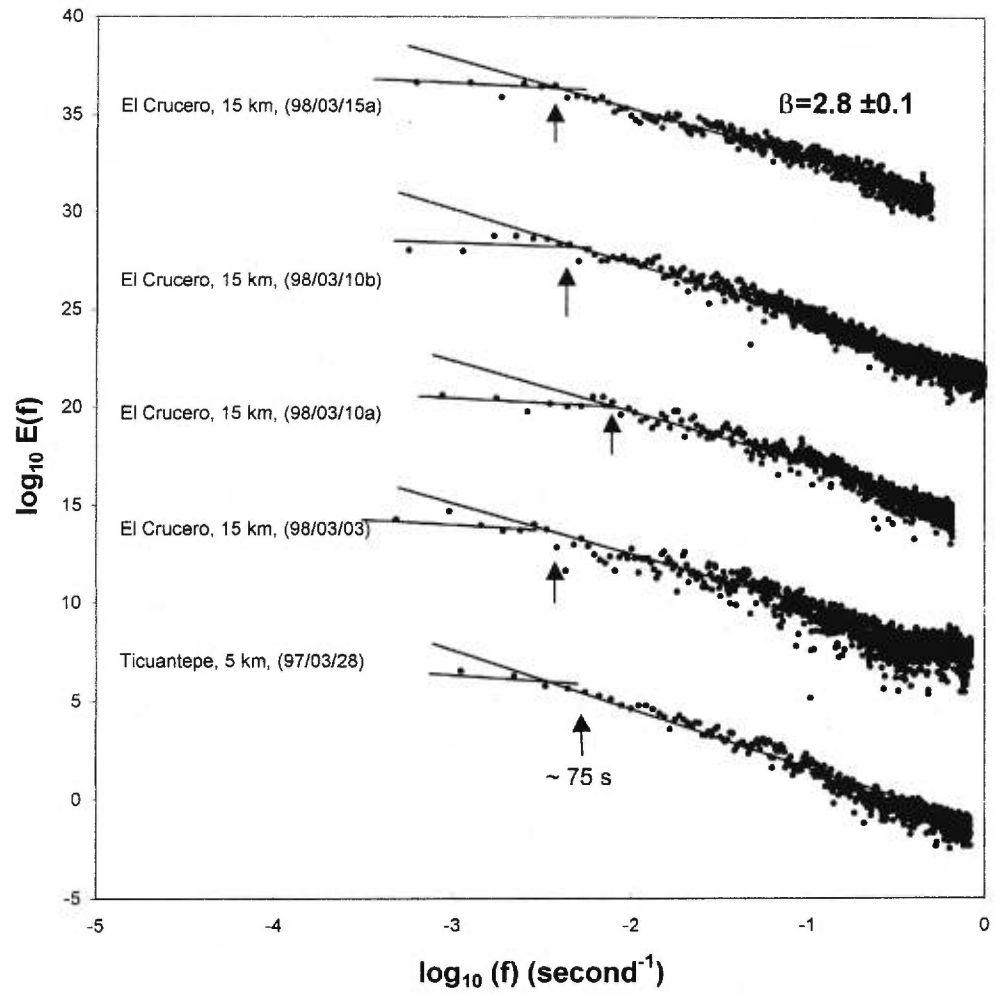
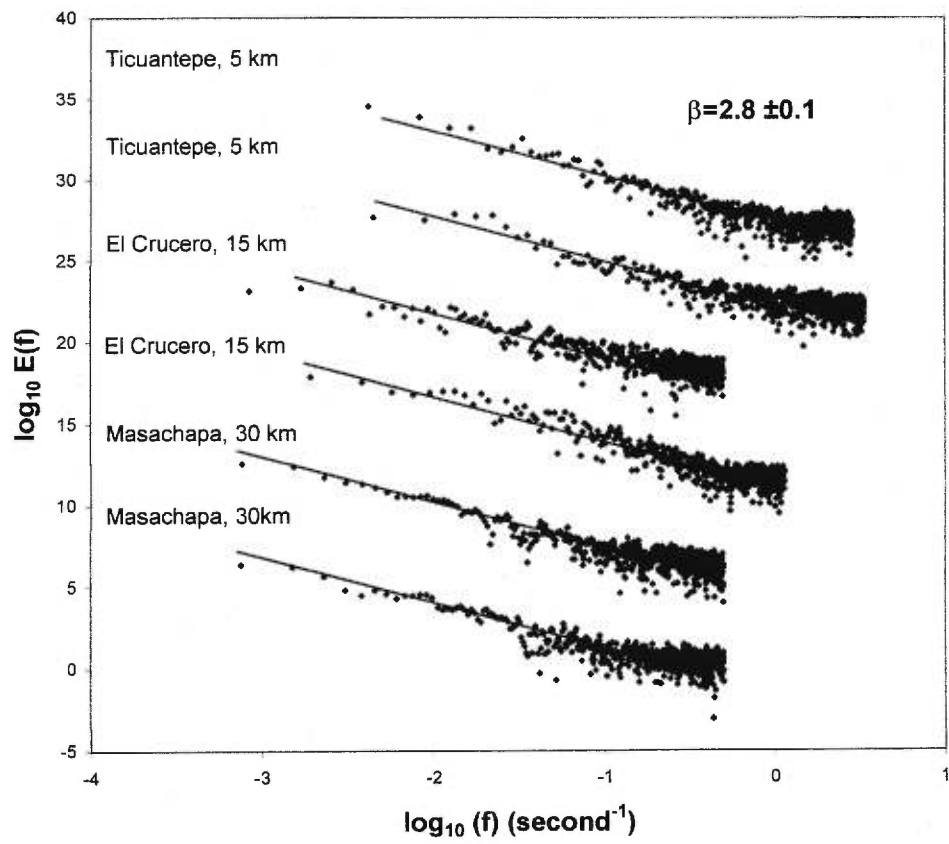


Figure 3.4

Power spectrum densities of SO₂ signals spatial series, Ticuantepe 27t and 28t at 5 km from the crater, El Crucero 27e and 17e2 at 15 km, and also Masachapa 18m1 and 18m2 at 30 km. A common $\beta=2.8 \pm 0.1$ value fits all series. Note also the flat trend at high frequencies. There is no visible break at low frequencies in spatial series.

Power spectrum densities,
spatial series



1996). The SO₂ plume, which may be represented by a succession of volcanic puffs, exhibits similar anisotropic behaviour as the turbulent atmosphere which transports it.

Multiscaling

Multiplicative cascades are proposed to explain high variability existing over a large range of scales (Schertzer and Lovejoy, 1996). Originally developed for studying turbulence, the multiplicative cascades model addresses, on a scale by scale basis, the variations of conservative fluxes in which a hierarchy of structures exist. This hierarchy implies that large structures modulate smaller structures in a non – linear manner. Scaling properties do not show exceptional behaviour at a second-order levels (spectral density β see above). It is thus necessary to generalize statistical moments to q^{th} orders and to analyse the variation of moments with the scale. Structure functions may be used for such temporal analysis:

$$\Delta S = S(t + \tau) - S(t) \quad (3.2)$$

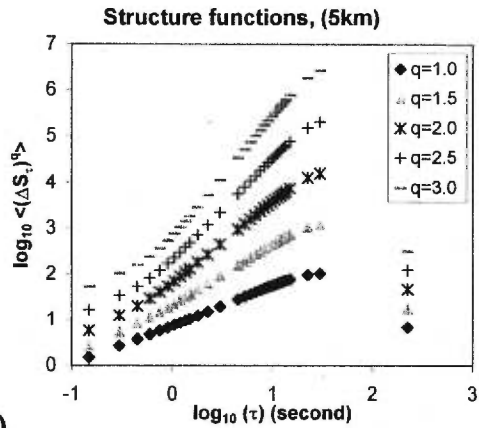
In conditions of multiscaling, structure functions of q^{th} moments will follow:

$$\langle (\Delta S_{\tau})^q \rangle \propto \langle \tau \rangle^{\zeta(q)} \quad (3.3)$$

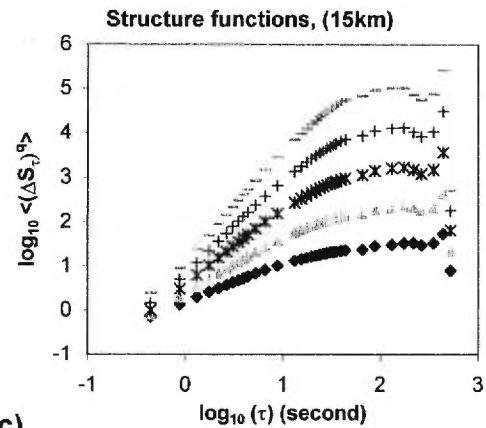
where τ is the temporal increment of the sample, S_{τ} is the SO₂ density over the interval, q is the order of the moment, and $\zeta(q)$ is the scale invariant structure function exponent. Each series was processed five times for different q values ($q = 1.0, 1.5, 2.0, 2.5, 3.0$), and a plot of $\log_{10}(\Delta S_{\tau})^q$ versus $\log_{10}(\tau)$ was generated. Statistical moments show a scaling trend versus the temporal-spatial increment of 1 to 300 seconds for the spatial series (Figure 3.5). Difficulties in obtaining a good linear

Figure 3.5

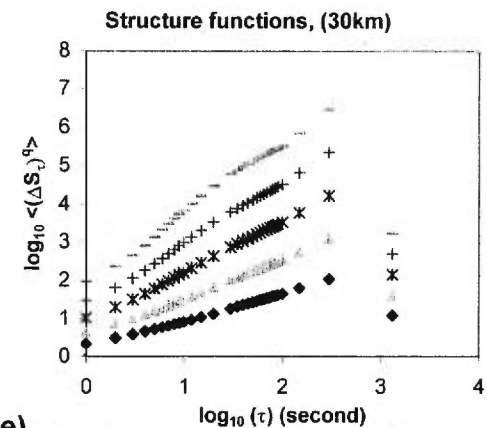
Structure functions of SO₂ signals spatial series. Ticuantepe (a) 27t and (b) 28t at 5 km from the crater, El Crucero (c) 27e and (d) 17e2 at 15 km, and also Masachapa (e) 18m1 and (f) 18m2 at 30 km.



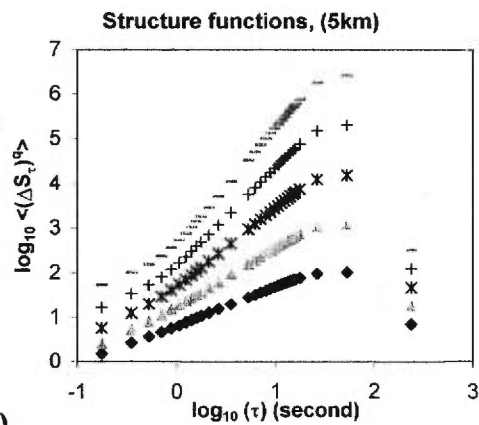
a)



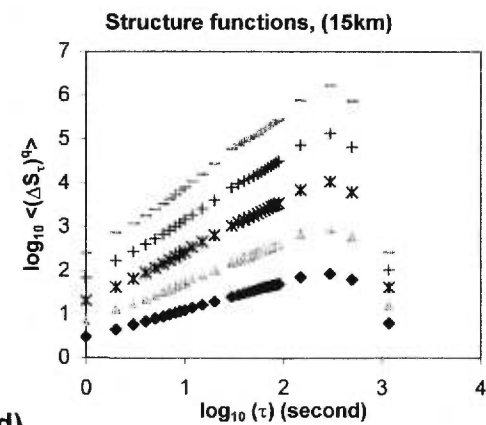
c)



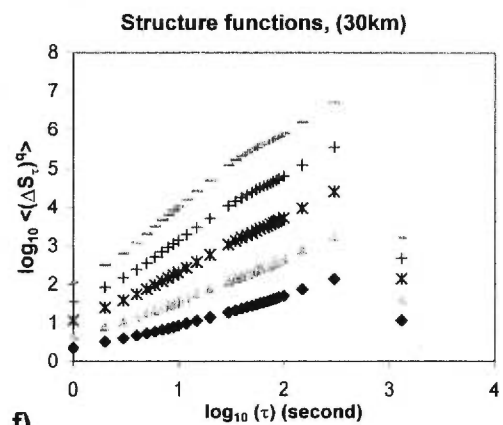
e)



b)



d)



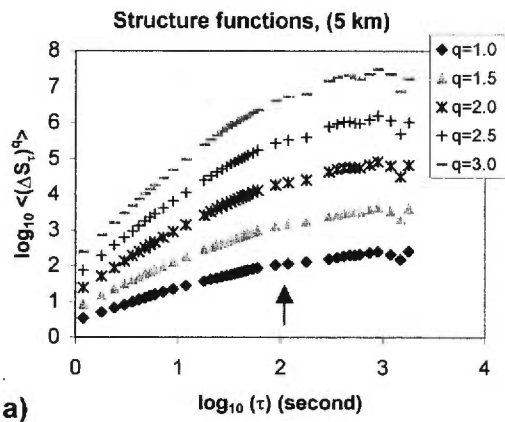
f)

trend at high resolutions also indicate that the data are of lower quality at the resolution of acquisition (≈ 1 s). However, the temporal series exhibits a second linear trend beginning at ± 75 seconds to the end of the series (Figure 3.6). The first moment, $\zeta(1) = H$ is the Hurst parameter. It represents the scaling of the average absolute fluctuations. If $H=0$, it indicates a conservative field which implies that the average absolute fluctuations of the process equal 0. If $H \neq 0$, it represents the degree of non-conservation of the process. The second moment is linked to the power spectrum scaling exponent by $\beta=1+\zeta(2)$. The average of the series is not conserved from one scale to another. The scaling exponent of the structure function $\zeta(q)$ shows a linear trend with q for simple scaling (monofractal) processes, or a non-linear and concave trend for multiscaling processes.

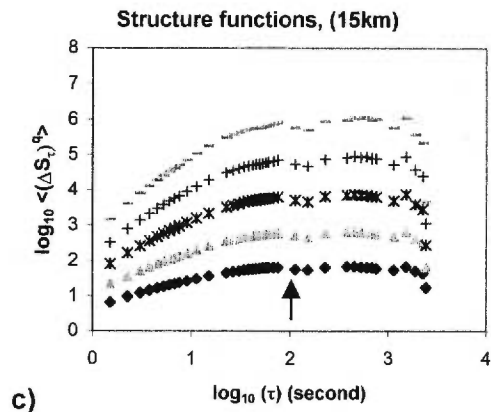
The statistical method of structure functions first confirms the scaling behaviour of the SO_2 signals for 0.5 to 75 seconds. Secondly, the multiscaling aspect is shown by the deviation of $\zeta(q)$ from the monofractal curve at higher moments of order. Thirdly, the structure functions present two different trends. It is proposed that the first trend be attributed to the atmospheric turbulence in which the volcanic SO_2 is entrained and transported. The measured gas follows the movement patterns of turbulence cells in the atmosphere. It is suggested that the long-term volcanic fluctuations may be more precisely characterized by acquiring longer temporal SO_2 signals. The break observed in the temporal series (~ 75 seconds) may be proportional to the size of the puff or the fragment of the dispersed volcanic plume. By using the characteristic time break (t) and the wind speed (v) measured at the time of measurements, an approximate puff length (l) for temporal series may be obtained.

Figure 3.6

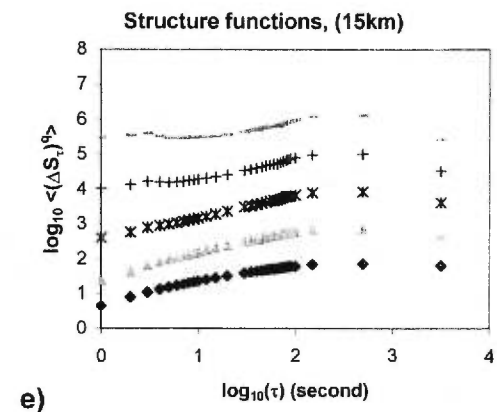
Structure functions of SO₂ signals temporal series (a) Ticuantepe 97/03/28, (b) El Crucero 98/03/03, (c) El Crucero 98/03/10a, (d) El Crucero 98/03/10b, (e) El Crucero 98/03/15a. Note the presence of a transitional zone, a break at ~75 seconds and a second trend at low frequencies.



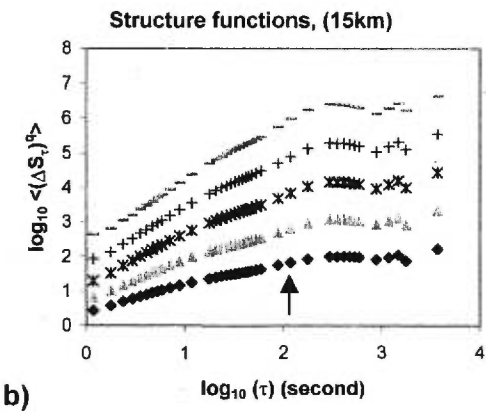
a)



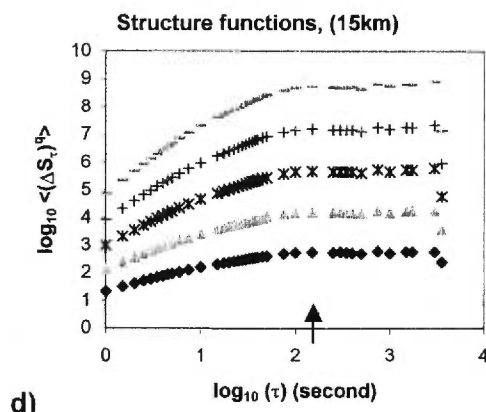
c)



e)



b)



d)

For the spatial series, the use of the lowest frequency and the vehicle speed (v) are preferred for calculation. In the temporal series, dimensions of about 510 to 970 meters may represent the large turbulence cells in which the SO_2 is entrained (Table 3.1). As for the dimensions obtained for the spatial series, their dimensions also represent puff widths or turbulence cells within the plume but the large dimensions obtained suggest that the plume itself may be considered a convective cell. Thus, it is logical to expect larger more homogenised, less concentrated puff at larger distances from the volcanic source. The second trend observed in the structure functions is probably to be associated with the long-term fluctuations of the degassing of the source, which correspond to the low-frequency fluctuations (St-Amand et al., 1998).

We then used the universal multifractality conditions to better evaluate the multiscaling properties of the SO_2 series. Universality is commonly accepted in physics/geophysics; a dynamic process starting at different initial conditions will not be seriously affected by perturbations and initial conditions and will always lead to similar final statistical results. Schertzer et al. (1995) argued that such a universality prevails in multifractality and that only a limited number of parameters among an infinity could be relevant to characterize the invariant function. Hence, two “universal” multifractal parameters, α and C_1 , may be defined to describe the $\zeta(q)$ function as:

$$\zeta(q) = qH - \frac{C_1}{\alpha - 1} (q^\alpha - q) \quad (3.4)$$

where α is the degree of multifractality, $\alpha=0$ being for the “ β -model” only in the case of monofractality, and a maximum of $\alpha=2$ for the lognormal model, and C_1 is the

Table 3.2 α , C_1 and H universal multifractal parameters.

Date	File names	Width ⁽¹⁾ (m)	α	av. α	C_1	av. C_1	$H^{(2)}$	av. H
<u>Temporal series</u>								
1 st regime								
97-03-28	t97	510	1.29	1.74	0.024	0.039	0.88	0.88
98-03-03	e03	710	1.80		0.086		0.85	
98-03-10	e10a	910	1.86		0.026		0.89	
	e10b	970	2.00		0.020		0.89	
2 nd regime								
28/03/97	t97		1.71		0.049		0.40	
<u>Spatial series</u>								
1 st regime								
Ticuantepe, 5 km								
97-03-27	27t	3100	1.88		0.018		0.89	0.88
97-03-28	28t	3100	1.50		0.023		0.88	
El Crucero, 15 km								
97-03-27	27e	8740	1.88		0.026		0.88	
16/03/94	17e2	17490	1.88		0.050		0.87	
Masachapa, 30 km								
98-03-18	18m1	18710	1.14		0.009		0.89	
	18m2	18710	1.10		0.009		0.89	

1-Maximum puff widths for temporal series (windspeed used), maximum puff width (or plume width) for spatial series (vehicle speed of $50 \pm 10 \text{ km h}^{-1}$ used).

2-Evaluated with $H = \zeta(1)$.

codimension of the singularity (intensity) contributing to the mean of the field. In order to evaluate the universal parameters, $\zeta(q)$ was estimated for $q = 0.01$ to 5.0 . It is also necessary to estimate $\zeta'(0)$ in a plot which is one of the major difficulties of this method. It is important to note that higher is the H parameter, the more difficult will be the estimation of the multiscaling component (the second part of equation 3.4). To estimate α and C_1 , the derivative of equation 3.4 is used. Thus:

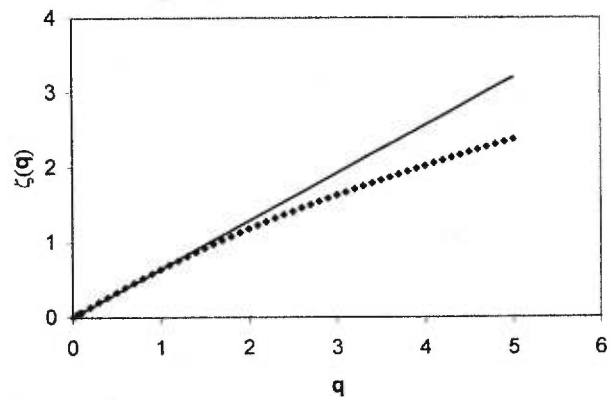
$$\log_{10}[q\zeta'(0) - \zeta(q)] = \log_{10}\left(\frac{C_1}{\alpha - 1}\right) + \alpha \log_{10}(q) \quad (3.5)$$

A plot of $\log_{10}[q\zeta'(0) - \zeta(q)]$ versus $\log_{10}(q)$ will provide the α and C_1 value. Multiscaling is confirmed by the $\zeta(q)$ - q graph where $\zeta(q)$ is the slope of the structure functions (Figure 3.7a, 3.8a,c, 3.9a). It is important to note that in the $\zeta(q)$ - q relation, the evaluated $\zeta(q)$ is best for $q \leq 3.0$, higher values of $\zeta(q)$ being dominated by the highest singularity (SO_2 values) in the series. This leads to an artificial linear trend in the $\zeta(q)$ - q plot for $q \geq 3$ (Figure 3.7a, 3.8c). In our case study, we observe a more or less accentuated deviation from the monofractal curve $\zeta(q) = qH$ for spatial and temporal series. The $\zeta(q)$ - q plot gives a slope of ≈ 2 , which is not surprising since the SO_2 signals are vertically integrated. Therefore, the multiscaling aspect of the $\zeta(q)$ function is masked by the monoscaling aspect of the signals, which comes from the high Hurst exponent ($H \approx 0.88$). The same effect was previously explained for the high $\beta = 2.8$ obtained for SO_2 signals, which for a non-integrated signal, a $\beta \approx 1.66$ would be expected for other atmospheric passive scalars (Gaonac'h et al., 1999). The second trend found in the temporal series structure functions also was investigated for the multiscaling properties, but only one series gave suitable results (Figure 3.8c).

Figure 3.7

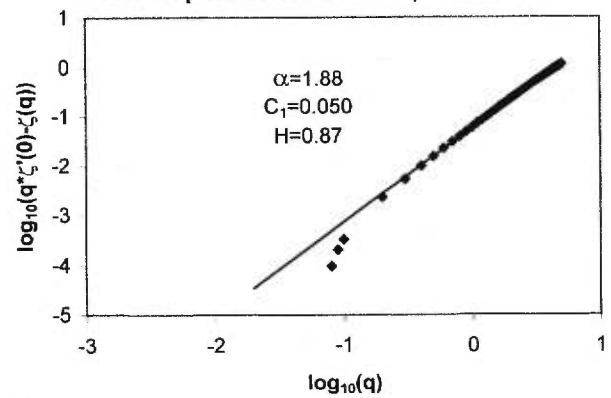
Example of multiscaling properties, El Crucero at 15 km, west from the vent, (98/03/17). (a) Scaling exponent structure function empirical curve (dots) and the monofractal curve qH (full line). Note the departure of the empirical curve from the monofractal curve which indicates multiscaling. Note also the linear trend for $q \geq 3.0$. (b) Universal parameters α and C_1 estimation.

Scaling exponent structure function



a)

Universal parameters α and C_1 estimation



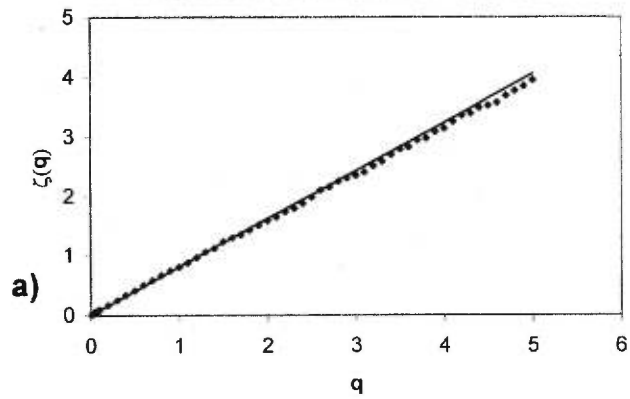
b)

Figure 3.8

Multiscaling properties of the temporal series t97, (97/03/28). First regime, (a) scaling exponent structure function. In this case, the empirical curve (dots) does not strongly deviate from the monofractal curve (full line). (b) Universal parameters α and C_1 estimation. Second regime, (c) scaling exponent structure function. Note the departure of the empirical curve from the monofractal curve which indicates multiscaling. Note also the linear trend for $q \geq 3.0$. (d) Universal parameters α and C_1 estimation.

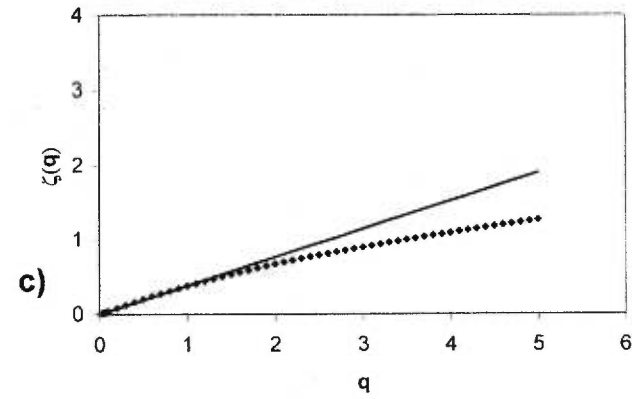
Firts regime

Scaling exponent structure function

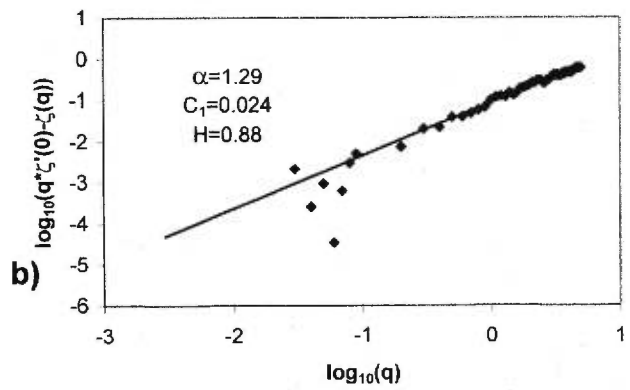


Second regime

Scaling exponent structure function



Universal parameters α and C_1 estimation



Universal parameters α and C_1 estimation

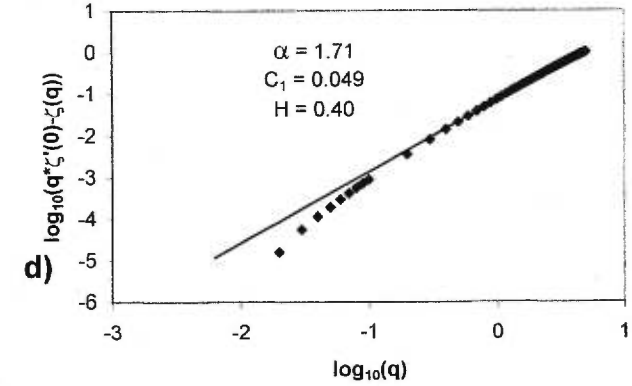
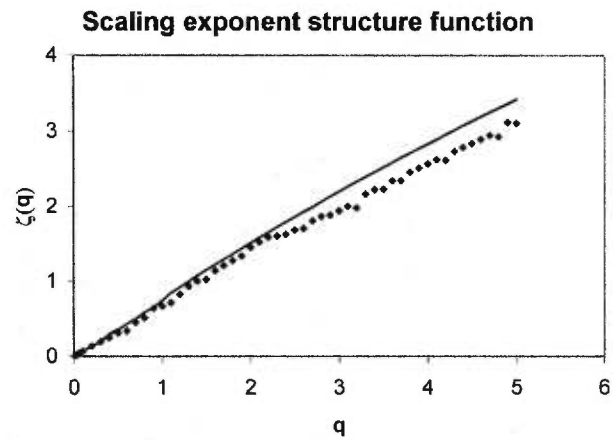
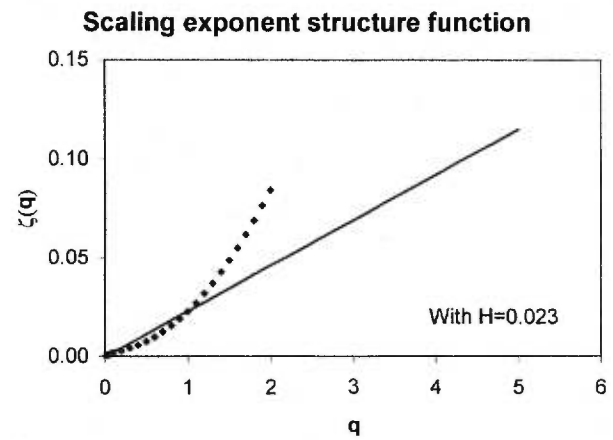


Figure 3.9

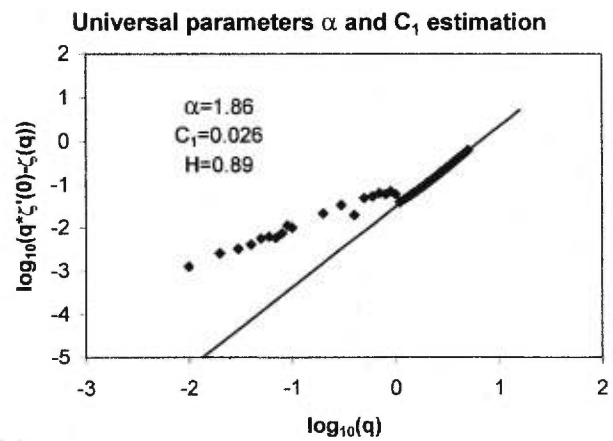
Multiscaling properties of the temporal series sp9810a, (98/03/10). First regime, (a) scaling exponent structure function. In this case, the empirical curve (dots) deviates from the monofractal curve (full line). (b) Universal parameters α and C_1 estimation. Second regime, (c) scaling exponent structure function. Note that the empirical curve (dots) is convex and above the monofractal curve (full line) which indicates that this series is not of sufficiently high quality.



a)



c)



b)

Others examinations of temporal series gave unrealistic results, with an empirical curve being convex and above the monofractal curve (Figure 3.9c). The universal parameters obtained for spatial series are quite similar at Ticuantepe (5km) and El Crucero (15 km) with $\alpha=1.88$, $C_1=0.029 \pm 0.012$ and $H \approx 0.88$ (Figure 3.7b). Two series taken at Masachapa (30km) show lower values of $\alpha= 1.12 \pm 0.02$ and $C_1=0.009$ while H is similar with $H=0.89$, which may be the result of a less concentrated and more homogenised plume at larger distances from the source. If we consider that our results are derived from the integration of SO_2 concentration in the atmosphere, α and C_1 will remain unaffected but H is expected to be twice that of the punctual H parameter of non-integrated passive scalars (Gaonac'h et al., 1999). Other research on atmospheric turbulence have obtained empirical universal parameters of $\alpha=1.66 \pm 0.06$, $C_1=0.08$ and $H=0.41 \pm 0.02$ (Schmitt et al., 1996; Gaonac'h et al., 1999). Thus, α , C_1 , and H values represent the turbulence of the SO_2 transported in the atmosphere in the volcanic plume.

For the temporal series, two “regimes” may be observed with a “transition zone” between them. For the first regime, α values are 1.89 ± 0.08 , with the exception of one series with $\alpha = 1.29$ (Figure 3.8b, 3.9b). C_1 values give 0.023 ± 0.002 , except for one value of 0.086. H values are around 0.88 (Table 3.2). Wind, solar luminosity, presence of clouds, and conditions of dispersion are all factors that may affect the individual statistical signature. The values presented above for the first regime are similar to those obtained for vertical turbulence in the atmosphere with $\alpha=1.88$, $C_1=0.039$, and $H=0.88$ (Gaonac'h et al., 1999). Of the three temporal series that were analysed for a second observable “regime”, only one was suitable for

analysis, (t97), with $\alpha=1.71$, $C_1=0.049$, and $H=0.40$ (Figure 3.8d). However, with only 30 minutes of measurements, the second regime may represent the transition zone between the atmospheric turbulence “regime” and a possible volcanic turbulence “regime”. In order to determine if there is a genuine regime attributed to the volcanic source, acquiring series longer than one hour is necessary.

The fact that temporal and spatial series have similar statistical values shows that there is isotropic scaling in the two horizontal directions of SO₂ behaviour in the atmosphere where mixing and dilution is taking place, and that stratification is mostly the result of vertical anisotropic scaling.

Conclusions

The multifractal approach is now an accepted method to characterize highly variable geophysical phenomena. SO₂ measurements, which are highly variable in space and time, have been studied statistically in the present paper. Series were acquired during the 1997-1998 surveys at Masaya volcano at fixed locations under the plume for approximately one hour. Perpendicular cross-sectional measurements also were performed across the volcanic plume. The high variability of SO₂ signals is problematic when estimates are made for long periods of time, such as annual fluxes, which may not reflect the real annual SO₂ contribution nor the true evolution of the degassing. Comparison of average values of undersampled degassing cycle may lead to unrealistic interpretations and modelling of the degassing of the volcano. However, by knowing invariance laws, it may be possible to extrapolate statistically the variations for unknown time scales. Comparison may be possible for other

periods of activity of a particular volcano and also at other volcanoes. Eventually, it will be possible to apply the same method for other sources of gas, volcanic or industrial.

Masaya is degassing more or less continuously, and the volcanic plume formed by puffs or clouds of gas is frequently visible. Thus, the scaling behaviour of SO₂ signals is present on a range of 0.5 to 75 seconds with an average $\beta=2.8 \pm 0.1$ for temporal and spatial series. It is suggested that the β value obtained is linked to the atmospheric turbulence. Considering that the SO₂ signals are integrated through the atmosphere, a higher β than non-integrated signals is expected for our signals. The scaling\multiscaling properties were also confirmed by the use of structure functions. The turbulence behaviour is expected to be shown in the form of a break in the slope associated with a transitional zone in the structure functions; the other trend at low frequencies is attributed to the volcanic source variability. The universal multifractal parameters $\alpha=1.74$, $C_1=0.039$, and $H=0.88$ obtained for SO₂ degassing are similar to the atmospheric turbulence signature. The other regime is characterized by $\alpha=1.71$, $C_1=0.049$, and $H=0.4$, which may be a signature of the volcanic source of SO₂.

Since this is the first time that multifractal methods have been applied to SO₂ signals, it is important to mention this approach needs to be refined. New data sets are necessary to verify and extend the methodology at Masaya and other volcanoes. In order to extract the most useful information, a good data set needs to be longer than 1 hour, 3 to 5 hours being possibly a better time interval.

References

- Andres, R. J., Rose, W. I., Kyle, P. R., deSilva, S., Francis, P., Gardeweg, M., and Moreno Roa, H., 1991.** Excessive sulfur dioxide emissions from Chilean volcanoes. *Journal of Volcanology and Geothermal Research*, 46:323-329.
- Arya, S. P., 1999.** *Air Pollution Meteorology and Dispersion*. Oxford University Press, N.Y., 310 pp.
- Beaulieu, A., 1999.** The nature and origin of spatial and temporal variations in the gravity fields of Telica and Masaya Volcanoes, Nicaragua. Unpublished M.Sc. thesis, Département de géologie, Université de Montréal, Montréal, Canada, 138 pp.
- Bluth, G. J. S., Casadevall, T. J., Schnetzler, C. C., Doiron, S. D., Walter, L. S., Krueger, A. J., and Badruddin, M., 1994.** Evaluation of sulfur dioxide emissions from explosive volcanism: the 1982-1983 eruptions of Galunggung, Java, Indonesia. *Journal of Volcanology and Geothermal Research*, 63: 243-256.
- Bluth, G. J. S., Rose, W. I., Sprod, I. E., and Krueger, A. J., 1997.** Stratospheric loading of sulfur from explosive volcanic eruptions. *Journal of Geology*, 105: 671-683.
- Cadle, R. D., Lazrus, A. L., Huebert, B. J., Heidt, L. E., Rose, W. I., Woods, D. C., Chuan, R. L., Stoiber, R. E. Smith, D. B., and Zielinski, R. A., 1979.** Atmospheric implications of studies of Central American volcanic eruption clouds. *Journal of Geophysical Research*, 84: 6 961-6 968.
- Casadevall, T., Rose, W., Gerlach, T., Greenland, L. P., Ewert, J., Wunderman, R., and Symonds, R., 1983.** Gas emission and the eruptions of Mount St. Helens through 1982. *Science* 221: 1 383-1 385.
- Casadevall, T. J., Doukas, M. P., Neal, C. A., McGimsey, R. G., and Gardner, C.A., 1994.** Emission rates of sulfur dioxide and carbon dioxide from Redoubt Volcano, Alaska during the 1989-1990 eruptions. *Journal of Volcanology and Geothermal Research*, 62: 519-530.
- Chigirinskaya, Y., Schertzer, D., and Lovejoy, S., 1994.** Multifractal analysis of tropical turbulence, part II: vertical scaling and generalized scale invariance non-linear process in geophysics, *I(2/3)* 115-123.

- Delmelle, P., Baxter, P., Beaulieu, A., Burton, M., Francis, P., Garcia-Alvarez, J., Horrocks, L., Navarro, M., Oppenheimer, C., Rothery, D., Rymer, H., St-Amand, K., Stix, J., Strauch, W., and Williams-Jones, G., (in press).** Origin and effects of Masaya volcano's continued unrest probed in Nicaragua. *Eos, Transaction, American Geophysical Union.*
- Eatough, D. J., Caka, F. M., and Farber, R. J., 1994.** The Conversion of SO₂ to sulfate in the atmosphere. *Israel Journal of Chemistry*, 34: 301-314.
- Gaonac'h, H., Lovejoy, S., Schertzer, D., St-Amand, K., and Stix, J., 1999.** Direct measurements of the elliptical dimension of atmospheric dynamics using remote sensing of volcanic SO₂ gas. *European Conference.*
- Gerlach, T. M., and McGee, K. A., 1994.** Total sulfur dioxide emissions and pre-eruption vapour saturated magma at Mount St. Helens, 1980-1988. *Geophysical Research Letters*, 21: 2 833-2 836.
- Johnson, N., and Parnell, R. A., 1986.** Composition, distribution and neutralization of "acid rain" derived from Masaya volcano, Nicaragua. *Tellus*, 38B: 106-117
- Kolmogorov, A. N., 1941.** Local structure of turbulence in an incompressible liquid for large Reynolds numbers, *Comptes rendus de l'Academie des Science de l'U.R.S.S.*, 30: 299-303.
- Laferrière, A. and Gaonac'h, H., 1999.** Multifractal properties of visible reflectance fields from basaltic volcanoes. *Journal of Geophysical Research*, 104: 5115-5126.
- Lavallée, D. S., Lovejoy, S., Schertzer, D., and Ladoy, P., 1993.** Nonlinear variability and Landscape topography: analysis and simulation. In: , Eds. L. De Cola, N. L., *Fractals in Geography*, 158-192.
- Menyailov, I, 1975.** Prediction of eruptions using changes in the compositions of volcanic gases. *Bulletin of Volcanology*, 26: 367-378.
- Oppenheimer, C., Francis, P., and Stix, J., 1998.** Depletion rates of sulfur dioxide in tropospheric volcanic plumes. *Geophysical Research Letters*, 25: 2 671-2 674.
- Realmuto, V.J., Sutton, A. J., and Elias, T., 1997.** Multispectral thermal infrared mapping of sulfur dioxide plumes: A case study from the East Rift Zone of Kilauea Volcano, Hawaii. *Journal of Geophysical Research*, 102: 15 057-15 072.
- Richardson, L. F., 1922.** *Weather Prediction by Numerical Process.* Cambridge University Press, republished by Dover (1965). Pp.

- Rymer, H., van Wyk de Vries, B., Stix, J., and Williams-Jones, G., 1998.** Pit crater structure and processes governing persistent activity at Masaya Volcano, Nicaragua. *Bulletin of Volcanology*, 59: 345-355.
- Schertzer, D., and Lovejoy, S., 1996.** Resolution dependence and multifractals in remote sensing and geographical information systems. McGill University, Lectures Notes. Unpublished, 390 pp.
- Schmitt, F., Lavallée, D., Lovejoy, S., Schertzer, D., and Hooge, C., 1992.** Estimations directes des indices de multifractals universels dans le champ de vent et de température. *Comptes rendus de l'Academie des sciences, Paris, Série II*, 314: 749-754.
- Schmitt, F., Lovejoy, S., and Schertzer, D., 1995.** Multifractal analysis of the Greenland Ice-core project climate data. *Geophysical Research Letters*, 22: 1689-1692.
- Schmitt, F., Schertzer, D., Lovejoy, S., and Brunet, G., 1996.** Multifractal temperature and flux of temperature variance in fully developed turbulence. *Europhysics Letters*, 35 (3): 195-200.
- Stoiber, R. E., and Jepsen, A., 1973.** Sulfur dioxide contributions to the atmosphere by volcanoes. *Science*, 182: 577-578.
- Stoiber, R. E., Malinconico, L. L., and Williams, S.N., 1983.** Use of correlation the spectrometer at volcanoes. In: Eds H. Tazieff and J.C. Sabroux, *New York, Forecasting volcanic events*. 425-444.
- Stoiber, R. E., Williams, S. N., and Huebert, B. J., 1986.** Sulphur and halogen gases at Masaya Caldera Complex, Nicaragua: Total Flux and Variations with Time. *Journal of Geophysical Research*, 91: 12 215-12 231.
- Stoiber, R. E., Williams, S. N., Huebert, B., 1987.** Annual contribution of sulfur dioxide to the atmosphere by volcanoes. *Journal of Volcanology and Geothermal Research*, 33: 1-8.
- Turcotte, D. L., 1997.** *Fractals and Chaos in Geology and Geophysics*, 2nd ed., Cambridge University Press, N.Y., 398 pp.
- Williams-Jones, G., 1997.** The Distribution and Origin of Radon, CO₂, and SO₂ Gases at Arenal Volcano, Costa-Rica. Unpublished M.Sc. thesis, Département de géologie, Université de Montréal, Montréal, Canada, 135 pp.

GENERAL CONCLUSIONS

Conclusions

The study of soil gases and the monitoring of the volcanic plume has allowed a better understanding of the behavior of Masaya volcano. A recently developed statistical approach used on SO₂ COSPEC signals has permitted us to observe the degassing from perspective. Important conclusions may be drawn from this work, which are the following:

1. The spatial distribution of CO₂ and radon concentrations demonstrate that degassing is structurally controlled. The degree of soil development along with the type of volcanic materials in the sub-surface also affect the concentrations.
2. CO₂ concentrations are higher at the fumarole field but are also relatively high in some areas where no fumarolic activity is recorded indicating accumulation of gas pockets in the sub-surface. Flux distributions along CO₂ profiles also suggest also an accumulation of gas beneath less permeable materials. This an indication of heterogeneity of the sub-surface.
3. Isotopic signatures of CO₂ indicate the contribution of two possible sources: magmatic gas from the magma chamber and CO₂ derived from decomposition of carbonate rocks. Fractionation effects during degassing also may have affected the isotopic composition of the gas.
4. Petrologic analyses of volcanic bombs ejected in November 1997 show low levels of sulfur in glass inclusions, indicating a highly degassed magma near the surface. It suggests that the source of SO₂ may come from a deeper, less degassed source.
5. SO₂ flux monitoring indicates a high daily variability of the source and also enlightened certain problems associated with SO₂ atmospheric transport and

dispersion, wind variability and the coastal wind system. Most notably, there is an accumulation of plume gas at low topographic level attributed in part by change in air mass densities.

6. Simultaneous SO₂ flux measurements at two different distances near the active vent indicate little removal of gas for the first 20 km of transport.
7. Comparison of coastal measurements (30 km) with measurements made at 15 km from the vent indicate unusually high SO₂ fluxes at the coast, which suggest a major influence of the coastal wind system (a sea breeze bifurcating or folding the volcanic plume on itself).
8. The multiscaling approach used on SO₂ COSPEC signals characterized the behaviour of the SO₂ transported in the atmosphere. All signals showed scale invariance on a wide range of scales with a scaling exponent of $\beta=2.8 \pm 0.1$.
9. A second trend in the statistical study may indicate that the degassing source may have a characteristic signature.

Recommendations for Future Work

In the process of this study, many techniques of sampling and measuring have been used, along with the new statistical method. Soil gases and temperature measurements are relatively easy to make and should be used more extensively inside and outside Masaya caldera, particularly along structural weaknesses in order to map zones which are prone to diffuse degassing. Isotopic measurements should be extended to other gases such as He and S in order to better characterize the source of the degassing.

The SO₂ degassing of Masaya volcano should be closely monitored continuously to better understand the degassing behavior, not only during the dry season but also the rainy period (when measurements are possible).

It would be a major asset to continue the monitoring of the volcano at different distances from the source. Along with the monitoring of wet and dry deposition in the path of the plume, this would enable us to understand the environmental impact of the plume.

Since volcanic processes are highly variable and sometimes "undersampled", it is important to continue the development of statistical approaches such as the ones presented here. New sampling of longer temporal series (COSPEC measurements made at a fixed location for at least two to three hours) should be made at Masaya volcano. Also, the scaling and multiscaling properties should be applied to COSPEC signals at other volcanoes and to other gases as well.

Appendix A

**CO₂ and radon concentrations, $\delta^{13}\text{C}$ and temperature measurements of the 1997
survey at Masaya volcano**

Table A-1 CO₂, δ¹³C, radon and temperature measurements at lines A, B, and C for the 1997 survey.

a) Line A, (97/03/11).

Station	Local time	Cumulative distance (m)	CO ₂ %	δ ¹³ C	Std dev.	Radon ¹ (pCiL ⁻¹)	Radon ² (pCiL ⁻¹)	T °C
A ₁	833	0	0.01			4.3 ±0.6	4.5 ±0.8	25.1
A ₂	840	5	0.01					25.5
A ₃	844	10	0.01					25.3
A ₄	848	15	0.01					27.1
A ₅	852	20	0.01					27.4
A ₆	856	25	0.01					30.4
A ₇	902	30	0.01					27.3
A ₈	907	35	0.32			0.8 ±0.3	2.1 ±0.3	27.5
A ₉	916	40	0.68	-1.5 ± 0.2				29.6
A ₁₀	920	45	1.23	-2.3 ± 0.1				38.1
A ₁₁	930	50	4.16	-1.9 ± 0.1				42.1
A ₁₂	942	55	3.01	-2.0 ± 0.1				44.6
A ₁₃	950	60	4.30	-1.6 ± 0.1		62.0 ±0.3	112.4 ±5.6	47.4
A ₁₄	959	65	9.24	-1.4 ± 0.1				57.7
A ₁₅	1008	70	11.9	-1.6 ± 0.1				66.9
A ₁₆	1015	75	13.4	-1.1 ± 0.1				63.2
A ₁₇	1025	80	18.8	-1.9 ± 0.1				76.5
A ₁₈	1035	85	15.8	-1.7 ± 0.1				72.5
A ₁₉	1045	90	14.2	-1.7 ± 0.1				77.0
A ₂₀	1052	95	6.9	-1.6 ± 0.1				60.0
A ₂₁	1101	100	1.86	-1.6 ± 0.1		63.9 ±3.3	65.9 ±3.3	44.5
A ₂₂	1113	105	-0.05					24.9
A ₂₃	1120	115	-0.05			1.9 ±0.5	9.0 ±0.6	23.6

1-Measured for the period 97/03/11-97/03/17.

2-Measured for the period 97/03/17-97/03/25.

Table A-1 Continued, b) line B (97/03/15).

Station	Local time	Cumulative distance (m)	CO ₂ (%)	$\delta^{13}\text{C}$ (%)	Std dev.	Radon ¹ (pCiL ⁻¹)	T °C
B ₁	0946	0	0.01			10.8 ±0.8	33.0
B ₂	0952	12	0.02				29.7
B ₃	1002	24	0.62	-2.7	± 0.1		38.2
B ₄	1004	33	1.79	-1.8	± 0.1		61.7
B ₅	1010	44	1.31	-1.7	± 0.1		36.5
B ₆	1018	59	0.33				38.1
B ₇	1024	69	0.17				37.6
B _{7a}	1146	74	2.76			103.2 ±5.2	61.6
B ₈	1030	79	1.93	-1.7	± 0.1		58.8
B _{8a}	1148	84	1.63				57.1
B ₉	1036	89	1.63	-1.7	± 0.1		56.3
B _{9a}	1151	94	1.61				55.1
B ₁₀	1042	99	1.75	-1.7	± 0.1		52.1
B _{10a}	1153	104	1.74				52.8
B ₁₁	1047	109	1.79	-1.7	± 0.1		52.4
B _{11a}	1155	114	1.35			136.4 ±6.9	48.9
B ₁₂	1052	119	1.63	-1.7	± 0.1		50.2
B _{12a}	1157	124	1.33				48.3
B ₁₃	1100	129	1.24	-1.8	± 0.1		45.1
B _{13a}	1201	134	1.27				47.4
B ₁₄	1006	139	0.90	-2.0	± 0.2	40.1 ±2.1	42.1
B ₁₅	1116	149	0.01				28.2
B ₁₆	1123	159	0.02				25.2
B ₁₇	1128	169	-0.03				25.6
B ₁₈	1131	179	0.01			7.7 ±0.6	25.3

1-Measured for the period 97/03/15-97/03/22.

Table A-1 Continued, c) line C (97/03/09).

Station	Cumulative distance (m)	CO ₂ (%)	δ ¹³ C (%)	Std dev.	Radon ¹ (pCiL ⁻¹)	Radon ² (pCiL ⁻¹)	T °C
C ₁	0	-0.03			28.8 ±1.6	15.6 ±0.9	29.0
C ₂	5	-0.05					35.2
C ₃	10	-0.05					38.2
C ₄	15	-0.01					40.2
C ₅	20	0.04					43.0
C ₆	25	0.19					44.2
C ₇	30	0.9	-2.9 ± 0.1				48.5
C ₈	37	2.25	-2.3 ± 0.1		71.8 ±3.6	67.8 ±3.4	51.2
C ₉	42	2.53	-2.2 ± 0.1				50.2
C ₁₀	47	2.21	-2.2 ± 0.1				47.1
C ₁₁	52	2.14	-2.2 ± 0.1				47.0
C ₁₂	57	2.1	-2.2 ± 0.1				47.1
C ₁₃	62	1.94	-2.2 ± 0.1		62.6 ±3.2	78.7 ±3.9	45.5
C ₁₄	67	0.81	-2.9 ± 0.1				40.6
C ₁₅	72	0.53	-2.1 ± 0.1				33.8
C ₁₆	77	0.3					27.9
C ₁₇	82	0.5	-4.4 ± 0.1				27.4
C ₁₈	87	1.12	-1.9 ± 0.1				29.6
C ₁₉	92	2.16	-1.9 ± 0.1		72.1 ±3.7	70.9 ±3.5	39.0
C ₂₀	97	1.19	-3.0 ± 0.1				41.5
C ₂₁	102	-0.05					36.2
C ₂₂	107	-0.07					29.7
C ₂₃	112	-0.16					24.5
C ₂₄	117	-0.16					23.6
C ₂₅	122	-0.16			1.6 ±0.4	23.2 ±1.2	23.6

1-Measured for the period 97/03/09-97/03/16.

2-Measured for the period 97/03/16-97/03/25.

Table A-1 Continued, d) Nindirí crater, line N (24/03/97).

Station	Local time	Cumulative distance (m)	CO ₂ (%)	$\delta^{13}\text{C}$ (%)	Std dev.	Radon ¹ (pCiL ⁻¹)	T °C
N ₁	1039	0	0.10				28.0
N ₂	1055	5	0.10				31.6
N ₃	1106	10	0.18			4.6 ±0.3	31.1
N ₄	1111	15	0.30				30.2
N ₅	1117	20	0.34				31.5
N ₆	1124	25	0.86	-1.0 ± 0.1		8.5 ±0.7	31.5
N ₇	1137	32	0.26				31.7
N ₈	1145	35	0.98	-1.3 ± 0.1			31.1
N ₉	1152	40	1.23	-1.1 ± 0.1			32.5
N ₁₀	1201	45	1.61	-1.0 ± 0.1			32.6
N ₁₁	1215	50	2.01	-1.0 ± 0.1		8.9 ±0.4	32.4
N _{11a}	1326	53	4.12	-1.2 ± 0.1			
N _{11b}	1331	56	3.32	-1.5 ± 0.1			
N ₁₂	1315	59	4.11	-1.5 ± 0.1		25.9 ±1.3	32.4

1- Measured for the period 97/03/24-97/03/31.

Appendix B

**CO₂ and radon concentrations, $\delta^{13}\text{C}$ and temperature measurements of the 1998
survey at Masaya volcano**

Table B-1 CO₂, δ¹³C, radon and temperature measurements for lines A, N, Comalito extension, Museo, and Arenal for 1998.

a) Line A, (98/02/23).

Station	Local time	Cumulative distance(m)	CO ₂ (%)	δ ¹³ C (%)	Std dev.	Radon ¹ (pCiL ⁻¹)	T °C
A ₁	1235	0	0.00			1.5 ±0.4	27
A ₃	1245	10	0.00				29
A ₅	1257	20	0.00				31
A ₇	1310	30	0.00				27
A ₈	1336	35	0.00			2.3 ±0.5	29
A ₉	1350	40	0.20				29
A ₁₀	1403	45	0.07				39
A ₁₁	1421	50	0.80	-1.7	0.1		42
A ₁₂	1430	55	2.70	-2.1	0.1		45
A ₁₃	1445	60	0.80	-2.0	0.1	75.9 ±3.9	47
A ₁₄	1454	65	0.70	-2.1	0.1		55
A ₁₅	1507	70	7.6	-1.9	0.0		70
A ₁₆	1537	75	31.1	-2.3	0.3	300.5 ±15.0	73
A ₁₇	1543	80	12.1	-3.3	0.1		67
A ₁₈	1556	85	15.3	-1.8	0.1		71
A ₁₉	1605	90	14.5	-2.0	0.2		64
A ₂₀	1612	95	0.02	-2.4	0.1		56
A ₂₁	1623	100	0.30				33
A ₂₂	1630	105	0.01				34
A ₂₃	1636	115	0.00			3.3 ±0.2	28

1-Measured for the period 98/02/23-98/03/01.

Table B-1 Continued.

b) Nindirí crater, line N (98/03/23).

Station	Cumulative distance (m)	CO ₂ (%)	$\delta^{13}\text{C}$ (%)	Std dev.
N ₁	0	0.28		
N ₂	10	0.45		
N ₃	20	0.70		
N ₄	30	0.80	-1.9	0.5
N ₅	40	1.15	-1.8	0.2
N ₆	50	6.09	-1.8	0.1
N ₇	60	5.84	-1.5	0.1

Table B-1 Continued. extension Comalito 1998 (98/03/23).

c) Extension Comalito 1998 (98/03/23).

Station	Cumulative distance (m)	CO ₂ (%)	$\delta^{13}\text{C}$ (%)	Std dev.	T °C
Com ₁	10	1.79	-2.5	0.0	
Com ₂	20	1.33	-3.2	0.1	
Com ₅	30	6.25	-1.6	0.1	74.6
Com _{6a}	40	0.96	-2.8	0.2	29.3
Com _{6b}	40	0.96	-2.8	0.1	29.3
Com _{7a}	50	0.55	-2.8	0.0	37.8
Com _{7b}	50	0.55	-2.8	0.3	37.8

Table B-1 Continued, line Museo (98/03/23).

d) Line Museo (98/03/23).

Station	Cumulative distance (m)	CO ₂ (%)	$\delta^{13}\text{C}$ (%)	Std dev.	T °C
M _{2a}	15	0.14			33.2
M _{2b}	15	0.14			33.2
M _{3a}	30	0.36			43.6
M _{3b}	30	0.36			43.6
M _{4a}	45	6.38	-2.0	± 0.2	52.8
M _{4b}	45	6.38	-1.8	± 0.1	52.8
M _{5a}	60	6.10	-2.0	± 0.1	41.8
M _{5b}	60	6.10	-2.1	± 0.1	41.8
M _{5c}	60	6.10	-2.1	± 0.1	41.8
M _{6a}	75	7.60	-2.3	± 0.1	47.2
M _{6b}	75	7.60	-2.3	± 0.1	47.2
M _{7a}	90	7.98	-2.1	± 0.1	41.6
M _{7b}	90	7.98	-2.1	± 0.1	41.6

Table B-1 Continued.

e) Line Arenal (98/03/22).

Station	Cumulative distance (m)	CO ₂ %	$\delta^{13}\text{C}$ (%)	Std dev.
Arenal _{1a}	0	0.12		
Arenal _{1b}	0	0.14		
Arenal _{2a}	15	0.47	-6.6	± 0.1
Arenal _{2b}	15	0.47		
Arenal _{3a}	30	0.20		
Arenal _{3b}	30	0.20		
Arenal _{4a}	45	0.11		
Arenal _{4b}	45	0.11		
Arenal _{5a}	60	0.20		
Arenal _{5b}	60	0.20		
Arenal _{6a}	75	0.08		
Arenal _{6b}	75	0.08		
Arenal _{7a}	90	0.06		
Arenal _{7b}	90	0.06		
Arenal _{8a}	105	0.09		
Arenal _{8b}	105	0.09		
Arenal _{9a}	120	0.13		
Arenal _{9b}	120	0.13		
Arenal _{10a}	135	0.07		
Arenal _{10b}	135	0.07		

Appendix C

**CO₂ fluxes measurements (raw data) of the 1997 survey at Masaya volcano
(Table C-1 line A, Table C-2 line B, and Table C-3 line C), and
corresponding graphs.**

Table C-1 Raw data of fluxes measurements conducted on line A.

Station A ₁₅	Time (min.)	CO ₂ (% vol.)	T (°C)	Time (min.)	CO ₂ (% vol.)	T (°C)	Station A ₁₅	Time (min.)	CO ₂ (% vol.)	T (°C)	Time (min.)	CO ₂ (% vol.)	T (°C)
A ₁₄													
97/03/17	0.0	0.00	32.2	14.5	6.51	39.1	97/03/17	0.0	0.00	33.6	14.5	7.03	36.8
	0.5	0.01	32.1	15.0	6.62	39.1	#1	0.5	0.01	33.6	15.0	7.09	36.6
	1.0	0.32	33.2	15.5	6.72	39.2		1.0	0.52	35.0	15.5	7.17	36.6
CO ₂ at 20 cm	1.5	0.76	35.0	16.0	6.82	39.3	CO ₂ at 75 cm	1.5	1.12	35.5	16.0	7.21	36.5
17.8 % vol.	2.0	1.10	35.7	16.5	6.94	39.3	3.13 % vol.	2.0	1.67	35.9	16.5	7.13	36.3
CO ₂ at 70 cm	2.5	1.55	35.9	17.0	7.06	39.2	CO ₂ at 55 cm	2.5	1.95	36.3	17.0	7.13	36.2
17.8 % vol.	3.0	1.82	36.2	17.5	7.10	38.9	19.8 % vol.	3.0	2.39	36.8	17.5	7.17	36.3
Pressure	3.5	2.12	36.7	18.0	7.18	38.8	Pressure	3.5	2.70	37.5	18.0	7.21	36.4
982 mbar	4.0	2.50	37.2	18.5	7.22	38.6	982 mbar	4.0	3.05	38.1			
	4.5	2.79	37.5	19.0	7.28	38.4		4.5	3.37	38.2			
	5.0	3.07	37.5	19.5	7.40	38.1		5.0	3.69	38.2			
	5.5	3.35	37.5	20.0	7.46	38.0		5.5	4.00	38.2			
	6.0	3.57	37.4	20.5	7.51	37.9		6.0	4.30	38.1			
	6.5	3.80	37.4	21.0	7.54	37.8		6.5	4.60	38.1			
	7.0	4.05	37.4	21.5	7.65	37.6		7.0	4.84	38.0			
	7.5	4.24	37.5	22.0	7.73	37.6		7.5	5.07	37.9			
	8.0	4.46	37.7	22.5	7.80	37.6		8.0	5.31	37.8			
	8.5	4.63	37.7	23.0	7.83	37.5		8.5	5.51	37.7			
	9.0	4.80	38.0	23.5	8.00	37.3		9.0	5.70	37.7			
	9.5	5.01	38.2	24.0	8.05	37.6		9.5	5.86	37.7			
	10.0	5.16	38.2					10.0	6.02	37.8			
	10.5	5.32	38.2					10.5	6.14	37.8			
	11.0	5.52	38.1					11.0	6.26	37.8			
	11.5	5.64	38.3					11.5	6.35	37.7			
	12.0	5.80	38.7					12.0	6.45				
	12.5	5.95	38.8					12.5	6.53				
	13.0	6.10	38.9					13.0	6.69	37.2			
	13.5	6.21	39.0					13.5	6.85	37.2			
	14.0	6.35	39.1					14.0	6.95	36.2			

Table C-1 Continued.

Station #	Time (min.)	CO ₂ (% vol.)	T (°C)	Time (min.)	CO ₂ (% vol.)	T (°C)	Station A ₂₁	Time (min.)	CO ₂ (% vol.)	T (°C)	Time (min.)	CO ₂ (% vol.)	T (°C)
97/03/14	0	0.0	41.2	14.5	3.00	40.3	97/03/17	0.0	0.00	39.1	14.5	3.00	40.3
#2	2	2.0	41.2	15.0	2.90	40.1		0.5	0.01	39.1	15.0	2.90	40.1
	4	4.7	42.8	15.5	3.13	39.7	CO ₂ at 75 cm	1.0	0.01	40.1	15.5	3.13	39.7
Directly on fumaroles	6	7.0	43.1	16.0	3.21	39.5	2.61 % vol.	1.5	0.13	40.2	16.0	3.21	39.5
Pressure	8	9.3	43.6	16.5	3.25	39.4	CO ₂ at 28 cm	2.0	0.33	40.1	16.5	3.25	39.4
982 mbar	10	10.4	43.3	17.0	3.29	39.4	6.46 % vol.	2.5	0.48	40.1	17.0	3.29	39.4
	12	11.6	43.5	17.5	3.33	39.3	Pressure	3.0	0.60	40.3	17.5	3.33	39.3
	14	12.8	43.3	18.0	3.35	39.2	982 mbar	3.5	0.70	40.2	18.0	3.35	39.2
	16	14.8	43.4	18.5	2.93	38.9		4.0	0.96	40.1	18.5	2.93	38.9
	18	15.1	43.8	19.0	3.49	39.0		4.5	1.08	40.0	19.0	3.49	39.0
	20	16.3	44.3	19.5	3.53	39.3		5.0	1.18	40.0	19.5	3.53	39.3
	22	17.1	44.5	20.0	3.53	39.4		5.5	1.27	40.2	20.0	3.53	39.4
	24	17.9	44.9	20.5	3.57	39.3		6.0	1.39	40.4	20.5	3.57	39.3
	26	18.7	44.7	21.0	3.61	39.1		6.5	1.55	40.4	21.0	3.61	39.1
	28	18.7	44.5	21.5	3.65	39.1		7.0	1.67	40.4	21.5	3.65	39.1
	30	19.4	44	22.0	3.67	39.4		7.5	1.81	40.3	22.0	3.67	39.4
	32	19.5	43.6					8.0	1.94	40.3			
	34	19.9	43.6					8.5	2.06	40.5			
	36	20.3	43.5					9.0	2.14	40.7			
	38	20.6	44.1					9.5	2.26	41.0			
	40	20.7	43.8					10.0	2.28	41.2			
	42	21.0	44.2					10.5	2.42	41.2			
	44	21.1	44					11.0	2.50	41.2			
	46	21.1	43.7					11.5	2.57	41.1			
	48	21.1	43.6					12.0	2.65	41.1			
								12.5	2.73	41.1			
								13.0	2.85	41.1			
								13.5	2.89	41.0			
								14.0	2.97	40.5			

Table C-1 Continued.

Station A ₁₅ A ₁₆	Time (min.)	CO ₂ (% vol.)	T (°C)	Station A ₁₅ A ₁₆	Time (min.)	CO ₂ (% vol.)	T (°C)	Station A ₁₅ A ₁₆	Time (min.)	CO ₂ (% vol.)	T (°C)
97/03/14	0	0.00	39.3	97/03/14	0	0.0	41.2	97/03/14	0	0.00	38.2
#1	2	0.00	39.3	#2	2	2.0	41.2	#3	2	2.27	38.2
	4	0.05	40.2		4	4.7	42.8		4	3.88	38.7
Directly on	6	0.11	40.9	Directly on	6	7.0	43.1	Directly on	6	4.56	38.1
fumaroles	8	0.17	41.0	fumaroles	8	9.3	43.6	fumaroles	8	5.10	38.2
	10	0.21	40.5		10	10.4	43.3		10	5.38	38.1
	12	0.25	40.2		12	11.6	43.5		12	5.55	38.0
Pressure	14	0.31	40.3	Pressure	14	12.8	43.3	Pressure	14	5.55	37.6
982 mbar	16	0.37	40.7	982 mbar	16	14.3	43.4	982 mbar	16	5.74	37.2
	18	0.45	40.9		18	15.1	43.8		18	5.62	37.3
	20	0.48	40.7		20	16.3	44.3		20	5.78	37.8
	22	0.52	40.4		22	17.1	44.5		22	5.78	37.1
	24	0.57	40.6		24	17.9	44.9				
	26	0.60	40.7		26	18.7	44.7				
	28	0.65	40.2		28	18.7	44.5				
	30	0.68	39.9		30	19.4	44				
	32	0.68	39.8		32	19.5	43.6				
	34	0.72	39.5		34	19.9	43.6				
	36	0.76	39.3		36	20.3	43.5				
	38	0.76	39.3		38	20.6	44.1				
	40	0.80	38.4		40	20.7	43.8				
	42	0.80	37.9		42	21.0	44.2				
	44	0.82	37.9		44	21.1	44				
	46	0.80	37.9		46	21.1	43.7				
					48	21.1	43.6				

Table C-2 Raw data of fluxes measurements conducted on line B.

Station B ₈	Time (min.)	CO ₂ (% vol.)	T (°C)	Station B ₈	Time (min.)	CO ₂ (% vol.)	T (°C)	Station B ₈	Time (min.)	CO ₂ (% vol.)	T (°C)	Station B _{11a}	Time (min.)	CO ₂ (% vol.)	T (°C)
#1	0	0.00	30.2	#2	0.0	0.00	39.5	#3	0.0	0.00	Out of order	#1	0.0	0.00	Out of order
97/03/15	1	0.55	41.6	97/03/15	0.5	0.17	39.7	97/03/15	0.5	0.09	Out of order	97/03/15	0.5	0.01	0.01
1245 hrs	2	1.16	42.8	1200 hrs	1.0	0.46	42.8	1315 hrs	1.0	0.29	CO ₂ at 75 cm	1345 hrs	1.0	0.01	0.01
CO ₂ at 75 cm	3	1.40	42.8		1.5	0.70	44.6		1.5	0.40	1.61%	CO ₂ at 75 cm	1.5	0.09	0.09
1.75 % vol.	4	1.55	42.9		2.0	0.92	44.0		2.0	0.54	Pressure	Pressure	2.0	0.17	0.17
Pressure	5	1.67	43.3	Pressure	2.5	1.10	43.0	Pressure	2.5	0.72	964 mbar	964 mbar	2.5	0.28	0.28
964 mbar	6	1.71	43.6	964 mbar	3.0	1.20	43.6	964 mbar	3.0	0.76			3.0	0.40	0.40
	7	1.75	43.9		3.5	1.37	43.6		3.5	0.84			3.5	0.52	0.52
	8	1.75	44.6		4.0	1.47	43.4		4.0	0.88			4.0	0.64	0.64
	9	1.79	44.3		4.5	1.53	43.7		4.5	0.94			4.5	0.72	0.72
					5.0	1.59	43.0		5.0	0.98			5.0	0.83	0.83
					5.5	1.61			5.5	1.04			5.5	0.90	0.90
					6.0	1.63			6.0	1.06			6.0	0.96	0.96
					6.5	1.65			6.5	1.10			6.5	1.02	1.02
									7.0	1.12			7.0	1.08	1.08
									7.5	1.16			7.5	1.12	1.12
									8.0	1.19			8.0	1.16	1.16
									8.5	1.22			8.5	1.20	1.20
									9.0	1.18			9.0	1.23	1.23
									9.5	1.22			9.5	1.25	1.25
									10.0	1.18			10.0	1.27	1.27
									10.5	1.20			10.5	1.31	1.31
									11.0	1.22			11.0	1.35	1.35
									11.5				11.5	1.37	1.37
									12.0				12.0	1.39	1.39
									12.5				12.5	1.41	1.41
									13.0				13.0	1.43	1.43
									13.5				13.5	1.46	1.46
									14.0				14.0	1.47	1.47

Table C-2 Continued.

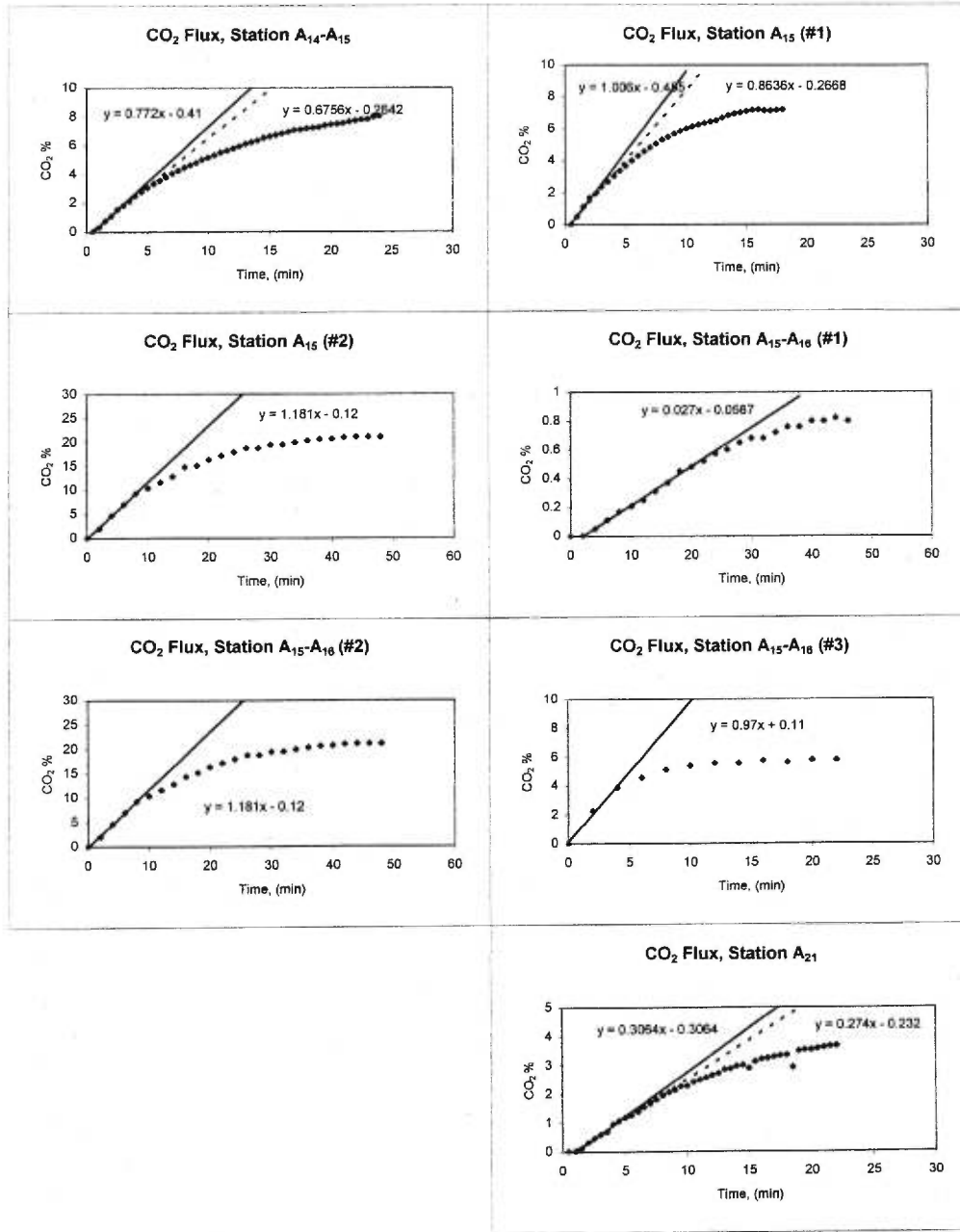
Station B _{11a}	Time (min.)	CO ₂ (% vol.)	T (°C)	Station B ₁₃ B ₁₄	Time (min.)	CO ₂ (% vol.)	T (°C)	Station B ₁₃ B ₁₄	Time (min.)	CO ₂ (% vol.)	T (°C)
#2	0.0	0.00	Out of order	#1	0.0	0.0	Out of order	#2	0.5	-0.09	Out of order
97/03/15	0.5	0.01	Out of order	97/03/15	0.5	-0.14	Out of order	B13-B14	1.0	-0.04	Out of order
1400 hrs	1.0	0.29		1410 hrs	1.0	-0.04		1430 hrs	1.5	0.01	
	1.5	0.56		CO ₂ at 75 cm	1.5	0.01			2.0	0.01	
	2.0	0.80		1.24%	2.0	0.01			2.5	0.01	
Pressure	2.5	1.00		Pressure	2.5	0.03		Pressure	3.0	0.07	
964 mbar	3.0	1.14		965 mbar	3.0	0.07		965 mbar	3.5	0.09	
	3.5	1.25			3.5	0.13			4.0	0.17	
	4.0	1.35			4.0	0.15			4.5	0.21	
	4.5	1.41			4.5	0.21			5.0	0.27	
	5.0	1.47			5.0	0.25			5.5	0.33	
	5.5	1.51			5.5	0.33			6.0	0.36	
	6.0	1.55			6.0	0.37			6.5	0.41	
	6.5	1.58			6.5	0.40			7.0	0.44	
	7.0	1.60			7.0	0.44			7.5	0.48	
	7.5	1.63			7.5	0.48			8.0	0.50	
	8.0	1.63			8.0	0.48			8.5	0.52	
	8.5	1.63			8.5	0.52			9.0	0.54	
					9.0	0.54			9.5	0.56	
					9.5	0.56			10.0	0.58	
					10.0	0.56			10.5	0.60	
					10.5	0.58			11.0	0.64	
					11.0	0.60			11.5	0.68	
					11.5	0.60			12.0	0.72	
					12.0	0.64			12.5	0.74	
					12.5	0.66			13.0	0.76	
					13.0	0.68			13.5	0.80	
					13.5	0.68			14.0	0.80	
					14.0	0.72			14.5	0.82	

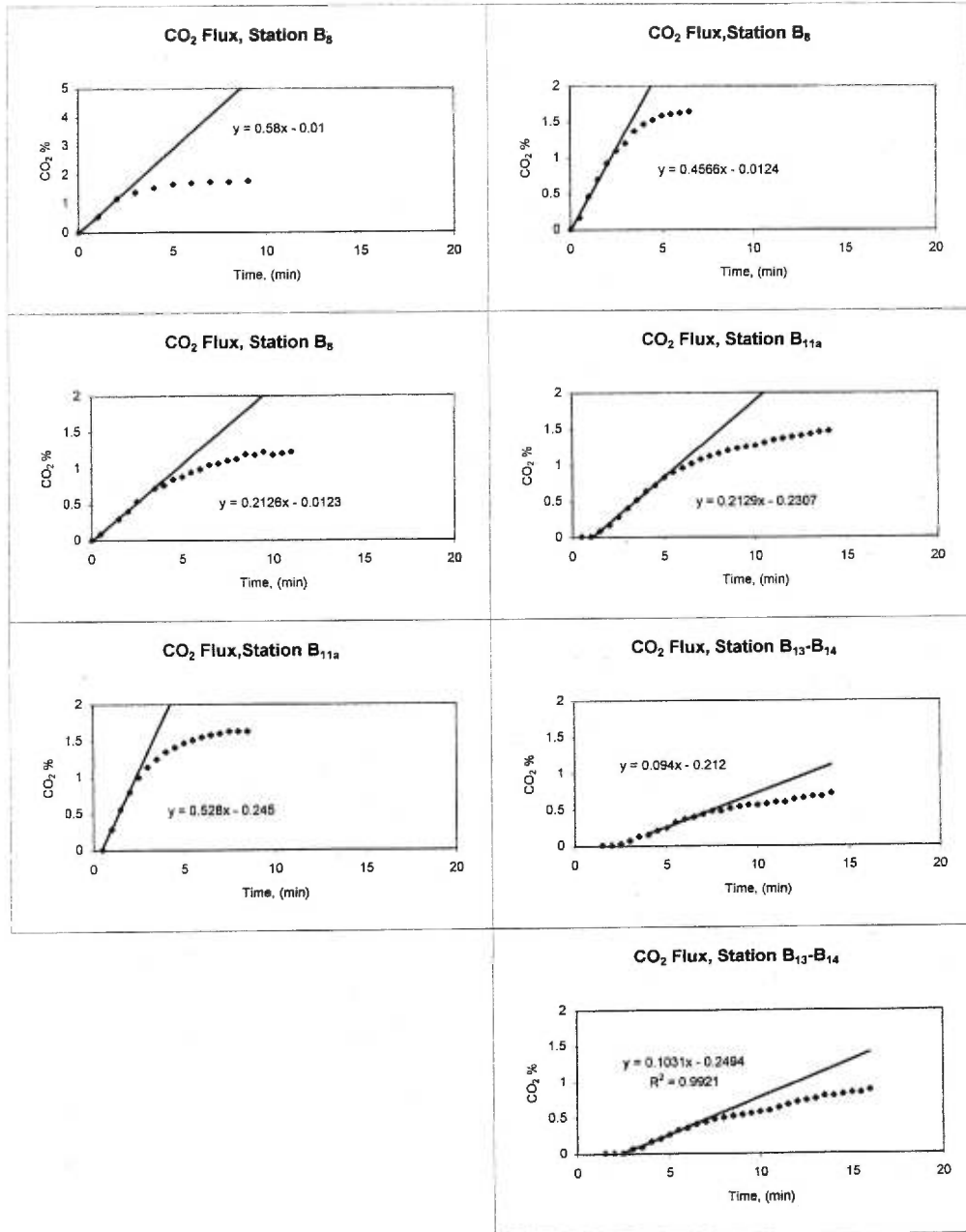
Table C-3 Raw data of fluxes measurements conducted on line C.

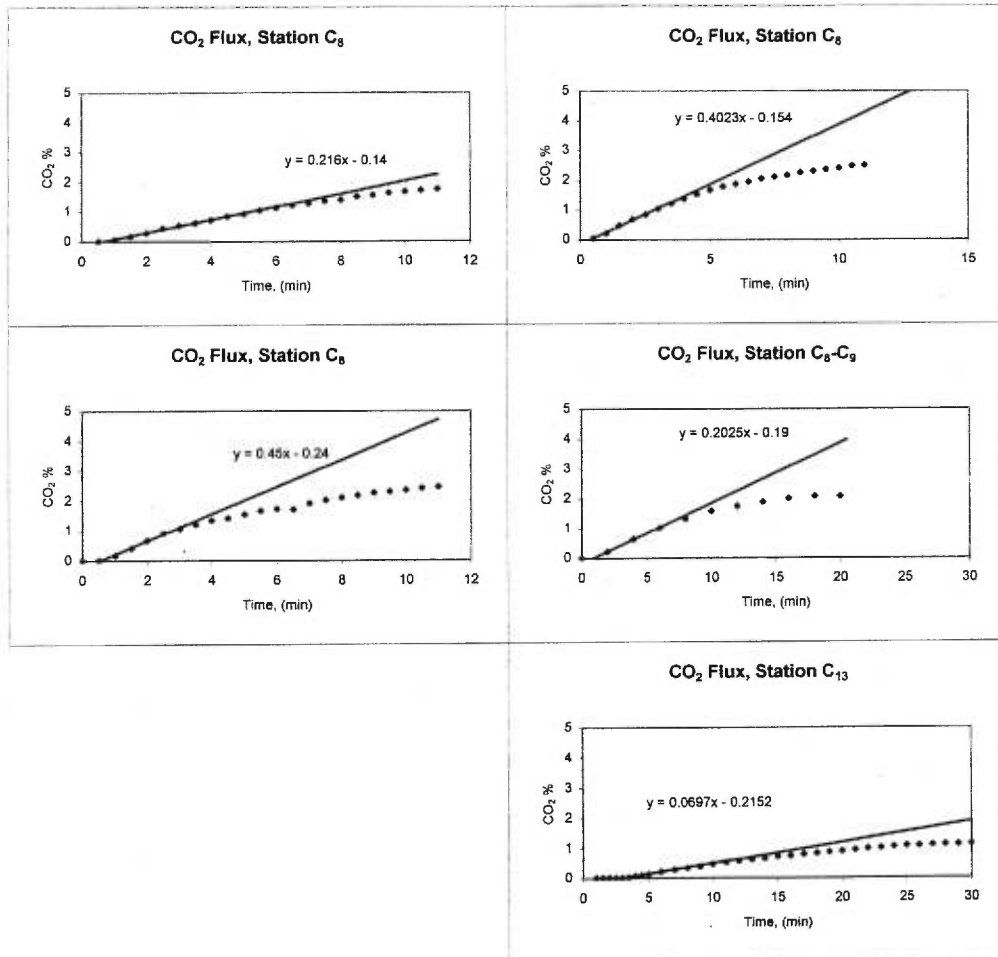
Station C ₈	Time (min.)	CO ₂ (% vol.)	T (°C)	Station C ₈	Time (min.)	CO ₂ (% vol.)	T (°C)	Station C ₈	Time (min.)	CO ₂ (% vol.)	T (°C)	Station C ₉	Time (min.)	CO ₂ (% vol.)	T (°C)
#1	0.0	0.00	40.5	#2	0.0	0.00	41.1	#3	0.0	0.00	32.4		0	0.00	32.4
970316	0.5	0.05	40.4	970316	0.5	0.01	41.2	970316	0.5	0.01	32.6		2	0.21	33.5
CO ₂ at 75 cm	1.0	0.21	40.5	CO ₂ at 75 cm	1.0	0.17	42.1	CO ₂ at 75 cm	1.0	0.05	34.4		4	0.63	33.4
2.62 % vol.	1.5	0.48	40.6	2.24 % vol.	1.5	0.41	42.4	2.36 % vol.	1.5	0.17	35.1		6	1.02	34.9
	2.0	0.68	40.7		2.0	0.68	42.3		2.0	0.29	35.4		8	1.32	35.4
Pressure	2.5	0.84	40.3	Pressure	2.5	0.92	42.0	Pressure	2.5	0.44	35.4	Pressure	10	1.58	35.6
980 mbar	3.0	1.04	40.1	980 mbar	3.0	1.08	41.9	980 mbar	3.0	0.54	35.4	985 mbar	12	1.74	36.0
	3.5	1.20	40.2		3.5	1.22	41.9		3.5	0.61	35.4		14	1.88	35.3
	4.0	1.37	40.3		4.0	1.35	41.8		4.0	0.72	35.4		16	2.00	34.6
	4.5	1.53	40.3		4.5	1.43	41.8		4.5	0.84	35.3		18	2.07	34.4
	5.0	1.67	40.3		5.0	1.55	41.5		5.0	0.92	35.5		20	2.07	34.4
	5.5	1.79	40.1		5.5	1.67	41.6		5.5	1.04	36.0				
	6.0	1.87	40.1		6.0	1.73	41.5		6.0	1.12	36.5				
	6.5	1.95	40.2		6.5	1.71	41.3		6.5	1.20	36.8				
	7.0	2.05	40.4		7.0	1.91	41.2		7.0	1.27	37.2				
	7.5	2.11	40.3		7.5	2.02	41.2		7.5	1.35	37.3				
	8.0	2.17	40.3		8.0	2.10	41.2		8.0	1.41	37.3				
	8.5	2.25	40.2		8.5	2.18	41.0		8.5	1.51	37.2				
	9.0	2.30	40.2		9.0	2.26	40.7		9.0	1.55	36.8				
	9.5	2.36	40.3		9.5	2.30	40.6		9.5	1.63	36.4				
	10.0	2.40	40.1		10.0	2.36	40.3		10.0	1.67	36.3				
	10.5	2.47	39.9		10.5	2.42	40.0		10.5	1.71	36.1				
	11.0	2.50	39.7		11.0	2.46	39.4		11.0	1.75	36.1				

Table C-3 Continued.

Station	Time (min.)	CO ₂ (% vol.)	T (°C)	Time (min.)	CO ₂ (% vol.)	T (°C)
C ₁₃	0.0	-0.04	32.6	22.0	0.98	34.3
970316	0.5	-0.04	32.6	23.0	1.00	34.3
CO ₂ at 75 cm	1.0	0.01	36.2	24.0	1.04	34.2
2.24 % vol.	1.5	0.01	36.6	25.0	1.08	34.2
	2.0	0.01	37.0	26.0	1.08	34.1
Pressure	2.5	0.01	37.5	27.0	1.10	34.9
987 mbar	3.0	0.01	37.6	28.0	1.12	35.9
	3.5	0.03	38.2	29.0	1.12	36.6
	4.0	0.07	38.0	30.0	1.14	37.0
	4.5	0.09	38.0			
	5.0	0.13	37.2			
	6.0	0.21	36.8			
	7.0	0.27	36.3			
	8.0	0.33	36.2			
	9.0	0.37	36.3			
	10.0	0.45	36.4			
	11.0	0.52	36.6			
	12.0	0.56	36.6			
	13.0	0.60	36.5			
	14.0	0.64	36.1			
	15.0	0.72	35.9			
	16.0	0.74	35.7			
	17.0	0.79	35.2			
	18.0	0.82	34.8			
	19.0	0.86	34.7			
	20.0	0.90	34.4			
	21.0	0.94	34.3			







Appendix D

Petrologic analysis of bombs from the 12 November 1997 explosive event at Masaya volcano.

Table D-1 Pélé's hair, glass shards and glassy materials analyses.

a) Pélé's hair analyses

	cp971	cp972	cp973	cp97-1	cp961	cp962	cp963	cp96-1
SiO ₂	52.07	51.88	51.61	51.63	51.86	51.68	51.35	51.67
TiO ₂	1.36	1.30	1.31	1.43	1.37	1.37	1.35	1.46
Al ₂ O ₃	14.18	14.08	14.13	14.30	14.23	14.08	14.18	14.26
FeO	13.68	14.00	14.09	13.86	13.60	13.94	14.19	13.89
MnO	0.24	0.27	0.26	0.24	0.24	0.27	0.27	0.24
MgO	4.78	4.76	4.89	4.76	4.87	4.83	4.87	4.74
CaO	9.08	8.96	9.08	9.15	9.22	9.15	9.09	9.11
Na ₂ O	2.92	3.01	2.98	2.94	2.95	2.99	3.00	2.97
K ₂ O	1.46	1.50	1.41	1.45	1.43	1.46	1.45	1.44
P ₂ O ₅	0.20	0.21	0.20	0.20	0.21	0.20	0.21	0.20
Total	100.00	100.00	100.00	100.00	100.00	100.00	100.00	100.00
Cl	325	353	361	336	375	351	542	314
S	55	47	55	57	47	32	71	8

Table D-1 Continued.

b) Glass inclusions

	001i2	001i2bis	001i5	003i1a	003i1b	003i1c	003i2	003i4	003i6IIa	003i6IIb
SiO ₂	51.59	52.25	51.42	51.55	51.79	51.89	51.47	52.44	52.13	52.03
TiO ₂	1.41	1.40	1.49	1.22	1.29	1.35	1.33	1.32	1.32	1.38
Al ₂ O ₃	13.57	13.90	13.91	14.00	13.98	13.25	13.81	13.75	14.23	14.15
FeO	15.16	13.68	14.75	14.28	14.12	14.61	14.51	13.92	13.55	13.76
MnO	0.29	0.26	0.32	0.26	0.26	0.25	0.29	0.26	0.21	0.26
MgO	4.90	4.98	4.79	5.03	5.00	5.32	5.08	4.97	4.81	4.79
CaO	7.51	8.31	7.59	8.57	8.49	8.45	8.44	7.75	8.95	8.84
Na ₂ O	2.77	2.69	2.70	3.11	3.09	2.86	2.92	2.98	2.99	2.98
K ₂ O	2.58	2.2	2.80	1.76	1.77	1.80	1.92	2.40	1.56	1.57
P ₂ O ₅	0.20	0.20	0.19	0.19	0.18	0.20	0.20	0.18	0.21	0.21
Total	100.00	100.00	100.00	100.00	100.00	100.00	100.00	100.00	100.00	100.00
Cl	494	383	494	422	402	426	403	412	384	392
S	278	79	87	165	158	175	102	55	63	55

Table D-1 Continued.

b) Glass inclusions continued.

	003i7IIa	003i7IIb	003i7IIbr	003i1	003i2	003i3	003i5	003i6
SiO ₂	52.17	52.15	52.33	51.80	51.33	51.38	51.18	51.50
TiO ₂	1.32	1.40	1.30	1.32	1.38	1.48	1.44	1.42
Al ₂ O ₃	14.28	14.34	14.3	14.22	13.94	13.23	13.75	13.81
FeO	13.48	13.48	13.28	14.04	14.32	15.04	14.85	14.33
MnO	0.26	0.26	0.27	0.27	0.27	0.31	0.25	0.27
MgO	4.73	4.69	4.76	4.76	4.93	5.15	4.99	4.99
CaO	8.90	8.83	8.91	8.58	8.42	8.02	8.25	8.30
Na ₂ O	3.05	3.02	2.96	2.92	3.15	2.84	3.02	3.05
K ₂ O	1.58	1.61	1.64	1.85	2.03	2.31	2.03	2.10
P ₂ O ₅	0.20	0.20	0.21	0.19	0.19	0.20	0.19	0.19
Total	100.00	100.00	100.00	100.00	100.00	100.00	100.00	100.00
Cl	383	372	374	365	385	426	406	378
S	55	55	71	112	120	104	81	97

Table D-1 Continued.

c) Glass shards analyses.

	001e1	001e2	001e3	001e3r	003e1	003e1bis	003e2
SiO ₂	51.54	51.87	51.87	51.64	51.81	52.26	52.92
TiO ₂	1.29	1.34	1.37	1.35	1.34	1.46	1.47
Al ₂ O ₃	14.13	14.14	14.16	14.14	14.21	14.59	14.45
FeO	14.04	13.85	13.76	14.17	14.28	14.24	13.58
MnO	0.29	0.23	0.26	0.25	0.26	0.27	0.27
MgO	4.85	4.81	4.86	4.84	4.82	4.89	4.93
CaO	9.16	9.14	9.08	9.04	9.04	8.46	8.40
Na ₂ O	3.03	2.93	2.97	2.91	2.61	2.35	2.41
K ₂ O	1.43	1.46	1.44	1.42	1.41	1.24	1.34
P ₂ O ₅	0.20	0.20	0.21	0.20	0.20	0.21	0.20
Total	100.00	100.00	100.00	100.00	100.00	100.00	100.00
Cl	353	342	321	332	351	360	363
S	71	40	8	24	40	55	63

Table D-1 Continued.

c) Glass shards continued.

	005e2	005e3	005e3r	005e3rr
SiO ₂	51.50	51.63	51.61	51.68
TiO ₂	1.29	1.34	1.34	1.35
Al ₂ O ₃	14.17	14.20	14.10	14.17
FeO	14.09	13.86	13.97	13.93
MnO	0.25	0.25	0.27	0.26
MgO	4.82	4.90	4.81	4.79
CaO	9.21	9.16	9.17	9.11
Na ₂ O	3.00	2.95	3.02	2.98
K ₂ O	1.44	1.47	1.48	1.48
P ₂ O ₅	0.20	0.20	0.20	0.20
Total	100.00	100.00	100.00	100.00
Cl	331	352	320	354
S	63	23	32	32

Appendix E

Program used to treat SO₂ COSPEC signals for: a) power spectrum density Matlab program, and b) structure functions Fortran program.

```
% a) Power spectrum density program
%Eve-Lise
%May 1998
```

```
clear all
load name_of_file.txt
t=name_of_file(:,1);
Conc=name_of_file(:,2);
clear name_of_file
l=input('Length in time of the series: ');
```

```
figure
plot(t*l/length(t),Conc,'x')
xlabel('Time (in seconds)')
ylabel('SO2 concentration')
title('title')
```

```
%[p f]=psd(Conc,'linear');
[p f]=psd(Conc);
```

```
figure
loglog(f,p,'or')
xlabel('t in second^-^1')
ylabel('PSD of SO2 concentration ')
imin=input('i minimum : ');
i=imin+1:length(f);
a=polyfit(log(f(i)),log(p(i)),1)
hold on
```

```
plot(f(i),exp(a(1)*log(f(i))+a(2)), 'b')
%gtext('\beta=3.41')
%grid
```

- c (b) Structure Functions Program
- c H  l  ne Gaonac'h
- c 20 nov.1998

c File input: sp97

```

10 character*10 infile,outfile
   PARAMETER (size=3001)
   parameter(nteta=43)
   real*4 q
   real*4 coord(size),datain(size)
   real*4 tr(nteta)
   INTEGER*2
teta(nteta)/1,2,3,4,5,6,7,8,9,10,12,15,20,30,35,40,45,50,55,60,65,70,75,80,9
0,100,125,200,250,300,350,400,450,500,550,600,700,800,900,1000,1250,15
00,3000/

```

- c The nteta maximum must correspond to size-1
- c The 43 values of nteta are arbitrary chosen with a larger
- c number near the low ntetas values (see above).

```

write(*,*) 'entry file name'
read(*,*) infile
write(*,*) 'output file name'
read(*,*) outfile
write(*,*) 'what is q?'
read(*,*) q

```

```
open(unit=17,file=infile,status='old', readonly, recordtype='stream')
```

- c IMPORTANT
- c Input file in kaleidagraph. Saved under the tab-delimited
- c text format.
- c Verify that the file do not contain any column title. If
- c any, remove it.

```

do 9 l=1,size
  read(17,*) x,y
  coord(l)=x
  datain(l)=y
9 CONTINUE

```

- c datain correspond to SO2 values that we will analyse.
- c Initialisation of the output table of structure functions.

```
do ieta=1,nteta
  tr(ieta)=0.0
enddo

do ieta=1,nteta
  t=teta(ieta)
  sum=0.
  sum2=0.
  numb=0.

  do i=1,size
    if((i+t).gt.size) go to 8
    sum=sum+ (abs(datain(i+t)-datain(i)))**q
    numb=numb+1
  enddo

8 sum2=sum2+sum/numb
  tr(ieta)=sum2
c write(*,*) 'tr=',tr(ieta)
c pause
enddo

write(*,*) 'opening output'

open(unit=35,file=outfile,status='new', recordtype='stream')

do ieta = 1,nteta
  write(35,*) teta(ieta),char(9),tr(ieta)
enddo

close(17)
close(35)

write(*,*) 'Do you want to do another analyse?'
write(*,*) 'If yes type 0, if no type 1'
read (*,*) x
if(x.eq.0) go to 10
stop

end
```

Appendix F

Parameters of SO₂ signals files used for power spectrum density and structure functions analysis.

Table F-1 Parameters of SO₂ signals analysed.

Date	File names	Length series (seconds)	Length series (points)	SO ₂ flux (td ⁻¹)
Temporal series				
97-03-28	t97	1800	3001	*
98-03-03	e03	3705	6238	*
98-03-10	e10a	4257	3232	*
	e10b	3600	7144	*
98-03-15	e15a	3200	3200	*
	e15b*	2370	2370	*
Ticuantepe				
97-03-25	25t	293	947	1053
97-03-27	27t	225	1500	323
97-03-28	28t	240	1357	561
98-03-17	17t1	348	609	2014
	17t2	270	446	1484
	17t3	348	546	2342
	17t4	405	374	1602
	17t5	390	325	1800
	17t6	324	596	1843
	17t7	396	325	2170
	17t8	423	398	2520
	17t9	375	596	2325
	17t10	339	350	1850
	17t11	330	275	2477
	17t12	288	450	2007
	17t13	474	798	4363
	17t14	384	648	3312
	17t15	429	749	3754
	17t16	360	648	2023
	17t17	405	699	1805
	17t18	435	796	2925
	17t19	480	794	2321
	17t20	396	620	2967

Table F-1 Continued.

Date	File names	Length series (seconds)	Length series (points)	SO ₂ flux (t d ⁻¹)
El Crucero				
97-03-07	7e	435	733	232
97-03-12	12e	428	766	398
97-03-25	25e	555	497	384
97-03-27	27e	525	1195	277
98-03-13	13e2	287	287	824
	13e3	289	289	728
	13e4	266	266	771
	13e5	245	245	645
	13e6	261	261	321
	13e7	357	357	633
	13e8	288	288	606
	13e9	468	468	1248
	13e10	166	166	618
	13e11	248	248	771
	13e12	256	256	950
98-03-17	17e1	725	725	3060
	17e2	1183	1183	2259
	17e3	739	739	2872
	17e4	739	739	2136
	17e5	690	690	2681
	17e6	633	633	2244
	17e7	1050	1050	1736
	17e8	1141	1141	3228
98-03-18	18e1	732	662	1332
	18e2	915	791	1706
	18e3	675	639	1299
	18e4	780	650	1259
	18e5	600	538	635
	18e6	660	599	1204
	18e7	780	627	1394
	18e8	960	809	1657
	18e9	960	728	1200
	18e10	720	544	830

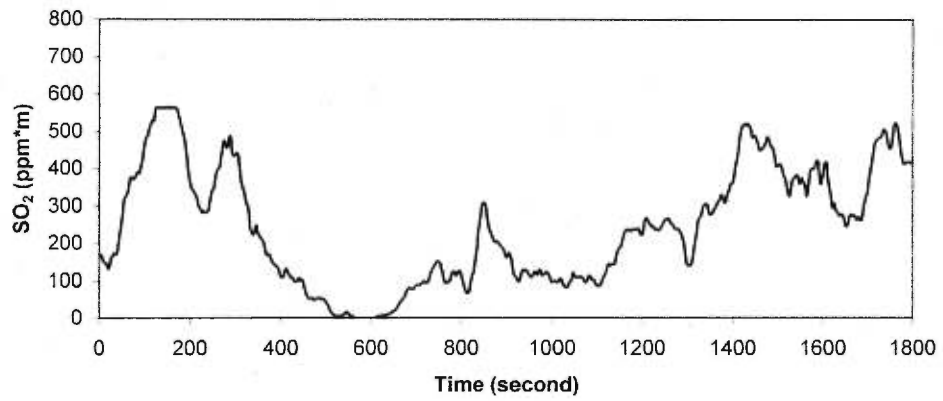
Table F-1 Continued.

Date	File names	Length series (seconds)	Length series (points)	SO ₂ flux (t d ⁻¹)
Masachapa				
98-03-18	18m1	1326	1326	3420
	18m2	1306	1306	4011
	18m3	1455	1455	4541
	18m4	1625	1625	4794
	18m6	1223	1223	3454

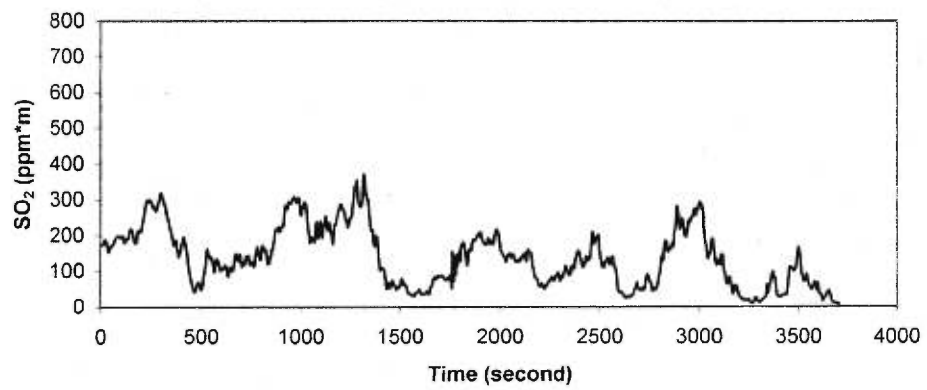
Appendix G

SO₂ COSPEC signals from Masaya volcano, Nicaragua.

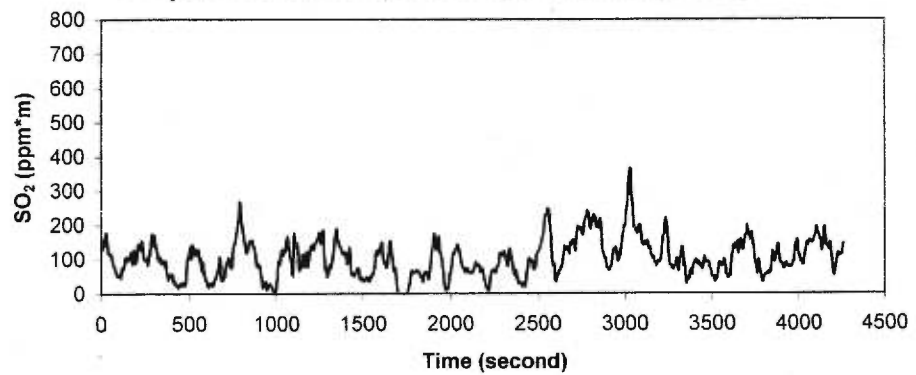
Temporal series t97, 97/03/27, Ticuantepe (5km)



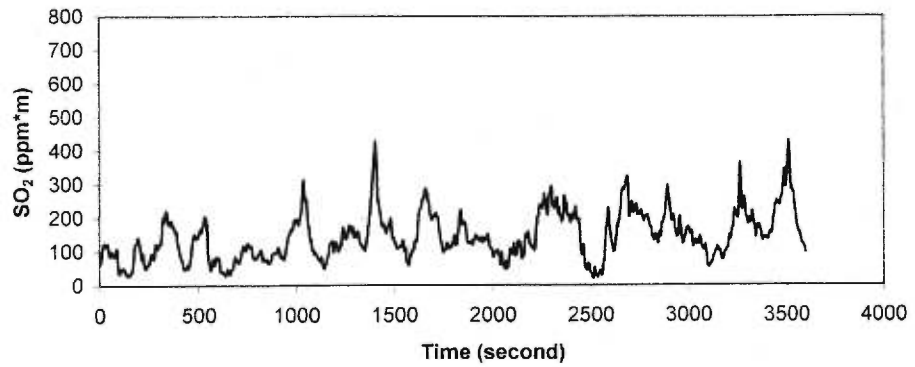
Temporal series e03, 98/03/03, El Crucero (15 km)



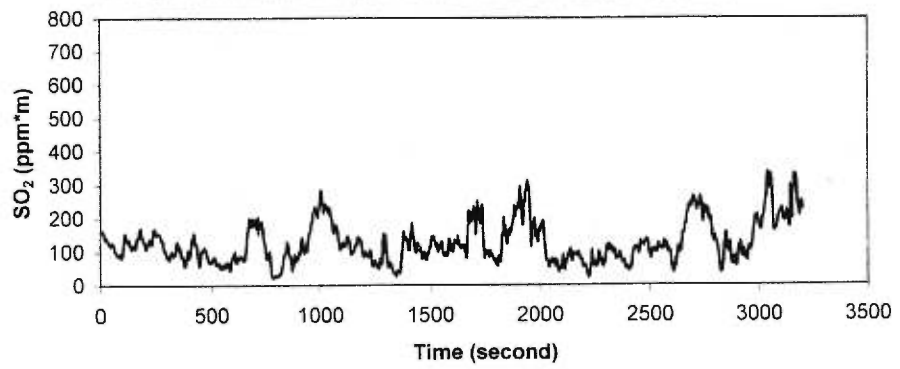
Temporal series e10a, 98/03/10, El Crucero (15 km)



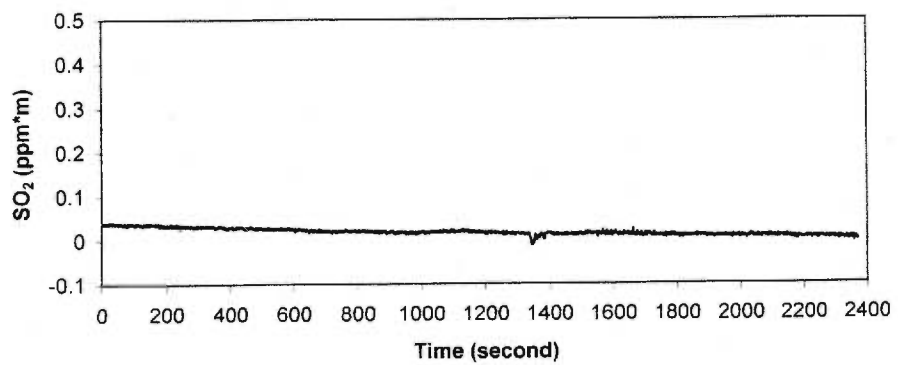
Temporal series e10b, 98/03/10, El Crucero (15 km)



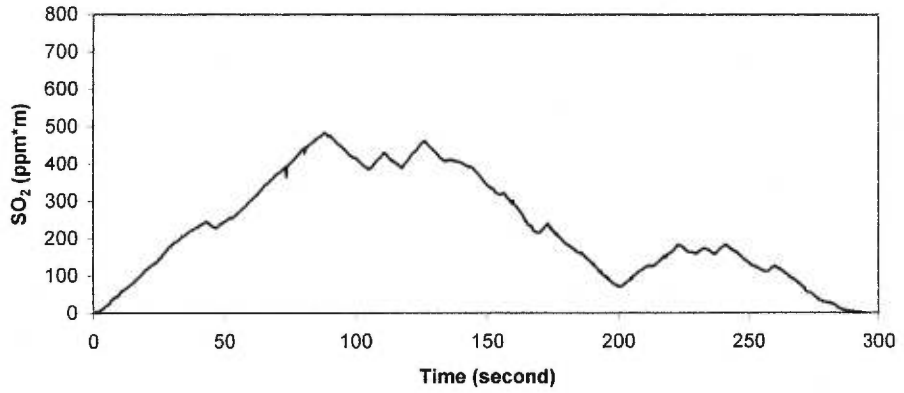
Temporal series e15a, 98/03/15, El Crucero (15 km)



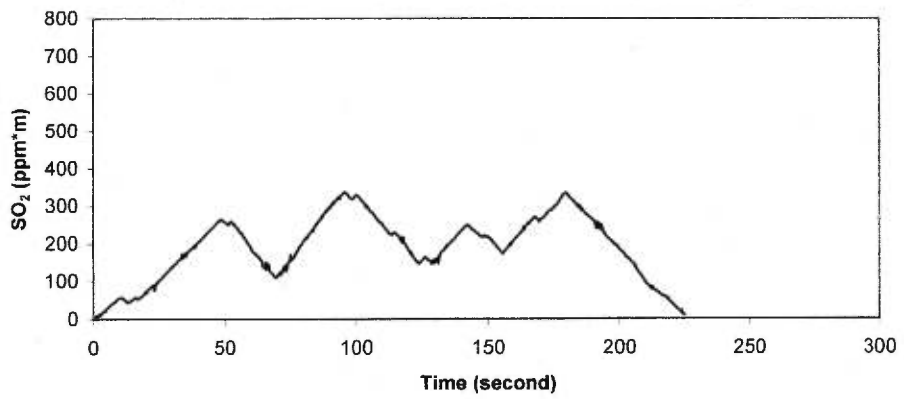
Temporal series e15b, 98/03/15, El Crucero (15 km)



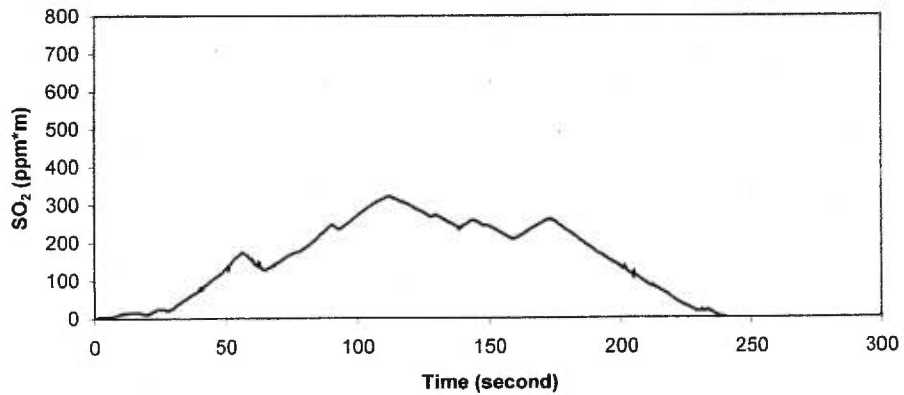
Spatial series 25t, 97/03/25, Ticuantepe (5 km)



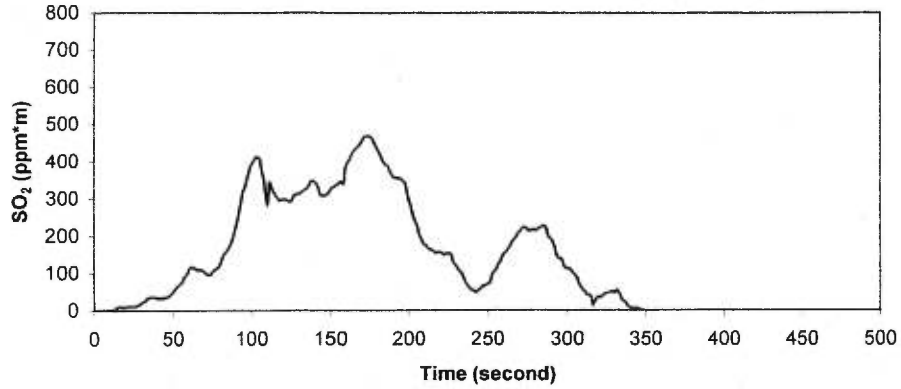
Spatial series 27t, 97/03/27, Ticuantepe (5 km)



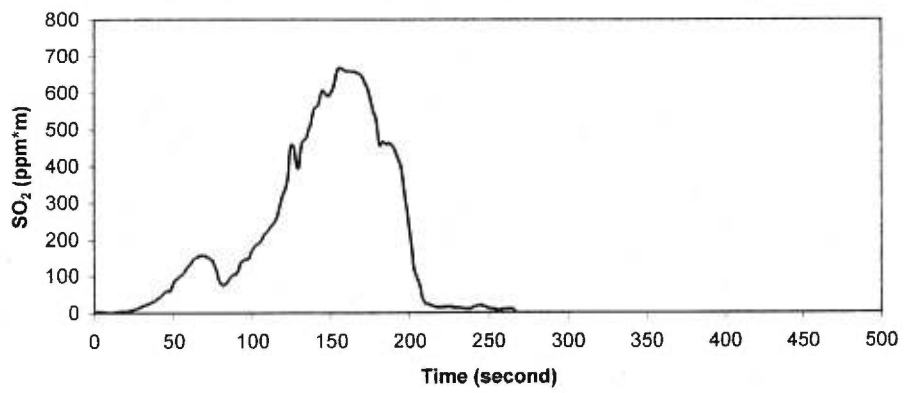
Spatial series 28t, 97/03/28, Ticuantepe (5 km)



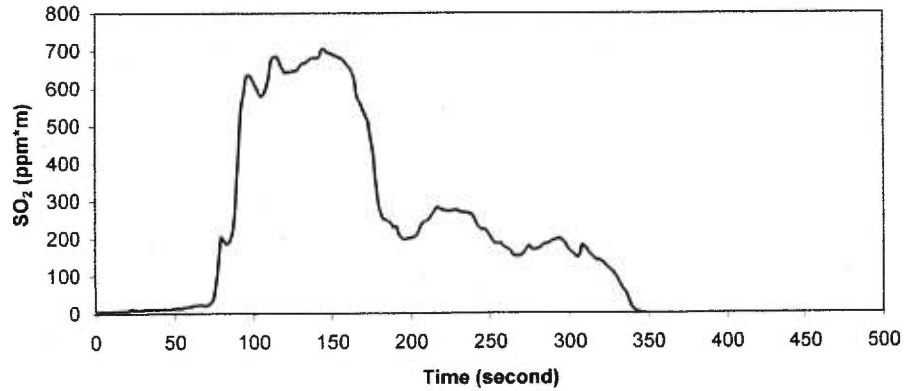
Spatial series 17t1, 98/03/17, Ticuantepe (5 km)



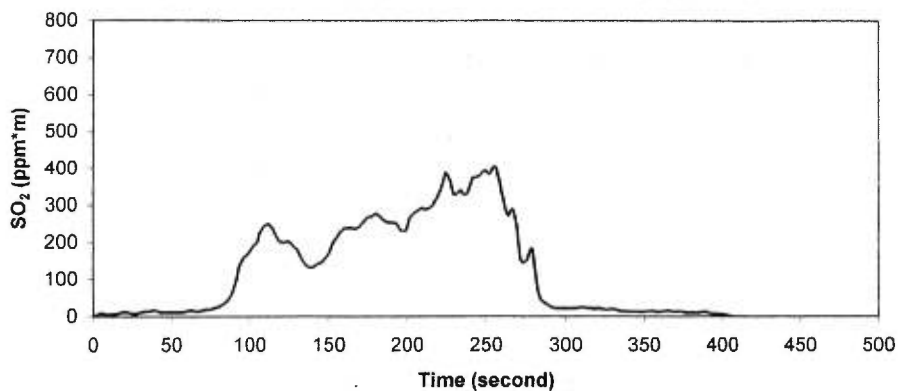
Spatial series 17t2, 98/03/17, Ticuantepe (5 km)



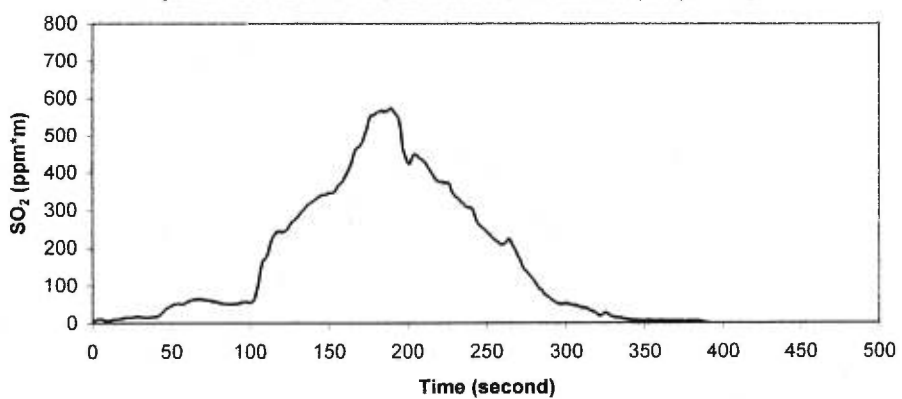
Spatial series 17t3, 98/03/17, Ticuantepe (5 km)



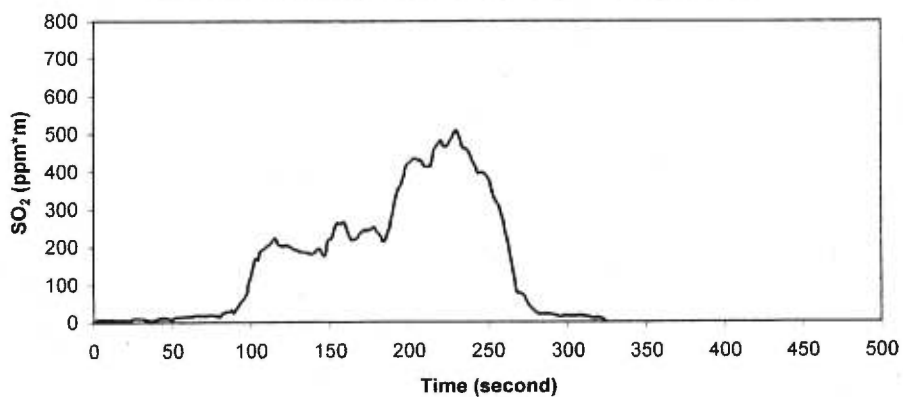
Spatial series 17t4, 98/03/17, Ticuantepe (5 km)



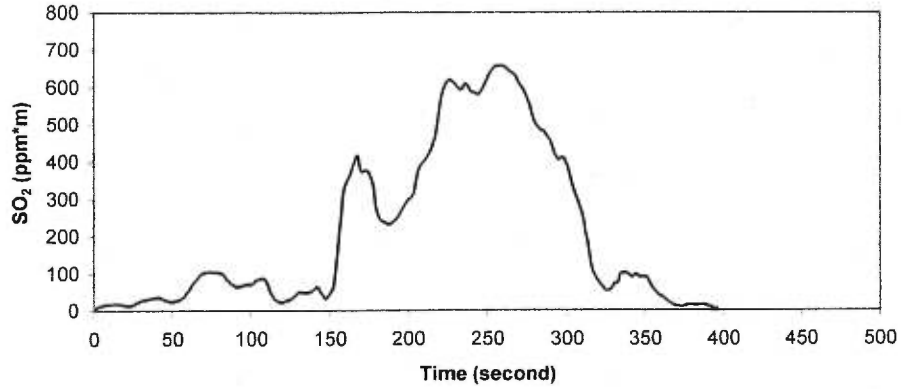
Spatial series 17t5, 98/03/17, Ticuantepe (5 km)



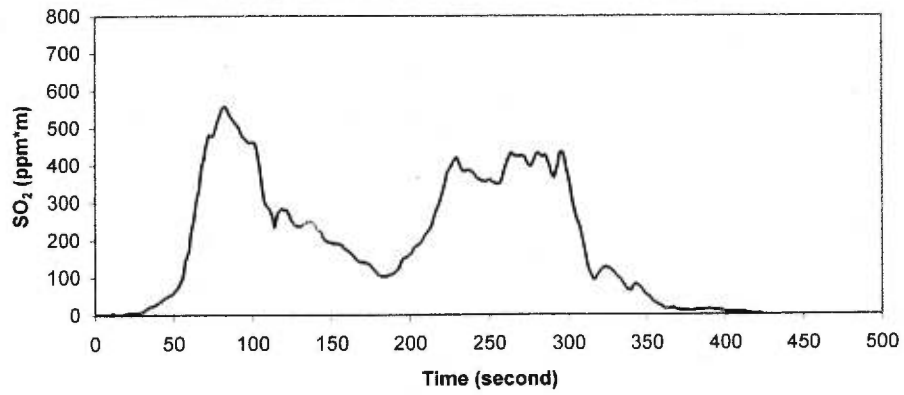
Spatial series 17t6, 98/03/17, Ticuantepe (5 km)



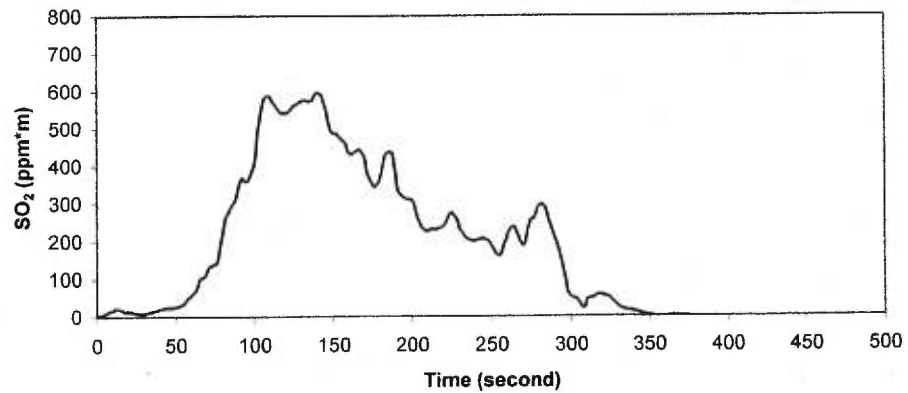
Spatial series 17t7, 98/03/17, Ticuantepe (5 km)



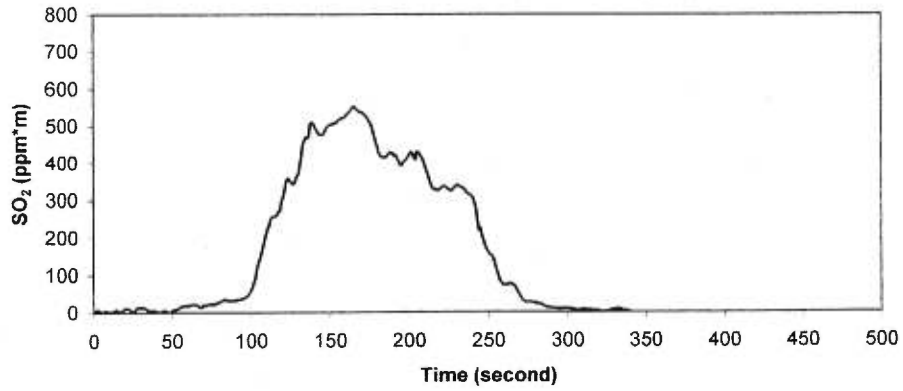
Spatial series 17t8, 98/03/17, Ticuantepe (5 km)



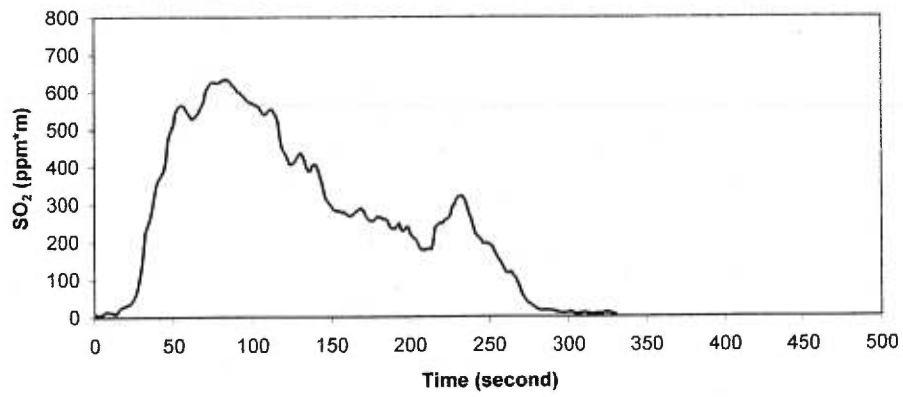
Spatial series 17t9, 98/03/17, Ticuantepe (5 km)



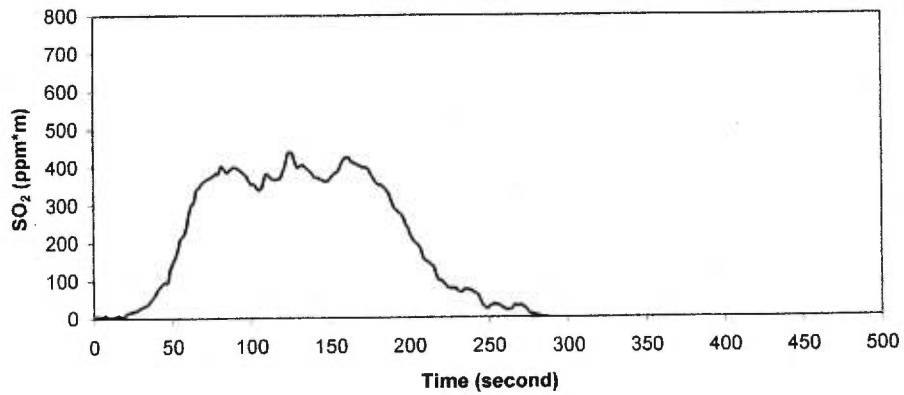
Spatial series 17t10, 98/03/17, Ticuantepe (5 km)



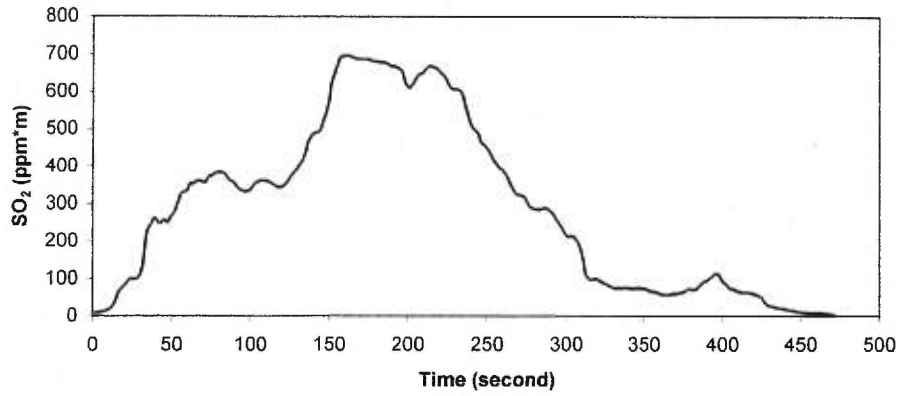
Spatial series 17t11, 98/03/17, Ticuantepe (5 km)



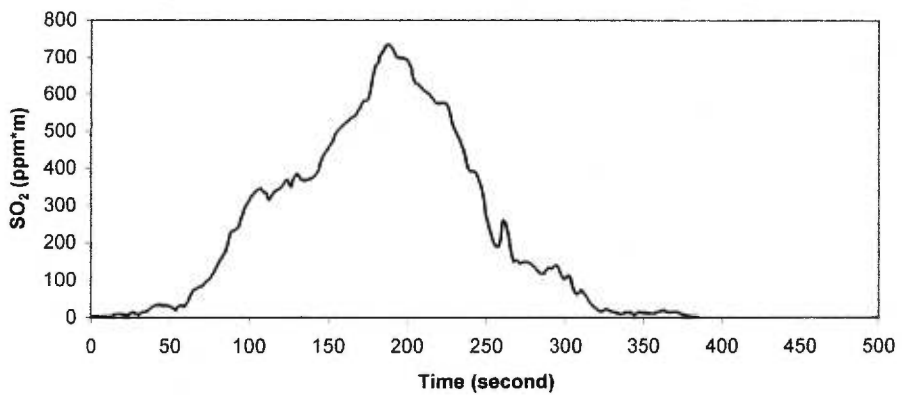
Spatial series 17t12, 98/03/17, Ticuantepe (5 km)



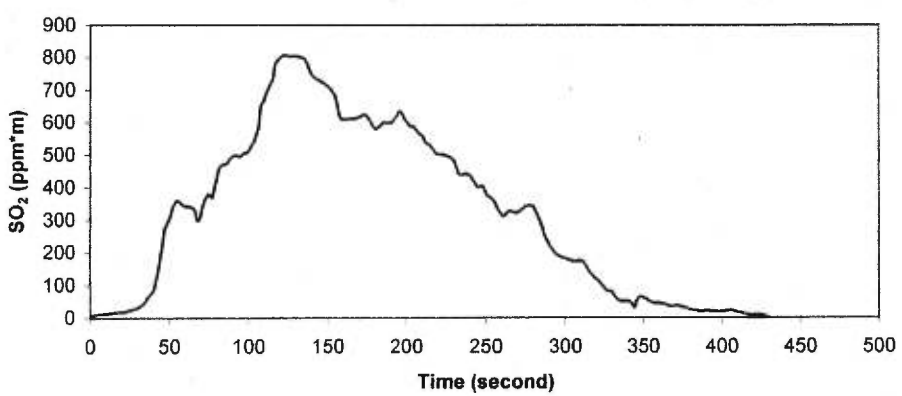
Spatial series 17t13, 98/03/17, Ticuantepe (5 km)



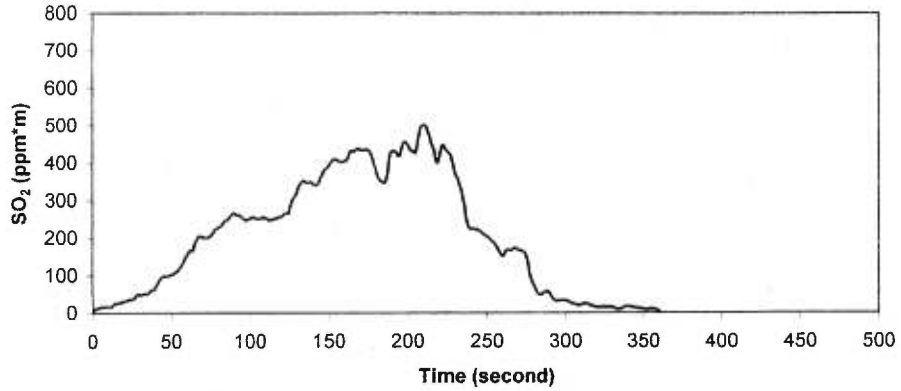
Spatial series 17t14, 98/03/17, Ticuantepe (5 km)



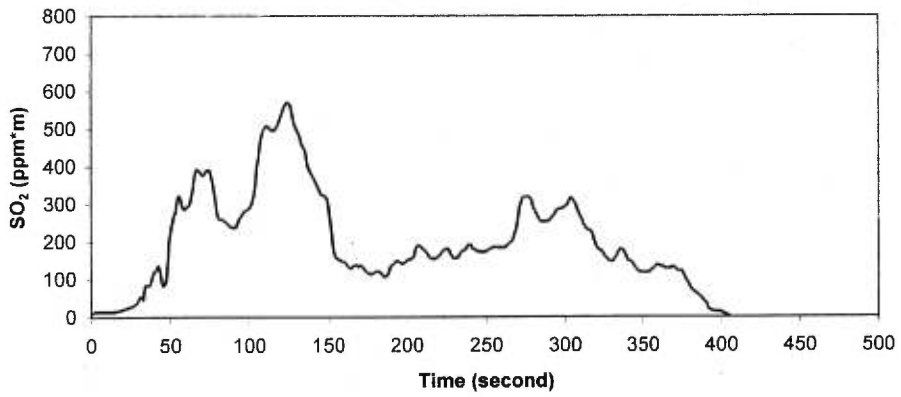
Spatial series 17t15, 98/03/17, Ticuantepe (5 km)



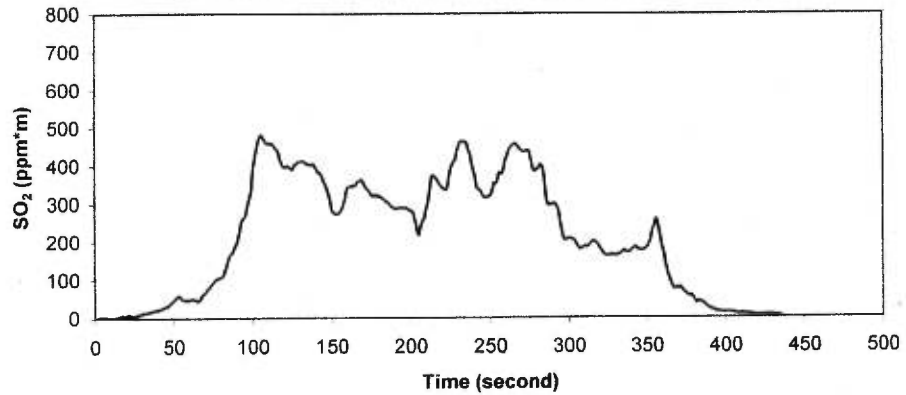
Spatial series 17t16, 98/03/17, Ticuantepe (5 km)



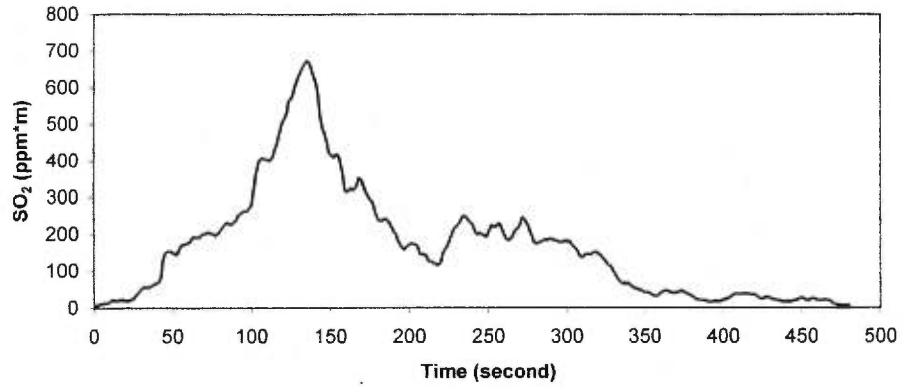
Spatial series 17t17, 98/03/17, Ticuantepe (5 km)



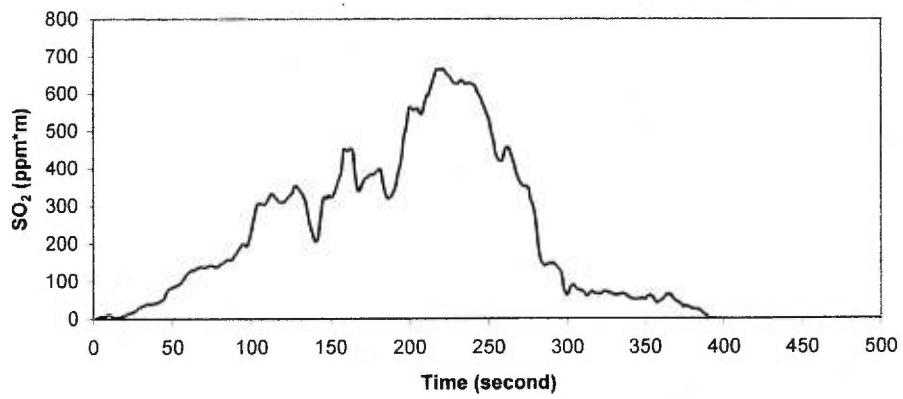
Spatial series 17t18, 98/03/17, Ticuantepe (5 km)



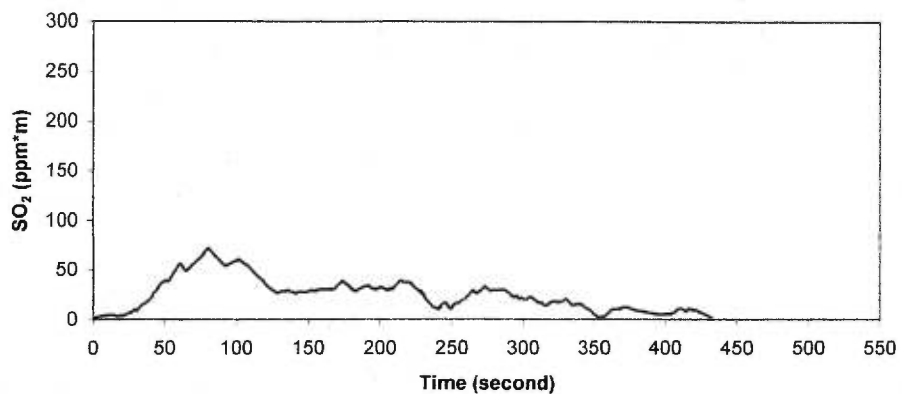
Spatial series 17t19, 98/03/17, Ticuantepe (5 km)



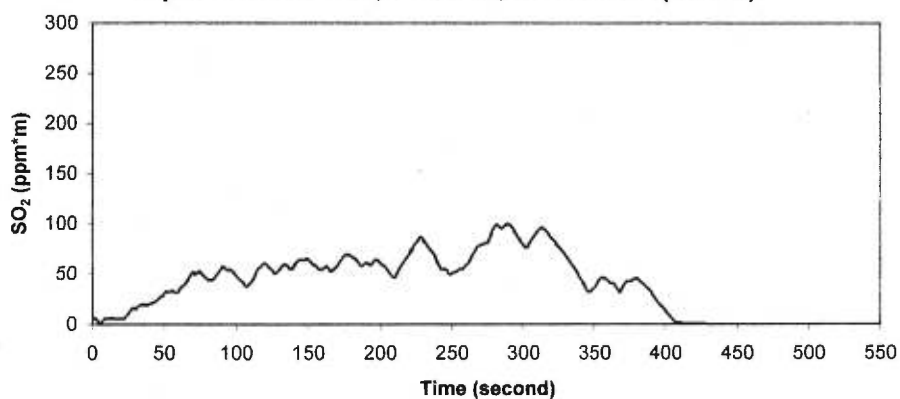
Spatial series 17t20, 98/03/17, Ticuantepe (5 km)



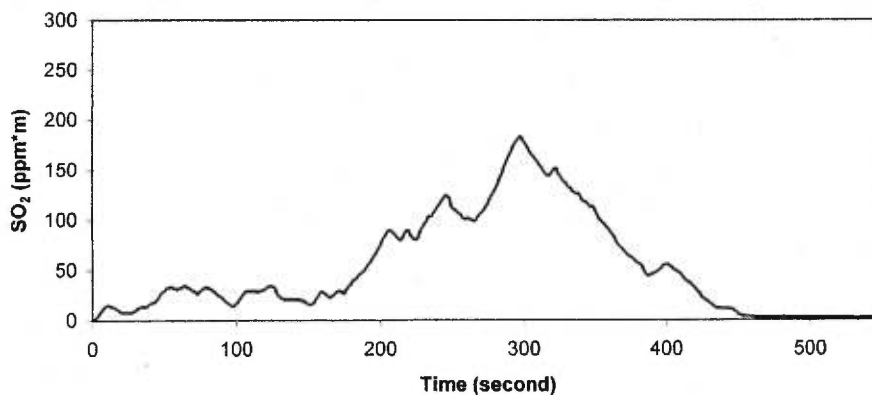
Spatial series 7e, 97/03/07, El Crucero (15 km)



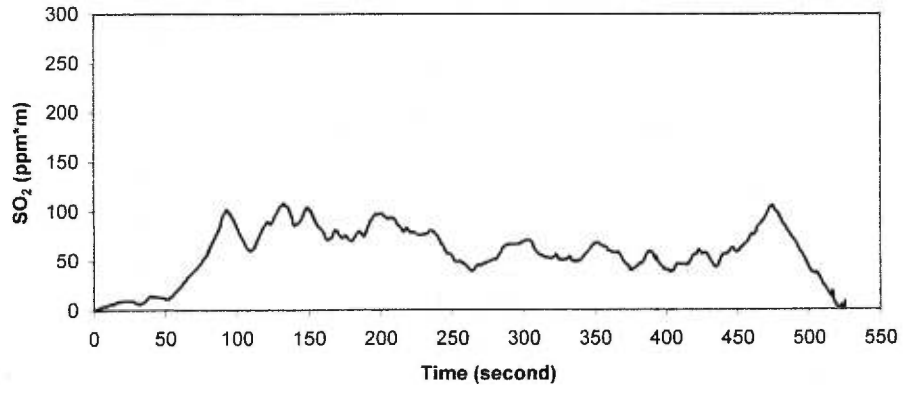
Spatial series 12e, 97/03/12, El Crucero (15 km)



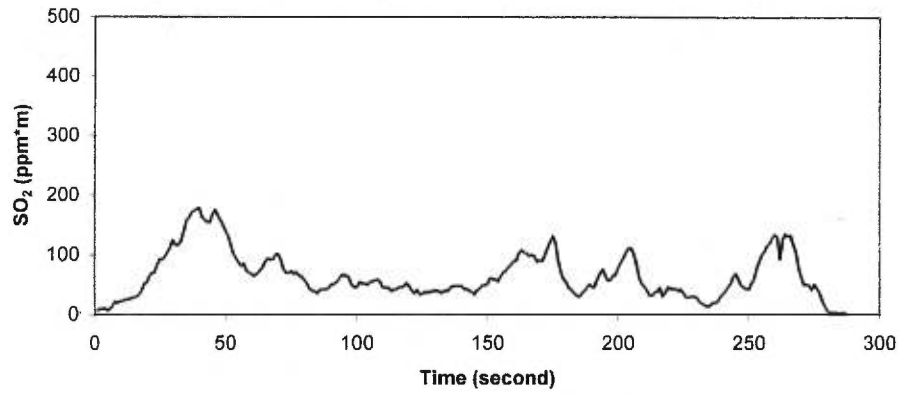
Spatial series 25e, 97/03/25, El Crucero (15 km)



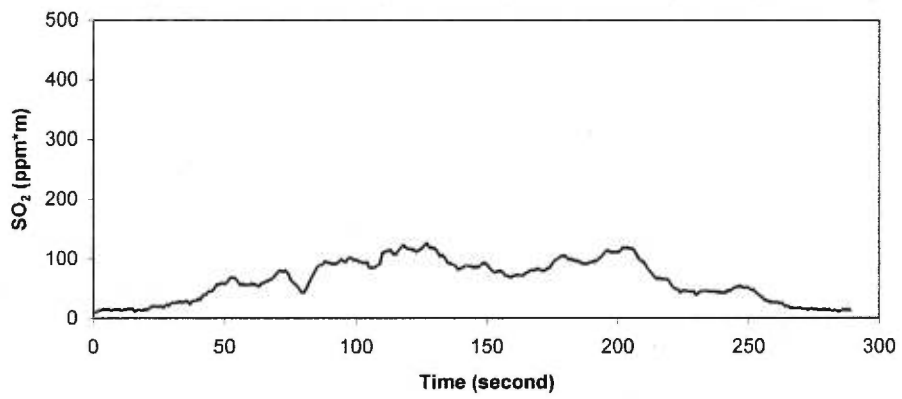
Spatial series 27e, 97/03/27, El Crucero (15 km)



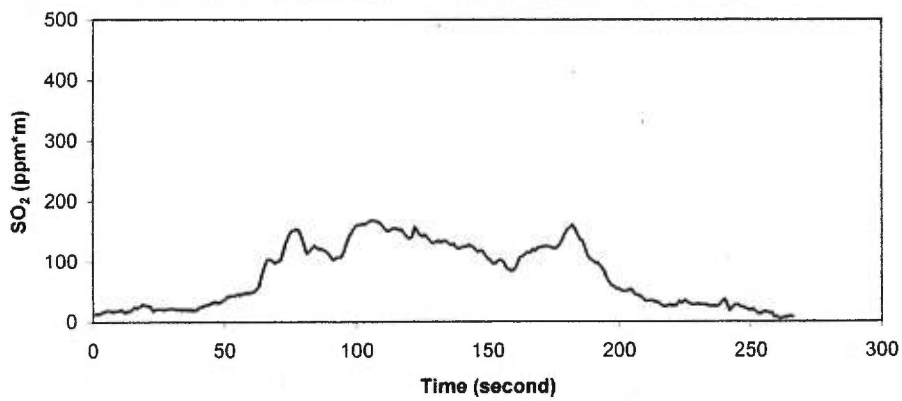
Spatial series 13e2, 98/03/13, El Crucero (15 km)



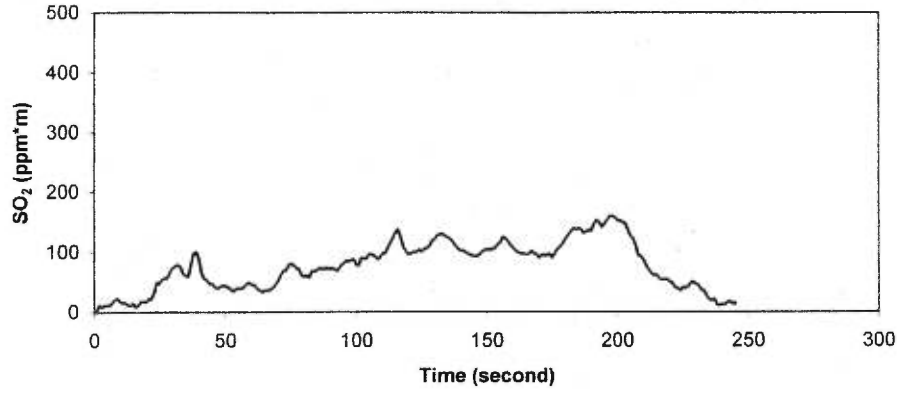
Spatial series 13e3, 98/03/13, El Crucero (15 km)



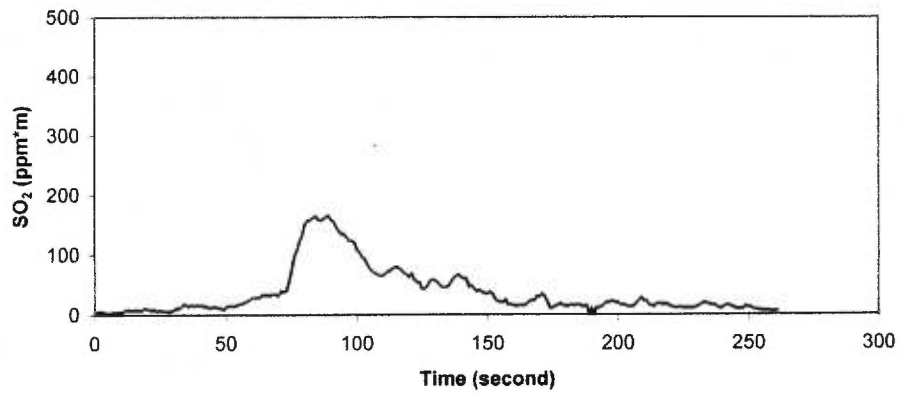
Spatial series 13e4, 98/03/13, El Crucero (15 km)



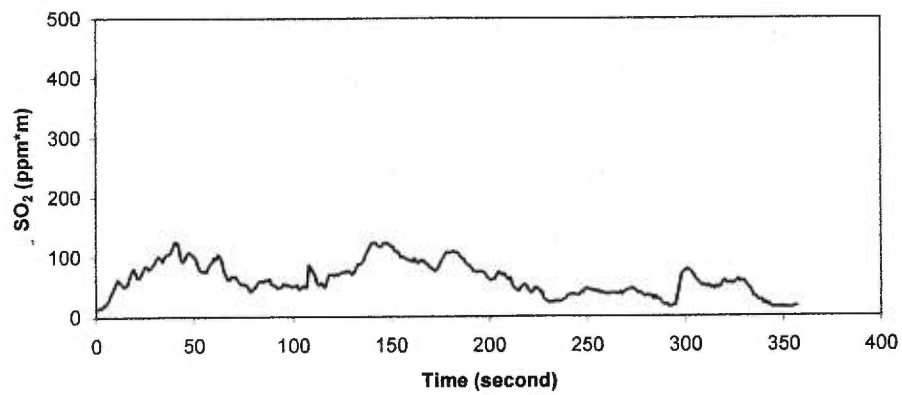
Spatial series 13e5, 98/03/13, El Crucero (15 km)



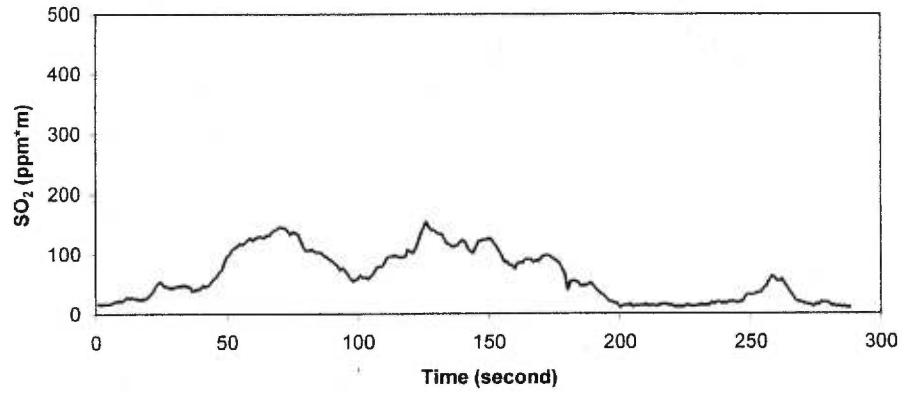
Spatial series 13e6, 98/03/13, El Crucero (15 km)



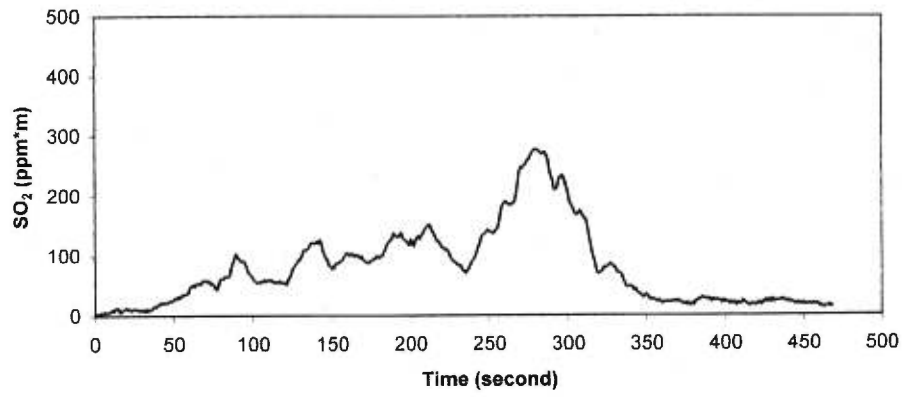
Spatial series 13e7, 98/03/13, El Crucero (15 km)



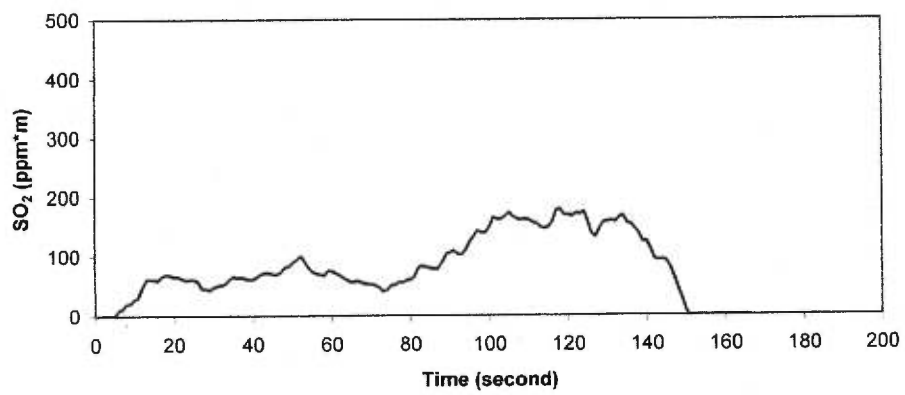
Spatial series 13e8, 98/03/13, El Crucero (15 km)



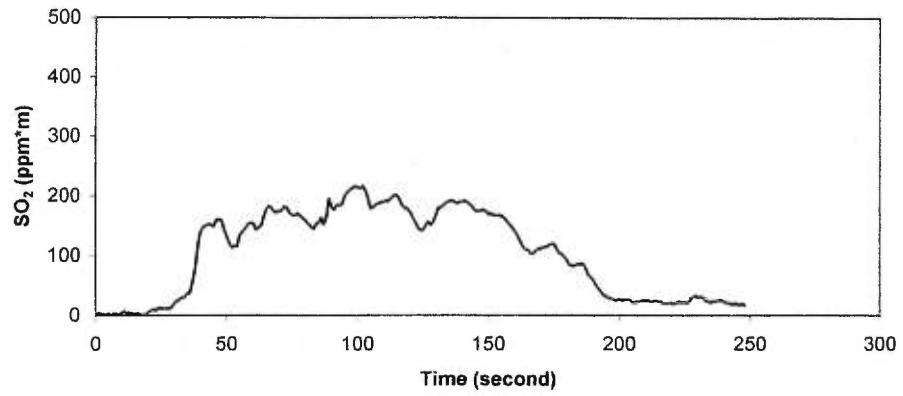
Spatial series 13e9, 98/03/13, El Crucero (15 km)



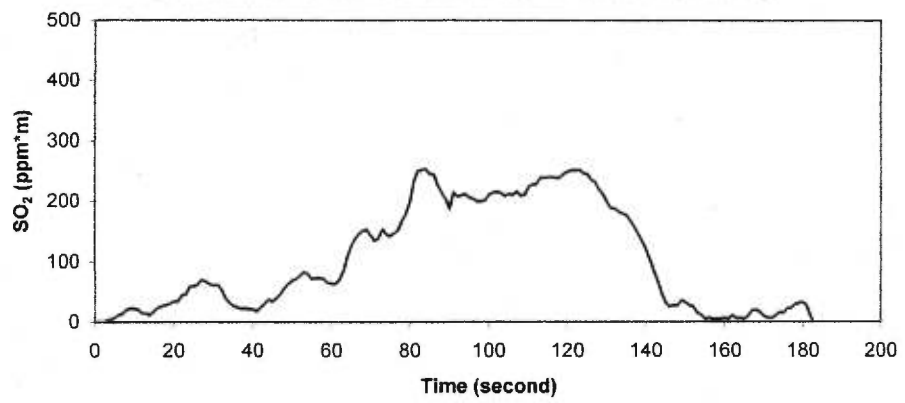
Spatial series 13e10, 98/03/13, El Crucero (15 km)



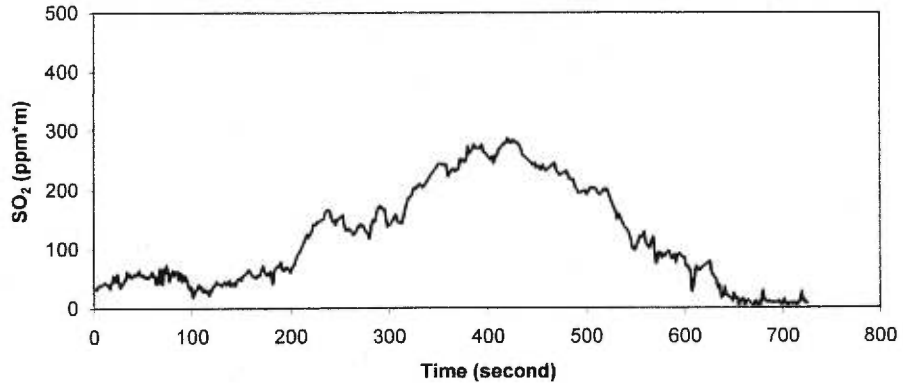
Spatial series 13e11, 98/03/13, El Crucero (15 km)



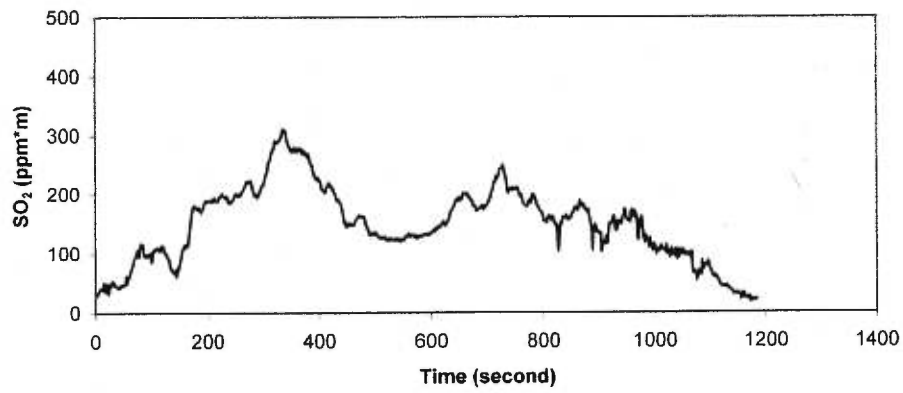
Spatial series 13e12, 98/03/13, El Crucero(15 km)



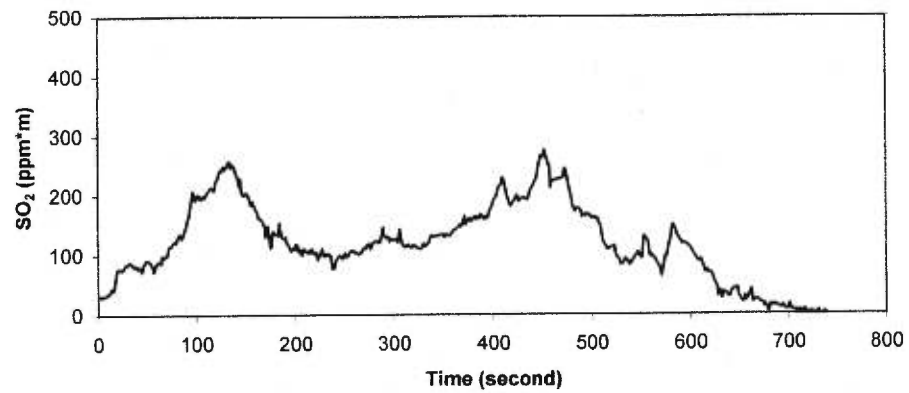
Spatial series 17e1, 98/03/17, El Crucero (15 km)



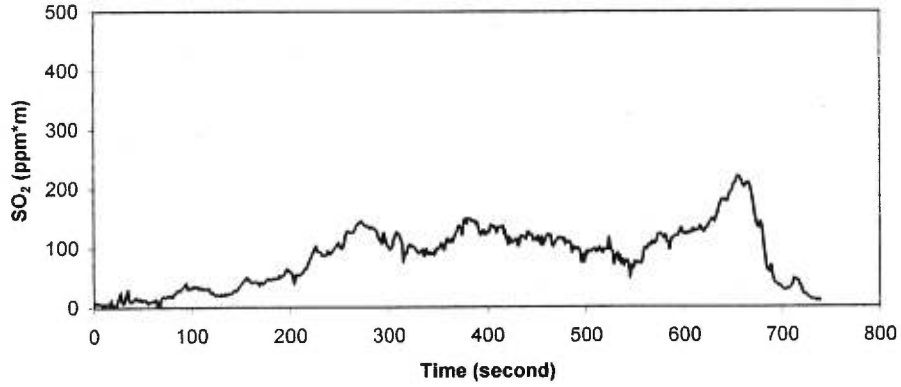
Spatial series 17e2, 98/03/17, El Crucero (15 km)



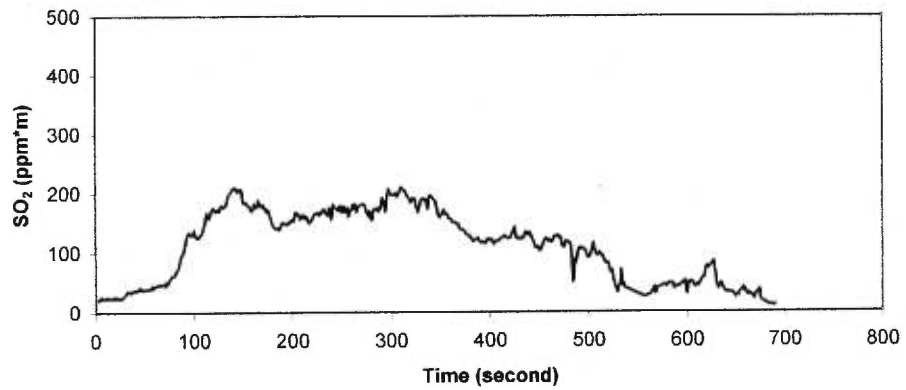
Spatial series 17e3, 98/03/17, El Crucero (15 km)



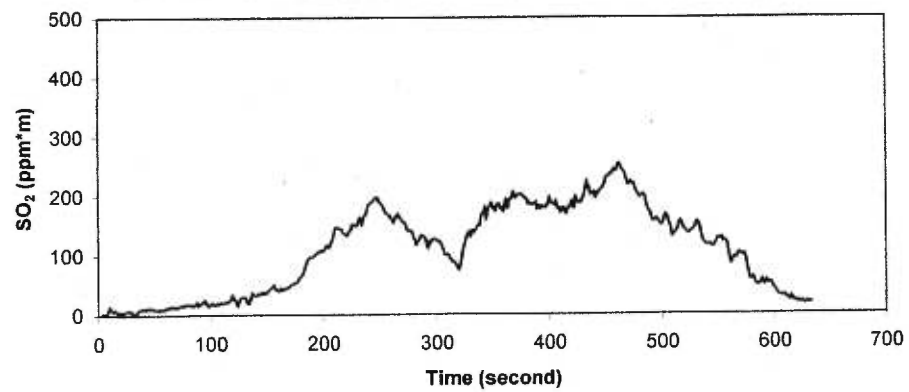
Spatial series 17e4, 98/03/17, El Crucero (15 km)



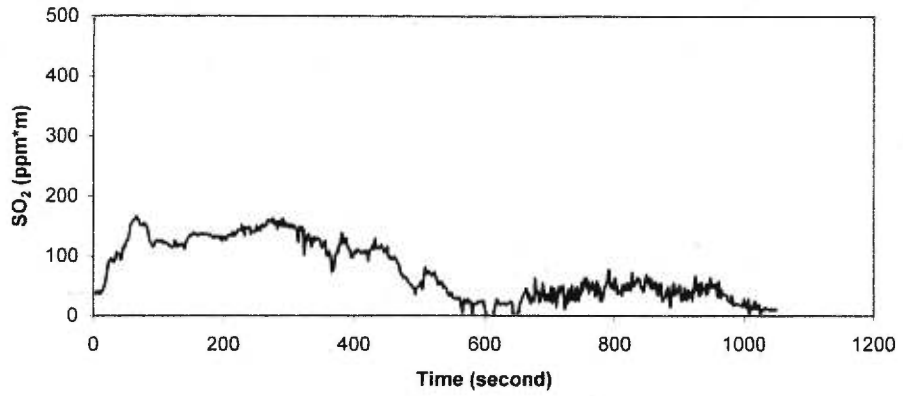
Spatial series 17e5, 98/03/17, El Crucero (15 km)



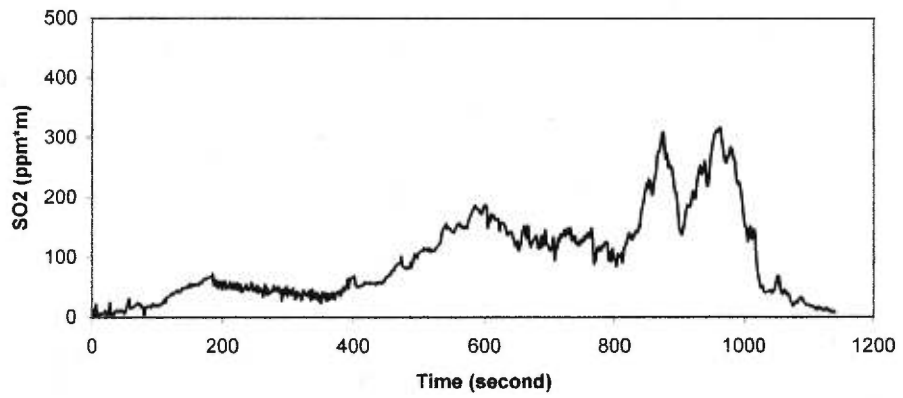
Spatial series 17e6, 98/03/17, El Crucero (15 km)



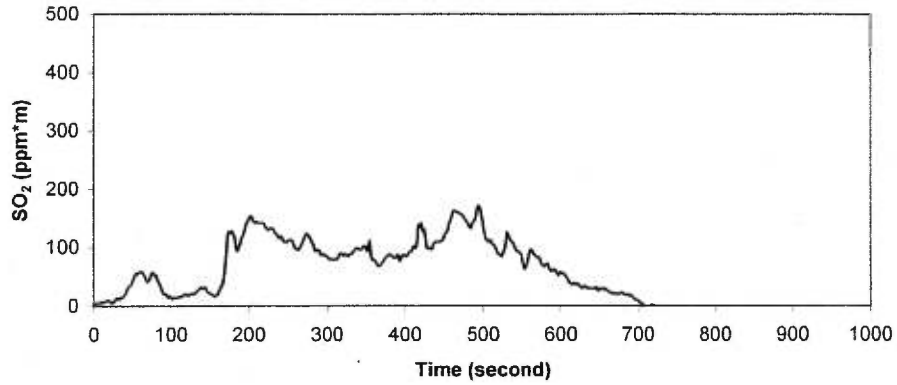
Spatial series 17e7, 98/03/17, El Crucero (15 km)



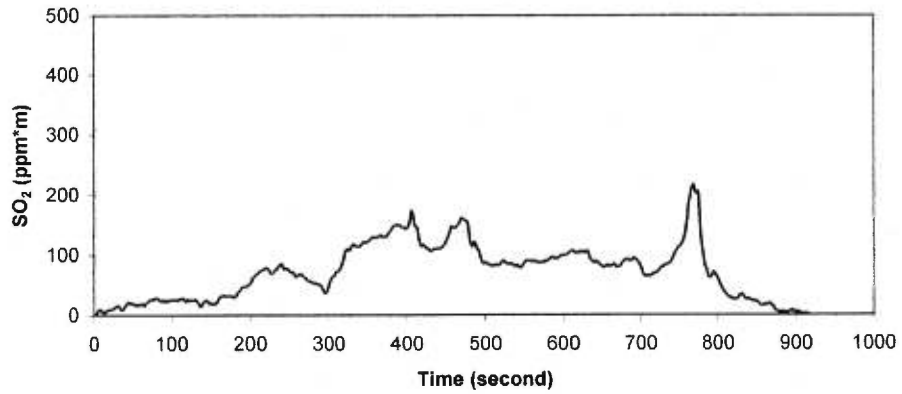
Spatial series 17e8, 98/03/17, El Crucero (15 km)



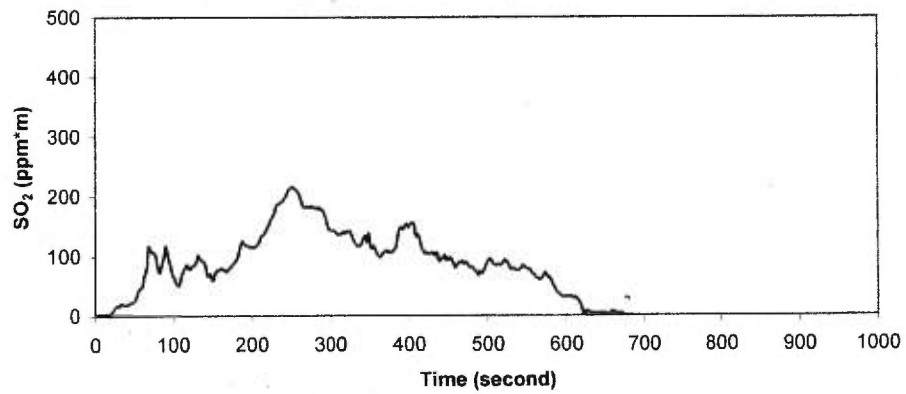
Spatial series 18e1, 98/03/18, El Crucero (15 km)



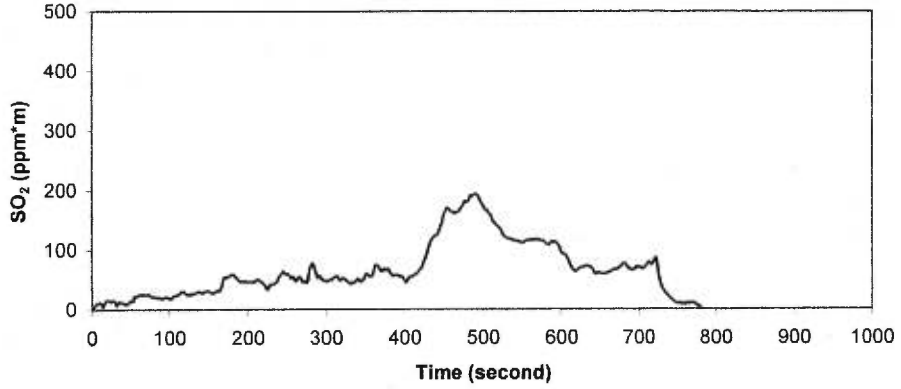
Spatial series 18e2, 98/03/18, El Crucero (15 km)



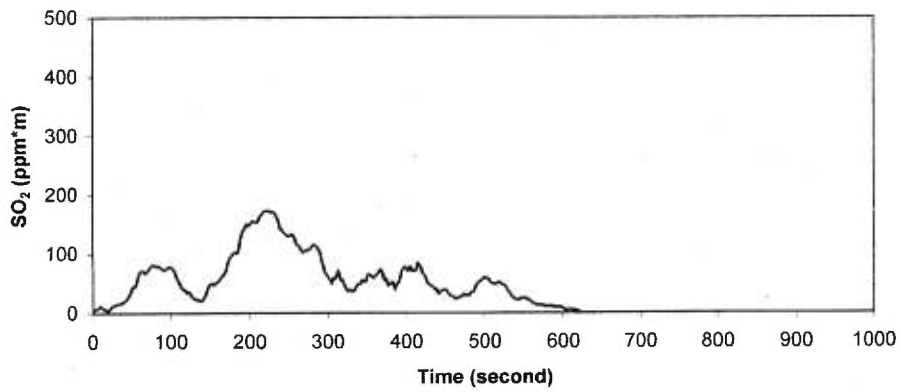
Spatial series 18e3, 98/03/18, El Crucero (15 km)



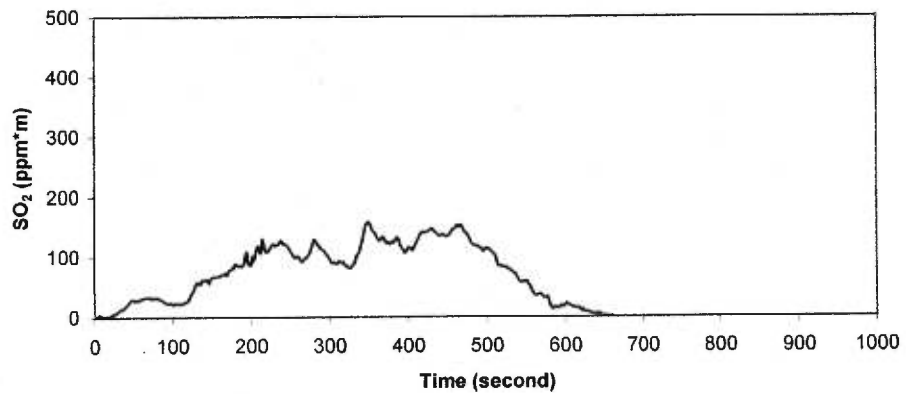
Spatial series 18e4, 98/03/18, El Crucero (15 km)



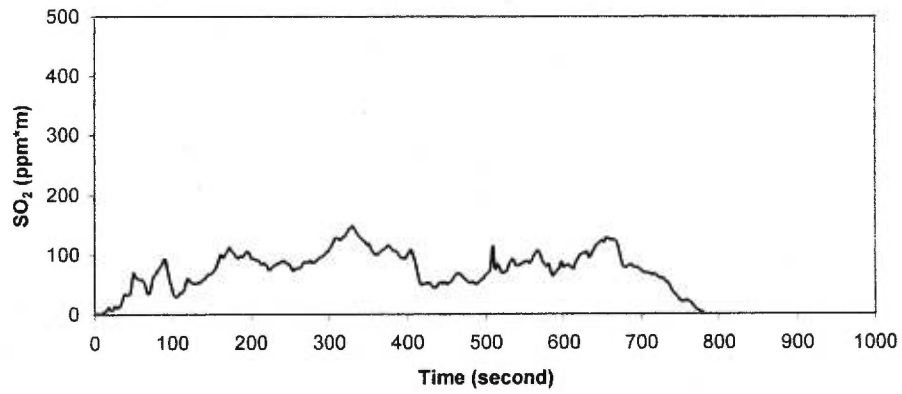
Spatial series 18e5, 98/03/18, El Crucero (15 km)



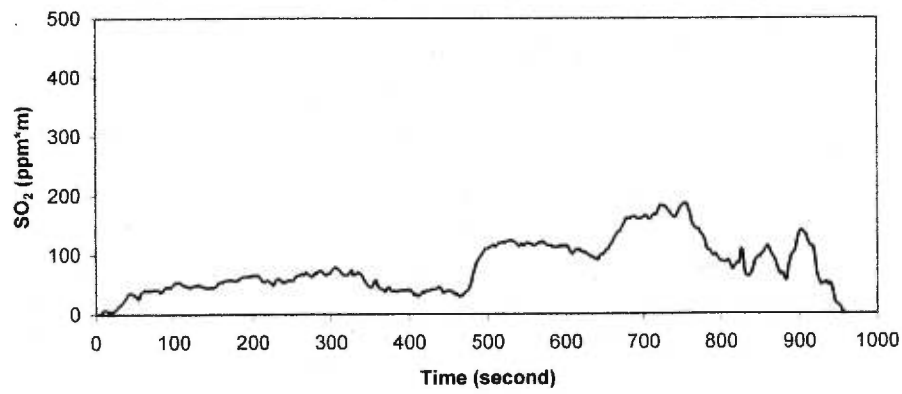
Spatial series 18e6, 98/03/18, El Crucero (15 km)



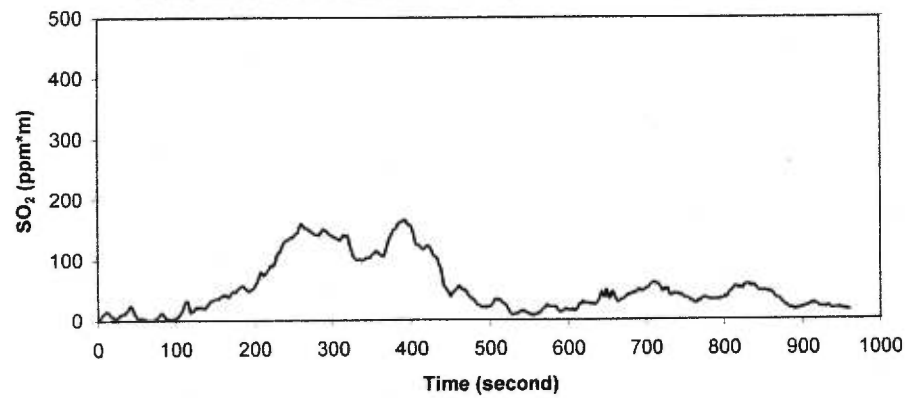
Spatial series 18e7, 98/03/18, El Crucero (15 km)



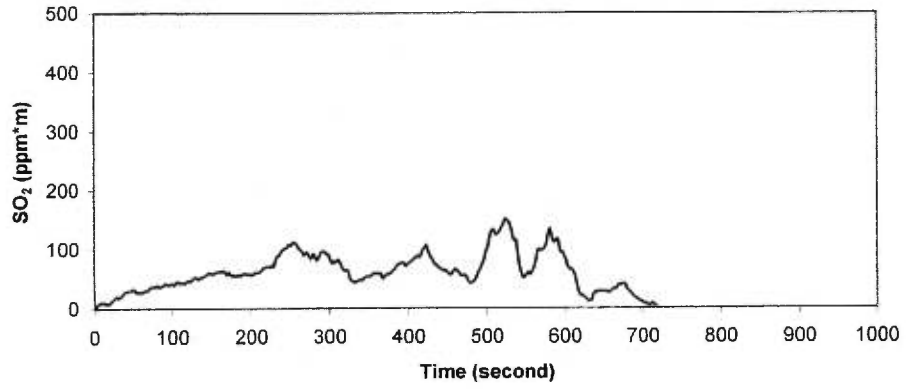
Spatial series 18e8, 98/03/18, El Crucero (15 km)



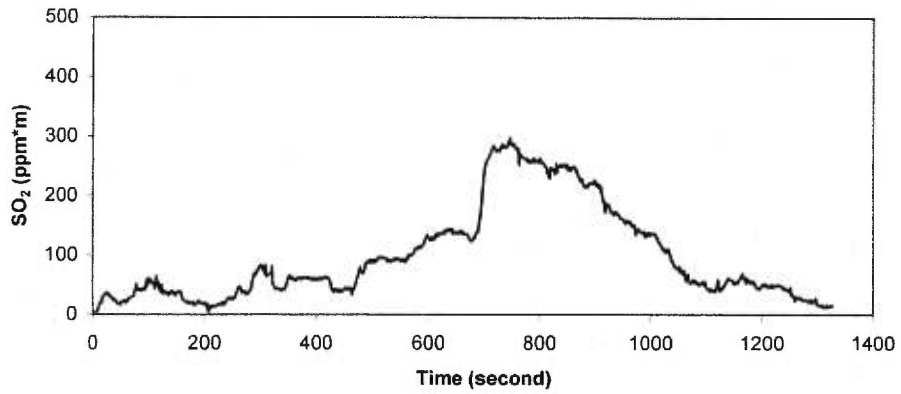
Spatial series 18e9, 98/03/18, El Crucero (15 km)



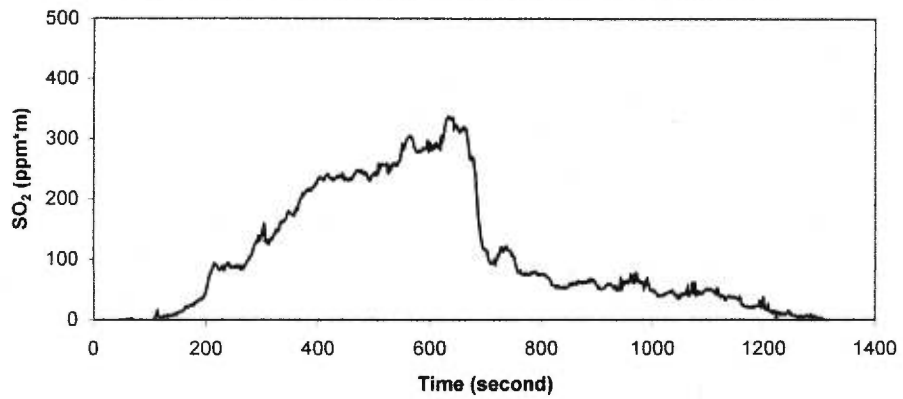
Spatial series 18e10, 98/03/18, El Crucero (15 km)



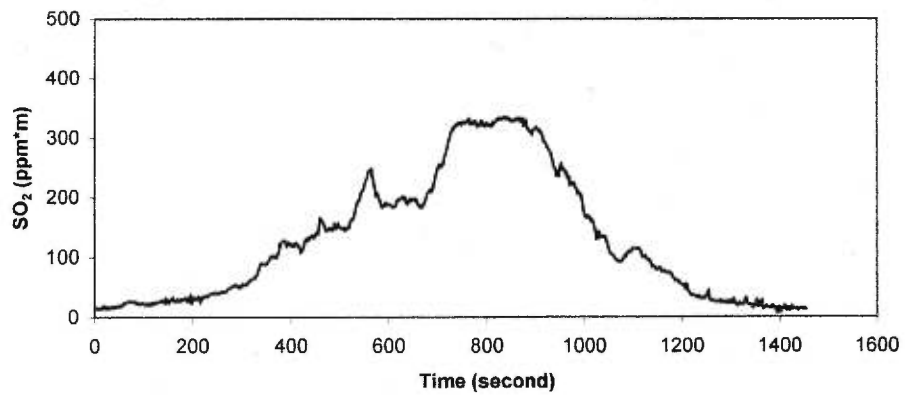
Spatial series 18m1, 98/03/18, Masachapa (30 km)



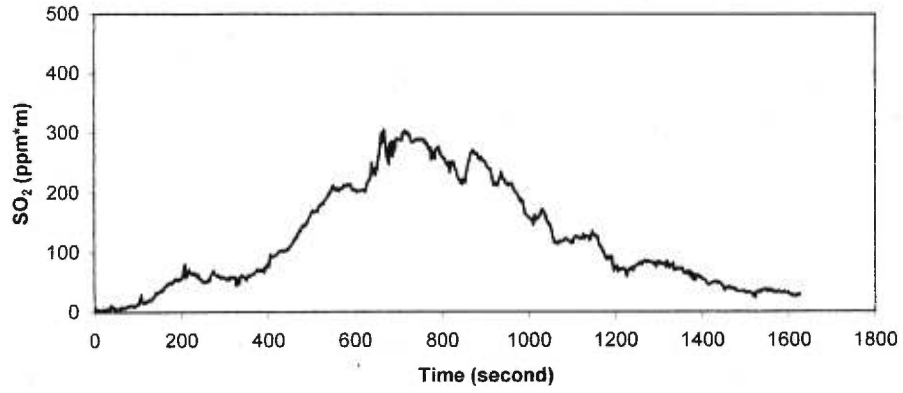
Spatial series 18m2, 98/03/18, Masachapa (30 km)



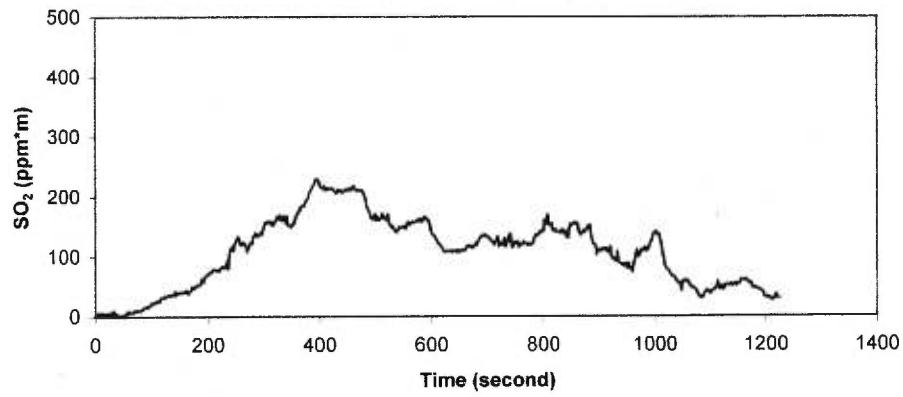
Spatial series 18m3, 98/03/18, Masachapa (30 km)



Spatial series 18m4, 98/03/18, Masachapa (30 km)



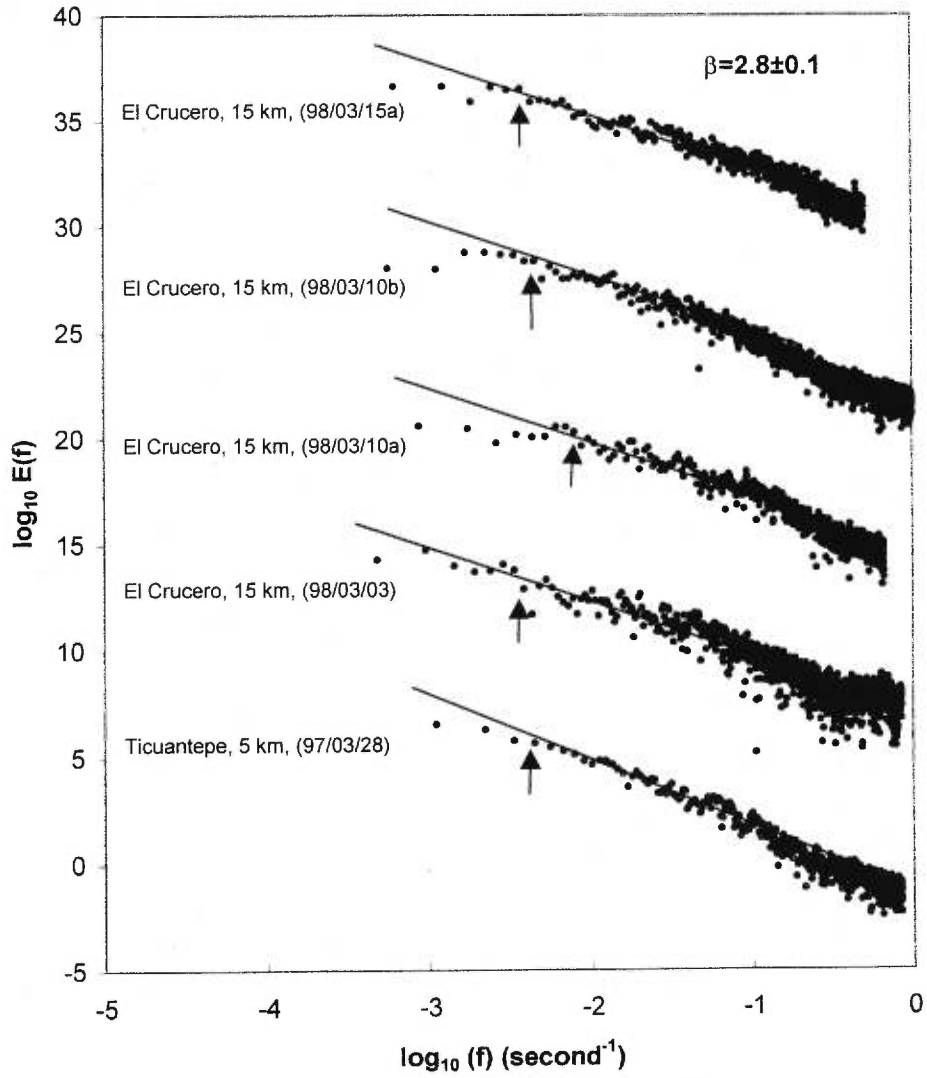
Spatial series 18m6, 98/03/18, Masachapa (30 km)



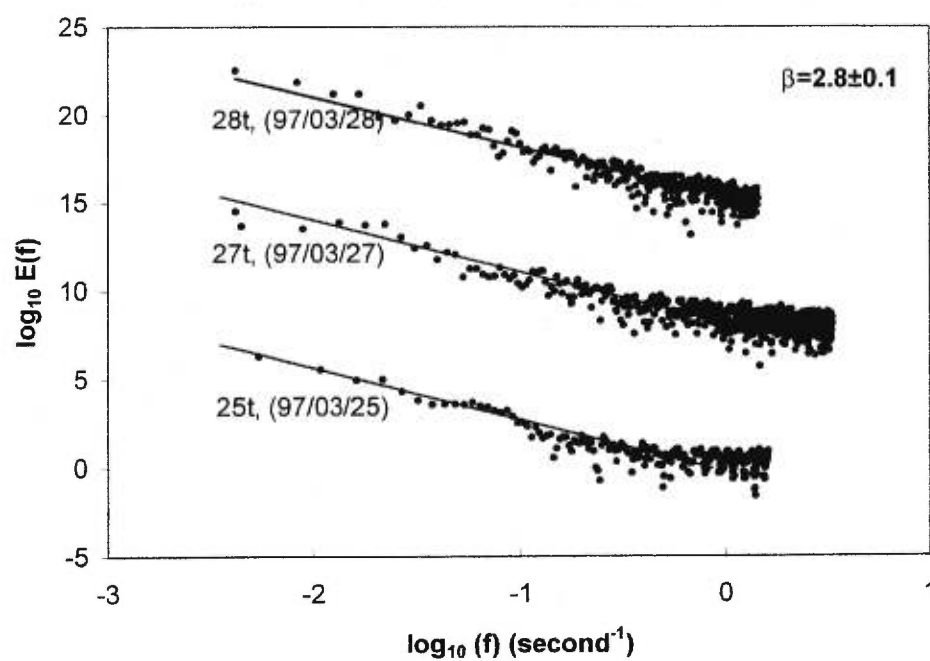
Appendix H

Power spectrum density of SO₂ signals from Masaya volcano.

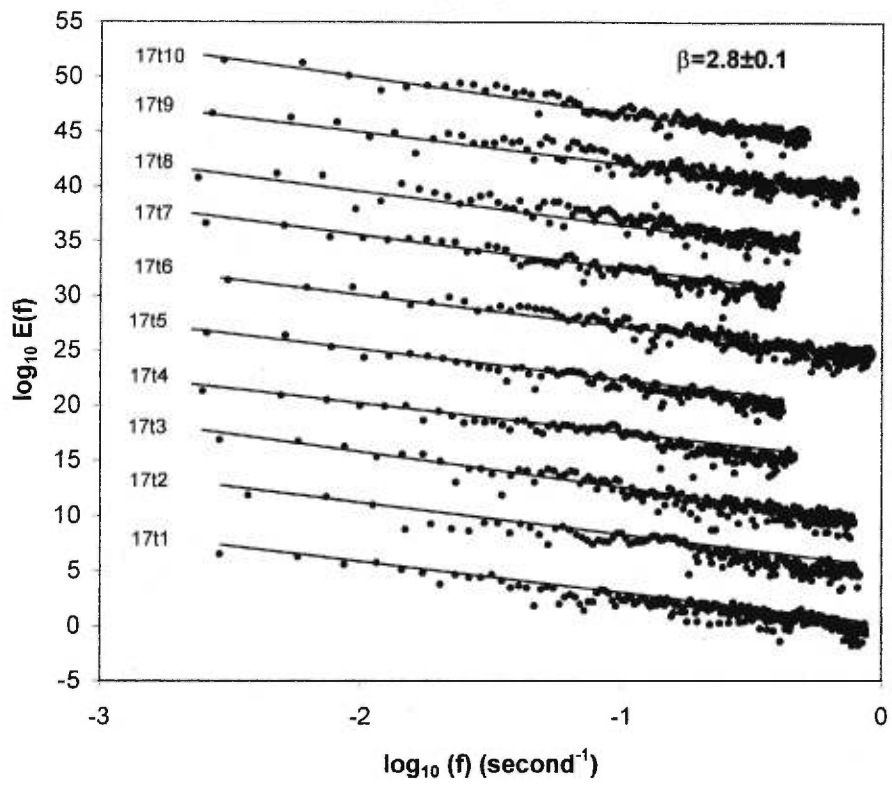
**Power spectrum densities,
temporal series**



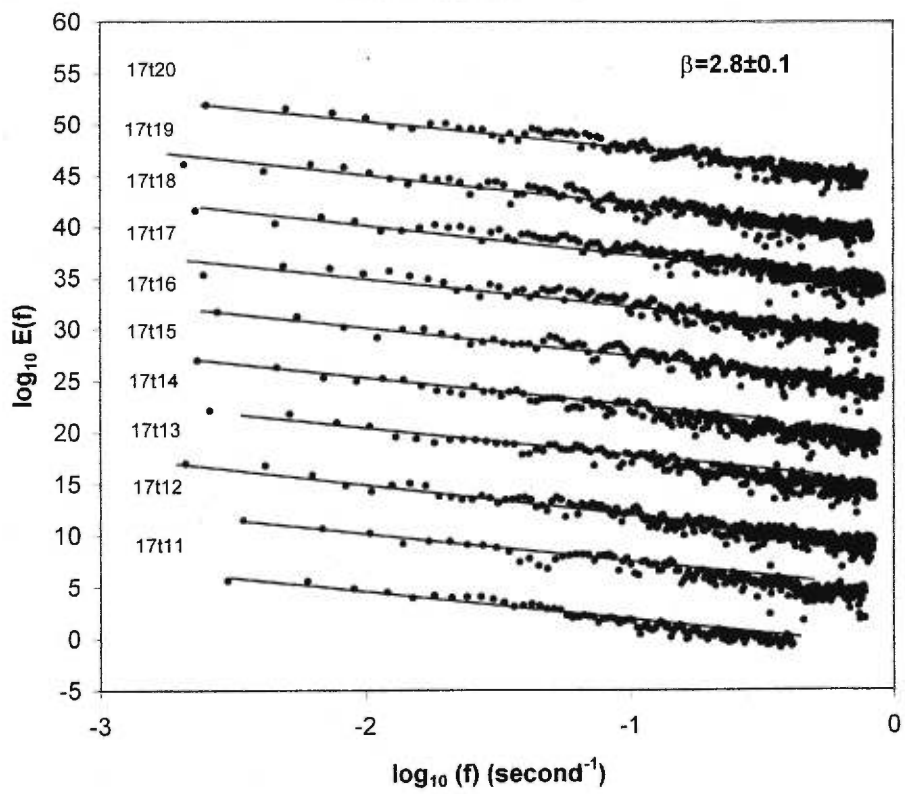
**Power spectrum densities,
spatial series, Tiquantepe (5 km)**



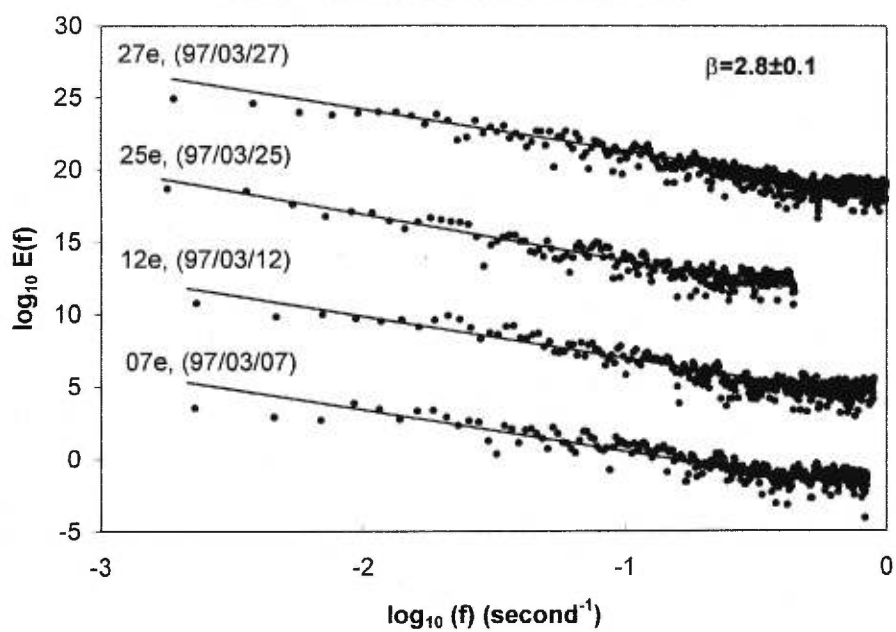
Power spectrum densities, spatial series 98/03/17,
Ticuantepe (5 km)



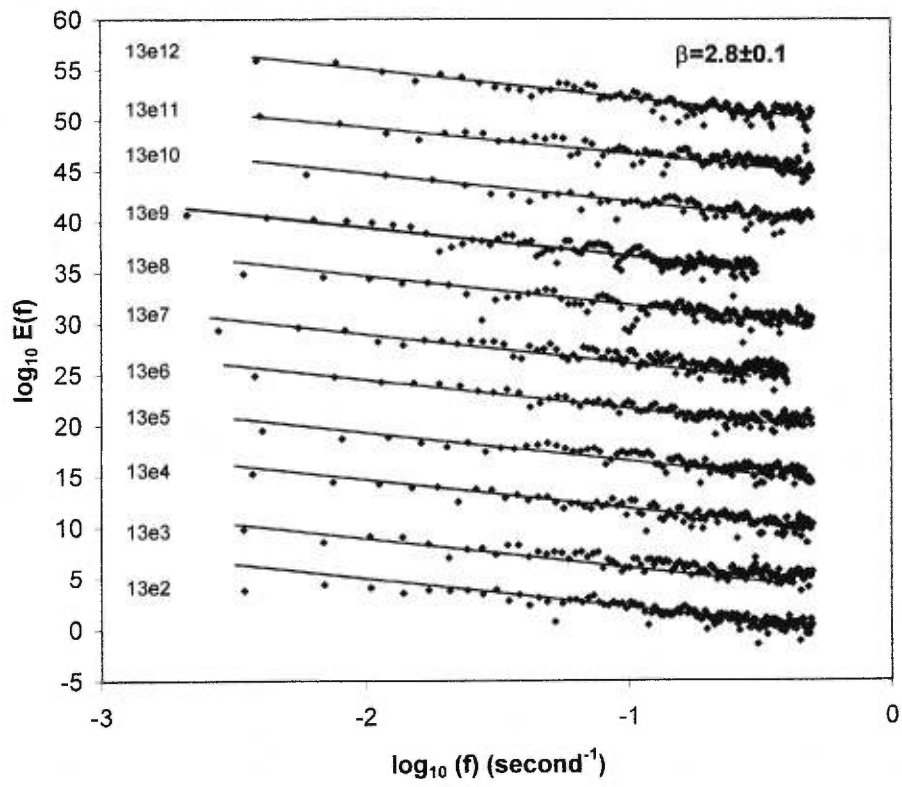
Power spectrum densities, spatial series 98/03/17,
Ticuantepé (5 km)



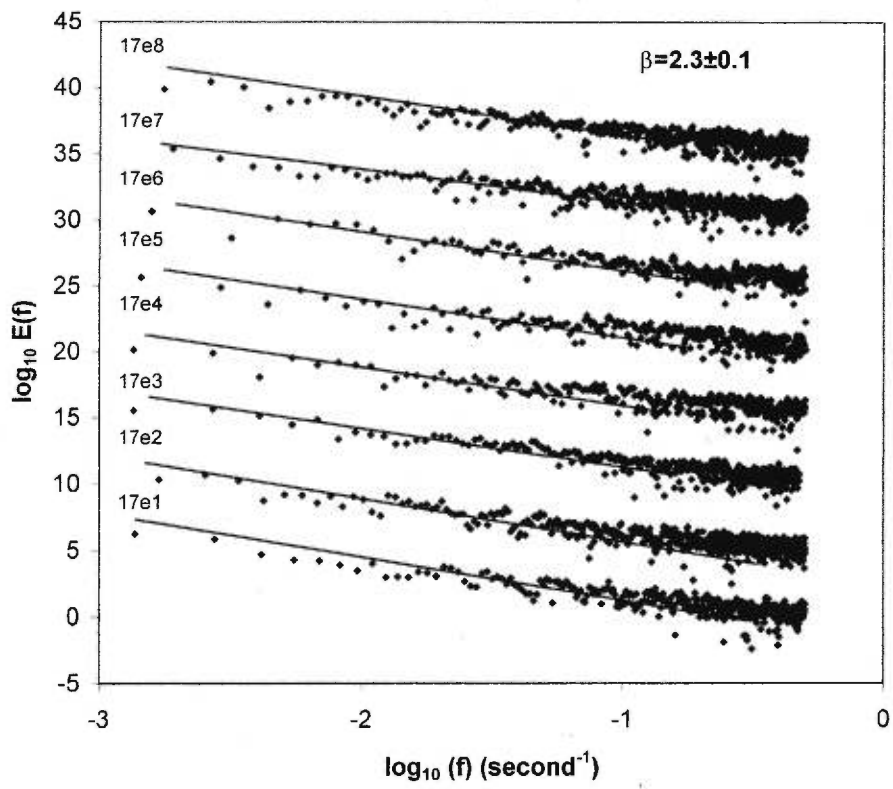
Power spectrum densities,
spatial series, El Crucero (15 km)



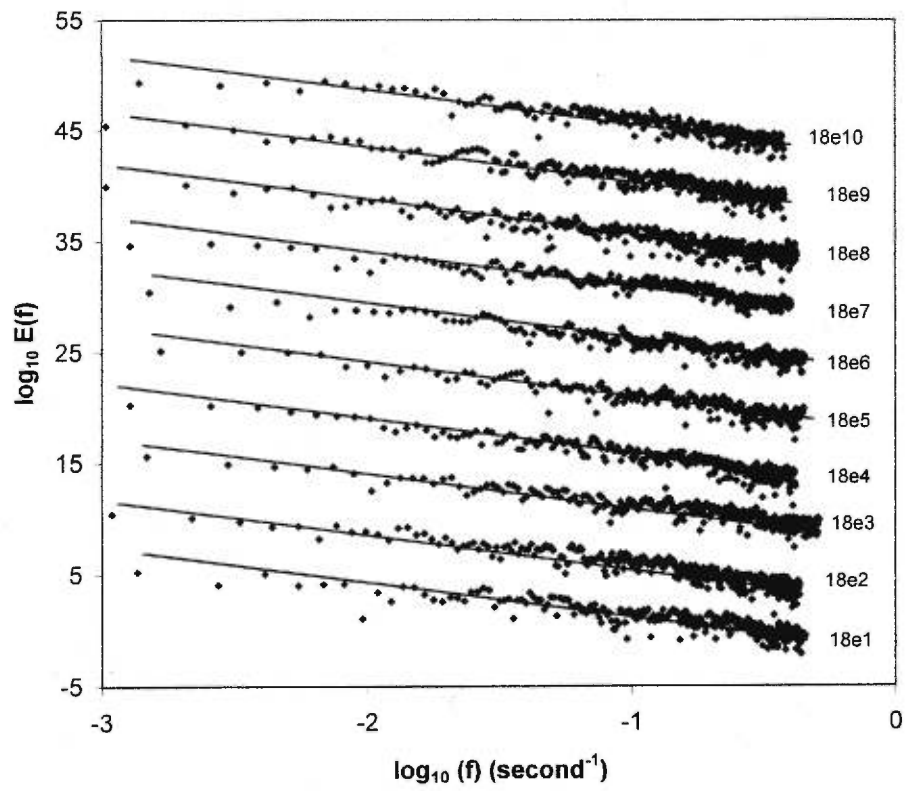
Power spectrum densities, spatial series 98/03/13,
El Crucero (15 km)



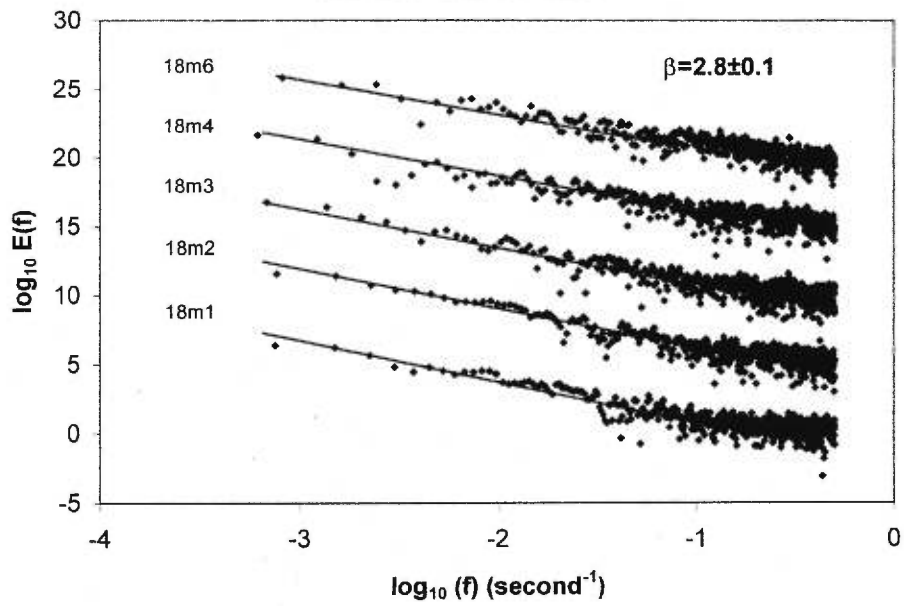
Power spectrum densities, spatial series 98/03/17,
El Crucero (15 km)



Power spectrum densities, spatial series 98/03/18,
El Crucero (15 km)



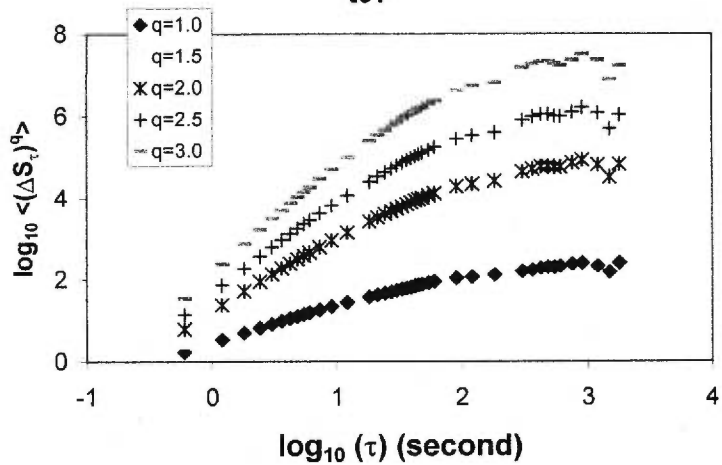
Power spectrum densities, spatial series 98/03/18,
Masachapa (30 km)



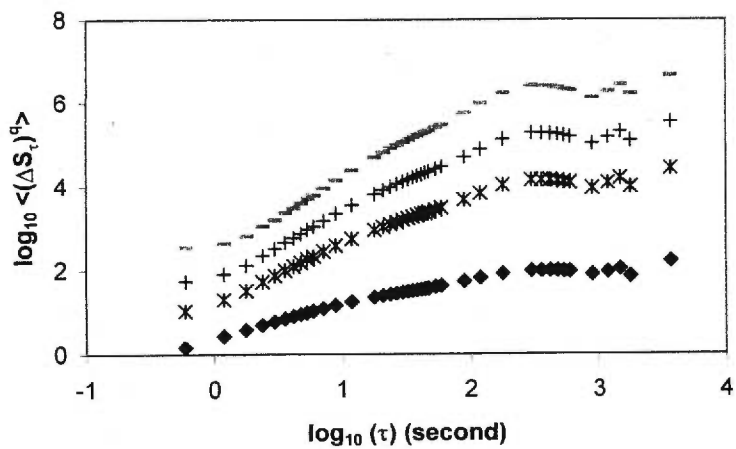
Appendix I

**Structure functions analysis of SO₂ signals from Masaya volcano.
(Legend of the first chart applies to the rest of the appendix I)**

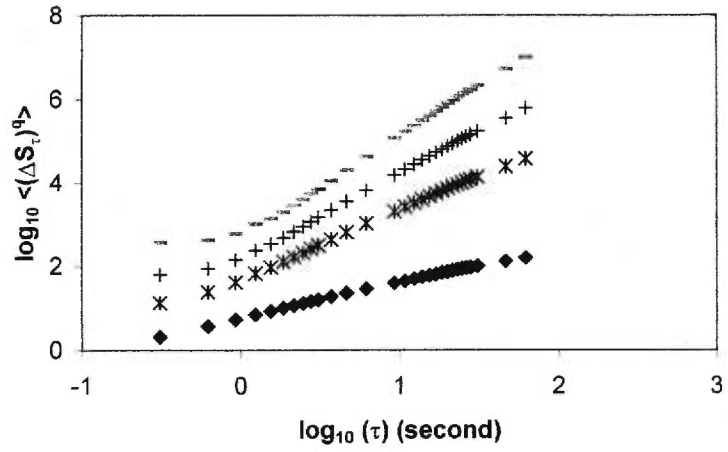
Structure functions, Tiquantepe (5 km)
t97



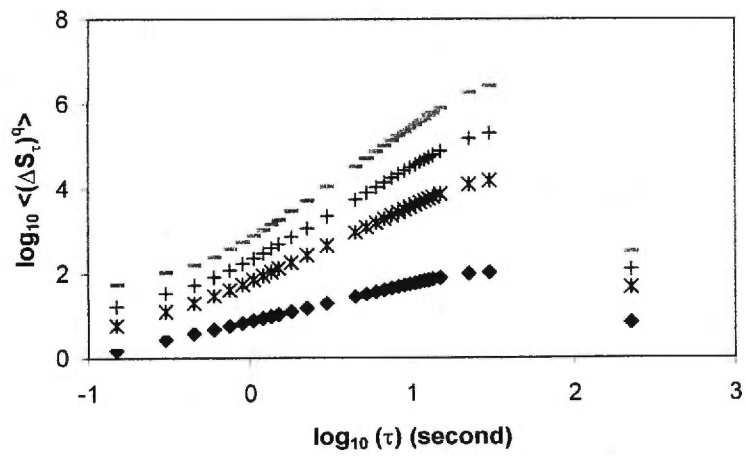
Structure functions, El Crucero (30 km)
e03



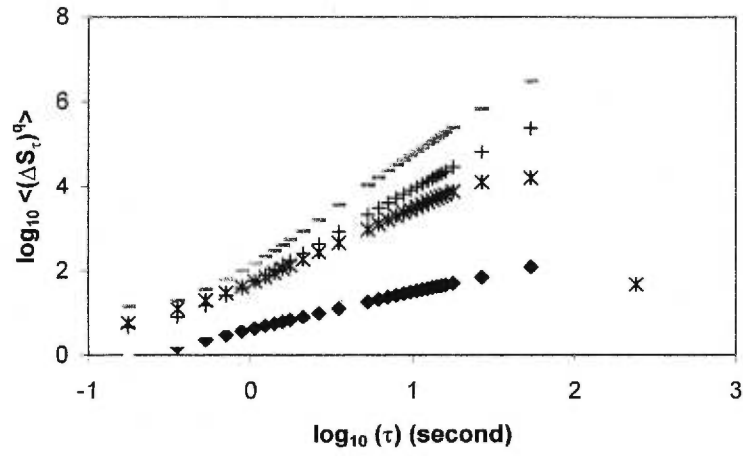
Structure functions, Ticuantepe (5 km)
25t



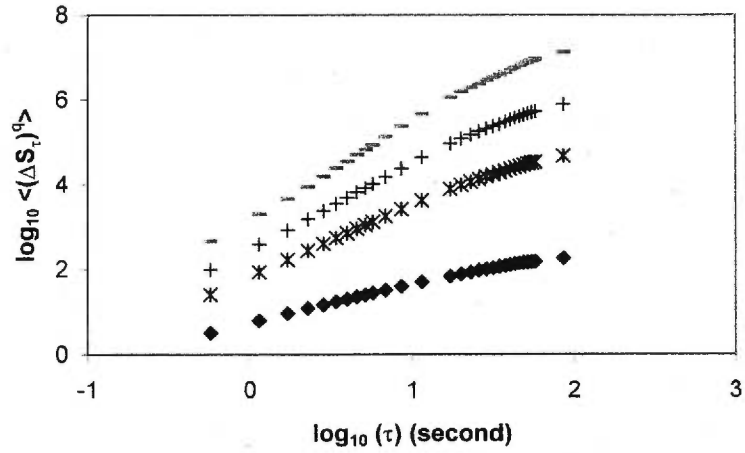
Structure functions, Ticuantepe (5 km)
27t



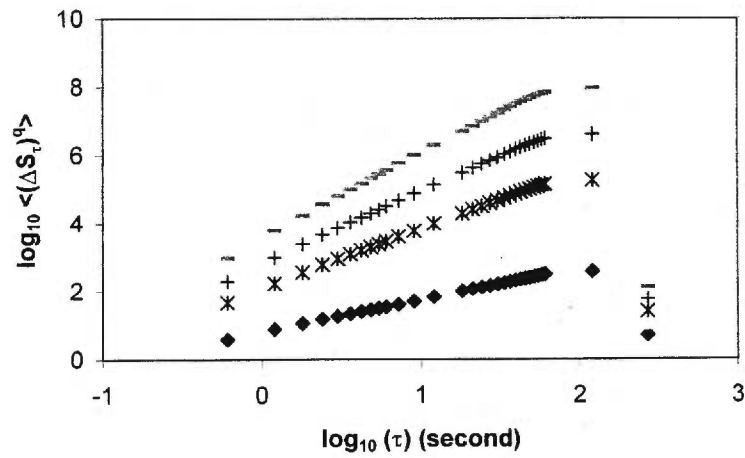
Structure functions, Ticuantepe (5 km)
28t



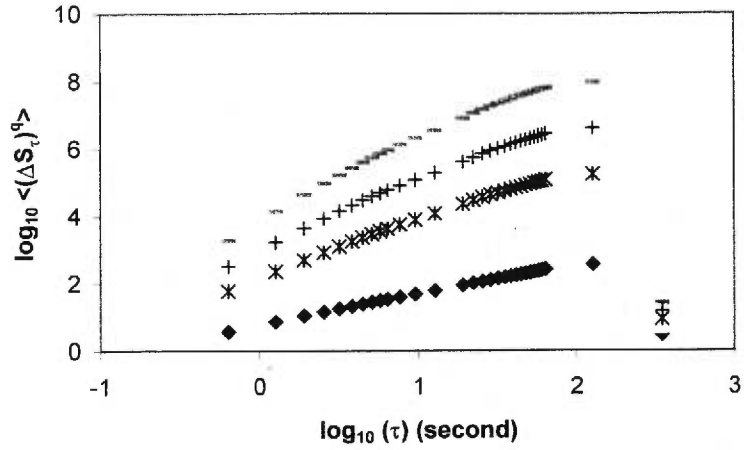
Structure functions, Ticuantepe (5 km)
17t1



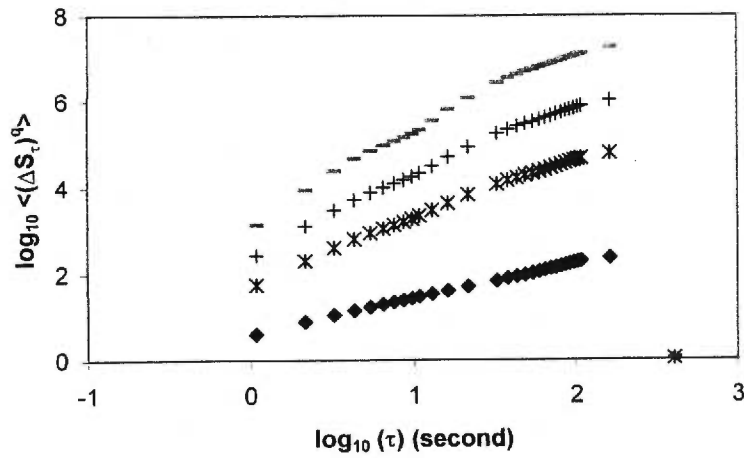
Structure functions, Ticuantepe (5 km)
17t2



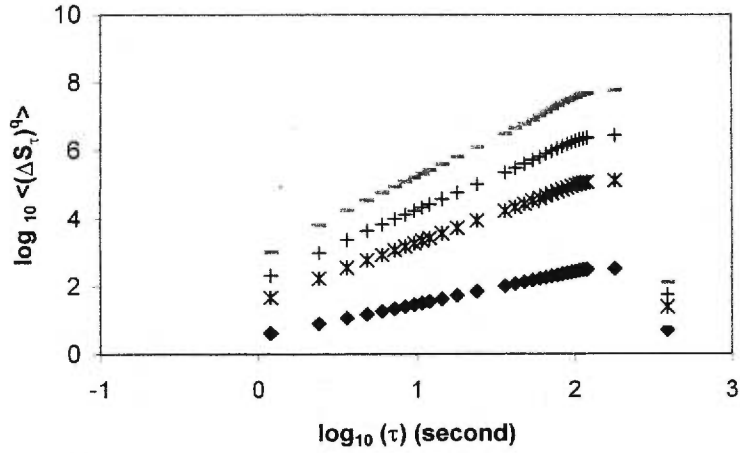
Structure functions, Ticuantepe (5 km)
17t3



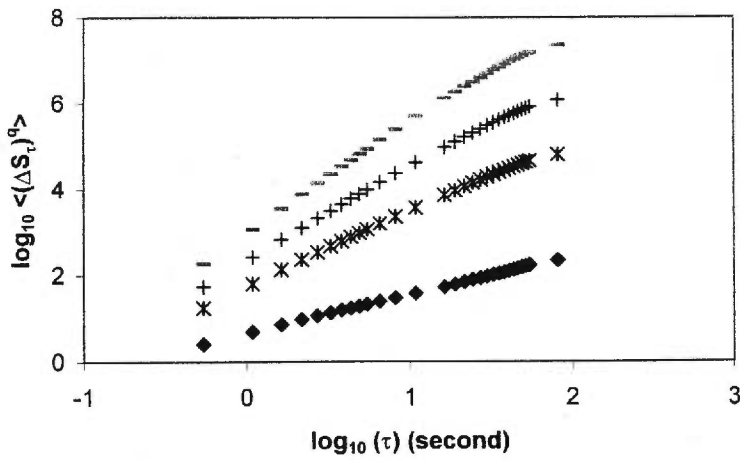
Structure functions, Ticuantepe (5 km)
17t4



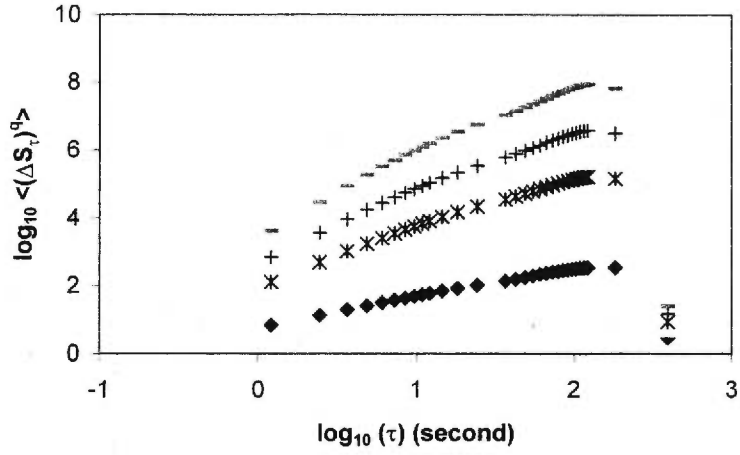
Structure functions, Ticuantepe (5 km)
17t5



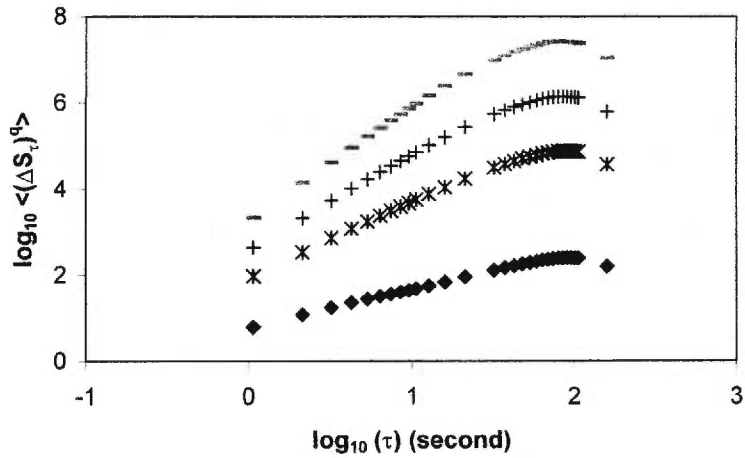
Structure functions, Ticuantepe (5 km)
17t6



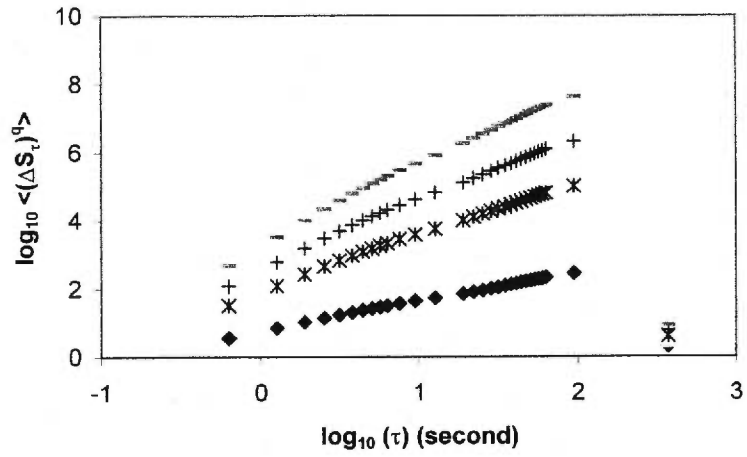
Structure functions, Ticuantepe (5 km)
17t7



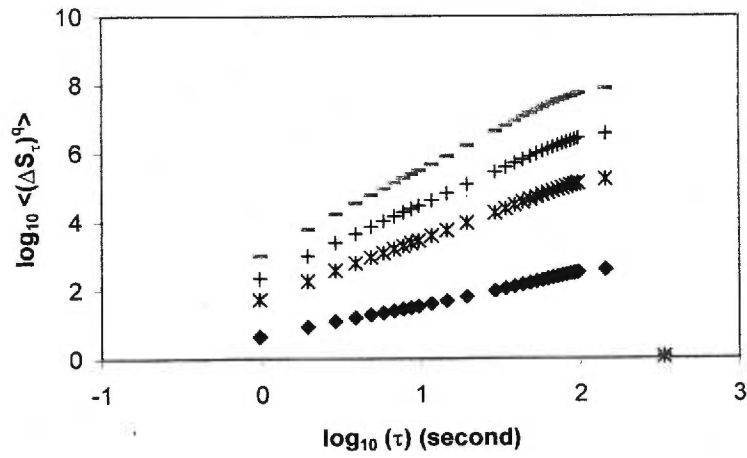
Structure functions, Ticuantepe (5 km)
17t8



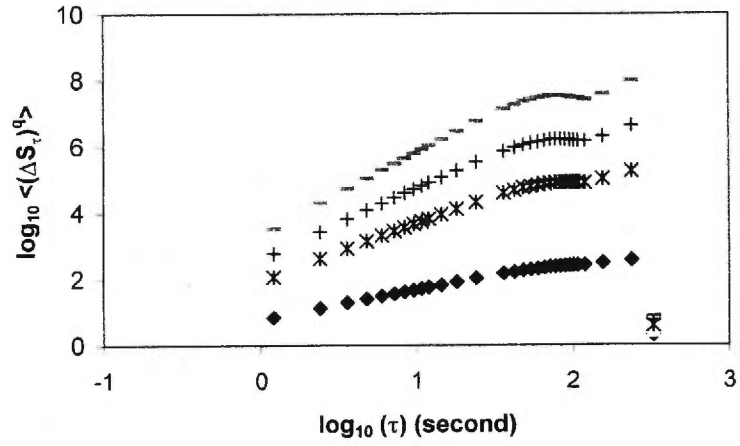
Structure functions, Ticuantepe (5 km)
17t9



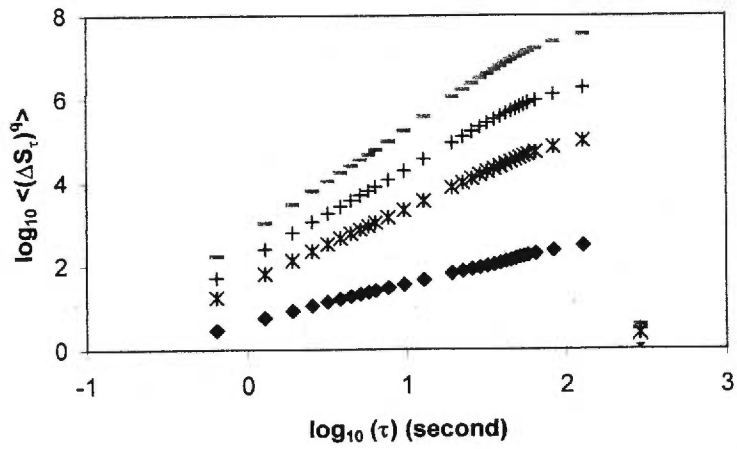
Structure functions, Ticuantepe (5 km)
17t10



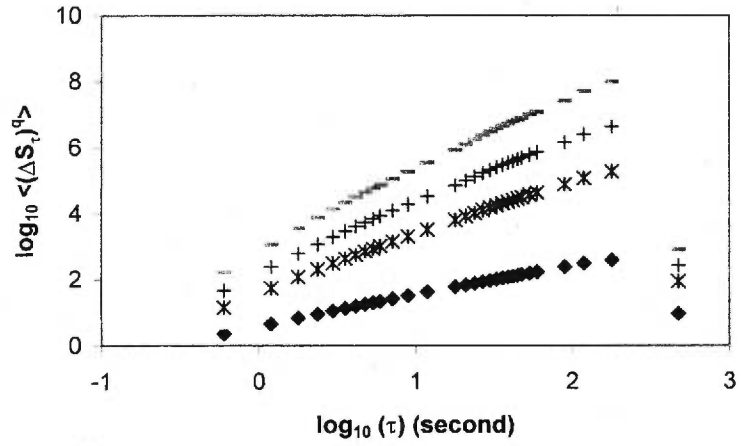
Structure functions, Ticuantepe (5 km)
17t11



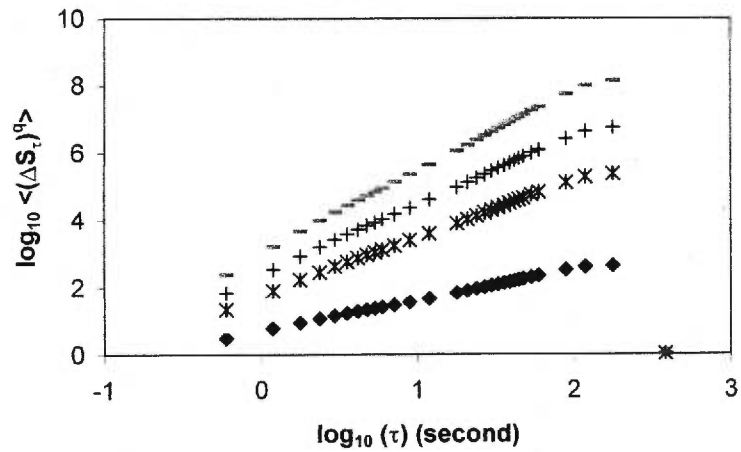
Structure functions, Ticuantepe (5 km)
17t12



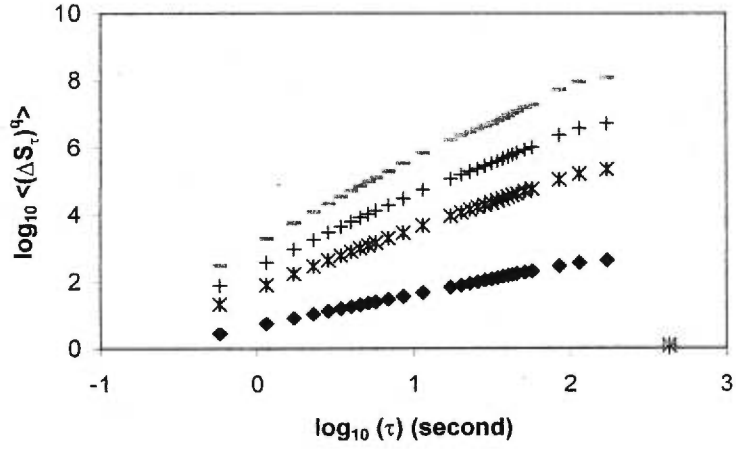
Structure functions, Ticuantepe (5 km)
17t13



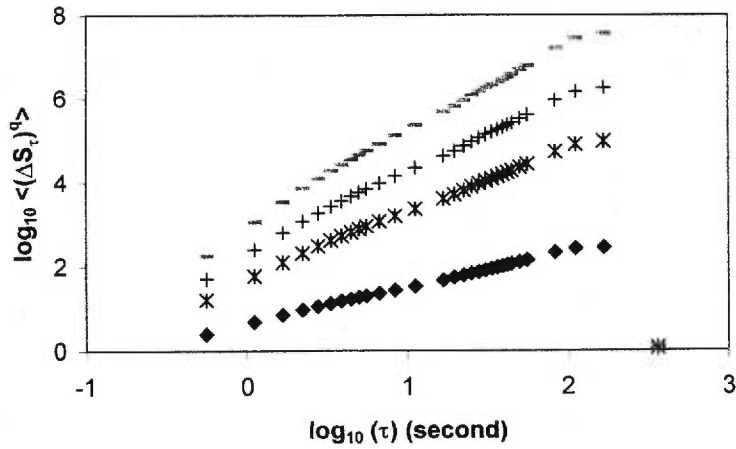
Structure functions, Ticuantepe (5 km)
17t14



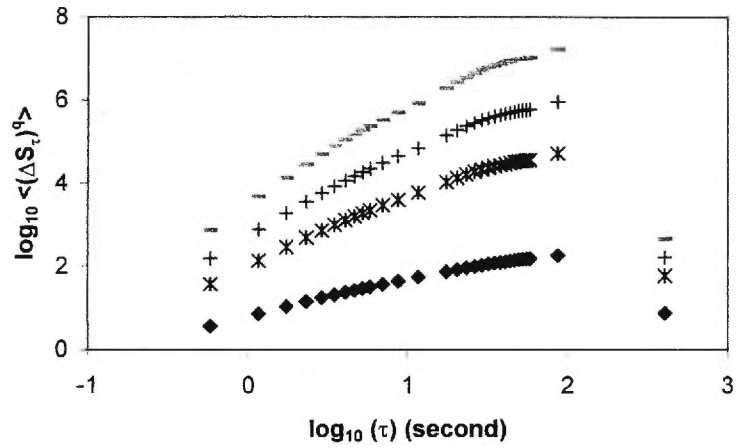
Structure functions, Ticuantepe (5 km)
17t15



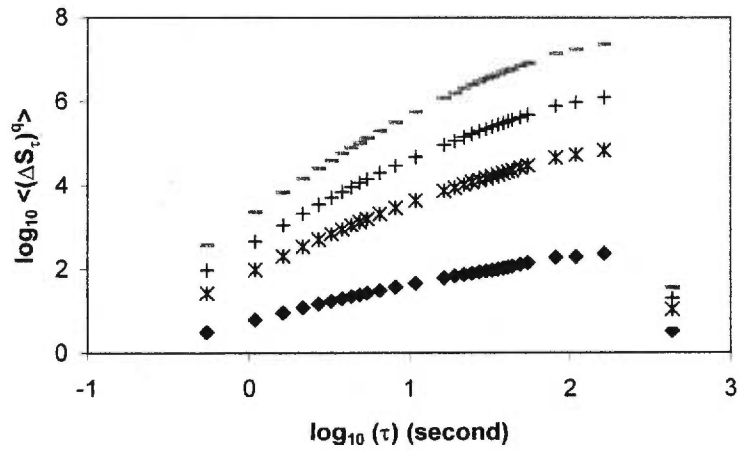
Structure functions, Ticuantepe (5 km)
17t16



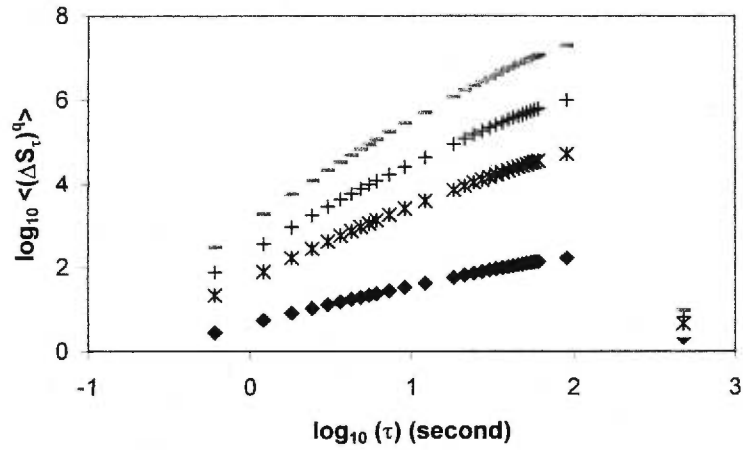
Structure functions, Ticuantepe (5 km)
17t17



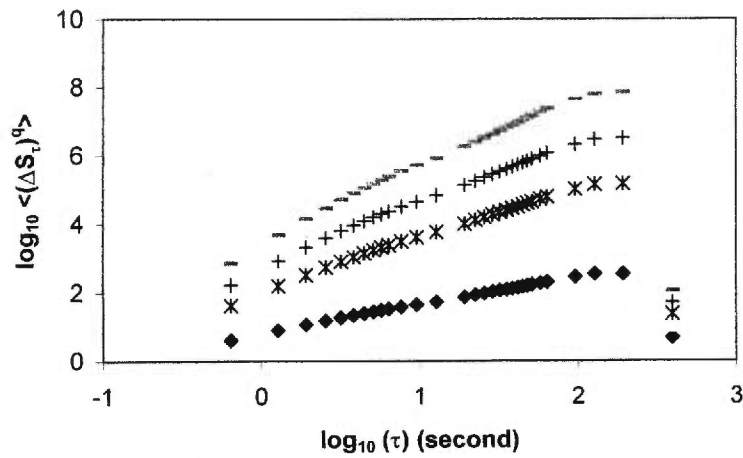
Structure functions, Ticuantepe (5 km)
17t18



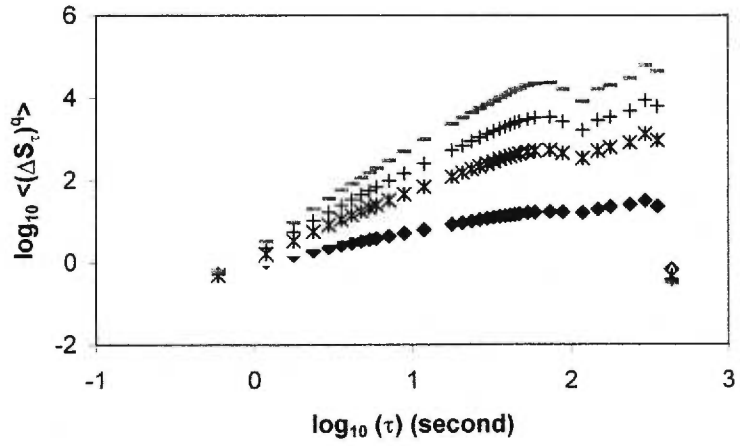
Structure functions, Ticuantepe (5 km)
17t19



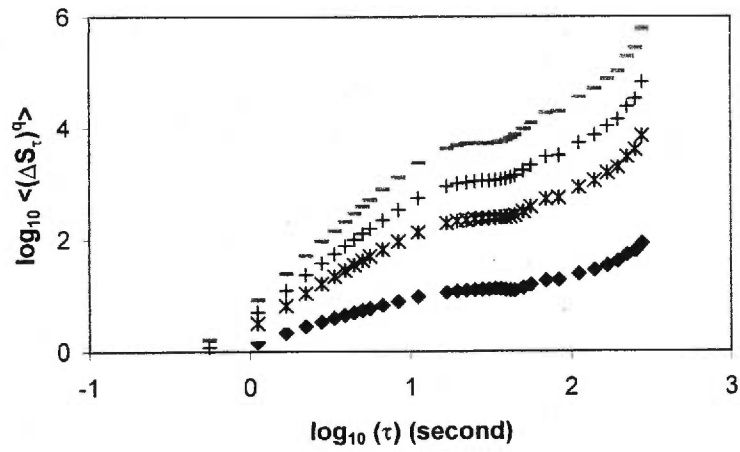
Structure functions, Ticuantepe (5 km)
17t20



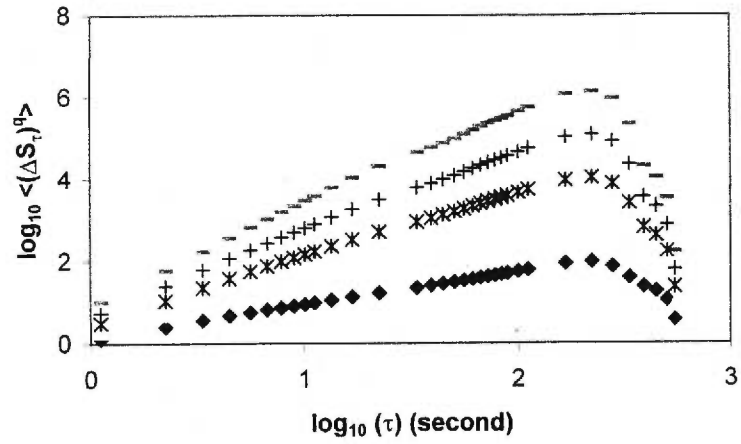
Structure functions, El Crucero (15 km)
7e



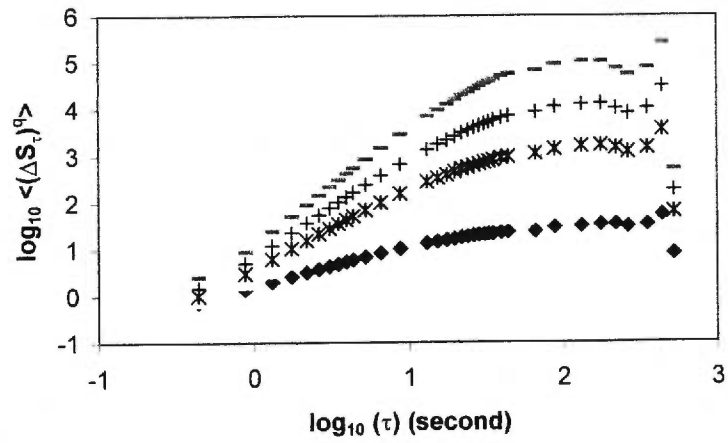
Structure functions, El Crucero (15 km)
12e



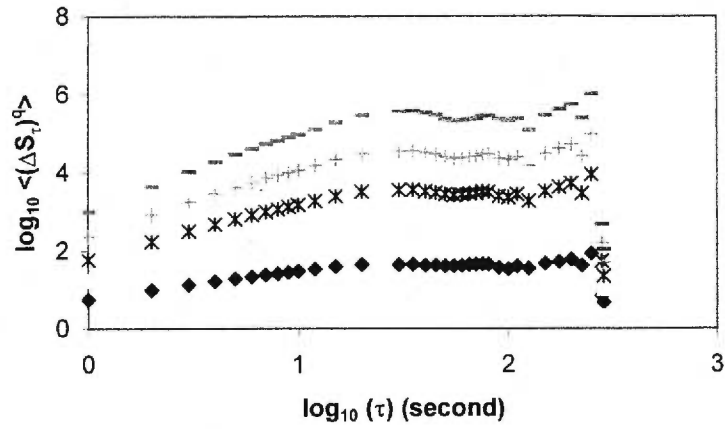
Structure functions, El Crucero (15 km)
25e



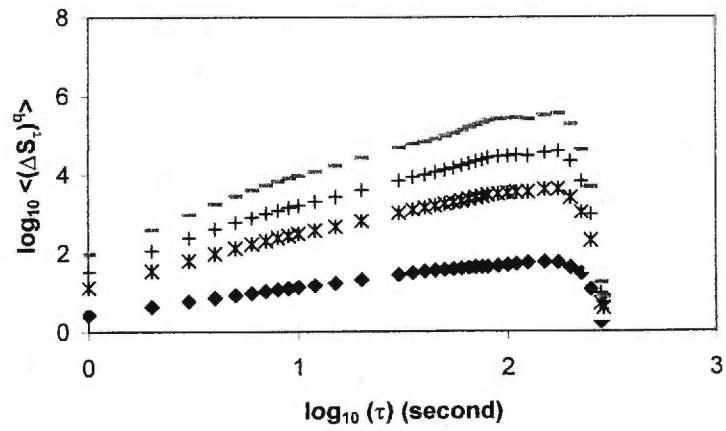
Structure functions, El Crucero (15 km)
27e



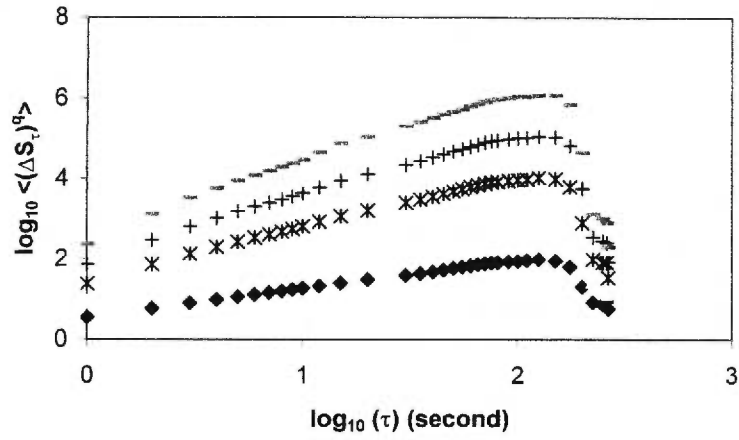
Structure functions, El Crucero (15 km)
13e2



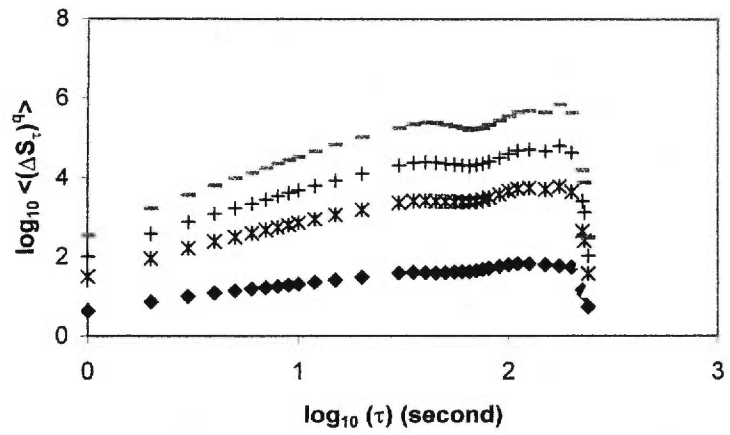
Structure functions, El Crucero (15 km)
13e3



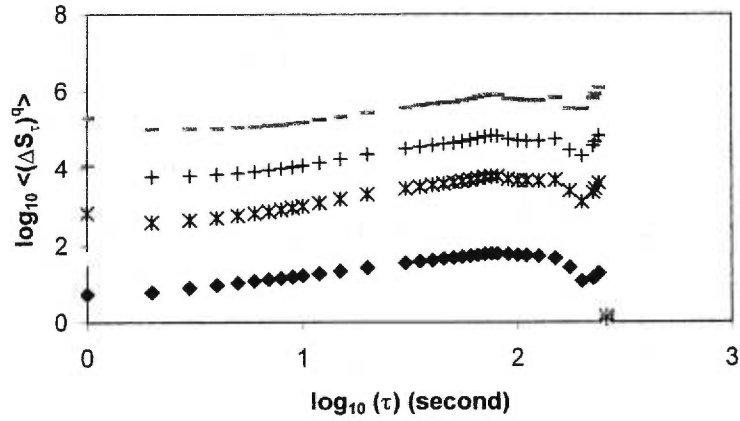
Structure functions, El Crucero (15 km)
13e4



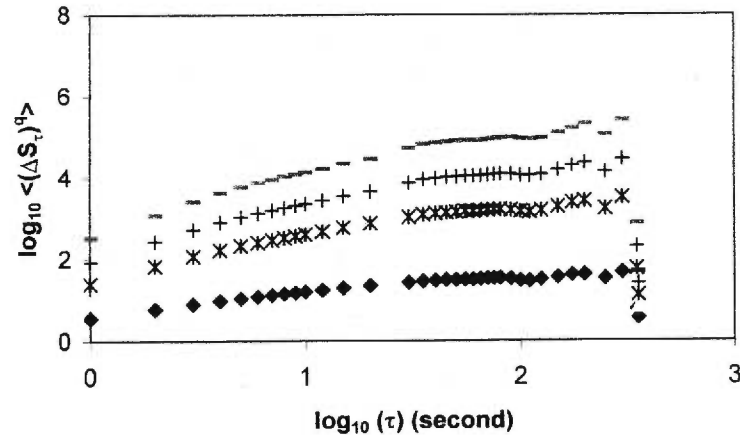
Structure functions, El Crucero (15 km)
13e5



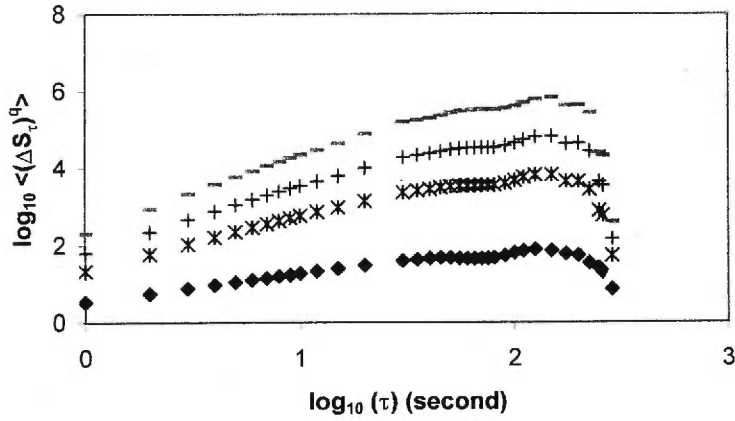
Structure functions, El Crucero (15 km)
13e6



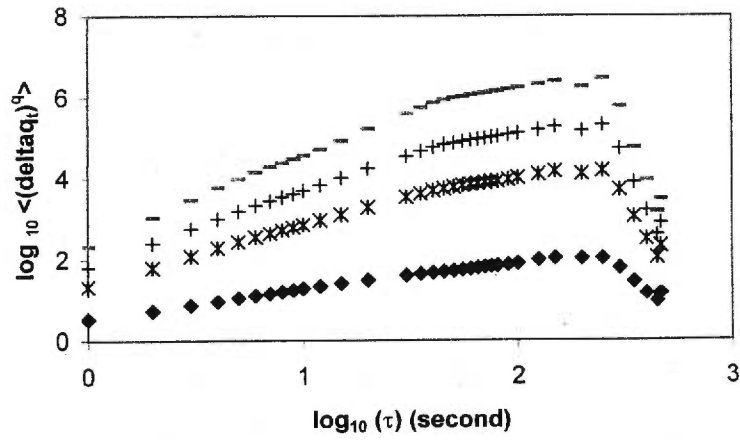
Structure functions, El Crucero (15 km)
13e7



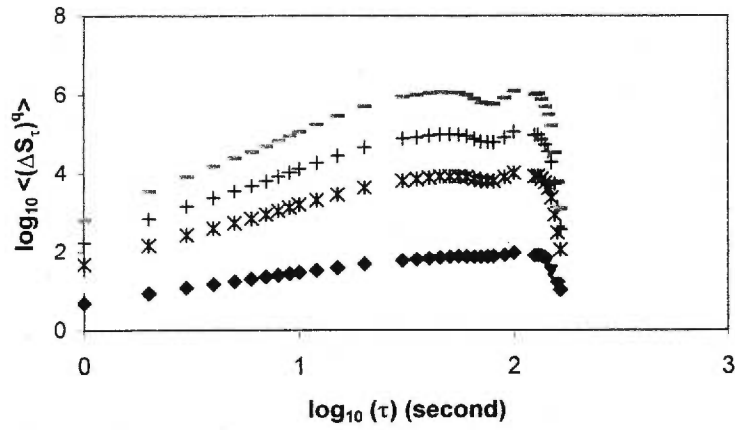
Structure functions, El Crucero (15 km)
13e8



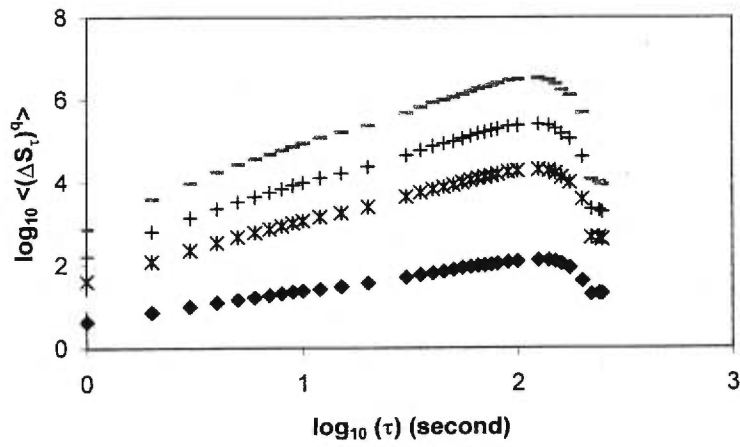
Structure functions, El Crucero (15 km)
13e9



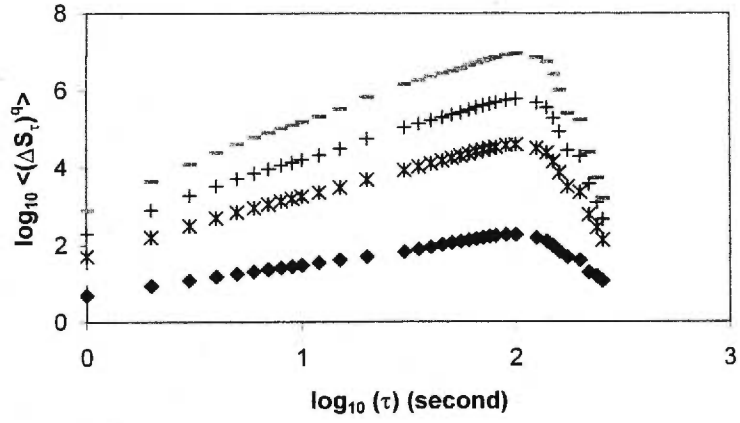
Structure functions, El Crucero (15 km)
13e10



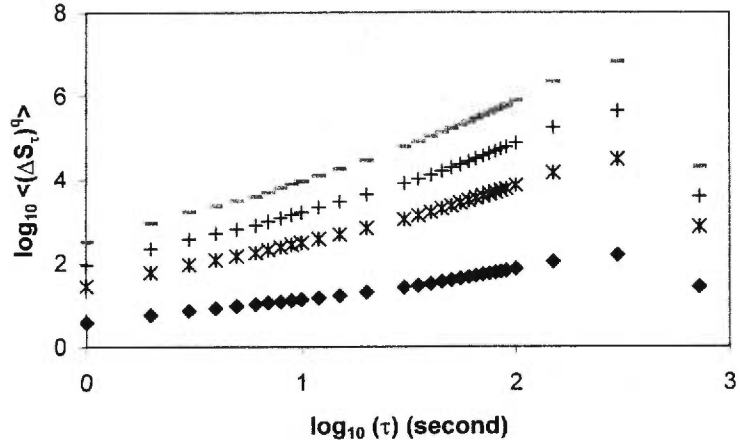
Structure functions, El Crucero (15 km)
13e11



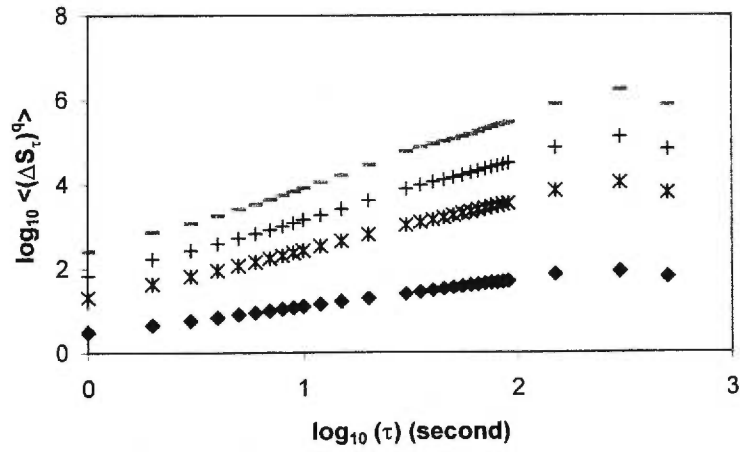
Structure functions, El Crucero (15 km)
13e12



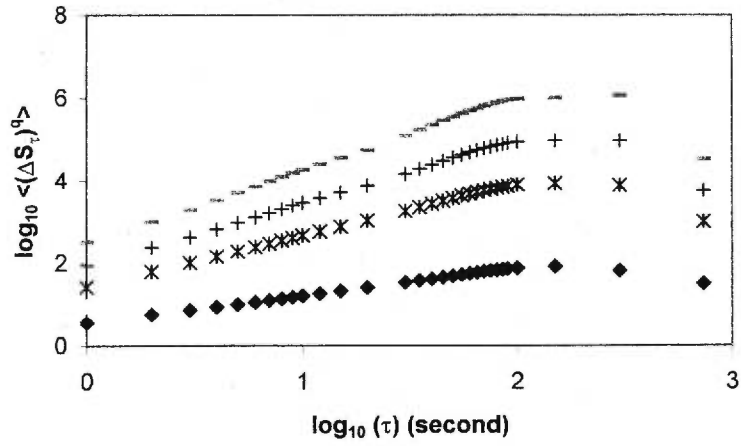
Structure functions, El Crucero (15 km)
17e1



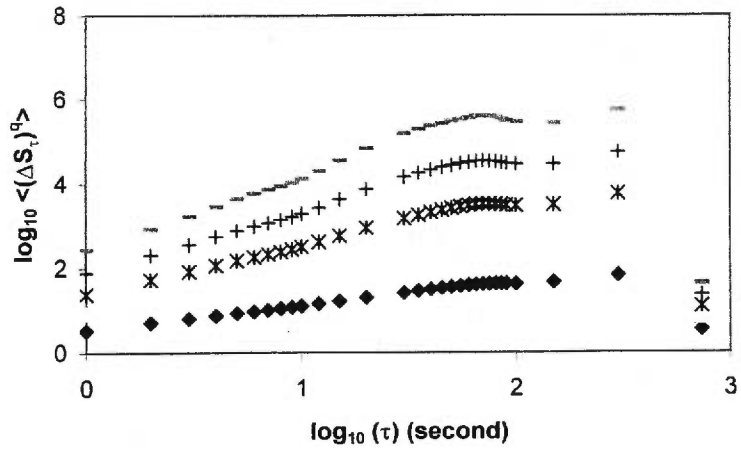
Structure functions, El Crucero (15 km)
17e2



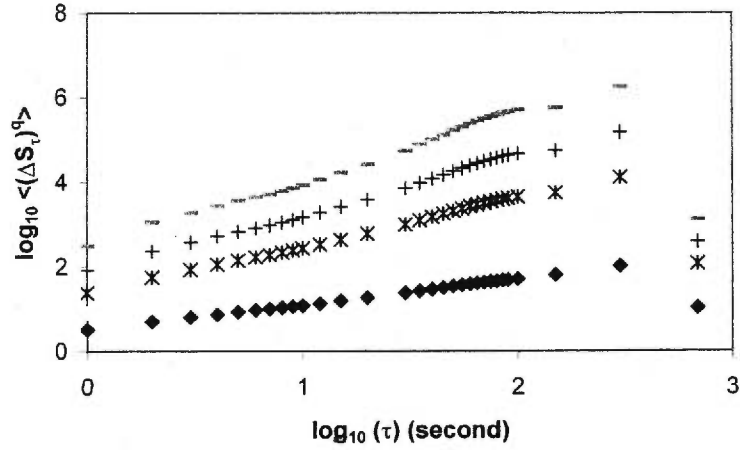
Structure functions, El Crucero (15 km)
17e3



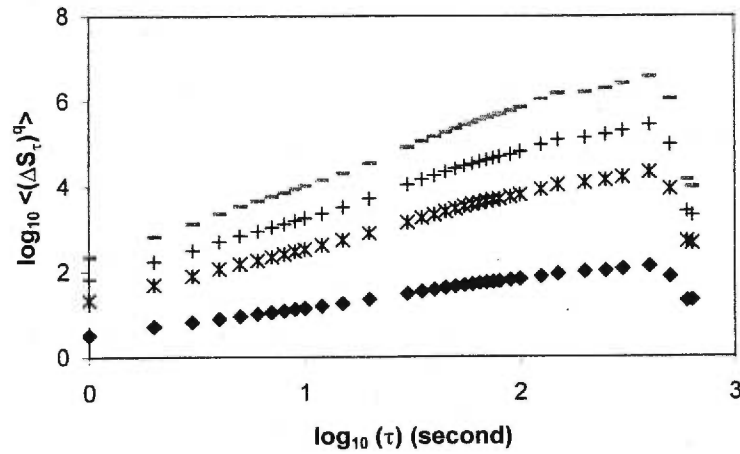
Structure functions, El Crucero (15 km)
17e4



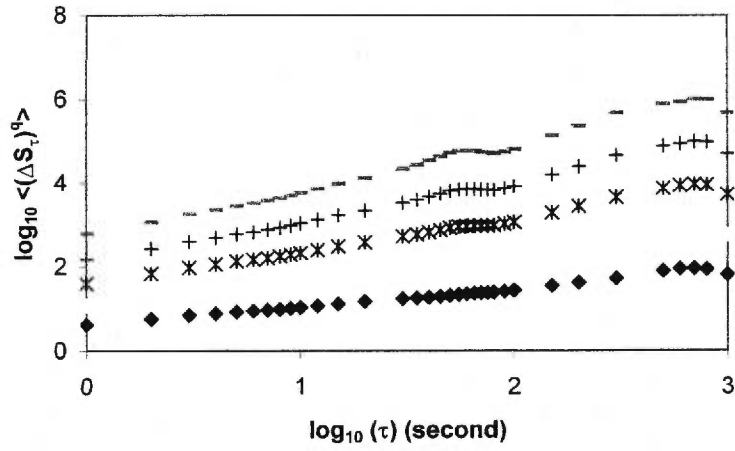
Structure functions, El Crucero (15 km)
17e5



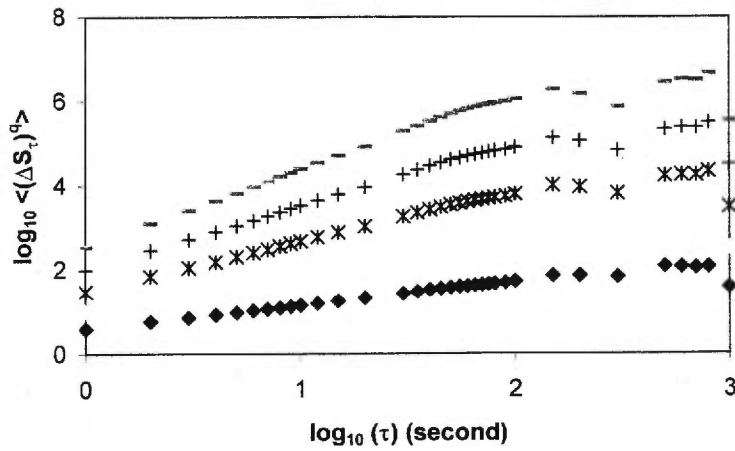
Structure functions, El Crucero (15 km)
17e6



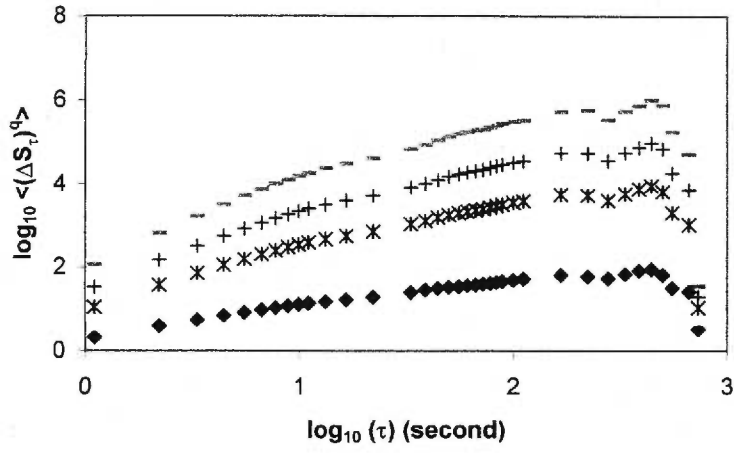
Structure functions, El Crucero (15 km)
17e7



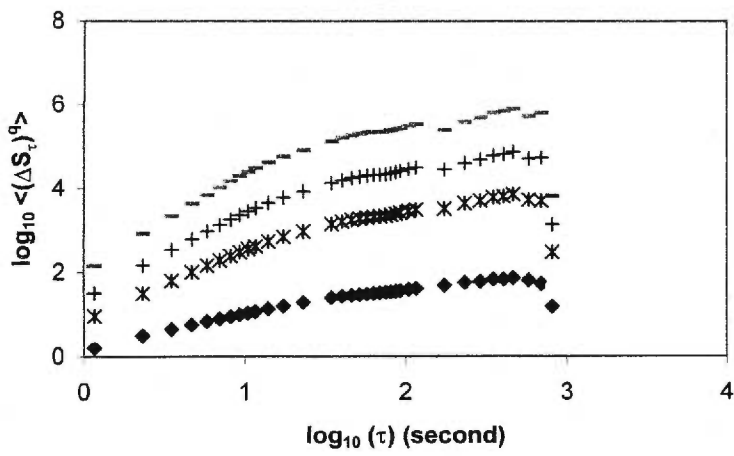
Structure functions, El Crucero (15 km)
17e8



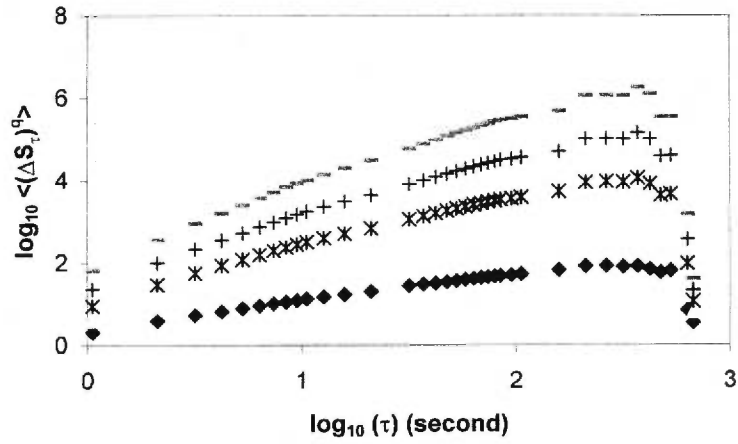
Structure functions, El Crucero (15 km)
18e1



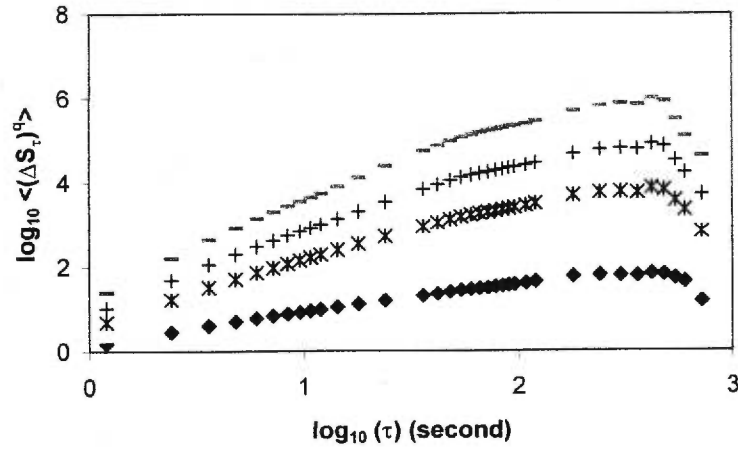
Structure functions, El Crucero (15 km)
18e2



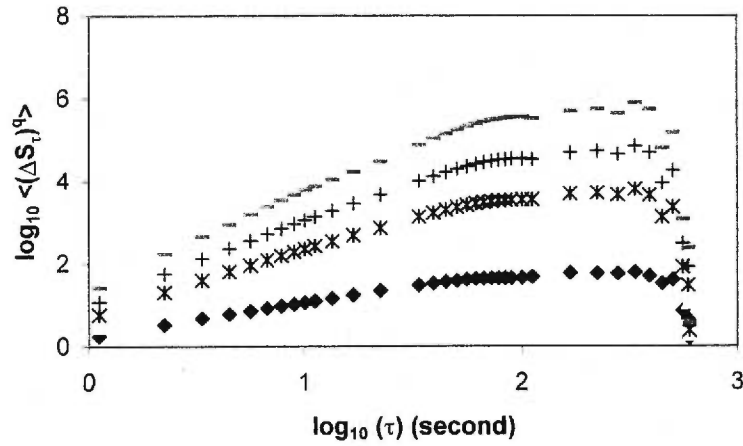
Structure functions, El Crucero (15 km)
18e3



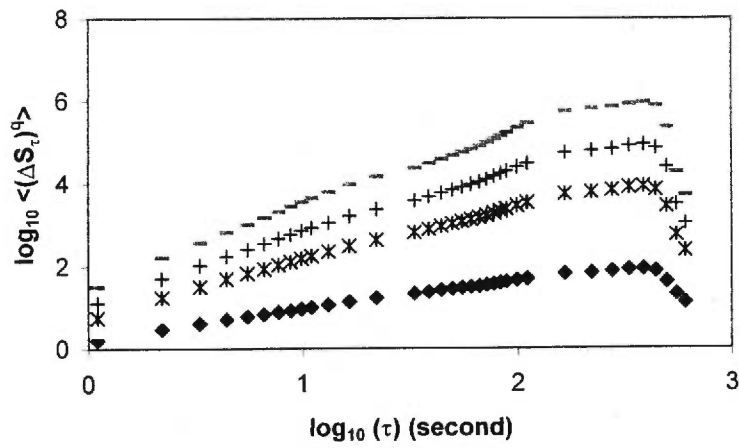
Structure functions, El Crucero (15 km)
18e4



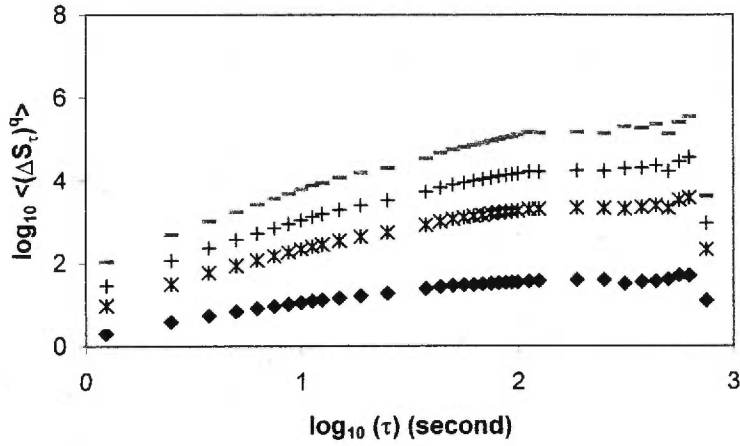
Structure functions, El Crucero (15 km)
18e5



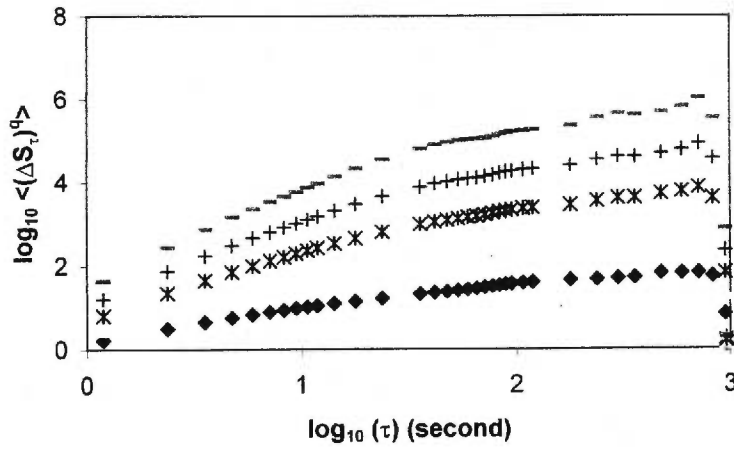
Structure functions, El Crucero (15 km)
18e6



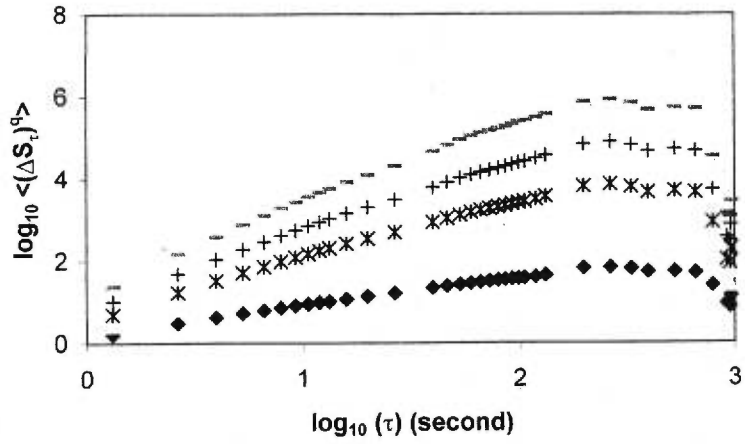
Structure functions, El Crucero (15 km)
18e7



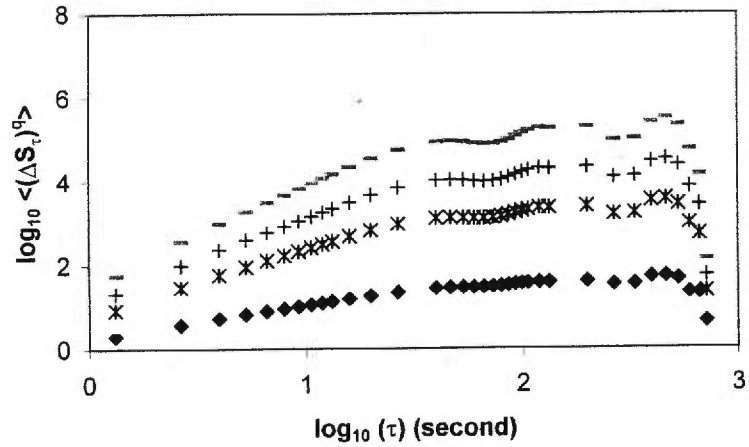
Structure functions, El Crucero (15 km)
18e8



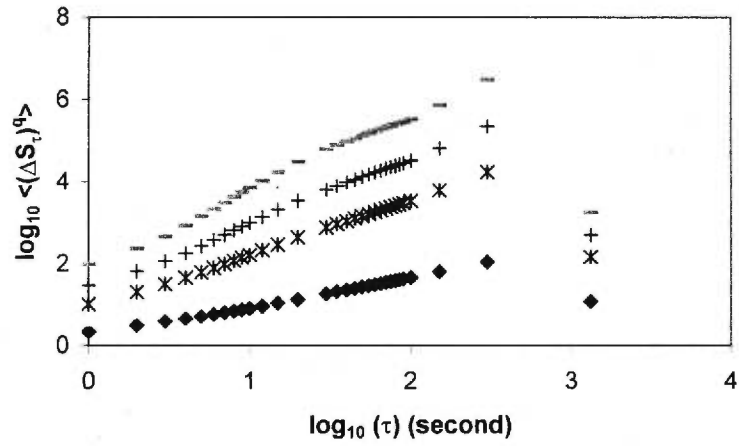
Structure functions, El Crucero (15 km)
18e9



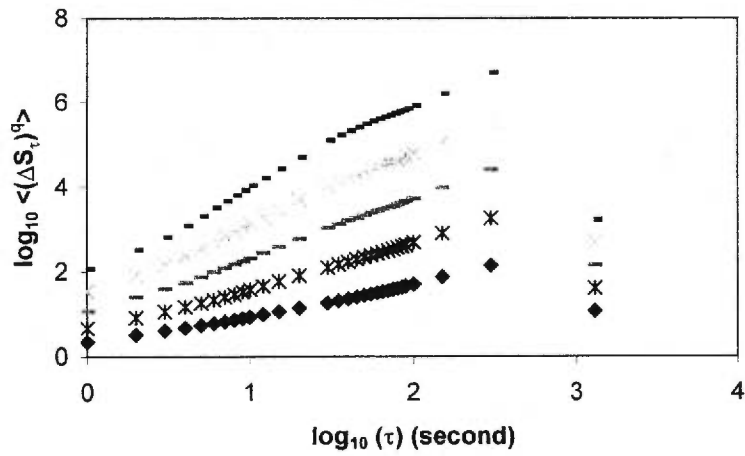
Structure functions, El Crucero (15 km)
18e10



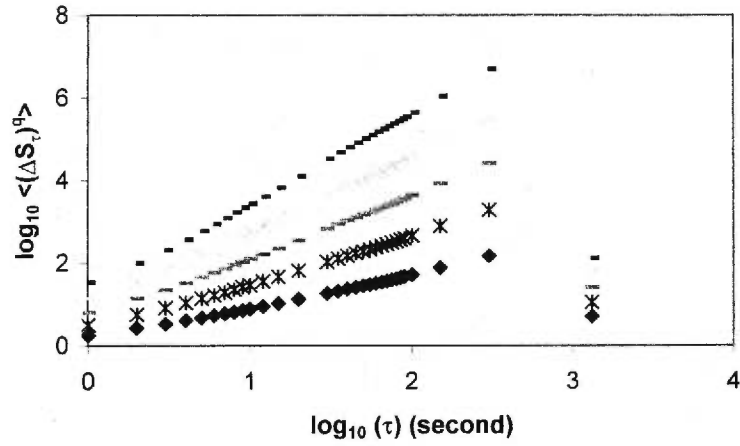
Structure functions, Masachapa (30 km)
18m1



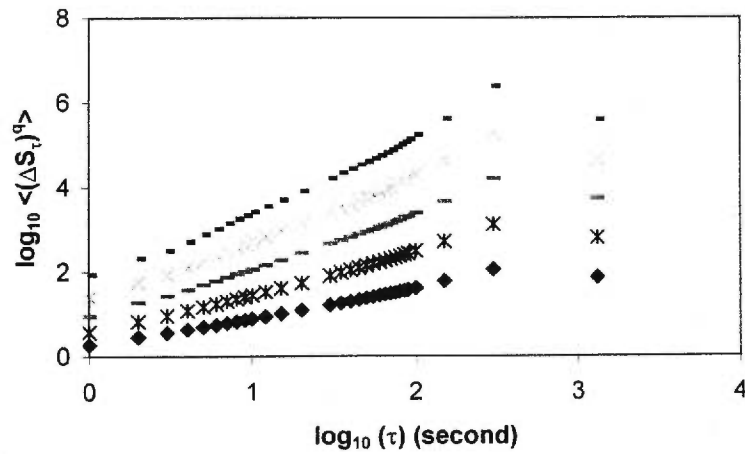
Structure functions, Masachapa (30 km)
18m2



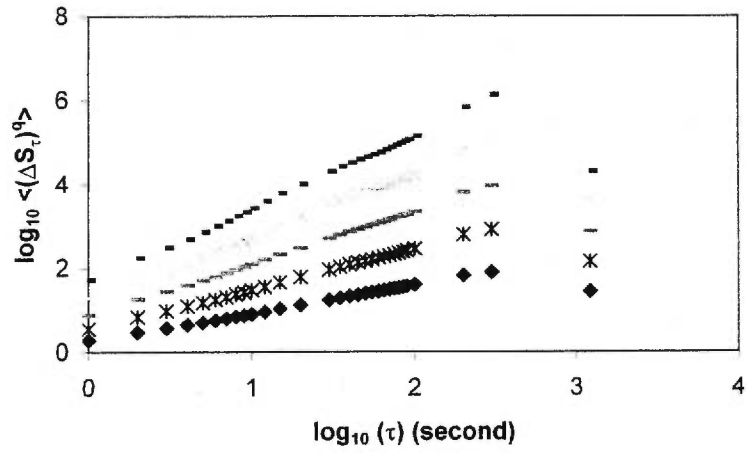
Structure functions, Masachapa (30 km)
18m3



Structure functions, Masachapa (30 km)
18m4



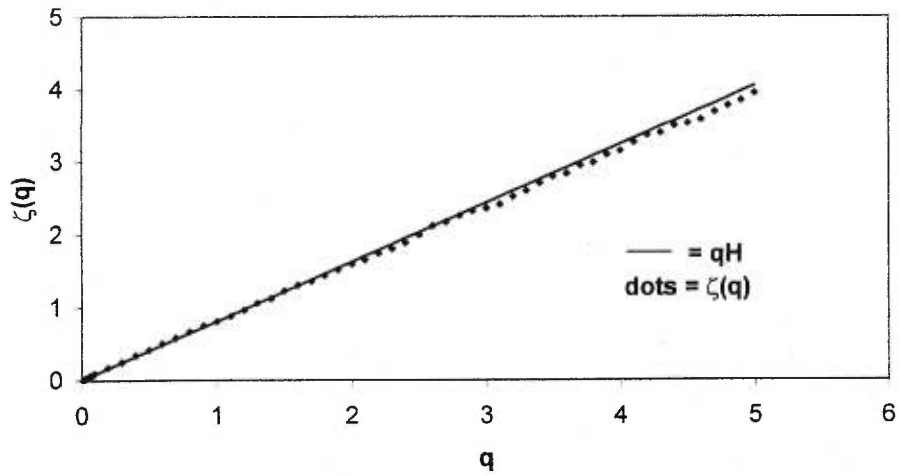
Structure functions, Masachapa (30 km)
18m6



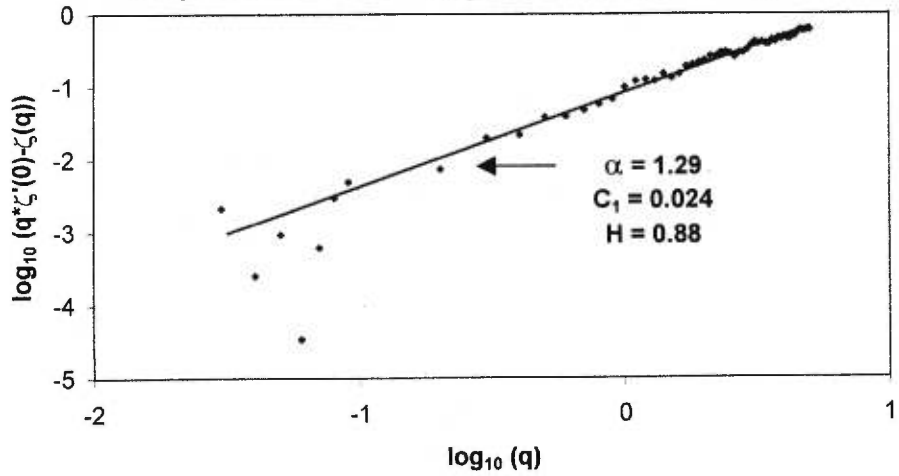
Appendix J

**Multiscaling properties and universal parameters of SO₂ signals from Masaya
volcano.**

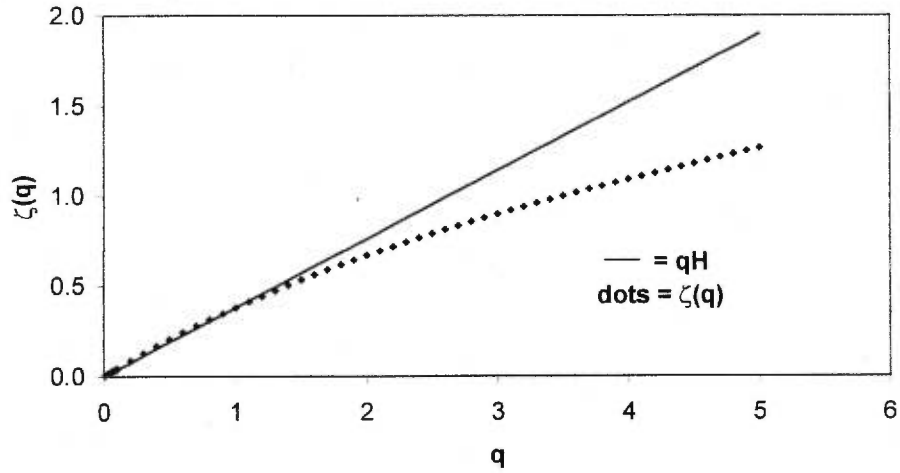
Empirical curve $\zeta(q)$ vs. monofractal curve qH ,
temporal series t97, 1st regime, Ticuantepe (5 km)



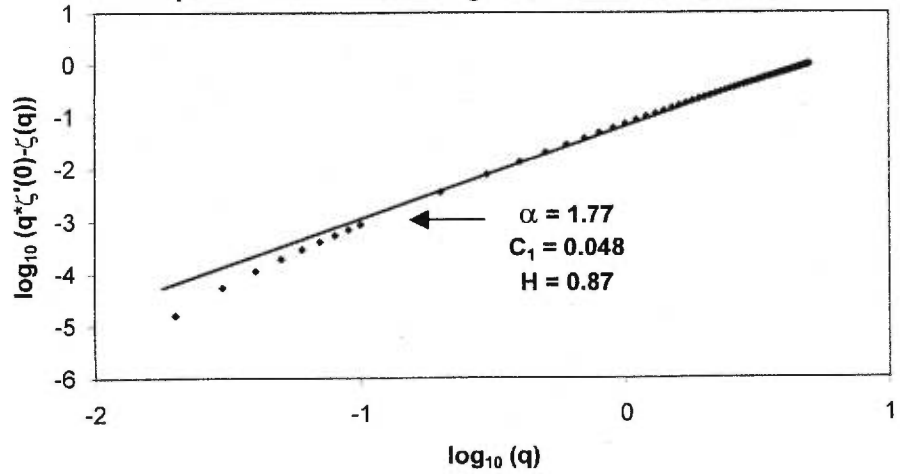
Universal parameters α and C_1 estimations,
temporal series t97, 1st regime, Ticuantepe (5 km)



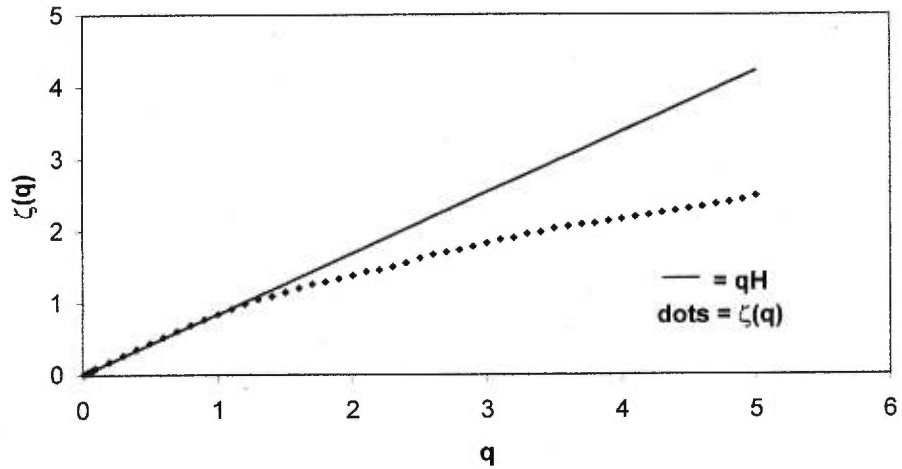
Empirical curve $\zeta(q)$ vs. monofractal curve qH ,
temporal series t97, 2nd regime, Ticuantepe (5 km)



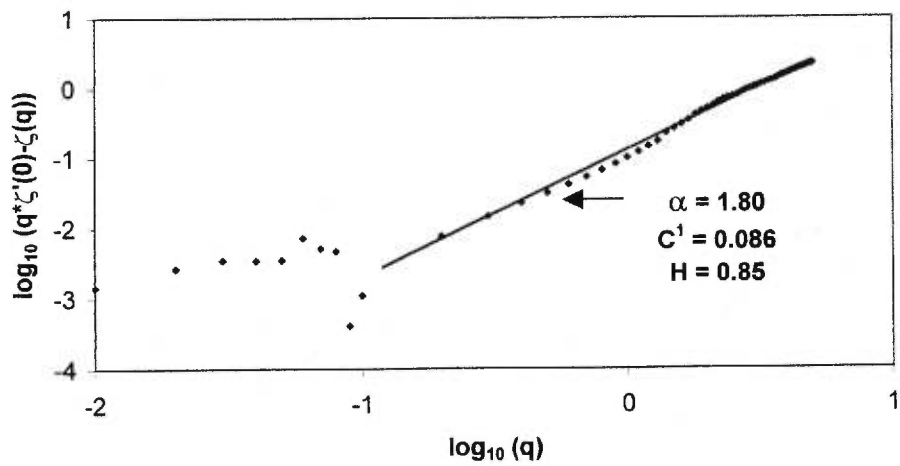
Universal parameters α and C_1 estimations,
temporal series t97, 2nd regime, Ticuantepe (5 km)



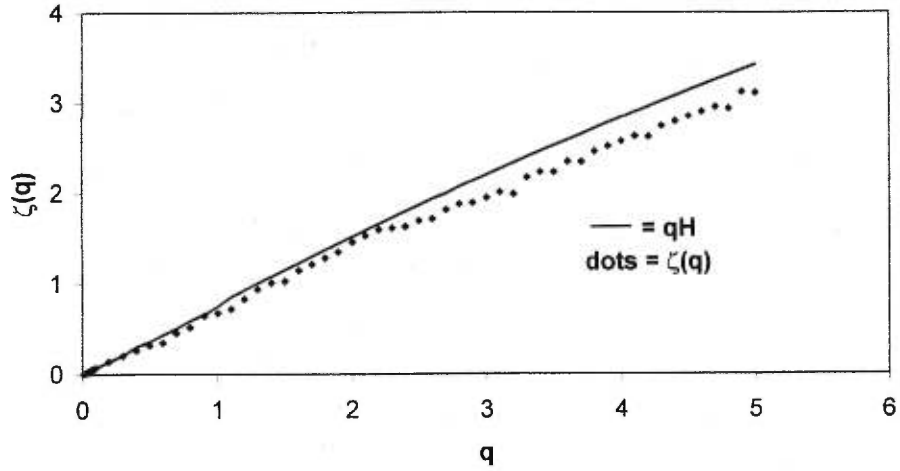
Empirical curve $\zeta(q)$ vs. monofractal curve qH ,
temporal series e03, 1st regime, El Crucero (15 km)



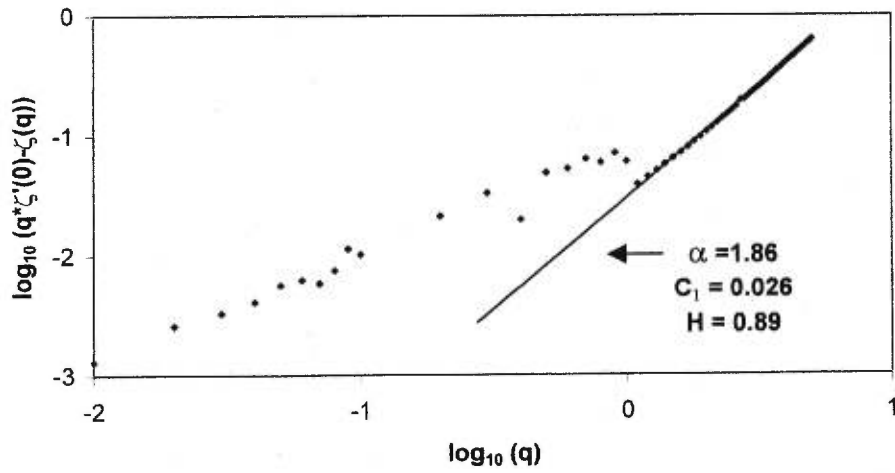
Universal parameters α and C_1 estimations,
temporal series e03, 1st regime, El Crucero (15 km)



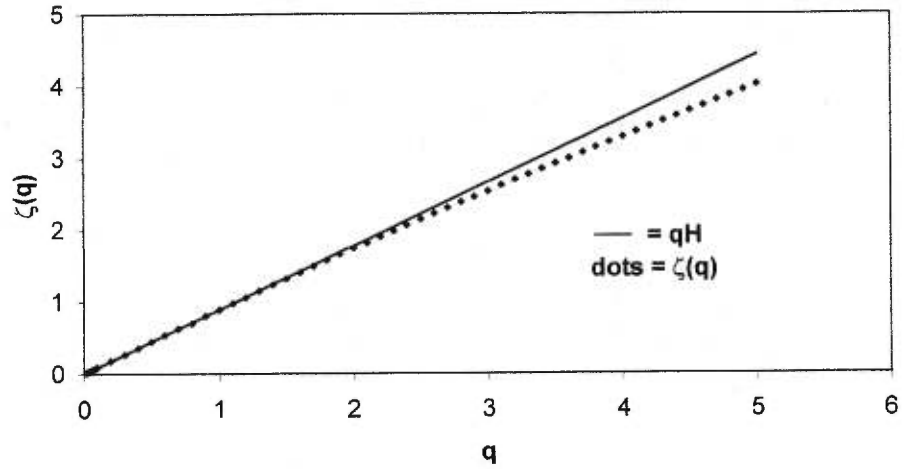
**Empirical curve $\zeta(q)$ vs. monofractal curve qH
temporal series e10a, 1st regime, El Crucero (15 km)**



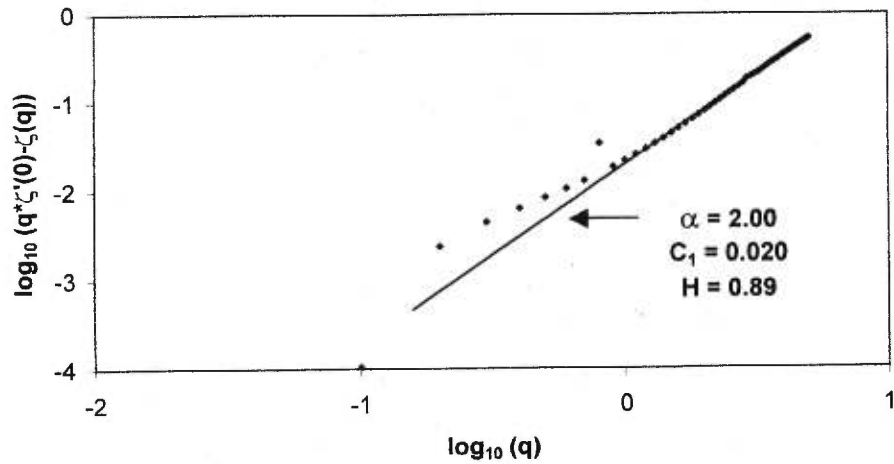
**Universal parameters α and C_1 estimations,
temporal series e10a, 1st regime, El Crucero (15 km)**



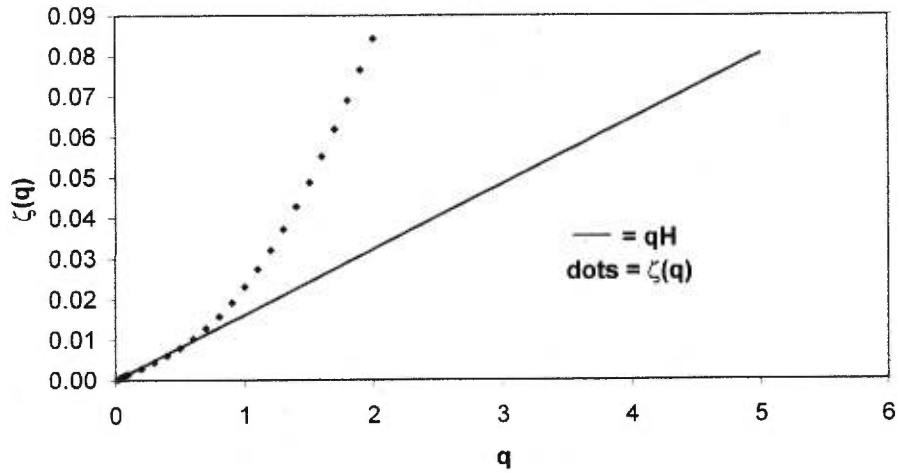
Empirical curve $\zeta(q)$ vs. monofractal curve qH ,
temporal series e10b, 1st regime, El Crucero (15 km)



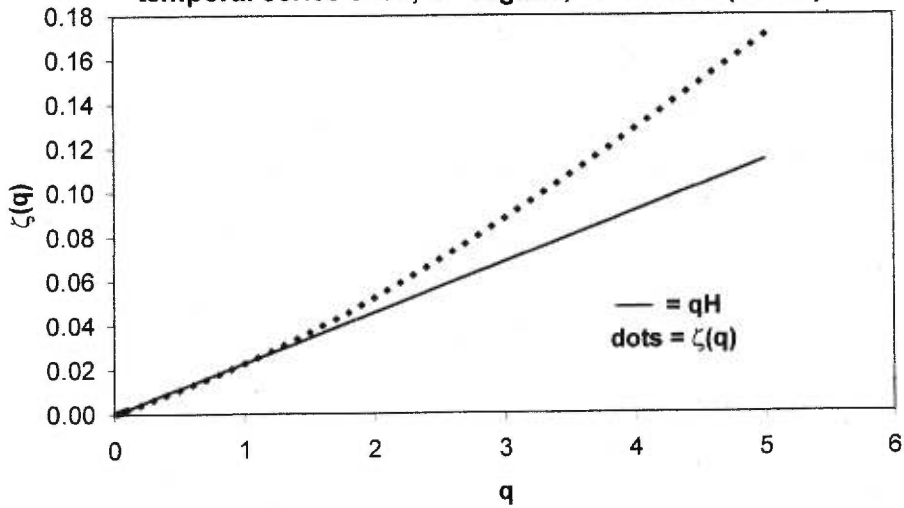
Universal parameters α and C_1 estimations,
temporal series e10b, 1st regime, El Crucero (15 km)



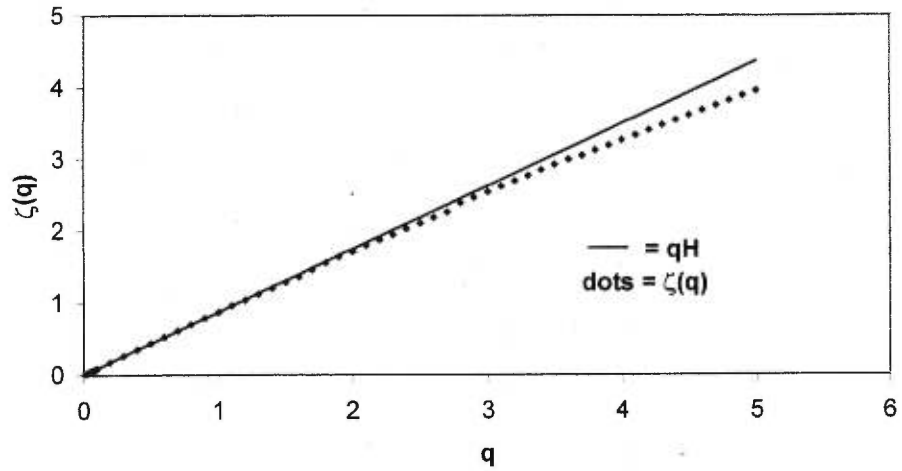
**Empirical curve $\zeta(q)$ vs. monofractal curve qH
temporal series e10a, 2nd regime, El Crucero (15 km)**



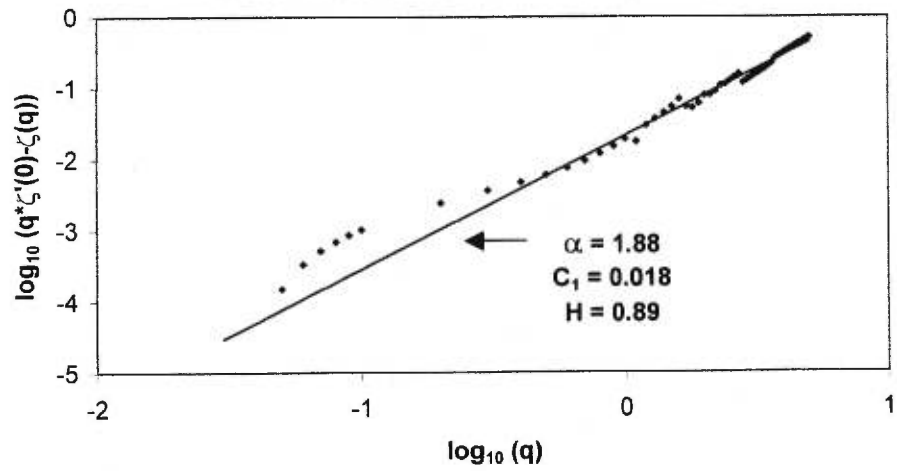
**Empirical curve $\zeta(q)$ vs. monofractal curve qH ,
temporal series e10b, 2nd regime, El Crucero (15 km)**



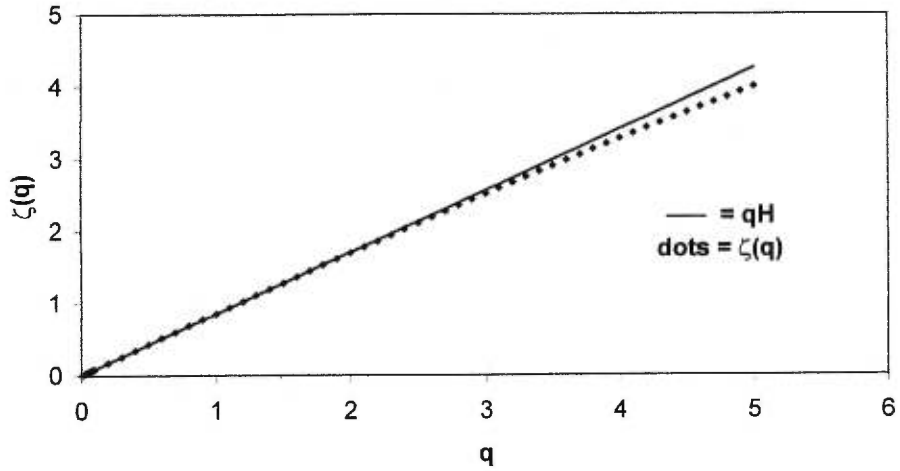
**Empirical curve $\zeta(q)$ vs. monofractal curve qH ,
spatial series 27t, Tiquantepe (5 km)**



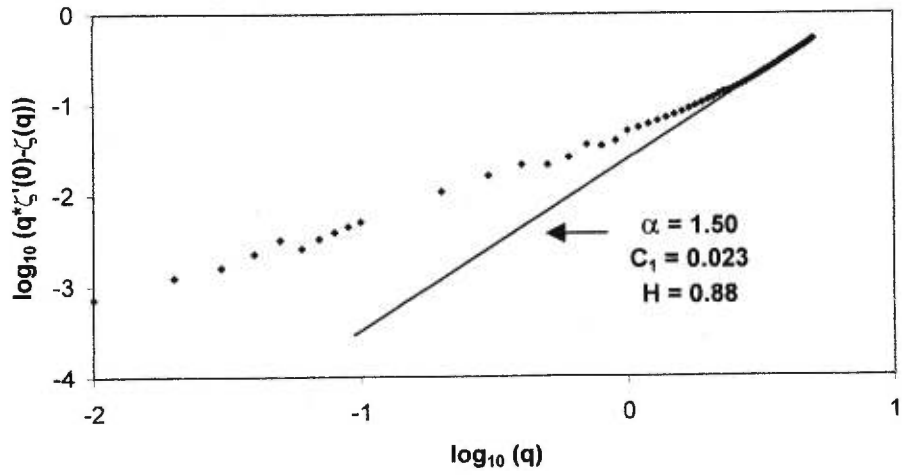
**Universal parameters α and C_1 estimations,
spatial series 27t, Tiquantepe (5 km)**



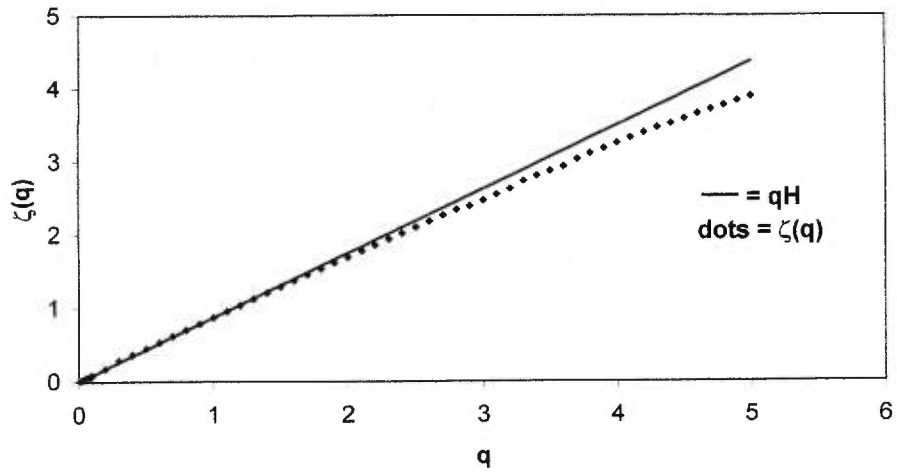
**Empirical curve $\zeta(q)$ vs. monofractal curve qH ,
spatial series 28t, Tiquantepe (5 km)**



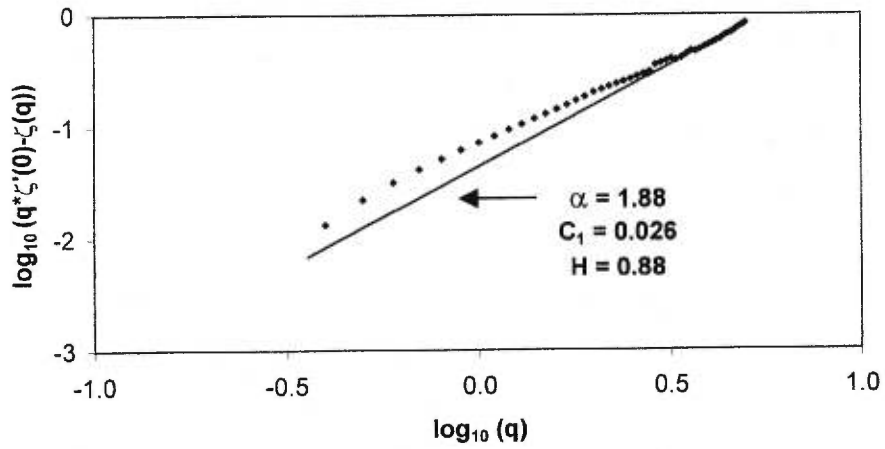
**Universal parameters α and C_1 estimations,
spatial series 28t, Tiquantepe (5 km)**



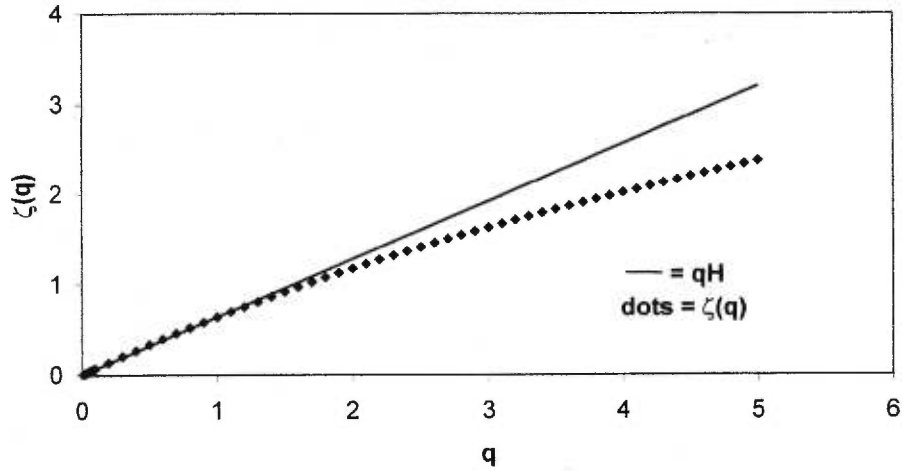
**Empirical curve $\zeta(q)$ vs. monofractal curve qH ,
spatial series 27e, El Crucero (15 km)**



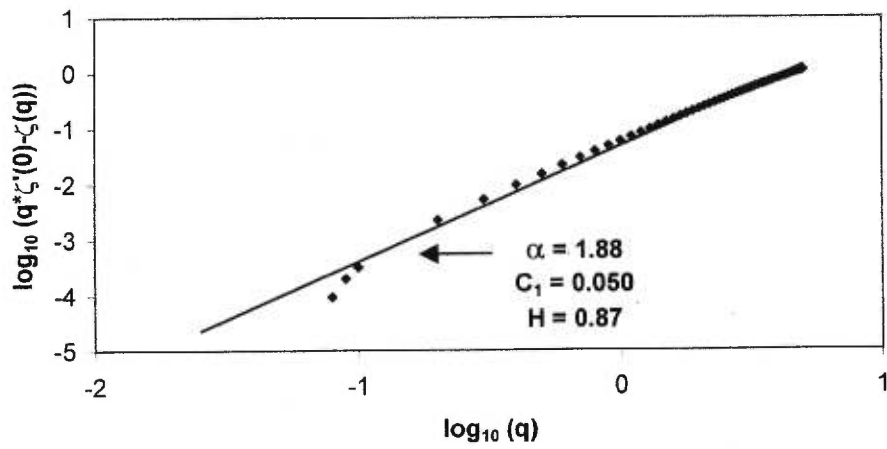
**Universal parameters α and C_1 estimations,
spatial series 27e, El Crucero (15 km)**



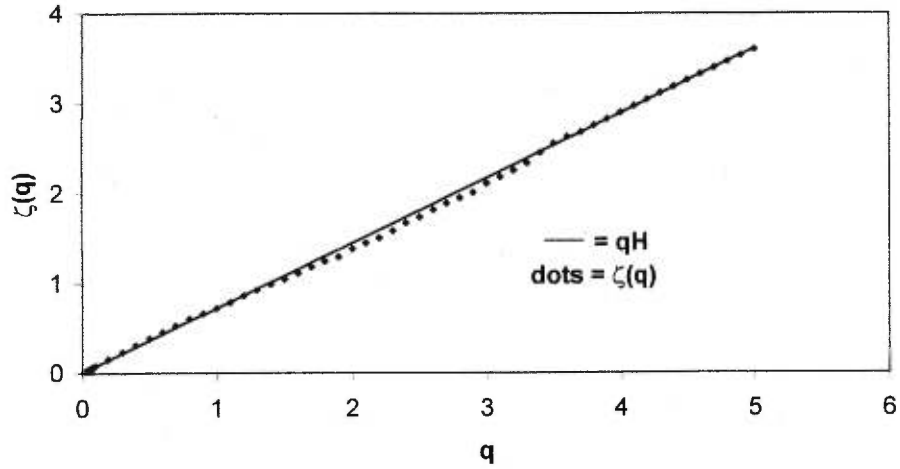
**Empirical curve $\zeta(q)$ vs. monofractal curve qH ,
spatial series 17e2, El Crucero (15 km)**



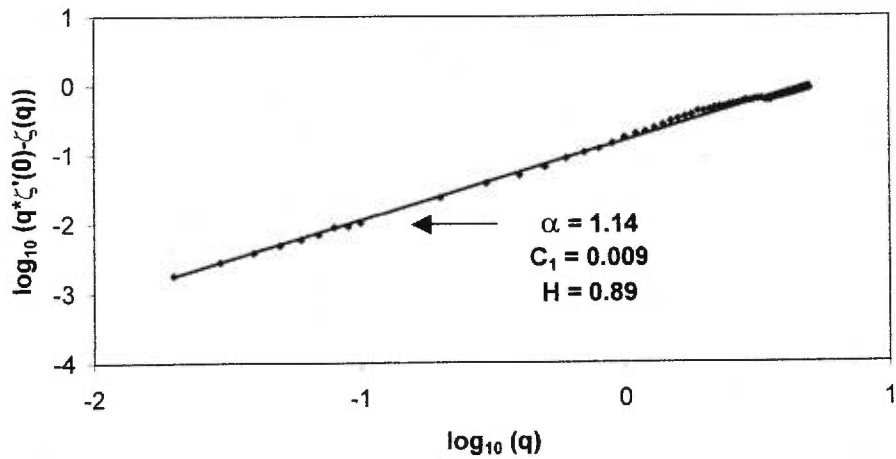
**Universal parameters α and C_1 estimations,
spatial series 17e2, El Crucero (15 km)**



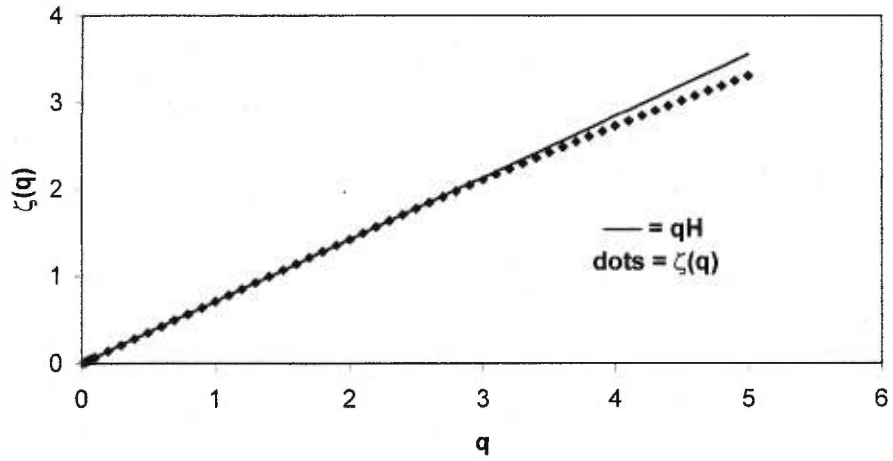
**Empirical curve $\zeta(q)$ vs. monofractal curve qH ,
spatial series 18m1, Masachapa (30 km)**



**Universal parameters α and C_1 estimations,
spatial series 18m1, Masachapa (30 km)**



**Empirical curve $\zeta(q)$ vs. monofractal curve qH ,
spatial series 18m2, Masachapa (30 km)**



**Universal parameters α and C_1 estimations,
spatial series 18m2, Masachapa (30 km)**

